University of Southampton

Faculty of Natural and Environmental Sciences

School of Ocean and Earth Science

Alteration products of seafloor massive sulphides: a source of critical metals?

by

Christian Star Bishop, MGeol

ORCiD - 0000-0003-0652-3008

Thesis for the degree of Doctor of Philosophy

30th June, 2025

University of Southampton

Abstract

Faculty of Natural and Environmental Science

School of Ocean and Earth Sciences

Thesis for the degree of Doctor of Philosophy

Alteration products of seafloor massive sulphides: a source of critical metals?

By Christian Star Bishop

The global shift toward renewable energy technologies has driven demand for critical and strategic metals (e.g., Cu and Zn). As terrestrial deposits become more expensive and difficult to explore, seafloor massive sulphide (SMS) deposits emerge as promising alternative metal resources. When exposed at the seafloor, sulphides oxidise, forming secondary minerals including Fe-oxyhydroxide (FeOOH) and atacamite, which trap metals otherwise lost to seawater. Despite their potential significance, key unknowns remain regarding their variety, metal content, approximate tonnage, and geochemical evolution at the seafloor, leaving their resource potential and long-term fate uncertain. This study investigates secondary FeOOH deposits at the Semenov hydrothermal field (13°30′N, Mid-Atlantic Ridge) and aims to understand their formation, evolution, and resource potential. Here, I distinguish two types of FeOOH: i) metal-poor (<0.4 wt.% Cu+Zn) primary precipitates forming hydrothermal chimneys with Mn-oxide banding and green smectite; and ii) metal-rich (average 2.55 wt.% Cu+Zn) secondary FeOOH deposits occurring as fine-grained ochres, layered and brecciated deposits, remnant hydrothermal chimneys, and massive deposits. Approximately 50,000 - 880,000 t of secondary FeOOH material at Semenov is estimated that can sequester 1,300-22,400 t Cu and Zn. These figures suggest that secondary FeOOH could serve as viable supplementary resources. However, Semenov sits close to the MAR and does not represent an off-axis deposit. Therefore, understanding how the geochemical composition of FeOOH evolves at Semenov is crucial to determining whether sulphide weathering products in older, off-axis SMS deposits can retain their economic value over extended timescales. Initially, these deposits inherit metals directly from their sulphide protolith. Seawater interaction then modifies their composition, imparting a REE fingerprint with negative Ce anomaly while sulphur is depleted. Crucially, Cu and Zn mobilised during sulphide oxidation (pH 4.5–8.2) can become sequestered onto FeOOH through adsorption. With sufficient seawater mixing with these Cu-rich pore waters, atacamite veins can precipitate, further concentrating Cu within secondary FeOOH deposits. Laboratory studies suggest that, with time, the initial FeOOH mineralogy (which is dominated by ferrihydrite) transforms to goethite with the potential release of up to 90% Cu and Zn up to 57%. Despite this, goethite crystallisation from ferrihydrite may not be extensive under seafloor conditions at SMS deposits, and thus secondary FeOOH deposits can continue to function as long-term metal traps. In contrast, Au and Ag are not incorporated into secondary FeOOH or atacamite, but concentrate at the shrinking sulphide phase as it progressively oxidises. On completion of sulphide oxidation, Au and Ag depart from the secondary FeOOH deposits. It is speculated that these precious metals are re-mobilised as thiosulphate complexes that precipitate upon seawater contact or at the FeOOH-sulphide boundary deeper within the SMS deposit, potentially creating hitherto unrecognised enrichment zones. The fate of sulphide weathering products depends on the interplay between oxidation and reduction. Sulphide oxidation typically follows non-linear kinetics, with secondary FeOOH forming protective barriers that preserve sulphide cores and weathering products under oxic conditions. Under reducing conditions, however, FeOOH and atacamite may dissolve, potentially stripping metals from the system. Beyond resource potential, secondary FeOOH and atacamite can serve as exploration vectors. Atacamite highlights Cu-enriched areas and potential drilling targets for underlying Cu-rich sulphide ores. Seafloor samples can be rapidly screened by portable XRF to map Cu anomalies in real-time during surveys, guiding drilling efforts toward concealed ore bodies. This advances our understanding of sulphide weathering and metal cycling on the seafloor while providing a framework for evaluating weathering products as both resources and exploration guides for critical metals.

Table of Contents

Table of Tables

Table of Figures

List of Accompanying Digital Materials

1. Bishop et al. (2025a). **Images and descriptions** of Fe-oxyhydroxide and massive sulphide samples from Semenov Hydrothermal Field of the Mid-Atlantic Ridge during the RRS James Cook cruise JC224 (March-April 2022). NERC EDS British Oceanographic Data Centre NOC. https://doi.org/10.5285/2e0a9d33-56f6-622d-e063-7086abc06e59
2. Bishop et al. (2025b). **Geochemical composition, isotopic measurements and X-ray diffraction (XRD)** results of Fe-oxyhydroxide and massive sulphide samples from Semenov Hydrothermal Field of the Mid-Atlantic Ridge during the RRS James Cook cruise JC224 (March-April 2022). NERC EDS British Oceanographic Data Centre NOC. https://doi.org/doi:10.5285/2e0aa2c7-6331-62b9-e063-7086abc06891
3. Bishop et al. (2025c). **Geochemical and mineralogical** analysis of sulphide materials and seawater from oxidative dissolution experiments, from samples obtained from Wetar Island, Indonesia (~2002), from RV Celtic Explorer cruise CE11009 (2011) and from RRS James Cook cruises JC082 (2013) and JC138 (2016). NERC EDS British Oceanographic Data Centre NOC. https://doi.org/doi:10.5285/2ea9a7f7-c47f-2bff-e063-7086abc06652
4. Bishop, C., Josso, P., Lichtschlag, A., Roberts, S., Belgrano, T., Milton, J., Lesage, M., & Murton, B. (2025d). **Geochemical analyses, sequential leaching and X-ray diffraction (XRD)** results of Fe-oxyhydroxide and massive sulphide samples from the Semenov Hydrothermal Field, Mid-Atlantic Ridge, during RRS James Cook cruise JC224 (March-April 2022). NERC EDS British Oceanographic Data Centre NOC. https://doi.org/doi:10.5285/3724bb78-2139-edbe-e063-7086abc0903f
5. Bishop, C., Josso, P., Lichtschlag, A., Roberts, S., Belgrano, T., Lesage, M., & Murton, B. (2025e). **Raw laser-ablation inductively couple plasma mass spectrometer** (LA-ICP-MS) data and **images of laser-ablation (LA) targets** of Fe-oxyhydroxide and massive sulphide samples from the Semenov Hydrothermal Field of the Mid-Atlantic Ridge during the RRS James Cook cruise JC224 (March-April 2022). NERC EDS British Oceanographic Data Centre NOC. https://doi.org/doi:10.5285/373699c7-6323-d4fa-e063-7086abc08606
6. Bishop, C., Josso, P., Lichtschlag, A., Roberts, S., Belgrano, T., Milton, J., Lesage, M., & Murton, B. (2025f). **Raw laser-ablation time-of-flight inductively couple plasma mass spectrometer** (LA-TOF-ICP-MS) data from sample 82_HY_06 from the Semenov Hydrothermal Field of the Mid-Atlantic Ridge during the RRS James Cook cruise JC224 (March-April 2022). NERC EDS British Oceanographic Data Centre NOC. https://doi.org/doi:10.5285/37352554-2193-8984-e063-7086abc047f5

Research Thesis: Declaration of Authorship

Print name: **Christian Star Bishop**

Title of thesis: **Alteration Products of Seafloor Massive Sulphides: A Source of Critical metals?**

I declare that this thesis and the work presented in it are my own and has been generated by me as the result of my own original research.

I confirm that:

1. This work was done wholly or mainly while in candidature for a research degree at this University;
2. Where any part of this thesis has previously been submitted for a degree or any other qualification at this University or any other institution, this has been clearly stated;
3. Where I have consulted the published work of others, this is always clearly attributed;
4. Where I have quoted from the work of others, the source is always given. With the exception of such quotations, this thesis is entirely my own work;
5. I have acknowledged all main sources of help;
6. Where the thesis is based on work done by myself jointly with others, I have made clear exactly what was done by others and what I have contributed myself;
7. Parts of this work have been published as:

Bishop et al. (2025a). Images and descriptions of Fe-oxyhydroxide and massive sulphide samples from Semenov Hydrothermal Field of the Mid-Atlantic Ridge during the RRS James Cook cruise JC224 (March-April 2022) NERC EDS British Oceanographic Data Centre NOC. https://doi.org/10.5285/2e0a9d33-56f6-622d-e063-7086abc06e59

Bishop et al. (2025b). Geochemical composition, isotopic measurements and X-ray diffraction (XRD) results of Fe-oxyhydroxide and massive sulphide samples from Semenov Hydrothermal Field of the Mid-Atlantic Ridge during the RRS James Cook cruise JC224 (March-April 2022). NERC EDS British Oceanographic Data Centre NOC. https://doi.org/doi:10.5285/2e0aa2c7-6331-62b9-e063-7086abc06891

Bishop et al. (2025c). Geochemical and mineralogical analysis of sulphide materials and seawater from oxidative dissolution experiments, from samples obtained from Wetar Island, Indonesia (~2002), from RV Celtic Explorer cruise CE11009 (2011) and from RRS James Cook cruises JC082 (2013) and JC138 (2016). NERC EDS British Oceanographic Data Centre NOC. https://doi.org/doi:10.5285/2ea9a7f7-c47f-2bff-e063-7086abc06652

Bishop, C., Josso, P., Lichtschlag, A., Roberts, S., Belgrano, T., Milton, J., Lesage, M., & Murton, B. (2025d). Geochemical analyses, sequential leaching and X-ray diffraction (XRD) results of Fe-oxyhydroxide and massive sulphide samples from the Semenov Hydrothermal Field, Mid-Atlantic Ridge, during RRS James Cook cruise JC224 (March-April 2022). NERC EDS British Oceanographic Data Centre NOC. https://doi.org/doi:10.5285/3724bb78-2139-edbe-e063-7086abc0903f

Bishop, C., Josso, P., Lichtschlag, A., Roberts, S., Belgrano, T., Lesage, M., & Murton, B. (2025e). Raw laser-ablation inductively couple plasma mass spectrometer (LA-ICP-MS) data and images of laser-ablation (LA) targets of Fe-oxyhydroxide and massive sulphide samples from the Semenov Hydrothermal Field of the Mid-Atlantic Ridge during the RRS James Cook cruise JC224 (March-April 2022). NERC EDS British Oceanographic Data Centre NOC. https://doi.org/doi:10.5285/373699c7-6323-d4fa-e063-7086abc08606

Bishop, C., Josso, P., Lichtschlag, A., Roberts, S., Belgrano, T., Milton, J., Lesage, M., & Murton, B. (2025f). Raw laser-ablation time-of-flight inductively couple plasma mass spectrometer (LA-TOF-ICP-MS) data from sample 82_HY_06 from the Semenov Hydrothermal Field of the Mid-Atlantic Ridge during the RRS James Cook cruise JC224 (March-April 2022). NERC EDS British Oceanographic Data Centre NOC. https://doi.org/doi:10.5285/37352554-2193-8984-e063-7086abc047f5

Bishop, C., Murton, B., Lichtschlag, A., Roberts, S., and Lesage, M. (2025g). Environmental and economic perspectives on Fe-oxyhydroxide and atacamite at seafloor massive sulphide deposits, EGU General Assembly 2025, Vienna, Austria, 27 Apr–2 May 2025, EGU25-16655, https://doi.org/10.5194/egusphere-egu25-16655

Bishop, C.S, Lichtschlag, A, Roberts, S., Lesage, M., Murton, B.J., Fe-oxyhydroxide deposits at Semenov Hydrothermal Field (13°30'N), Mid-Atlantic Ridge: insights into formation, modification and resource potential, *Mineralium Deposita*, https://doi.org/10.1007/s00126-025-01376-6

Signature: .....Date:30th June 2025

Acknowledgements

Throughout my PhD, life has been a rollercoaster, from the highs of getting my first paper accepted in a journal to those sinking feelings when things go disastrously wrong! These past four years have undoubtedly been some of the most rewarding experiences of my life. I will truly cherish the time I have had here and will talk about it for decades to come.

I have so many people to thank for helping me achieve this milestone. First and foremost, I must thank my supervisor, Prof. Bramley J. Murton, for his guidance and patience with my not-quite-there-yet writing skills! Bram has always been there when I need him, and I am so grateful for his vast knowledge that has helped me immensely. I am particularly grateful for the opportunity to participate in a seagoing research expedition and to work on some of the most interesting (and hotly debated) research in the field.

Dr. Anna Lichtschlag also deserves a massive thank you, again for your patience, but also because your different perspective on my research has helped me think more critically about my work. One specific example being the 'so what?' aspect of my research! My gratitude extends to Prof. Stephen Roberts, who has been incredibly helpful with my PhD and without whom Chapter 6 wouldn't exist. Dr. Maxime Lesage from Green Minerals has been an excellent supervisor throughout my PhD, I remember our engaging conversations and your engineering perspective that always provided valuable insights into my research. A massive thank you goes to everyone at Green Minerals who provided me with this opportunity of a lifetime.

Special thanks go to everyone involved in the JC224 research expedition: the science party, officers, crew, and the HyBIS team. Each and every person was instrumental to the expedition's success, and I am deeply grateful to them all. Aboard the James Cook, I met and became friends with amazing scientists including Isobel Yeo, Pierre Josso, Andrew Martin, Katie McFall, John Jamieson, Sven Petersen, Simon Allerton, and Paul Lusty, all of whom provided invaluable discussions and insights that shaped my thesis. Special recognition goes to Andrew Martin and Sven Petersen, who were extremely helpful in writing my first paper. I am particularly thankful to Pierre Josso, you have been both a great friend and scientist, helping me through tough times, and without you, my second study would not have been possible.

Thomas Belgrano was also essential to my second study. Without our chance meeting at the rock prep lab in Southampton, I would not have had the nano-powder standards needed to calibrate and quality control my laser data. So, a big thank you for that crucial contribution and to all of our discussions since then. Speaking of people at the university who were essential to my studies, huge thanks go to Dr. Matt Cooper, Prof. Andy Milton, Dr. Richard Pearce, Dr. Kate Peel, Dr. Agnieszka Michalik and Dan Doran. Without any of you, the labs at Southampton would fall apart!

Thank you to my office mates Acer Figueroa, Szu-ying Lai, and Micaela Small, who made my PhD experience fun within the office. I will always be jealous of how beautifully you can sing, Acer! Outside of university, I am grateful to my close friends Adam and Tom for our memorable camping trips together and being genuinely great people. To all my other friends who have been a blessing in my life, including my friends back home in Wales, Liam and Will, as well as my friends in England; Adz, Elliott, Jordan, Dan, and Tom. Thank you for your friendship and support. To my family who have helped and supported me through tough times. With a special thanks to my sister Hazel who tries her best to bring the family together!

As I well up while writing this, my personal life near the end of my PhD has been tumultuous at best. But my biggest appreciation goes to Chloe, without whom my life would have been vastly different. Without you, I wouldn't have pursued this PhD and never would have met some of the most brilliant people in my life. I am forever thankful for the memories we shared, how we grew together, and for your unwavering support.

Finally, to my mother, who never saw the man I've become, but who surely passed on to me her love of rocks.

This thesis was funded by "Project ULTRA" NERC grant NE/S004068/1 awarded to Prof. Bramley J. Murton. This work was supported by a PhD studentship funded by Green Minerals.

Definitions and Abbreviations

2SE	Two times the standard error
ANZG	Australian and New Zealand Guidelines
BET	Brunauer-Emmett-Teller
BGS	British Geological Survey
BODC	British Oceanography Data Centre
CANMET	Canada Centre for Mineral and Energy Technology
Ccp-FeOOH	Fe-oxyhydroxide derived by the oxidation of chalcopyrite ($CuFeS_2$). Typically found in massive sulphide samples with active oxidation.
Ce/Ce*	Cerium anomaly
cm	Centimetre
Critical metals	Metals that are deemed essential for modern technology and societal needs but their supply is potentially at risk
CRM	Certified reference material
DLSR	Digital single-lens reflect
DO	Dissolved oxygen
EDS	Energy dispersive X-ray spectroscopy
eSMS	Extinct seafloor massive sulphide
Eu/Eu*	Europium anomaly
FeOOH	Fe-oxyhydroxide
Gossan	Iron containing secondary deposits, largely comprises of reddish oxides typically occurring above a terrestrial sulphide ore deposit.
HCl	Hydrochloric acid
HD	High-definition
HDPE	High-density polyethylene
HF	Hydrofluoric acid
HNO_3	Nitric acid
HyBIS	Hydraulic benthic interactive sampler system
ICP-MS	Inductively couple plasma mass spectrometry
ICP-OES	Inductively couple plasma optical emission spectrometry
JC224	RRS James Cook research expedition number 224

LA-ICP-MS	Laser ablation inductively coupled plasma mass spectrometry
LA-TOF-ICP-MS	Laser ablation time-of-flight inductively coupled plasma mass spectrometry
ka	kilo-annum (thousand years)
M	Molarity
µm	Micro meter
µmol	Micromole
LDPE	Low-density polyethylene
mbsl	Metres below sea level
MAR	Mid-Atlantic Ridge
mL	Millilitre
Modified FeOOH	Secondary FeOOH deposits with no visible sulphide association by either LA-ICP-MS or reflective microscopy. Typically found in fully oxidised sulphide samples that comprise almost entirely of Fe-oxyhydroxide.
MOR	Mid-Ocean Ridge
NERC	Natural environment research council, now UKRI
NIST	National Institute of Standards and Technology
NOCS	National Oceanography Centre Southampton
OCC	Oceanic core complex
ODP	Ocean Drilling Program
OREAS	Ore Research & Exploration Assay Standards
Primary FeOOH	Fe-oxyhydroxide deposits formed by the primary precipitation of low-temperature, Fe-rich hydrothermal fluid.
Project ULTRA	Project awarded to Prof. Bramley j. Murton by NERC (NE/S004068/). The study aims to test the hypothesis that ultramafic hosted SMS deposits form extensive sub-surface mineralisation and undergo significant post-formational modification at and beneath the seafloor under the influence of highly variable pH conditions as a result of interaction with ultramafic rocks and during serpentinisation.
Py-FeOOH	Fe-oxyhydroxide derived by the oxidation of pyrite (FeS_2). Typically found in massive sulphide samples with active oxidation.
p-XRF	Portable X-ray fluorescence
REE	Rare earth element

ROV	Remotely operated vehicle
RRS	Royal Research Ship
Secondary FeOOH	Fe-oxyhydroxide deposits formed by the oxidation of sulphide mineral phases by oxygenated seawater.
SMS	Seafloor massive sulphide
SRM	Standard reference material
Strategic metals	Metals that are vital for industrial and energy infrastructure but are not currently supply constrained
TAG	Trans-Atlantic Geotraverse
USGS	United States Geological Survey
VMS	Volcanogenic massive sulphide
XRD	X-ray diffraction
wt.%	Weight percent
%RE	Percent of relative error
%RSD	Percent relative standard deviation

Chapter 1 Introduction

1.1 Rationale

1.1.1 Global resource demand and challenges

An increase in the growth of developing countries, globalisation, population, digitalisation and the transition to sustainable technology has been reflected by a rapid growth in demand of metals and materials. The Organisation for Economic Co-operation and Development (OECD, 2019) suggests that the consumption of metallic ores will increase from 9 Gt to 20 Gt by 2060. There is also a rising concern for the security of specific metals that are primarily exported from countries with geopolitical concern, such as China for Ga (~97%) or the Democratic Republic of Congo for Co (70%; Figure 1.1). The rising concerns of specific metals deemed important to modern technology and societal needs, but at a risk of supply disruption, has led many nations to develop criticality assessments (European Commission, 2023; Australian Government, 2024; Mudd et al., 2024; U.S. Geological Survey, 2024), including the UK criticality assessment with 34 critical metals listed (Table 1.1; Mudd et al., 2024). Some nations have included 'strategic' metals into their criticality assessment, with Cu listed in both Australia (Australian Government, 2024) and the EU (European Commission, 2023). Strategic metals, like Cu, are vital for industrial and energy infrastructure but are not currently supply constrained. The purpose of criticality assessments is to guide policies aimed at securing the supply of these minerals and enhancing economic resilience required for the functioning of society (Mudd et al., 2024). Although there is considerable research into developing a circular economy (e.g., recycling), critics argue that it lacks clear theoretical foundations, poorly defined limits, and faces structural obstacles. (Corvellec et al., 2022). Until these problems are resolved, and there are sufficient resources banked in the supply chain, critical metals must continue be supplied from primary sources (Ali et al., 2017; Mudd et al., 2024).

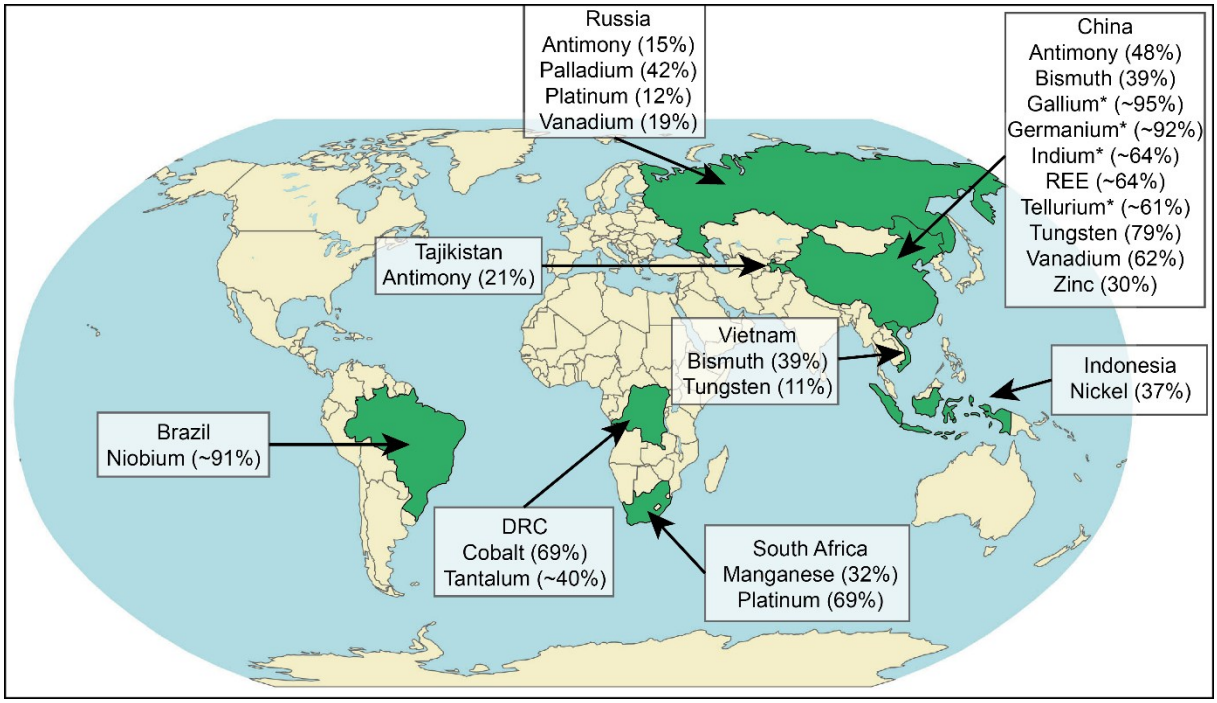

Figure 1.1. Major global producers of selected UK critical metals for 2022 (Idoine et al., 2024). DRC – Democratic Republic of the Congo. Metals with an asterisk (*) have no primary production data and are based on smelter or refinery production.

Table 1.1. UK critical metal list (Mudd et al., 2024). *Appeared on the UK critical metal list in 2021. Data provided after Idoine et al. (2024). N/A – Not applicable.

Critical metal	Lead producing country	Lead refining country
Aluminium (Al)	Australia (28.9%	China (57.3%)
Antimony (Sb)	China (48.0%)	China (63.4%)
Bismuth (Bi)	China (38.6%)	China (81.3%)
Borates	Turkey (54.2%)	N/A
Cobalt (Co)*	DRC (69.1%)	China (70.6%)
Gallium (Ga)*	N/A	China (94.8%)
Germanium (Ge)	N/A	China (92.2%)
Hafnium (Hf)	N/A	France (50.0%)
Indium (In)*	N/A	China (64.4%)
Iridium (Ir)	South Africa (81.6%)	N/A
Iron (Fe)	Australia (36.5%)	China (55.8%)
Lithium (Li)*	Australia (49.4%)	China (56.6%)
Magnesite	China (60.6%)	N/A
Magnesium (Mg)*	N/A	China (93.3%)
Manganese (Mn)	South Africa (32.1%)	China (24.6%)
Natural graphite (C)*	China (63.9%)	N/A
Nickel (Ni)	Indonesia (37.0%)	China (28.9%)
Niobium (Nb)*	Brazil (90.9%)	Brazil (89.4%)
Palladium (Pd)	Russia (41.7%)	N/A
Phosphorus (P)	China (41.8%)	China (78%)
Platinum (Pt)	South Africa (69.0%	N/A
Rare earth elements (REEs)*	China (64.0%)	China (86.8%)
Rhenium (Re)	N/A	Chile (55.9%)
Rhodium (Rh)	South Africa (78.8%)	N/A
Ruthenium (Ru)	South Africa (90.5%)	N/A
Silicon (Si)*	N/A	N/A
Sodium (Na) compounds	China (45.8%	N/A
Tantalum (Ta)*	DRC (39.8%)	China (45.5%)
Tellurium (Te)*	N/A	China (60.5%)
Tin (Sn)*	China (28.7%)	China (51.0%
Titanium (Ti)	China (33.0%)	China (51.6%)
Tungsten (W)*	China (79.2%)	N/A
Vanadium (V)*	China (61.5%	China (50.0%)
Zinc (Zn)	China (30.0%)	China (45.9%)

1.1.2 Search for new resource: from terrestrial to seafloor massive sulphide deposits

The increasing demand for critical and strategic metals in the future requires an increase in their production, however, terrestrial deposits are becoming difficult to find as many easily accessible deposits are exhausted (Ali et al., 2017). Exacerbated by the geopolitical concerns of securing critical/strategic metals, attention has turned to increasing the diversification of metal sources through the extraction of seafloor mineral resources. Specifically, three types of marine mineral deposits are currently under consideration: ferromanganese nodules, ferromanganese crusts and seafloor massive sulphide (SMS) deposits (Petersen et al., 2016). Ferromanganese nodules and crusts are rich in metals such as Co, Ni, Mn and rare earth elements (REEs) (Hein & Koschinsky, 2014), while SMS deposits can be rich in Co, Cu, Zn, Ga, Ge and In (Krasnov et al., 1995; Fouquet et al., 2010; Hannington et al., 2010; Monecke et al., 2016). SMS deposits are the focus of this thesis because, compared with Fe–Mn deposits, they exhibit higher concentrations of some economically critical metals, such as Cu and Zn, as well as other valuable metals including Au, and Ag, which enhance their economic viability and may offer a more sustainable alternative to terrestrial mining in meeting future metal demands (Hein et al., 2013; Petersen et al., 2016).

The first active submarine hydrothermal vent was observed in 1977 at the Galapagos Rift in the Pacific (Lonsdale, 1977). In the following year, the first SMS deposits were located at the axis of the East Pacific Rise (Francheteau et al., 1979). The InterRidge global database of active submarine hydrothermal vent fields provides a comprehensive list of submarine hydrothermal vent fields and as of 2020, a total of 721 vent fields among which 666 are confirmed or inferred active and 55 are inactive (Beaulieu & Szafrański, 2020). A first order approximate of the endowment in some of the critical metals in SMS deposits (e.g., Bi, Ga, Ge, In, Sb, Te) show that their grades are unlikely to be economic drivers for deep-sea mining of SMS deposits (Monecke et al., 2016). While there are a small number of exceptions, such as Co-rich sulphide, up to ~0.3-0.5 wt.% found at Rainbow, Ashadze-1 and Fåvne hydrothermal fields (Fouquet et al., 2010; Sahlström et al., 2023), the majority of SMS deposits typically range from a few up to hundreds of ppm Co (Toffolo et al., 2020). Instead, mining SMS deposits will likely be driven by their base (i.e., Cu and Zn) and precious metal (i.e., Au and Ag) content, with some critical metals possibly recovered as co- or by-products (Hannington et al., 2010; Monecke et al., 2016). The average metal grade of sulphide in SMS deposits contains approximately 4.3 wt.% Cu, 10.7 wt.% Zn, 1.7 ppm Au and 107 ppm Ag (Hannington et al., 2010). The grades of Cu and Zn in SMS deposits is shown to be higher than those found in their ancient, terrestrial analogies known as volcanogenic massive sulphide (VMS) deposits at 1.10-2.04 wt.% Cu and 1.83-5.63 wt.% Zn (Franklin et al., 1981; Barrie & Hannington, 1999). However, the disparity of the metal grades between terrestrial and marine deposits result from the preferential retrieval of high-grade surface sulphide material at SMS deposits may not be representative of the bulk composition of

the deposits. Unfortunately, reliable estimates of metal concentrations for entire deposits have only been possible where extensive sub-seafloor drilling information is available (Petersen et al., 2016). A few SMS deposits have been drilled scientifically through the Ocean Drilling Program (ODP), notably the Trans-Atlantic Geotraverse deposit (TAG; Humphris et al., 1995; Hannington et al., 1998b; Murton et al., 2019). Moreover, the only deposit to have a resource defined by drilling is Solwara 1 in the Eastern Manus Basin of Papua New Guinea. Solwara 1 reports grades of 7.2 wt.% Cu, 0.4 wt.% Zn, 5.0 g/t Au, and 23 g/t Ag, with an indicated tonnage of 1.03 Mt (Lipton et al., 2018). The lack of drilling information regarding SMS deposits also leads to the uncertainty of their size estimates, and such data only exist for a few sites (Petersen et al., 2016). Of these sites, the Transatlantic Geo-Traverse (TAG) is one of the largest known deposits at an estimated ~26 Mt (Murton et al., 2019), however, the median size of other SMS systems is approximated to be at 70,000 tonnes and a third of the systems are considered to be less than 3000 tonnes (Hannington et al., 2010). Estimates presented by Hannington et al. (2011) suggest a total of 600 Mt of SMS ore, while this is small in comparison to known VMS deposits at 13.7 billion tonnes (Franklin et al., 2005), it does not consider the potential for extinct SMS deposits located further off-axis. These hidden, older, extinct SMS deposits could dramatically increase the resource potential of SMS deposits (Petersen et al., 2018; Murton et al., 2019; Jamieson & Gartman, 2020).

A crucial factor affecting the economic potential of SMS deposits is their stability in the marine environment. When exposed to oxygenated seawater, primary sulphide minerals undergo oxidation to form secondary alteration products. Key secondary weathering products are Fe-oxyhydroxide (FeOOH) and atacamite ($Cu_2Cl(OH)_3$), which form through the progressive breakdown of the primary sulphide assemblages (Grundl & Delwiche, 1993; Hannington, 1993; Blowes et al., 2003). Recent studies suggest that these alteration minerals can retain economic metals (e.g., Cu, Zn, Au and Ag) that might otherwise be released into seawater during oxidation (Herzig et al., 1991; Dekov et al., 2011; Hu et al., 2022; Hou et al., 2024). This metal retention capability of secondary FeOOH and atacamite may represent an additional metal resource that have been previously overlooked in SMS resource assessments. Moreover, older, extinct SMS deposits located off-axis may have experienced prolonged oxidation, resulting in greater accumulations of secondary FeOOH and atacamite making these secondary products more important to consider.

1.2 Aim of the study

Seafloor massive sulphide deposits host both abundant metals and unique weathering environments at the seafloor, yet we lack a complete understanding of (1) the oxidation kinetics of sulphide weathering at SMS deposits and the impact of secondary FeOOH formation on this, (2) the geochemical evolution that SMS alteration products undergo at the seafloor, and (3) their preservation at SMS deposits and their implications for resource potential. This thesis uses the Semenov hydrothermal field (13°30'N, Mid-Atlantic Ridge) as a natural laboratory to bridge these gaps through the following specific research questions:

- How can the mineralogical and textural morphologies of FeOOH deposits at hydrothermal fields, such as Semenov, be used to distinguish variations in metal content, and how does the metal content of secondary FeOOH vary across Semenov hydrothermal field?
- What are the mechanisms governing the mobilisation, redistribution and retention of Cu, Zn, Au and Ag during sulphide oxidation, and how do post-formational modifications alter the composition of secondary FeOOH over time?
- What are the kinetics and timescales of sulphide oxidation, how does secondary FeOOH formation impact sulphide oxidation rates, and how do these interactions dictate the fate of metals at SMS systems?
- Can secondary FeOOH and atacamite serve as additional resources or exploration vectors for critical/strategic metals in SMS deposits?

To answer these question, four core studies were performed, using datasets at deposit to mineral scale and experimental approaches: **Chapter 3** details the geological mapping at the Semenov hydrothermal field; **Chapter 4** focuses on the morphological and geochemical variation of primary and secondary FeOOH deposits at Semenov; **Chapter 5** demonstrates metal mobilisation during sulphide weathering and subsequent processes that impact the geochemical composition of secondary FeOOH; and **Chapter 6** focuses on the oxidation kinetics of sulphide simulating seafloor conditions. Together, this thesis traces the evolution of sulphide weathering products: from their initial formation, modification at the seafloor and their eventual fate. The results of this thesis aim to enhance our understanding of metal cycling at the seafloor. Additionally, these findings aim to improve our ability to evaluate whether sulphide weathering products could serve as resource at SMS deposits or provide exploration guides.

1.3 Thesis structure

This thesis is organised into seven chapters that collectively address the processes governing sulphide alteration in SMS deposits and their implications for resource evaluation and exploration guides.

Chapter 1 establishes the scientific context and provides an overview of the study. It begins with a rationale outlining the growing global demand for critical and strategic metals, then discusses the potential of seafloor massive sulphide deposits as a secure source of these metals and proposes sulphide weathering products as an additional resource. It then outlines the specific research questions and provides a roadmap for the thesis. This is followed by an overview of SMS formation, weathering, and the development of key alteration products (i.e., atacamite and FeOOH). I then discuss the potential of these alteration products as a secondary resource, an exploration guide, and their relevance to environmental impacts during seafloor mining operations. The chapter also briefly describes terrestrial analogues of SMS deposits, known as VMS deposits, comparing both systems, including the formation of secondary FeOOH. Finally, it details the study area, including the geotectonic setting and geology.

Chapter 2 describes the methodology used in this thesis. It covers the sampling procedure deployed during the RRS James Cook 224 (JC224) expedition (March–April 2022), the analytical methods used to obtain the datasets, and the accuracy and precision of the resulting data.

Chapter 3 establishes the geological framework of the Semenov hydrothermal field, integrating high-resolution dive footage from the remotely operated vehicles (ROVs), i.e., the Hydraulic Benthic Interactive Sampler (HyBIS) system (JC224) and the Isis ROV (JC254, specifically at Semenov-4) with the locations of collected samples. The geological mapping defines the key morphological features such as faults, outcrops, chimneys and atacamite mineralisation that provides the essential spatial context upon which the discussion in Chapter 7 builds approximate estimates of FeOOH surface extent, thickness and tonnage.

Chapter 4 investigates multiple FeOOH samples (n=37) and a small number of massive sulphide samples (n=5) collected at Semenov during the RRS James Cook JC224 expedition in 2022 for 'Project ULTRA'. This chapter investigates the formation, modification and resource potential of FeOOH deposits at Semenov hydrothermal field. Data acquired from this study is compared with previous studies to explore the variation in metal content between FeOOH deposits at SMS systems and the reasons for this variability. The objectives of this chapter are to discriminate metal-poor primary versus metal-rich secondary FeOOH, quantify how seawater interactions modify Cu-Zn enrichment in secondary FeOOH, and assess the use of secondary FeOOH as an exploration guide for underlying sulphide.

Chapter 5 focusses on the mobility and behaviour of economic metals (i.e., Cu, Zn, Au and Ag) during the oxidation of sulphide minerals into their weathering products (i.e., FeOOH and atacamite) and the subsequent compositional changes in FeOOH. The primary objective of Chapter 5 is to develop a comprehensive weathering model for SMS deposits. While chapter four focuses on FeOOH formation at the bulk scale sample, Chapter 5 extends this analysis to the mineral scale. Examining processes at the mineral scale is used to determine how specific sulphide phases (i.e., chalcopyrite and pyrite) oxidise and mobilise economic metals into alteration products such as FeOOH and atacamite. This approach minimises contamination of other mineral phases (e.g., barite, silica, calcite, sulphide minerals) that can arise from analysing bulk samples, thereby yielding clearer and more robust data.

Chapter 6 investigates the in-situ weathering of sulphide minerals under laboratory conditions that simulate the seafloor. The key objectives of this study are to investigate: (i) Rates of sulphide oxidation at SMS deposits and understanding the reaction kinetics during the oxidation of sulphide, (ii) how mineralogy, composition and texture influence the rate of reactions and (iii) the influence of FeOOH formation on the rate of sulphide oxidation and the role of FeOOH in retaining the metal tenor of SMS deposits during oxidation. Together, these objectives aim to increase our understanding of the economic and environmental implications of oxidative dissolution of sulphide material associated with SMS mining operations.

Chapter 7 revisits the research questions that form the core objectives of this thesis. It provides a synthesis of the study's findings and construct a narrative describing the evolution of seafloor massive sulphide deposits. These narratives trace the process from initial sulphide formation through subsequent weathering and the development of alteration products, and examines the various modification processes affecting these alteration mechanisms**.** The chapter discusses the potential of sulphide weathering products as an additional resource and as exploration guides at SMS deposits. In addition, it provides new research questions that rose from this work that may be addressed in the future.

1.4 Seafloor massive sulphide systems

1.4.1 Overview

Seafloor hydrothermal circulation initiates as cold seawater infiltrates permeable pathways within the upper oceanic crust and, driven by a magmatic heat source, establishes a thermal convection cell. (Tivey, 2007; Fouquet et al., 2010). As the seawater infiltrates the crust, it initially reacts at relatively low temperatures (40-60^{o}C) with the surrounding rock, beginning to modify the fluid's chemistry before it reaches deeper, hotter zones (Figure 1.2; Alt, 1995; Tivey, 2007). At temperatures above 150^{o}C, the fluid reacts with ferrous bearing minerals such as olivine and pyroxene, resulting in the production of H_2 consuming oxygen, leading to reducing conditions (Alt, 1995). At temperatures greater than 200^{o}C, Mg is consumed to secondary silicates such as chlorite, resulting in the production of H_2, which is then consumed by the hydrolysis of primary silicates in the mafic rock (Seyfried & Mottl, 1982; Alt, 1995). In a seawater dominated system, low pH conditions can persist as silicate hydrolysis is limited with removal of Mg^{2+} generating H^{+}, leading to an excess of H^{+} in the fluid (Seyfried & Mottl, 1982; Mottl, 1983). The resultant reactions produces a slightly acidic, anoxic and chemically reduced hydrothermal fluid that leaches S and base metals from the host rock within the reaction zone at temperatures of approximately 400^{o}C, 2-3 km below the seafloor (Seewald & Seyfried, 1990; Alt, 1995). The superheated, enriched fluid then ascends along high-permeability pathways towards the seafloor. As it approaches the surface, the fluid experiences changes in redox conditions and cooling when mixing with oxygenated seawater, possibly resulting in the precipitation of sulphide minerals, including chalcopyrite, pyrite, sphalerite and sulphate minerals such as barite and anhydrite at depth.

In focused-flow systems, hydrothermal fluid (>300^{o}C) released at the seafloor precipitates sulphide, and form black smoker hydrothermal chimneys (Von Damm et al., 1985; Alt, 1995; Tivey, 2007). These chimneys are characterised by an inner core that often consists of high-temperature Cu-bearing minerals (e.g., chalcopyrite), with the outer layers containing Zn- and Fe-bearing sulphides, reflecting the cooling and mixing process (Haymon & Kastner, 1981; Haymon, 1983). Over time, tectonic activity, anhydrite dissolution, or mass wasting can cause these chimneys to collapse. The repetition of chimney growth and collapse, eventually coalesce, forming SMS deposits (Knott et al., 1998; Fouquet et al., 2010). Seawater infiltration during periods of reduced hydrothermal activity further alters these structures, initiating dissolution and re-precipitation processes that contribute to complex internal textures and mineral zoning (Petersen et al., 2000). Low-temperature (<70°C) hydrothermal fluids venting at the seafloor result from extensive mixing of high-temperature fluid with seawater at depth, leading to early sulphide precipitation below the seafloor. The resultant fluid is metal poor, but enriched in Si, Mn and Fe, and when released at the seafloor, precipitates as primary FeOOH and Mn-oxide (Alt,

1988; Hekinian et al., 1993). Low temperature hydrothermal fluid is typically associated with diffuse venting and can occur over the full life span of a hydrothermal vent system, occurring at the earliest stages of hydrothermal venting and at the fringes of high temperature venting systems (Hannington et al., 1995). Globally, hydrothermal fields cluster in distinct tectonic environments (Figure 1.3). Approximately 56% of active vent fields are located at mid-ocean ridges (MORs), with volcanic arcs, back-arc spreading centres, and intraplate settings accounting for roughly 21%, 20%, and 1% of vent fields, respectively (Figure 1.3; Beaulieu and Szafrański, 2020).

Sulphide at the seafloor are often exposed to oxygenated seawater and weather over time. Sulphide weathering produces secondary alteration products, notably secondary FeOOH and atacamite (along with its polymorphs paratacamite and botallackite). This sulphide oxidation can modify the original metal distributions and include economic metals in their alteration products, which could affect the economic potential of SMS deposits (e.g., Hu et al., 2022; Hou et al., 2024).

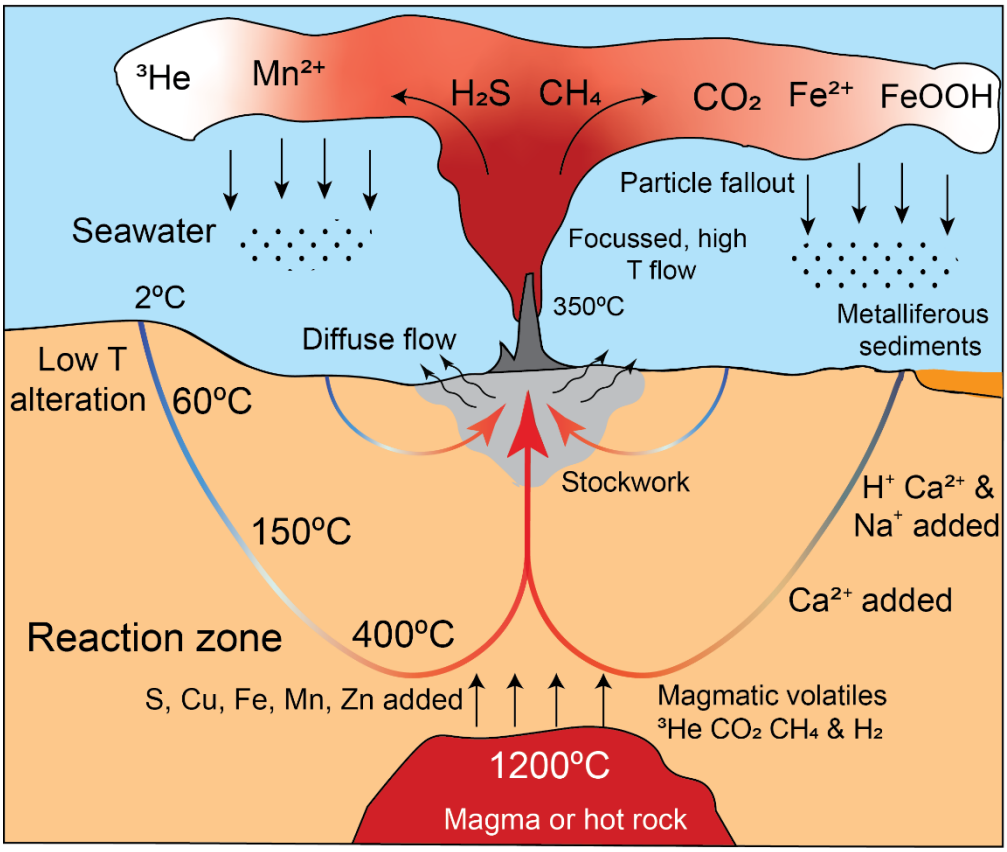

Figure 1.2. Schematic cross section of an idealised formation of a generic ridge vent system. Diagram modified after Tivey (2007), SPC (2013), (Yu et al., 2021).

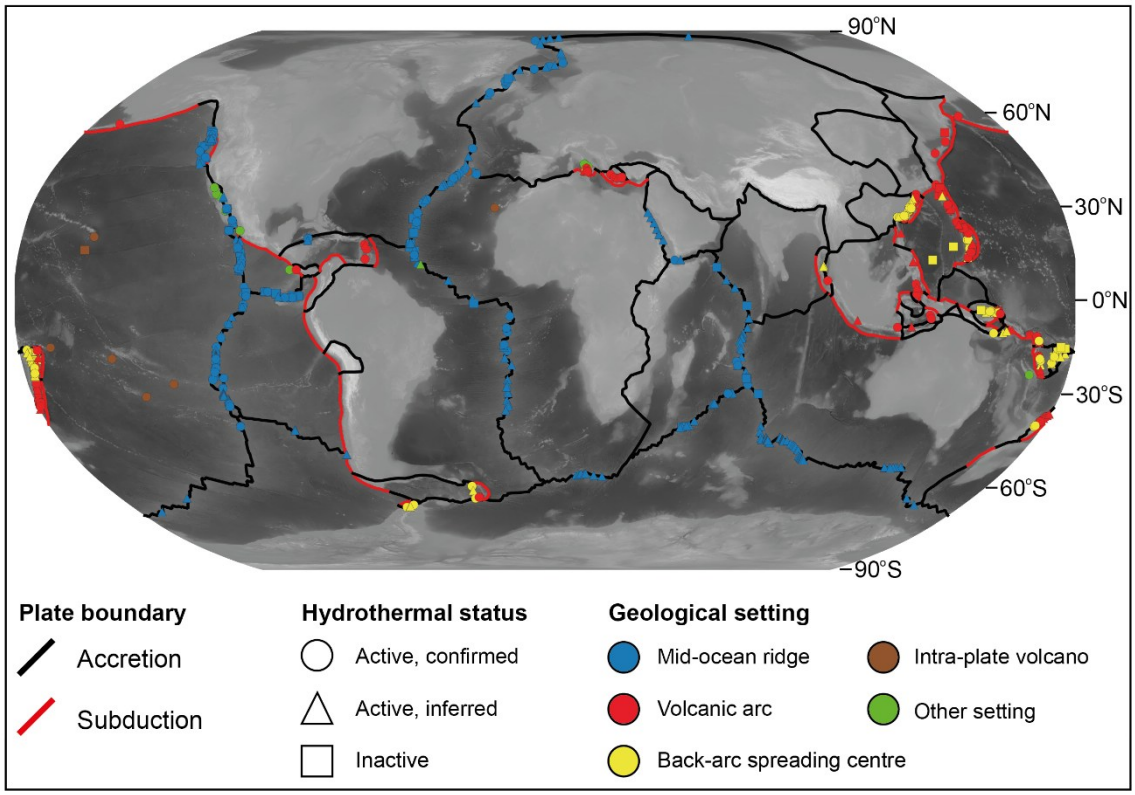

Figure 1.3. Global distribution of submarine hydrothermal fields related to plate tectonics. Tectonic plate boundaries after Bird (2003) and vent site information provided by InterRidge Vents Database after Beaulieu and Szafrański (2020). Base map is after Gebco Bathymetric Compilation Group (2024).

1.4.2 Alteration processes at the seafloor

1.4.2.1 Oxidation of sulphide minerals

Sulphide phases are unstable in oxic conditions and will break down into their alteration products through oxidation. Oxidation in terrestrial systems typically is dominated by low pH and variably reducing conditions, however, at the seafloor, the ocean serves as an infinite buffer solution with pH remaining circumneutral and the seawater being pre-dominantly oxic (Emmons, 1917; Hannington, 1993; Fallon et al., 2017). The oxidation of Fe-rich sulphide minerals, such as pyrite, in circumneutral pH will lead to the formation of secondary FeOOH (Eq. 1.1; Nicholson et al., 1988; Knight et al., 2018).

$$\boldsymbol{FeS_2 + 3.75O_2 + 3.5H_2O = Fe(OH)_{3(s)} + 2SO_4^{2-} + 4H^+} \qquad \boldsymbol{Eq.1.1}$$

Metastable ferrihydrite ($5Fe_2O_3 \cdot 9H_2O$) initially precipitates from these reactions, but transitions to a more stable phase such as goethite (α – FeOOH; Eq. 1.2; Grundl & Delwiche, 1993; Blowes et al., 2003).

$$\boldsymbol{Fe^{2+} \rightarrow Fe^{3+} \rightarrow Fe(OH)_n^{3-n} \rightarrow transitional\ FeOOH \rightarrow crstalline\ FeOOH} \qquad \boldsymbol{Eq.1.2}$$

The oxidation of Cu-bearing minerals such as chalcopyrite ($CuFeS_2$) results in the formation of secondary sulphide, such as covellite, chalcocite and bornite depending on temperature and redox conditions (Janecky & Seyfried, 1984; Bowers et al., 1985). When chalcopyrite oxidises in circumneutral conditions by oxic seawater, FeOOH form from these reactions (Eq. 1.3; Knight et al., 2018).

$$\boldsymbol{CuFeS_2 + 5H_2 + 8.5H_2O = CuO + Fe(OH)_3 + 4\,SO_4^{2-} + 8H^+} \qquad \boldsymbol{Eq.1.3}$$

Additionally, the reaction of Cu-sulphides with oxic seawater produces acidic pore fluids, mobilising Cu as cuprous chloride complexes ($CuCl_2^-$ and $CuCl_3^{2-}$) and Cu^{2+} ions (Rose, 1976; Hannington, 1993) that migrate outward and re-precipitate as copper salts ($Cu_2Cl(OH)_3$) when mixing with sufficient seawater to increase Eh and pH (Dekov et al., 2011). The type of copper salt that precipitates depends on the pH, dissolved Cu and the ratio of Cl^- to H^+ in solution, with paratacamite typically forming at a lower pH (pH 4) relative to atacamite (Sharkey & Lewin, 1971; Woods & Garrels, 1986; Dekov et al., 2011). A study by Pollard et al. (1989) demonstrated that metastable botallackite precipitates initially and is converted to atacamite or paratacamite depending on the concentration of Cu^{2+} in solution. Botallackite recrystallised to atacamite at high Cu^{2+} concentrations (e.g., hundreds of ppm) relative to paratacamite at low Cu^{2+} concentrations (e.g., at tens of ppm; Pollard et al., 1989; Hannington, 1993).

1.4.2.2 Galvanic interactions and microbial oxidation

While galvanic interactions and biological influences are not directly investigated within this thesis, they are nonetheless significant during sulphide weathering (Singer & Stumm, 1970; Knight et al., 2018).

Galvanic interactions occur when two sulphides of different rest potentials are in contact with one another where one acts as the electron donor (anode) and the other acts as the electron receiver (cathode). This electron transfer increases the rate of oxidative dissolution with respect to the anode (Mehta & Murr, 1983; Fallon et al., 2019). Bacteria such as *Gammaproteobacteria* can catalyse galvanic interaction due to the production of H_2SO_4. Furthermore, recently discovered 'cable bacteria' act as a pathway for electrons allowing galvanic interactions to occur at a centimetre scale (Meysman, 2018; Meier et al., 2019) resulting in galvanic interactions possible even if sulphide phases are not in contact with one another.

Microorganisms enhance the alteration of sulphides by oxidation. For example, *Thiobacillus ferrooxidans* can attack sulphides directly or indirectly, oxidising Fe (Lundgren & Silver, 1980). These types of bacteria could accelerate the oxidation of Fe^{2+} to Fe^{3+} by a factor of 10^6 (Singer & Stumm, 1970). Direct oxidation of the sulphides occurs where the bacteria attach to the sulphide surface, resulting in dissolution of the Fe (Lundgren & Silver, 1980). Microbial oxidation by bacteria (such as *Thiobacillus ferrooxidans)* are generally active across a pH range of 1-6 and at a temperature from ~10°C and up to ~55°C, above which chemical oxidation dominates (Lundgren & Silver, 1980). As such, bacteria are active during active hydrothermal venting and unlikely to occur at the seafloor when the hydrothermal system is extinct (Lundgren & Silver, 1980). However, following the cessation of active hydrothermal venting, these types of bacteria are replaced with bacteria that thrive on the chemical energy of sulphides by oxidation (Sylvan et al., 2012). Thus, sulphides exposed at the seafloor are exposed to oxidising bacteria throughout all stages of a SMS deposits, from active hydrothermal venting to extinct SMS systems.

1.5 The potential of alteration products

Hydrothermally extinct SMS deposits on slow-spreading ridges, are expected to have greater sulphide tonnage compared to active deposits on fast-spreading ridges and thus, present the most prospective deposits (Hannington et al., 2011). However, these older, extinct SMS deposits have also experienced prolonged exposure to seawater and oxidising conditions, leading to extensive alteration of their primary sulphide minerals. Understanding this alteration is critical, as it impacts the metal content and economic potential of the deposit.

In terrestrial environments, sulphide weathering has been well documented, with studies showing that economic base metals (e.g., Cu and Zn) and precious metals (e.g., Au and Ag) are mobilised and re-concentrated to form supergene deposits (Emmons, 1917; Sillitoe & McKee, 1996; Yesares et al., 2014). However, there is a relative paucity of research concerning the weathering of sulphide material in SMS deposits (Hekinian et al., 1993; Knight et al., 2018; Hu et al., 2022; Hu et al., 2023; Maslennikov et al., 2023; Hou et al., 2024), highlighting the need for a detailed understanding of these processes in marine settings.

1.5.1 Economic implications

Sulphide alteration products, particularly secondary FeOOH and atacamite, are central to the geochemical evolution of extinct SMS deposits. Secondary FeOOH is notable for its high surface area and reactivity, which enable it to adsorb and incorporate economic metals such as Cu, Zn, Pb, Au, and Ag (Leckie et al., 1980; Benjamin & Leckie, 1981; Benjamin, 1983; Jambor & Dutrizac, 1998). Secondary FeOOH from SMS deposits can be rich in Cu (averaging 1.10 wt.%; Melekestseva et al., 2022), Zn (1.37 wt.%; Hu et al., 2022), Au and Ag (9.1 ppm Au and up to 125 ppm Ag; Herzig et al., 1991). Despite these promising observations for the economic extraction of secondary FeOOH, no comprehensive, large-scale study of FeOOH deposits across an entire SMS deposit has been conducted. As a result, our understanding of how to distinguish between metal-poor primary FeOOH and metal-rich secondary FeOOH is limited. Furthermore, detailed information about their grade variations and morphological characteristics remains inadequate. Moreover, there has been little study regarding how the sulphide protolith (i.e., chalcopyrite or pyrite) or possible post-formational modification processes (e.g., goethite crystallisation) may impact the metal content of secondary FeOOH. This lack of knowledge limits our understanding of how the long-term metal content of sulphide weathering products may change over time and the eventual fate of these secondary products (Cornell & Schwertmann, 2003; Maslennikov et al., 2023; Hou et al., 2024).

Atacamite (and polymorphs paratacamite and botallackite) is another common alteration product observed at SMS deposits (Hekinian & Fouquet, 1985; Herzig et al., 1991; Fouquet et al., 1993; Hannington, 1993; Hrischeva & Scott, 2007; Dekov et al., 2011; Murton et al., 2019).

Atacamite is primarily composed of Cu (~60%) and can incorporate Au concentrations similar to its primary sulphide protolith when precipitated in close proximity to the parent sulphide; when formation occurs away from the protolith, Au is normally poor (Dekov et al., 2011). While atacamite may have low concentrations of economic metals such as Zn, Au and Ag, the concentration of Cu is nonetheless, very high and might be an additional resource.

The greatest concern regarding the use of alteration products as a resource lies in estimating their tonnage. As of yet, there has been no study detailing the tonnage of these alteration products and as such, their potential as an alteration product resource, remains unknown. However, sulphide alteration products could potentially also be used as an exploration tool. Atacamite, where found, is commonly associated with FeOOH or blocks of massive sulphide and is a useful indicator of weathered Cu-sulphide in the substrate (Herzig et al., 1991; Hannington et al., 1993). Studies indicate that secondary FeOOH deposits can become enriched in metals like Cu and Zn through a two-step process: oxidation of underlying sulphides releases these metals, which then adsorb onto secondary FeOOH surfaces (Hu et al., 2022). Consequently, Cu and Zn concentrations in secondary FeOOH may serve as indicators of underlying sulphide fertility. Together, this suggests that exploration of extinct SMS deposits could be guided by the observation of atacamite presence and analysing the metal content in secondary FeOOH to identify areas with potentially valuable underlying sulphides.

1.5.2 Environmental implications

The possibility of mining SMS deposits raises environmental concerns. In-situ mining may result in habitat loss and plumes of sulphide material could impact benthic communities downstream through sedimentation or heavy metal release (Gwyther, 2008; Van Dover, 2011; Boschen et al., 2013). Exposing unaltered sulphide surfaces to oxic seawater can trigger oxidative dissolution. This process can leach economic base metals (i.e., Cu and Zn) and toxic trace metals (e.g., As, Cd, Sb and Pb), potentially resulting in harmful impacts to the marine ecosystem (Van Dover, 2011; Baker & Beaudoin, 2013; Boschen et al., 2013; Stauber et al., 2022).

Both goethite and ferrihydrite (FeOOH) have been extensively studied for their capacity to remove toxic trace metals from waste streams and acid mine drainage (Leckie et al., 1980; Huminicki & Rimstidt, 2009; Tabelin et al., 2020; Ding et al., 2023). This property suggests that naturally formed FeOOH might also mitigate the release of harmful metals during oxidative sulphide dissolution during potential seafloor mining operations (Knight et al., 2018). For example, studies show that FeOOH formation effectively retains Zn from the sulphide protolith (Hu et al., 2023), though its ability to adsorb other dissolved metals such as Cu, Sb or As remains unproven. Additionally, suspended sulphide particles produced during *in situ* mining may transport these particles away from the mining site over time and potentially result in extensive areas of heavy metal release. (Van Dover, 2011; Weaver et al., 2018; Morato et al., 2022).

However, FeOOH formation might both reduce sulphide oxidation and trap these metals, limiting their release and environmental impact (Fallon et al., 2018; Hu et al., 2023).

1.6 Terrestrial analogues of seafloor massive sulphide deposits

1.6.1 VMS deposits

Ancient analogues of modern SMS deposits, preserved in ophiolite terranes that have been tectonically emplaced onto continental crust, are the VMS deposits (Franklin et al., 1981; Hannington et al., 2005; Peltonen et al., 2008). In particular, the VMS deposits found in the Troodos ophiolite, often referred to as Cyprus-type VMS deposits, serve as terrestrial counterpart to contemporary mafic-hosted SMS deposits (Hannington et al., 1998b). This relationship provides valuable insights into the formation and evolution of both VMS and SMS deposits (Martin et al., 2023). Although some studies have proposed that ophiolite sequences, like the Troodos, contain VMS deposits analogous to MOR SMS deposits (e.g., Hannington et al., 1998b). Research also suggests that some VMS deposits such as Mala can exhibit chemical signature reflecting formation in subduction related environments (Martin et al., 2021; Patten et al., 2022).

1.6.2 Comparison of alteration processes in terrestrial and submarine settings

Ochre deposits within VMS deposits in the Troodos ophiolite are spatially associated with their underlying massive sulphide orebodies (e.g., Skouriotissa, North Mathiatis, Mousoulos; Robertson, 1976). These ochre deposits are composed of over 50% FeOOH, which are often granular and have well-bedded textures, are interpreted as the products of submarine alteration that occurred prior to the burial of sulphide minerals by pillow lavas and pelagic sediments (Constantinou, 1972; Constantinou & Govett, 1972; Constantinou & Govett, 1973). Similarly, bulk samples of secondary FeOOH from modern SMS deposits are often described as light to earthy red, granular, and ocherous, predominantly consisting of amorphous FeOOH along with accessory minerals such as jarosite, goethite, and amorphous silica (Herzig et al., 1991; Hekinian et al., 1993; Hrischeva & Scott, 2007). The close resemblance in both texture and mineralogy between terrestrial ochre and modern secondary FeOOH at SMS deposits emphasises a common genetic link. This link highlights the value of VMS deposits in enhancing our understanding of alteration processes at SMS deposits. It shows how metals such as Au and Cu can become enriched or depleted during weathering at SMS deposits. Additionally, the link provides insights into the long-term preservation of these metals in sulphide weathering products (Herzig et al., 1991).

1.7 Study location: the Semenov hydrothermal field

1.7.1 Geotectonic setting

The Semenov hydrothermal field is an ultramafic/mafic hosted SMS system discovered in 2007, located on an oceanic core complex (OCC) at the western flank of the slow spreading Mid-Atlantic Ridge (MAR; Beltenev et al., 2007; Murton & Rona, 2015). Semenov lies between the Fifteen-Twenty and Marathon Fracture Zones at 13°30'N, with water depths ranging from 2480 to 2950 m along an east-west trending seamount approximately 10 km long and 4.5 km wide (Beltenev et al., 2007; Beltenev et al., 2009; Pertsev et al., 2012).

The limited magma supply at slow spreading ridges results in asymmetric spreading of the ridge and the formation of extensive, low-angle detachment faults that expose lower crustal and upper mantle rocks, creating an OCC (Cann et al., 1997; Tucholke et al., 2008). Rocks sampled from the 13°30'N OCC include harzburgites, olivine gabbros, gabbronorites, gabbros, ferrograbbros, plagiogranites, tonalites, diorites and a basaltic substrate (Pertsev et al., 2012).

1.7.2 Seafloor massive sulphide deposits at Semenov hydrothermal field

Semenov hosts five distinct hydrothermal areas, four of which are inactive (Semenov-1, Semenov-3, Semenov-4, and Semenov-5), and one which remains active (Semenov-2; Figure 1.4; Pertsev et al. 2012; Cherkashov et al. 2013). Radiometric dating (^{230}U/Th) of massive sulphides at Semenov constrains the timing of sulphide deposition and associated hydrothermal activity. Analyses of 40 samples indicate that venting initiated at ~124 ka (Cherkashov et al., 2017; Kuznetsov et al., 2011). Massive sulphides recovered at Semenov consist mainly of Fe-sulphides (pyrite, pyrrhotite and marcasite) and Cu-sulphides (chalcopyrite, isocubanite and secondary Cu-sulphides), with pyrite-marcasite breccias that are cemented by microcrystalline silica, aragonite, quartz or barite. Alteration products include secondary Cu-sulphides, atacamite, FeOOH, and jarosite (Beltenev et al., 2009; Melekestseva et al., 2014; Melekestseva et al., 2017a; Melekestseva et al., 2017b; Melekestseva et al., 2018; Firstova et al., 2019; Melekestseva et al., 2020b; Firstova et al., 2022).

Semenov-1, positioned at a water depth of 2570–2620 m, represents a recently inactive hydrothermal system with ages between ~37.4 ka - ~12.9 ka (Beltenev et al., 2007, Beltenev et al., 2009; Kuznetsov et al., 2011; Pertsev et al., 2012). A single, large conical sulphide mound of ~175 m x 200 m dominates the area (Beltenev et al., 2007, Beltenev et al., 2009).

Semenov-2 is located at a water depth between 2360-2580 m. Semenov-2 is the only active hydrothermal area at Semenov with first activity dated at ~76ka (Beltenev et al., 2009; Kuznetsov et al., 2011). This field shows several hydrothermal mounds of which three are currently actively venting (Ash Lighthouse, Yellow Submarine and Michaelangelo). The

hydrothermal fluid is clear to whiteish, at a temperature of ~316°C, with the chimneys predominantly composed of anhydrite. Diffuse flow is abundant surrounding these active sites (Escartin et al., 2017).

Semenov-3 is located at a water depth between 2300–2640 m with dimensions of 1200 m x 650 m (Beltenev et al., 2009). This system is spatially related to basalt and serpentinised peridotites with hydrothermal activity estimated between 90.3 ka and 35.5 ka (Beltenev et al., 2009; Kuznetsov et al., 2011).

Semenov-4 is the deepest hydrothermal area within the Semenov field, occurring at water depths of 2560–3020 m. This system is also dated as the oldest, with hydrothermal activity initiating at ~123.8 ka and the most recent activity dated to 1.7 ka (Beltenev et al., 2009; Kuznetsov et al., 2011). It has the largest surface area of the district at ~2700 x 1600 m, likely due to the longest hydrothermal activity (Beltenev et al., 2009; Kuznetsov et al., 2011). Semenov-4 straddles both the hanging wall and the foot wall, resulting in this hydrothermal field being both ultramafic and mafic hosted (Pertsev et al., 2012).

Semenov-5 is located at a water depth between 2160–2340 m with a surface area of 700 x 500 m. This site appears to be the youngest, with ages between ~8 to ~14 ka. However, with only two samples dated, the true age range of this system might be very different to the reported data (Cherkashov et al., 2017). This site lies on the northern slope of the OCC, associated with basalt and serpentinised peridotite (Beltenev et al., 2009). The SMS deposit is exposed by mass wasting, with the presence of steep slump scarps associated with debris deposits (Escartin et al., 2017). Sulphide mineralisation at Semenov-5 is suggested to be associated with three ore forming systems including; deposition by black smoker hydrothermal venting, replacement of ultramafic rock below the seafloor, disseminated sulphide mineralisation within the host rocks and as stockwork around the sub-seafloor massive sulphide (Firstova et al., 2022).

Semenov represents a unique natural laboratory for investigating the oxidation and alteration of sulphide deposits. Its combination of active and extinct hydrothermal areas offers the opportunity to study a broad spectrum of weathering stages, from fresh massive sulphide to fully oxidised sulphide that comprise almost entirely of secondary FeOOH. Previous studies at Semenov have documented active sulphide oxidation and the formation of secondary alteration products such as FeOOH and atacamite (Melekestseva et al., 2017a; Melekestseva et al., 2018; Firstova et al., 2019), which are central to the thesis.

Semenov's varied hydrothermal activity, with distinct areas representing different stages of alteration, allows for detailed comparative analyses across a natural continuum. The diversity of the hydrothermal areas also facilitates investigations into post-formational modification processes that may impact the metal tenor of FeOOH (e.g., the transition of ferrihydrite to goethite) and the deportment of metals such as Cu, Zn, Au, and Ag during sulphide weathering.

Moreover, the co-occurrence of atacamite, which is closely associated with Cu enrichment, alongside FeOOH provides an ideal setting to explore differential metal retention in alteration products.

This thesis develops a comprehensive model of sulphide weathering processes at the Semenov hydrothermal field through multiple analytical approaches. The research combines geological mapping, mineralogical analysis, bulk and in-situ geochemistry, isotopic studies, and laboratory oxidation experiments to characterise the geochemical evolution of weathering products at SMS deposits. The systematic mapping of secondary FeOOH deposits provides approximate data on their spatial distribution and volumetric significance. These findings contribute to our understanding of metal cycling at the seafloor while also assessing whether secondary FeOOH and atacamite can function as both additional resources and effective exploration indicators for SMS deposits.

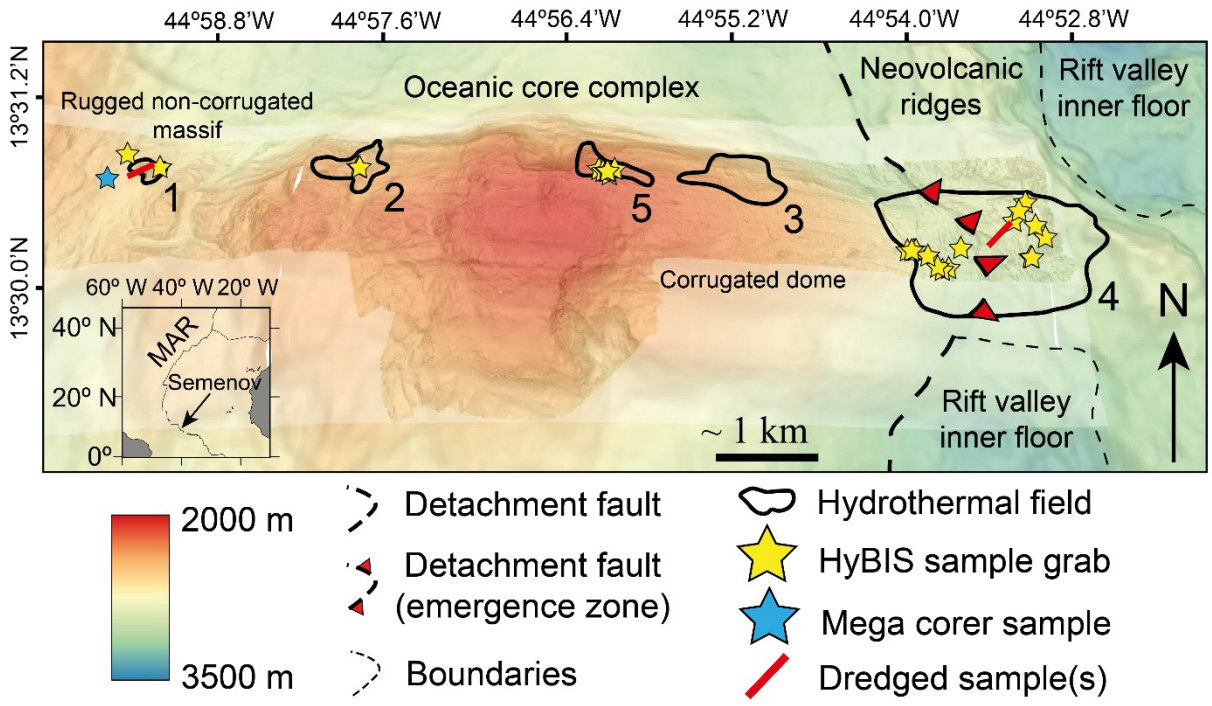

Figure 1.4. Location map of the Semenov hydrothermal field on the Mid-Atlantic Ridge illustrating sample locations by HyBIS, mega corer or dredged. Major tectonic features and the location of hydrothermal mounds after Firstova et al. (2022) and Pertsev et al. (2012). Bathymetry after Escartin (2014).

Chapter 2 Materials and analytical methods

The samples analysed for this thesis were primarily collected during one oceanographic expedition on the RRS James Cook expedition JC224 (March-April 2022) to the Semenov hydrothermal field (Figure 1.4). I participated in the first research expedition to the Semenov hydrothermal field, as part of the Natural Environmental Research Council (NERC) funded Project ULTRA (NE/S004068/). During the JC224 expedition, I took part in the recovery and processing of geological samples obtained by HyBIS remotely operated vehicle (ROV; Murton et al., 2012), RD2 drill cores and dredges. I led a dive (no. 82) on the HyBIS ROV at Semenov-5 to collect further samples of massive sulphide and FeOOH for my research.

Samples collected for Chapter 6 comprise polymineralic sulphide samples collected from three hydrothermal systems: the Moytirra vent field during the 2011 CE11009 VENTuRE survey (Wheeler et al., 2013), the Trans-Atlantic Geotraverse (TAG) hydrothermal system during the JC138 research expedition of the 2017 Blue Mining project (Murton & Shipboard Scientific Party, 2018) and the Beebee vent field during the 2013 research expedition JC82 (Webber et al., 2015). In addition, terrestrial sulphide samples were obtained from the Wetar Island VMS deposit (Scotney, 2002).

The following Chapter outlines the sampling of material at Semenov, geological mapping and the analytical methods employed for the compilation of this thesis. Sample preparation, including the creation of polished blocks, polished thick sections, sample powder preparation and acid digestion were achieved at the University of Southampton. I used the following methods to obtain bulk geochemical data; by Inductively Couple Plasma-Mass Spectrometry (ICP-MS; Agilent 8900) and Inductively Coupled Plasma-Optical Emission Spectrometry (ICP-OES; iCAP 6000) measured at the National Oceanography Centre. Radiogenic isotope (Pb-Nd-Sr) measurements were analysed by a Thermo Scientific Neptune Multi-Collector Inductively Coupled Plasma Mass Spectrometer (MC-ICP-MS) at the University of Southampton. Additionally, geochemical studies of minerals on polished blocks and sulphide powders were conducted by Scanning Electron Microscope-Energy Dispersive X-ray Spectroscopy (SEM-EDS) analysis to provide quantitative major geochemical analyses (>0.1 wt.%). Geochemical analyses by SEM-EDS of polished blocks also provided targets for Time of Flight Laser Ablation Inductively Coupled Plasma Mass Spectrometry (LA-TOF-ICP-MS) at the University of Southampton, and LA-ICP-MS analysis conducted at the British Geological Survey (BGS). The mineralogical composition of sample powders were analysed by X-ray Diffraction (XRD) at the University of Southampton. Surface area analysis of sample powders were measured by Brunauer-Emmett-Teller (BET) surface area analysis, using the multiple point N_2 surface area method, on a Micromeritics TriStar II 3020 BET at the University of Southampton.

All the data obtained in this thesis is available within the contained chapters, appendices and at the National Oceanography Centre British Oceanographic Data Centre (BODC).

2.1 Geological sample recovery

Forty-two samples comprising FeOOH (n=37) and massive sulphide (n=5) were used in this thesis and were collected using the HyBIS (Murton et al., 2012) ROV (n=30), dredging (n=11) and one sample obtained by a mega-corer during the JC224 research expedition (Figure 1.4). The samples were collected across Semenov hydrothermal field with the exception of Semenov-3. Samples span depths from 2206 metres below sea level (mbsl) at Semenov-5 located on the OCC to a maximum depth of 2874 mbsl acquired on the hanging wall side of the detachment fault at Semenov-4. The use of HyBIS allowed for precise positional information for the samples to be recorded and provided geological context in the preparation of geological maps. Once retrieved from the seafloor, the samples were processed on board by labelling the samples in order of acquisition based on the HyBIS dive footage. Samples obtained by dredging were labelled in order of their description due to lack of precise positional information. All samples were photographed onboard the RRS James Cook with a Nikon DLSR camera on a photographic table consisting of a black table, ruler, colour scale and dual flash lamps with umbrella diffusers. After initial photography of the whole-rock, most samples were cut into sections onboard, with one half labelled as an archive half, with the other a working half. The archive half was photographed again to record the cross-sectional view of the sample. Geological descriptions of the samples were conducted prior to being stored for onshore analysis. Sample imagery and descriptions from JC224 used in this thesis are detailed in Bishop et al. (2025a).

2.2 Seafloor mapping

To determine the surficial extent of FeOOH at Semenov hydrothermal field used for resource assessments presented in the discussion of this thesis, and to obtain a greater understanding of the geology at Semenov. The surface of Semenov-1, Semenov-2, Semenov-4 and Semenov-5 was mapped by videography using HyBIS footage from the Aurora tooling cameras and SCORPIO HD camera during the initial 2022 research expedition, and HD dive footage from the ROV ISIS using the mini Zeus HD video and SCORPIO camera during the second research expedition to Semenov hydrothermal field in 2024. Observed features (e.g. hydrothermal mounds, faults, surface geology) obtained by HD video footage from both ROVs were linked with bathymetric data. Samples obtained from dives were subsequently characterised by laboratory-based observations, which were linked back to imagery and mapping. Initial observations were made during the dive with subsequent review of the footage for interpretations of seafloor features and plotting of outcrop. Interpretations are based on visual observations from the ROVs and sample characterisation. Extrapolation of seafloor features are also interpretative as they were

not clearly observed during the survey. This led to the development of interpretative geological maps presented in Chapter 3.

2.3 Mineralogical analysis

2.3.1 Reflective Microscopy

This optical technique provides images of mineral textures and their relationships, enabling identification of FeOOH and sulphide assemblage and to provide targets for subsequent mineralogical analyses (i.e., SEM-EDS, LA-ICP-MS and LA-TOF-ICP-MS). Reflective microscopy was carried out through the analysis of polished blocks (n=40) and polished thick sections (n=11) at the University of Southampton. The FeOOH and sulphide blocks were observed under a LEICA DM2700 P microscope to produce reflective light microphotography, with images captured by the LEICA DMC 4500 processed using the Leica Application Suite X software.

2.3.2 XRD

XRD determines the crystalline mineralogy and is able to quantify both crystalline and amorphous phases in bulk samples of FeOOH and massive sulphide, thereby establishing the proportion and to identity FeOOH and sulphide minerals. In total, 36 samples were analysed by XRD, of which 30 samples consist of bulk FeOOH and massive sulphide samples obtained at Semenov. Three samples comprise sulphide material from the Moytirra, Beebee and TAG vent fields and an additional three from the Wetar Island VMS deposit presented in Chapter 6. Measurements by XRD were performed using a PANalytical X'Pert Pro diffractometer at the University of Southampton. Mineral identification of all samples were processed using Highscore v4.9 (supplied by Malvern Panalytical B.V. Amelo) with mineral quantification of 15 samples determined using the Siroquant v5.2 (supplied by Sietronics Pty Ltd©).

Each sample was prepared by initially crushing the material with an agate mortar and pestle, then weighing out 1.5 g of material, with an addition of 0.5 g of corundum to act as an internal standard. Samples were ground further in a McCrone mill for 8 minutes with isopropanol to form a slurry. This slurry was dried and side-loaded into XRD sample holders to mitigate any effects from preferred orientation. Analysis was performed using a PANalytical X'Pert Pro diffractometer machine fitted with a Cu X-ray tube including a diffracted beam monochromator to remove the effects of Fe fluorescence. Instrument specification were 35 kV, 40 mA utilising automatic slits and a step size of 0.02º 2(theta) at either 1 second or 2 seconds/step depending on the number of X-ray counts recorded.

Detection limits for bulk mineral analysis of mixed-mineralogy samples in this study (e.g. ferrihydrite, goethite, sulphides, amorphous phases) are estimated to be ~2–5 wt. %; the exact

limit depends on the crystallinity, phase mixing, and overall mineralogy present. Ferrihydrite is an amorphous FeOOH mineral phase is difficult to be directly identified and quantified by XRD. However, quantitative XRD with an internal standard provides a % amorphous content. As ferrihydrite is an amorphous mineral, the % amorphous content is assumed to be the % ferrihydrite for this study. The dataset of XRD analyses for samples obtained from Semenov are provided in Bishop et al. (2025b) with their quantitative mineralogy for selected samples shown in Bishop et al. (2025d) for Chapter 5. Both the dataset and quantitative mineralogy for samples used in the oxidative dissolution experiments in Chapter 6 are shown in Bishop et al. (2025c).

2.3.3 BET analysis

Measurements by BET surface area analysis provide the average surface area of sulphide powders used within Chapter 6 of this thesis. The surface area controls reaction kinetics and is a key parameter for interpreting oxidation rates. Six samples of polymineralic sulphide samples obtained from Moytirra, TAG, Beebe and Wetar Island VMS deposit were ground to 38-100 μm using an agate mortar and pestle. The sulphide powders were cleaned following the methodology outlined by Knight et al. (2018) and summarised in section 6.2.2. To determine the surface area of the cleaned powders, each sample was dried by heating at 60°C under vacuum for 2-3 hours to remove adsorbed water molecules, which ensures complete dehydration without altering the sample's structure. Surface area measurements were conducted using multi-point N_2 adsorption BET analysis on the Micromeritics TriStar II 3020 BET apparatus at the University of Southampton. Adsorption points to determine surface area were taken at relative pressures between 0.1 to 0.3 to ensure compliance with BET theory (Brunauer et al., 1938). BET isotherms for all samples were classified as Type II isotherms, which are characteristic of non-porous or macroporous materials and represent the formation of a multilayer of adsorbate on the surface. Type II isotherms indicate that the material has a well-developed external surface area and typically occur when physical adsorption is the primary mechanism (Brunauer et al., 1938).

Three samples were subject to duplicate measurements and achieved a percentage relative standard deviation (%RSD) between 10.5-15.1%. The C-values for the BET analyses ranged between 159-2656, reflecting strong interactions between nitrogen molecules and the sample surface. While higher C-values can suggest strong adsorption, they also indicate heterogeneity in surface energy distribution, which is consistent with the natural, heterogeneous nature of these sulphide minerals (Lowell et al., 2004). Full details on BET surface area measurements can be seen in Appendix A.1.

2.4 Solid geochemical analysis

2.4.1 SEM-EDS

This technique provides in-situ, semi-quantitative (Chapter 6) or quantitative (Chapter 5) major-element composition (>0.1 wt.%) of mineral phases to investigate the metal retention capabilities of FeOOH. Moreover, SEM-EDS is used to provide targets for LA-ICP-MS and LA-TOF-ICP-MS techniques while also used to calibrate measurements by LA-ICP-MS. Nine polished blocks and six sulphide powders were selected for SEM-EDS analysis using the Carl Zeiss Leo 1450VP SEM at the University of Southampton. The samples chosen were coated with a ~20 μm-thick carbon coating with the sulphide powder stuck onto conductive tape. The SEM is fitted with an EDS detector (Oxford Instruments X-Act 10 mm^2 area with silicon drift detector (SDD) and EDS Detector) for in-situ semi-quantitative and quantitative major elemental composition above 0.1-0.2 wt.%. The SEM-EDS was run on quantitative mode when measuring the polished blocks to provide targets and calibrating data obtained by LA-ICP-MS (section 2.4.2). Quantitative SEM-EDS is achieved by calibrating the data obtained by EDS against known minerals (O – Quartz, Na - Jadeite, Mg – MgO, Si – Silicon, P – Apatite, S – Pyrite, Cl – Oxford Instruments (OI) internal standard, Ca – Wollastonite, Fe – hematite and pyrite, Cu – (OI) internal standard, Zn – (OI) internal standard). For FeOOH, hematite was chosen as the most suitable mineral for Fe analysis and pyrite was chosen for Fe analysis of sulphide material. Before each set of quantitative EDS analyses, the electron beam current was measured using a Faraday cup and adjusted to maintain a constant probe current of 2.5 nA. Beam current was periodically re-checked (every 30–60 min) during analytical sessions and re-adjusted to 2.5 nA when necessary. To ensure quantitative accuracy, the majority of SEM-EDS analyses of mineral phases sum to 100 ± 3 wt.%. The exception of this are FeOOH minerals, which contain structural water that the SEM-EDS cannot detect, resulting in total weight percentages of only ~70–90 wt.% for these samples (Michel et al., 2007).

The SEM-EDS was run on semi-quantitative mode when measuring sulphide powders in Chapter 6. Analysis and processing of data was done using Aztec Energy software. The SEM-EDS data for Chapter 6 can be found in the BODC database after Bishop et al. (2025c) and Chapter 5 in Bishop et al. (2025d).

2.4.2 LA-ICP-MS

LA-ICP-MS provides quantitative spot analyses of sulphide minerals and their alteration products, providing compositional data across the spectrum of fresh to weathered minerals used in Chapter 5 of this thesis. Analyses were obtained using an ICP-MS (Agilent 8900 ICP-MS and ESL NWR193 laser ablation system) using platinum cones and standard lenses with a dwell time

of 6 ms per isotope. Ablation of the sample was done with an ESL image GEO 193 nm EXCIMER fitted with a TV 3 ablation cell at the British Geological Survey. The ablation cell has 0.65 l/min flow of helium mixed with 0.85 L/min of argon and 6 mL per minute of nitrogen before transport to ICP-MS. Analysis was performed by ablating spots ranging from 30 to 50 μm to a nominal depth of 25 μm. The fluence was 4 J/cm^2 with a laser repetition rate of 20 Hz. The analysis time for each spot was 27 seconds, comprising of 12 second measurement of the background and a 15 second measurement of the sample.

The data obtained were calibrated using USGS basalt glass reference material GSD-1G alongside nano-powder pellets prepared from OREAS-993 (sulphide-rich copper concentrate certified reference material, OREAS, Australia) and Fe-Mn oxide materials JMn-1 (Geological Survey of Japan), Nod-A-1 (USGS) and FeMnOx-1 (Jochum et al., 2016). Nano-powder pellets were produced at the University of Southampton by Thomas Belgrano following a method adapted from Garbe-Schönberg and Müller (2014). This included milling 1.5 g batches of the starting powders in a 45 mL agate vial with 32 g of 5 mm agate balls and 6–8 g of ultrapure Milli-Q water at 900 rpm for 30 minutes total milling time in a Fritsch (Germany) Pulverisette 7PLTM planetary ball mill. Nano-powder slurries were then dried at 60˚C overnight, re-homogenised in an agate pestle and mortar before pressing into 13 mm diameter pellets using a Specac (UK) stainless steel die, with the back surface of the pellet stabilised by a layer of microcrystalline cellulose (~0.2 g; Merck, Germany).

Quantitative SEM-EDS elemental analyses for the majority of spots analysed by LA-ICP-MS were employed as an internal standard reference for full quantification. For chalcopyrite, pyrite, and FeOOH, Fe was used as the internal standard reference, whereas Cu was used for atacamite (Bishop et al., 2025d). Where SEM-EDS data were unavailable, stoichiometric concentrations, Fe for pyrite and chalcopyrite and Cu for atacamite, were applied, and for FeOOH, the average Fe composition of FeOOH analysed by SEM-EDS within the sample was used (Bishop et al., 2025d).

For each chapter, accuracy (expressed as % relative error, %RE) and precision (as % relative standard deviation, %RSD) were assessed using certified reference materials (CRMs) analysed at semi-regular intervals during the analytical runs. Measurements of CRMs monitored reproducibility and accuracy throughout the dataset.

The reproducibility, represented the agreement between a set of results is calculated as shown on Eq. 2.1 with the accuracy, representing the agreement between the result and the true value, is shown on Eq. 2.2.

$$\%\ relative\ standard\ deviation = 100 \times \frac{absolute\ standard\ deviation}{average\ of\ CRM\ values} \qquad Eq\ 2.1$$

$$\%\ relative\ error = 100 \times \frac{absolute\ error}{CRM\ real\ value} \qquad Eq\ 2.2$$

The reference materials used for calibrating each element measured by LA-ICP-MS are detailed as follows: ^{27}Al, ^{29}Si, ^{42}Ca, ^{55}Mn, ^{56}Fe, ^{59}Co, ^{60}Ni, ^{63}Cu, ^{66}Zn, ^{75}As, ^{78}Se, ^{95}Mo, ^{107}Ag, ^{111}Cd, ^{115}In, ^{121}Sb, ^{125}Te, ^{139}La, ^{140}Ce, ^{141}Pr, ^{145}Nd, ^{147}Sm, ^{151}Eu, ^{157}Gd, ^{159}Tb, ^{163}Dy, ^{166}Er, ^{172}Yb, ^{197}Au, ^{208}Pb and ^{209}Bi were calibrated using GSD-1G, Nod-A-1, and FeMnOx-1. JMn-1 was used in addition to previous certified reference material to calibrate Si, Se, Mo, Ag, Cd, In, Pb, and Bi, while OREAS-993 was employed to further calibrate Al, Ca, Mn, Co, Ni, Cu, Zn, As, Sb, Te, La, Ce, Pr, Nd, Sm, Eu, Gd, Tb, Dy, Er, Yb, Au, Pb, and Bi. The accuracy and precision of the analyses were determined for each analyte using secondary reference materials that were measured as unknowns: OREAS-993 was used as secondary reference material for Si, Se, Mo, Ag, Cd, In, Pb and Bi with JMn-1 used as the secondary reference material for Al, Ca, Mn, Co, Ni, Cu, Zn, As, Sb, Te, La, Ce, Pr, Nd, Sm, Eu, Gd, Tb, Dy, Er, Yb and Au. Using either OREAS-993 and JMn-1 as secondary reference materials achieved the highest accuracy and precision for the measured elements. The majority of elements exhibit good precision and accuracy with concentrations within the reported uncertainty or within 10% of reference values, with the exception are Si (±20.0%), Zn (7.6%) and Cd (±33.8%; Table 2.1). The majority of elements exhibit %RSD of < 10%, except for Au (17.1%). See Appendix A.2 for a full record of quality control checks. Full dataset of LA-ICP-MS analyses can be found after Bishop et al. (2025d) with the raw data after Bishop et al. (2025e).

Table 2.1. Average accuracies and precisions of LA-ICP-MS analyses. The CRM used as the external reference is listed. * = Reported error of measurements against the uncertainty envelope of the CRM. N/A = Not applicable as Fe is used at the internal standard for processing the data. See Appendix A.2 for full details.

Element	Precision (%RSD)	Accuracy (%RE)	CRM	Element	Precision (%RSD)	Accuracy (%RE)	CRM
Al	0.9	3.8	JMn-1	Te	7.4	0.5	JMn-1
Si	4.8	20.0*	OREAS-	La	1.7	1.8	JMn-1
Ca	0.9	0.5	JMn-1	Ce	1.4	3.8	JMn-1
Mn	5.6	9.1	JMn-1	Pr	1.9	3.2	JMn-1
Fe	N/A	N/A	JMn-1	Nd	1.9	5.4	JMn-1
Co	1.9	1.3	JMn-1	Sm	2.0	2.6	JMn-1
Ni	1.9	0.6	JMn-1	Eu	2.1	4.4	JMn-1
Cu	3.1	0.1	JMn-1	Gd	2.2	1.6	JMn-1
Zn	2.4	7.6*	JMn-1	Tb	2.8	5.5	JMn-1
As	2.5	2.9	JMn-1	Dy	2.1	4.1	JMn-1
Se	4.7	1.9	OREAS-	Er	2.2	1.4	JMn-1
Mo	7.1	2.8	OREAS-	Yb	2.6	1.0	JMn-1
Ag	5.6	9.8	OREAS-	Au	17.1	7.1	OREAS-
Cd	8.2	33.8*	OREAS-	Pb	4.4	8.3	OREAS-
In	2.6	1.8	OREAS-	Bi	8.6	2.1	OREAS-
Sb	2.2	3.1	JMn-1				

2.4.3 LA-TOF-ICP-MS

Mass Spectrometer	Nu Instruments Vitesse ToF ICP-MS
Laser Ablation System	Elemental Scientific Lasers imageGEO193 laser ablation system with a TwoVol3 ablation chamber
RF Power	1350 W
Cones	Ni sample cone (319-646), Ni skimmer cone (325-294)

Gas Flows		**Ablation Conditions**	
Cool Gas (Ar)	13 L min^{-1}	Laser energy density	~3.0 J/cm^2
Auxiliary Gas (Ar)	2 L min^{-1}	Laser repetition rate	200–400 Hz
Make-up gas (Ar)	0.825 L min^{-1}	Laser beam size	1–2 μm^2
Cell (CRC) Gas 1 (He)	16 L min^{-1}	Laser tracking speed	200 $\mu m\ s^{-1}$
Cell (CRC) Gas 2 (H_2)	8 L min^{-1}	Spacing	0.75–1 µm
Ablation chamber carrier gas (He)	0.2 L min^{-1}	Ablation mode	Line
Ablation cup gas (He)	0.3 L min^{-1}		
Additional Gas (N_2)	0.002 L min^{-1}		

Two semi-quantitative 1mm^2 trace elemental maps at 2 µm x 2 µm resolution produced by LA-TOF-ICP-MS visualise the spatial heterogeneity of base and precious metals across weathering fronts, aiding to understand metal mobility in Chapter 5. This technique was applied using line scan analysis and the same instrument and method, adapted for sulphide, as (Standish et al., 2024). The analyses were performed using a Nu Instruments (Nu Instruments Ltd., Wrexham, UK) Vitesse TOF-ICP mass spectrometer coupled to an Elemental Scientific Lasers (Bozeman, MT, USA) imageGEO193 laser ablation system with a TwoVol3 ablation chamber and Dual Concentric Injector (DCI2) at the University of Southampton. The analyses were performed by ablating spot sizes of 1-2 µm with a laser repetition rate of 400 Hz and the laser beam energy at the sample maintained at approximately 3.0 J/cm^2. Full setup conditions are shown on

Table 2.2. The instrumental set-up permits fast quasi-simultaneous detection across almost the entire elemental mass range (20–260 m/z). Instrument optimisation was performed while ablating NIST SRM 610, a silicate glass reference material, to achieve high sensitivity across the elemental mass whilst minimising oxide production (UO+/U+ <1%) and laser-induced elemental fractionation ($^{238}U+/^{232}Th+ \approx 1$). Calibration was achieved by standard sample bracketing with NIST SRM 610 and USGS basalt glass reference material GSD-2G. Signal intensity data per sample pixel were exported for data reduction in Iolite 4 using the Trace Elements data reduction

scheme (Paton et al., 2011; Paul et al., 2023). Drift in the intensities for the reference materials were smoothed with a spline function ("Spline_Smooth 1") and concentrations reported by Jochum et al. (2005) were used in the calculations. Due to the complex variation in minerals (i.e., FeOOH, pyrite, chalcopyrite etc.) and porous nature of FeOOH, elemental maps achieved are considered semi-quantitative and are used to determine the general concentrations of metals. Elements presented in the study include cadmium (Cd), copper, arsenic (As), silver and gold (Au), of which NIST SRM 612 was used as a secondary reference material. Measurements are within uncertainty or within 10% of the reference values after NIST SRM 612, with the exception of Cd (-54%), Au (-53%) and As (+35%). These are known to exhibit heterogeneity in this glass material (Eggins & Shelley, 2002). During rastering of NIST SRM 612, most elements exhibit precision expressed as % relative standard deviation (RSD) better than 10.0 %, except for Cu (12.0%) and Au (11.1%). The raw datasets acquired from LA-TOF-ICP-MS can be seen after Bishop et al. (2025f).

Table 2.2. Setup conditions for LA-TOF-ICP-MS

Mass Spectrometer	Nu Instruments Vitesse ToF ICP-MS		
Laser Ablation System	Elemental Scientific Lasers imageGEO193 laser ablation system with a TwoVol3 ablation chamber		
RF Power	1350 W		
Cones	Ni sample cone (319-646), Ni skimmer cone (325-294)		
Gas Flows		**Ablation Conditions**	
Cool Gas (Ar)	13 L min^{-1}	Laser energy density	~3.0 J/cm^2
Auxiliary Gas (Ar)	2 L min^{-1}	Laser repetition rate	200–400 Hz
Make-up gas (Ar)	0.825 L min^{-1}	Laser beam size	1–2 µm^2
Cell (CRC) Gas 1 (He)	16 L min^{-1}	Laser tracking speed	200 µm s^{-1}
Cell (CRC) Gas 2 (H_2)	8 L min^{-1}	Spacing	0.75–1 µm
Ablation chamber carrier gas (He)	0.2 L min^{-1}	Ablation mode	Line
Ablation cup gas (He)	0.3 L min^{-1}		
Additional Gas (N_2)	0.002 L min^{-1}		

2.5 Wet geochemical analysis

Throughout geochemical analytical methods in this thesis, de-ionised 18 MΩ-grade water from a Millipore system was used for rinsing and dilution (referred to as Milli-Q®). All containers used to store acid or sample solutions in high-density polyethylene (HDPE) or low-density polyethylyene (LDPE) containers were cleaned by submersion in hydrochloric acid diluted to 20% concentration using Milli-Q for two days and rinsed with Milli-Q® in a cleanroom and left to dry. Measurements of geochemical analyses were achieved using MC-ICP-MS (Thermo Scientific) and ICP-MS (Agilent II) at the University of Southampton and ICP-OES (iCAP 6000) at the National Oceanography Centre Southampton. Instrument drift for ICP-MS was corrected by the analysis of internal standards within the 3% spiked nitric acid (Re-In at 5 ppb and Be at 20 ppb) with the ICP-OES corrected by the analysis of a known standard every 10 measurements. Measurements were calibrated against synthetic standards of known concentrations.

2.5.1 Bulk sample preparation, dissolution and analysis

Acid digestions followed by ICP-MS and ICP-OES measurements quantify major and trace element concentration in bulk samples, providing a baseline needed to assess metal distribution in sulphide and FeOOH samples. Bulk concentration of Na, Mg, Al, Ca, Mn, Fe, Cu and Sr were obtained by ICP-OES with the exception of Mn where the concentration was below 1000 ppm. Bulk concentrations of Li, Mn (below 1000 ppm), Ti, Co, Ni, Zn, As, Nb, Cd, Sb, Ba, REE, W, Pb, Bi, Th and U were obtained by ICP-MS.

Bulk samples were prepared by crushing in an agate mortar and pestle at the University of Southampton. Two sets of sample dissolution were carried out at the clean lab within the National Oceanography Centre Southampton (NOCS). For both, the following methodology applies: initially, Teflon pots used in acid digestion were cleaned by submersion in 50% concentrated HCl for 24 hours at 130^{o}C, followed by rinsing with Milli-Q®, submersion in 50% concentrated nitric (HNO_3) for 24 hours at 130^{o}C, and a final rinse with Milli-Q before left to dry overnight. This method ensured that there is no contamination in the Teflon pots. For digestion, approximately 50 mg of powdered sample was placed in a Teflon pot with 15 drops of sub boiled acid (6 M HNO_3 acid) to prevent the sample from escaping the pots due to static. This was followed by adding 2 mL of Romil SpA grade hydrofluoric acid (HF), with the lids being placed back on and left for 24 hours on a hot plate at 130^{o}C. Subsequently, the lids were taken off of the Teflon pots and left on the hot plate to incipient dryness and re-digested with sufficient (ca 5 mL) 6 M HCl acid. Again, the lids were placed back on the Teflon pots and left overnight on a hot plate at 130^{o}C. This step was repeated to ensure no more HF was in the solution, since this could form insoluble salts. The lids were taken off the Teflon pots and visually inspected to observe any residue that has not digested. After confirming that there is no residue, the dissolved

samples were transferred to pre-weighed, HDPE scintillation vials and made up to ~20 mL using an approximate 50:50 mixture of 6 M HCl and Milli-Q® to form an approximate 400-fold diluted mother solution.

Solutions were dried on a hotplate at 130°C to incipient dryness using 1 mL of mother solution. The samples were made to 4000-fold dilution with 3% HNO_3 acid containing an internal spike of Ru-Re at 5 ppb and Be at 20 ppb. Blanks were made during the acid digestion protocol to determine any contamination introduced or present and to determine the limit of detection (LOD) during analysis. Sample duplicates were also run to determine the inherit heterogeneity of the samples. Accuracy and reproducibility were determined by using triplicates or single measurements of certified raw material (CRM) that include (1) sulphide standards OREAS-620 (sulphide-rich Zn-Pb-Ag concentrate certified reference material, OREAS, Australia), OREAS-908 (copper oxide ore, OREAS, Australia), RTS-1 (Sulphide ore, CANMET) and CH-4 (Au-ore, CANMET) and; (2) Fe-Mn oxide standards JMn-1, Nod-A-1, Nod-P-1 (USGS), GSPN-2 (Mn nodule, Chinese Academy of Sciences) and GSPN-3 (Mn nodule, Chinese Academy of Sciences). Details of CRMs used during bulk analysis of samples are followed as;

- Chapter 4: Triplicates of CRMs JMn-1, RTS-1, and GSPN-2 were analysed repeatedly. Single measurements of GSPN-3, CH-4, Nod-A-1, and Nod-P-1 provided additional accuracy checks.
- Chapter 6: Triplicates of CRMs OREAS-620, OREAS-908, and RTS-1 were analysed, with CH-4 included as a single-run accuracy check.

The summary of the accuracy and reproducibility of the data for Chapter's 4 and 6 are reported on Table 2.3. Of the elements discussed within Chapter 4, major and trace element measurements exhibited good accuracy, the majority of elements were within 10% error of the expected values, except for Mg (± 13.0%), Ca (± 11.7%), Co (± 17.6%), Zn (± 10.0%) and La (± 11%). Precision exhibited good reproducibility with elements showing a standard deviation of ≤ 10.0%, except for As (± 14.5%). Of the elements discussed within Chapter 6, bulk geochemical analysis exhibited good accuracy (within 7% of CRM values) and reproducibility (within 7 %RSD) with the exception of As in OREAS-620 that showed a 65% error and Zn in CH-4 at 72% error. Poor As in OREAS-620 may reflect the three-acid digestion differing from the CRM's four-acid method or an issue with OREAS-620 itself, as As was measured accurately in OREAS-908, also dissolved by four-acid digestion. Similarly, poor Zn measurements in CH-4 may be the result of an issue with the CRM itself considering Zn was measured accurately in all other CRM. Further details regarding the measurements of each CRM are presented in Chapter 4 and Chapter 6 are presented in Appendix A.3 and Appendix A.4 respectively and also within the BODC database after Bishop et al. (2025b) and Bishop et al. (2025c).

To assess sample heterogeneity, duplicate analyses were performed of bulk samples. In Chapter 4, eight duplicate bulk samples showed offsets generally < 10 %, except Ti (10 %), Cu (10.4 %) and Yb (30.3 %; Appendix A.5). Similarly, in Chapter 6, six sulphide duplicates exhibited < 7 % RSD, with As slightly higher at 10.8 % (Appendix A.6).

Table 2.3. Average accuracies and precisions of CRM material used in bulk sample geochemical compositional data for Chapter 4 and Chapter 6. Blank values are where these elements were not used for the study.

Element	Average precision (%RSD) Chapter 4	Average accuracy (%RE) Chapter 4	Average precision (%RSD) Chapter 6	Average accuracy (%RE) Chapter 6
Li	7.8	9.9		
Mg	2.6	4.8		
Al	4.3	8.8		
Ca	3.1	12.6		
Sc	11.5	9.6		
Ti	10.5	9.1		
Mn	3.2	11.3		
Fe	2.1	5.7	1.2	2.5
Co	13.0	18.7		
Ni	15.3	7.5		
Cu	9.1	8.7	1.4	2.1
Zn	8.1	10.0	3.03	3.6
As	14.5	9.5		
Sr	7.8	7.5		
Nb	8.5	12.5		
Cd	24.0	19.2	2.5	4.5
Sb	43	7.4	1.4	4.5
Ba	13.0	15.3		
La	9.8	11.1		
Ce	9.2	9.3		
Pr	9.1	6.7		
Nd	7.9	7.1		
Sm	7.0	4.8		
Eu	8.3	5.7		
Gd	5.4	5.5		
Tb	4.2	8.6		
Dy	3.6	4.7		
Ho	3.4	7.0		
Er	2.7	2.9		
Tm	5.7	4.0		
Yb	6.2	6.6		
Lu	5.4	3.9		
W	18.0	26.4		
Pb	7.0	10.3	0.8	4.7
Bi	1.7	10.6		
Th	30	7.0		
U	10.1	12.7		

2.5.2 Pb-Nd-Sr isotopic analysis

Radiogenic isotopic analysis provides information to the source of these elements within bulk samples and to interpret their origin and modification. Additionally, Pb isotopes were used to derive a fluid-to-rock (F/R) to investigate how increasing seawater interaction affects the composition of bulk FeOOH samples presented in Chapter 4. To prepare samples for radiogenic isotope (Pb-Nd-Sr) analysis, an appropriate volume of mother solution (described in section 2.5.1) is dried down on a hot plate at 130°C and diluted with sub-boiled 3% HNO_3 to prepare samples that comprise approximately 120-200 ng Nd, 1 mg Sr and 250 ng Pb. Neodymium (n=16) and Sr (n=17) were extracted from bulk samples of FeOOH by using two-column passes: AG50-X8 200-400 mesh for the initial separation, followed by Sr-spec resin for Sr and LN Spec columns for Nd. Lead (n=20) was extracted from bulk samples of FeOOH (n=18) and massive sulphide (n=2) using AG1x8 anion exchange resin replicating the method of Lang et al. (2014). Pb isotopes were corrected for instrumental mass fractionation with the SBL74 spike $^{207}Pb/^{204}Pb$ (Taylor et al., 2015). This analysis was conducted at the University of Southampton using an MC-ICP-MS.

Three CRMs were used for Nd isotope systematics (Nod-A-1, Nod-P-1 & BHVO-1, USGS) with internal standard JNdi-1 (Tanaka et al., 2000). Two CRMs (Nod-A-1, Nod-P-1) with standard reference material NIST NBS 981 were used for Pb isotope systematics, and one CRM (BHVO-1) with internal standard NIST NBS 987 for Sr isotope fractionation. Measurements for BHVO-1, Nod-A-1 and Nod-P-1 all fall within the range of published values for each isotope systematic (Table 2.4). Lead isotope standard reference material NBS 981 showed $^{206}Pb/^{204}Pb$ = 16.9400 and a two-standard error (2SE) of 0.0023, $^{207}Pb/^{204}Pb$ = 15.4965 with a 2SE of 0.0026, and $^{208}Pb/^{204}Pb$ = 36.7124 with a 2SE of 0.0076 (from >100 analyses over the past 4 years). The Nd internal standard JNdi-1 averaged 0.512117 with a 2SE of 0.000006 (n=5), while NBS 987, used for Sr measurements, averaged 0.71027 with a 2SE of 0.00001 (n=6). The measured data is available in Bishop et al. (2025b).

Table 2.4. Measurements of CRM material for analysis of Pb-Nd-Sr isotopic systematics with measured two standard error (2SE). All measurements fall within the range of published values for each isotope systematic.

	Nod-A-1 measured	2SE	Nod-P-1 measured	2SE	Measured BHVO-1	2SE
$^{206}Pb/^{204}Pb$	18.9629	0.002	18.7033	0.0002	18.2266	0.0003
$^{207}Pb/^{204}Pb$	15.6814	0.0008	15.6356	0.0008	15.4949	0.0013
$^{208}Pb/^{204}Pb$	38.9368	0.0020	38.6811	0.0019	37.7393	0.0034
$^{143}Nd/^{144}Nd$	0.512153	0.000009	0.512443	0.000008	0.512993	0.000008
$^{87}Sr/^{86}Sr$	0.709233	0.000005	0.709279	0.000006	0.703496	0.000006

2.5.3 Seawater geochemistry

Analysis of dissolved metals in seawater samples presented in Chapter 6 quantifies metal release and uptake over two weeks, allowing the calculation of oxidation rates and time-series metal concentration to investigate oxidation kinetics of polymineralic sulphide material. Metals dissolved in the synthetic seawater (Fe, Cu, Zn, As, Sb, Cd, Pb) were measured by ICP-MS (Agilent II) at the University of Southampton. Instrument drift was corrected using Re, In, and Be spiked nitric acid, with reproducibility and accuracy assessed by seawater CRM (High-Purity Standards). The seawater CRM, which contains low metal concentrations (e.g., Cu, Zn, As), was also spiked with elemental Fe, Cu, Zn, As, Sb, Cd, and Pb standard solutions to create three separate CRMs with metal concentrations bracketing those expected during the experiment. The spiked CRMs were analysed in triplicates for each run (18 total measurements) and all elements showed good accuracy (i.e. within 10% of standard values) except for Fe (±142%; Table 2.5). Reproducibility was generally good with %RSD ≤ 8%, except Fe (24.5%; Table 2.5; Appendix A.7). Poor Fe measurements may have arisen due to the high matrix effect of 22x diluted seawater (Olivares & Houk, 1986). Duplicate experiments with separate aliquots of sample DE-02 exhibited similar compositional trends, with median %RSD values ranging from 26.7% to 45.8% (with Fe reaching 95.4%, Appendix A.8). The higher variability observed in duplicate experiments (median %RSD 26.7-45.8%) compared to analytical precision (%RSD ≤8%) reflects the combined effects of sample heterogeneity, matrix interference, and natural variability inherent in sulphide-seawater oxidation systems. This larger uncertainty is particularly relevant when extrapolating results to environmental and economic impacts, where such variability represents realistic bounds on metal release rates and concentrations, and is therefore incorporated into these broader impact assessments.

Table 2.5. Average accuracies and precisions of measured spiked seawater CRM (n=18) material used in seawater analysis for Chapter 5. For full details of CRM analysis including concentration, see Appendix A.7.

	Sp. 1 CRM		Sp. 2 CRM		Sp. 3 CRM	
	Average precision (%RSD)	Average accuracy (%RE)	Average precision (%RSD)	Average accuracy (%RE)	Average precision (%RSD)	Average accuracy (%RE)
Fe	36.9	90.6	9.3	21.7	27.3	313.0
Cu	7.0	9.0	6.3	1.7	7.0	2.0
Zn	9.5	1.6	8.2	1.1	6.4	4.2
Sb	3.5	5.6	4.5	5.9	3.3	2.1
Pb	3.7	4.6	4.8	9.2	6.0	1.6
As	5.3	12.9	5.3	6.6	6.4	7.7
Cd	3.8	6.7	4.3	4.5	4.7	1.4

2.5.4 Sequential leaching analysis

Sequential leaching experiments presented in Chapter 5 are used to investigate Cu and Zn distribution within sulphide weathering products, following the methodology adapted from Poulton and Canfield (2005). The four leaching solutions targeted sequentially (1) easily adsorbed fractions (using 1 M magnesium chloride buffered to pH 7), (2) carbonates and atacamite (using 1 M Na-acetate at pH 4.5), (3) ferrihydrite (using 1 M hydroxylamine-hydrochloride with 25% acetic acid), and (4) goethite (using 0.5 g/l Na-dithionite buffered with 0.2 M Na-citrate and 0.35 M acetic acid). 0.1 mL aliquots of leaching solutions were diluted to 10 mL with 3% HNO_3, spiked with 5 ppm Re and In, and 20 ppm Be. Major cations (Al, Ca, Cu, Fe, Mn, Sr) were analysed with ICP-OES and Zn with ICP-MS. Instrument drift was monitored with spiked HNO_3 for ICP-MS and standard measurements every 10 samples for ICP-OES. Accuracy and reproducibility of the analyses were assessed by analysing reference materials JMn-1, GSPN-2, RTS-1, in triplicate and further single analyses of Nod-P-1, GSPN-3, and CH-4.The majority of elements exhibit good accuracy within 10% of the CRM except for Zn (±48.7%), Mn (13.3%) and Ca (10.1%; Table 2.6; see Appendix A.9 for full details). Analysed elements exhibit good reproducibility with all elements with < 6% RSD except for Ca at 14.6%. Duplicate measurements of 82_HY_06$_a$ and 90_HY_04, showed good reproducibility with the majority of elements at < 5% RSD, except Ca (Appendix A.10).

Analyses of the parent leach solutions prior to use showed all elements below <1 ppm, indicating no contamination from reagents (Appendix A.11). In addition, Control experiments were conducted using sample 82_HY_06$_a$ and synthetic seawater (ASTM D1141-98; ReAgent Chemical Services Ltd) to assess potential dissolution during the procedure. No mineral dissolution was observed during shaking of the vials (Appendix A.11).

Table 2.6. Average accuracies and precisions of CRM material used in sequential leaching analysis. For full details of CRM analysis, see Appendix A.9.

Element	Average precision (%RSD)	Average accuracy (%RE)
Al	5.0	5.2
Ca	14.6	10.1
Mn	1.2	13.3
Fe	2.0	4.2
Cu	5.1	7.0
Zn	5.3	48.7
Sr	1.2	7.3

Chapter 3 Seafloor mapping at Semenov hydrothermal field

Geological mapping is fundamental for characterising the spatial distribution and morphological features of Semenov hydrothermal field, providing baseline data for resource assessment and exploration strategies. At the Semenov hydrothermal field, the surficial extent and distribution patterns of FeOOH deposits remain poorly constrained, limiting our understanding of both their economic potential and their utility as exploration indicators for underlying sulphide mineralisation. This chapter presents geological maps of the Semenov hydrothermal field, compiled through systematic seafloor mapping using ROV video footage and surface sampling. These maps establish the geological context and document the surficial distribution of FeOOH deposits, which will inform the resource assessment and exploration analysis presented in Chapter 7 of this thesis.

The geological interpretation of seafloor features requires ground-truthing to accurately distinguish between different deposit types based on their visual characteristics and compositional verification through on-board visual inspection and sample analysis. Massive sulphide deposits are identified in ROV footage by their characteristic red coloration, blocky textures and relatively smooth surface textures (e.g., Figure 3.1B), while FeOOH deposits exhibit distinct rough, crustal morphologies typically coated with manganese oxides that impart a black surface appearance (e.g., Figure 3.3C). Visual identification during ROV operations was validated through post-dive sample examination conducted on board during expedition JC224 to the Semenov hydrothermal field, followed by detailed geochemical analysis at NOCS and at the University of Southampton. However, several limitations must be acknowledged in this mapping approach, including variable lighting conditions and generally poor visibility during ROV operations, followed by geological complexities such as the potential for mixed lithologies at deposit boundaries and the inherent challenge of characterising three-dimensional deposit geometry from two-dimensional seafloor observations.

3.1 Semenov-1

Semenov-1 forms a conical hydrothermal mound with basal dimensions of approximately 200 m x 150 m at a relief of approximately 30 meters above the surrounding seafloor, representing typical morphology for mafic-hosted seafloor massive sulphide systems (Fouquet et al., 2010; Petersen et al., 2000). The seafloor surface at Semenov-1 comprises predominantly FeOOH deposits covering approximately 35% of the mapped area based on ROV video analysis, exhibiting characteristic rough, crustal morphologies with variable manganese oxide coatings producing dark surface coloration.

Sulphide talus derived from erosion of massive sulphide overlying FeOOH deposits covers an additional 10% of the seafloor area, concentrated on the mound flanks. Sulphide outcrops cover approximately <10% of Semenov-1. Sulphide exposures occur predominantly near the mound summit and as in-situ outcrops on steep slope sections, characterised by red coloration and smooth, competent surfaces typical of coherent sulphide mineralisation (Figure 3.1B). The sulphide exposures display blocky jointing patterns consistent with cooling and contraction processes in massive sulphide bodies

Pelagic sediment accumulates across approximately 45% of the mapped area, primarily at the mound base and topographic lows that provide sediment traps. Basalt talus overlying FeOOH deposits observed in the north eastern sector covers approximately <5% of the total area, with pillow basalt and angular morphology indicating proximal derivation from basaltic source terrain located east of Semenov-1

Semenov-1 retains a classic mound shaped morphology with exposure of sulphide at the summit, suggesting recent cessation of hydrothermal activity. Recovered chimney shaped FeOOH samples suggest previous hydrothermal discharge (Bishop et al., 2025a). Sediment relationships show pelagic accumulation without evidence for recent hydrothermal input, supporting interpretation of hydrothermal inactivity at Semenov-1

Sample 66_HY_05 recovered from a low-relief hydrothermal mound adjacent to Semenov-1 is brecciated FeOOH material, suggesting that similar low-relief mound features throughout the immediate area may represent additional FeOOH deposits (Figure 3.1).

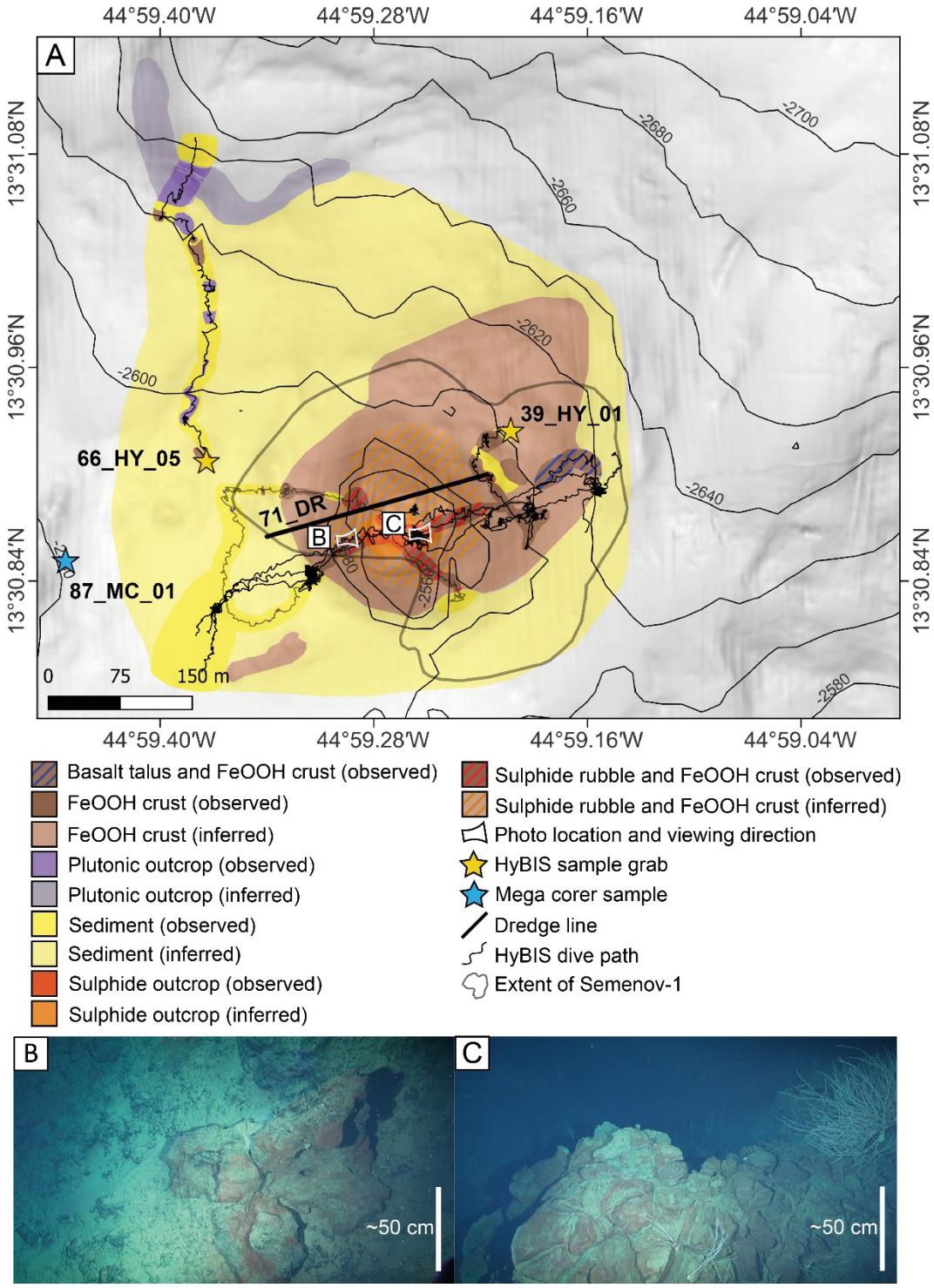

Figure 3.1. **(A)** Geological map of Semenov-1 with sample locations used in the study, geology interpreted from high-resolution bathymetry, surface samples and video surveys. **(B)** Exposed oxidised massive sulphide hydrothermal chimney. **(C)** Massive sulphide close to summit at Semenov-1.

3.2 Semenov-2

Semenov-2 comprises multiple low-relief hydrothermal mounds, distinguished from other Semenov sites by the presence of active hydrothermal venting. Active and inactive hydrothermal chimneys occur at mound summits, discharging clear hydrothermal fluids. The seafloor surface comprises predominantly basalt talus covering approximately 50% of the mapped area based on ROV video analysis, exhibiting pillow basalts, with angular morphology characteristic of volcanic debris (Figure 3.2).

Deposits of FeOOH cover approximately 30% of the mapped seafloor area, displaying typical rough, crustal morphologies with variable surface coloration (Figure 3.2E). Sample recovery at Semenov-2 acquired only two FeOOH samples (77_HY_02 and 77_HY_03), both exhibiting brecciated textures indicative of mechanical fragmentation processes. Additional areas displaying crustal morphologies appear as grey to white deposits, potentially representing alternative hydrothermal precipitates, though these remain unsampled and therefore classified conservatively as FeOOH deposits (Figure 3.2C).

Sedimentary accumulations account for approximately 20% of the mapped area, comprising both pelagic and hydrothermal sediment types. Hydrothermal sediment represents a mixture of hydrothermal precipitates and pelagic components, distinguished by characteristic orange coloration resulting from FeOOH content (Figure 3.2B).

Massive sulphide exposures remain limited, occurring at only two documented locations and generally obscured by manganese oxide coatings that mask the red sulphide coloration. Atacamite mineralisation occurs as discrete green crystalline aggregates on hydrothermal crust surfaces (Figure 3.2C), representing secondary copper mineralisation formed through oxidation of underlying copper-bearing sulphides (Hannington, 1993).

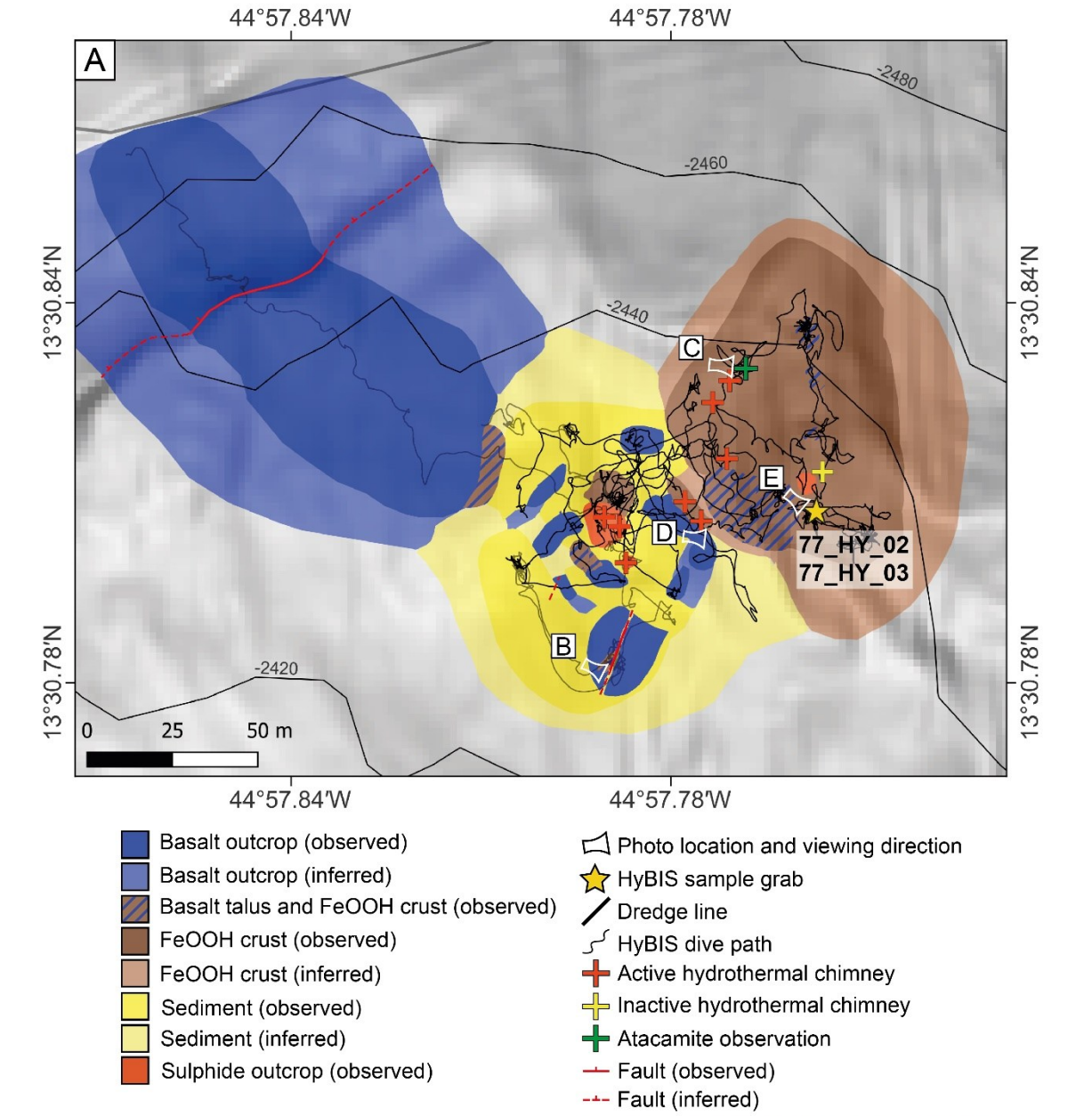
A
44°57.84'W
44°57.78'W
13°30.84'N
13°30.78'N
-2480
-2460
-2440
-2420
C
E
D
B
77_HY_02
77_HY_03
0
25
50 m
Basalt outcrop (observed)
Basalt outcrop (inferred)
Basalt talus and FeOOH crust (observed)
FeOOH crust (observed)
FeOOH crust (inferred)
Sediment (observed)
Sediment (inferred)
Sulphide outcrop (observed)
Photo location and viewing direction
HyBIS sample grab
Dredge line
HyBIS dive path
Active hydrothermal chimney
Inactive hydrothermal chimney
Atacamite observation
Fault (observed)
Fault (inferred)

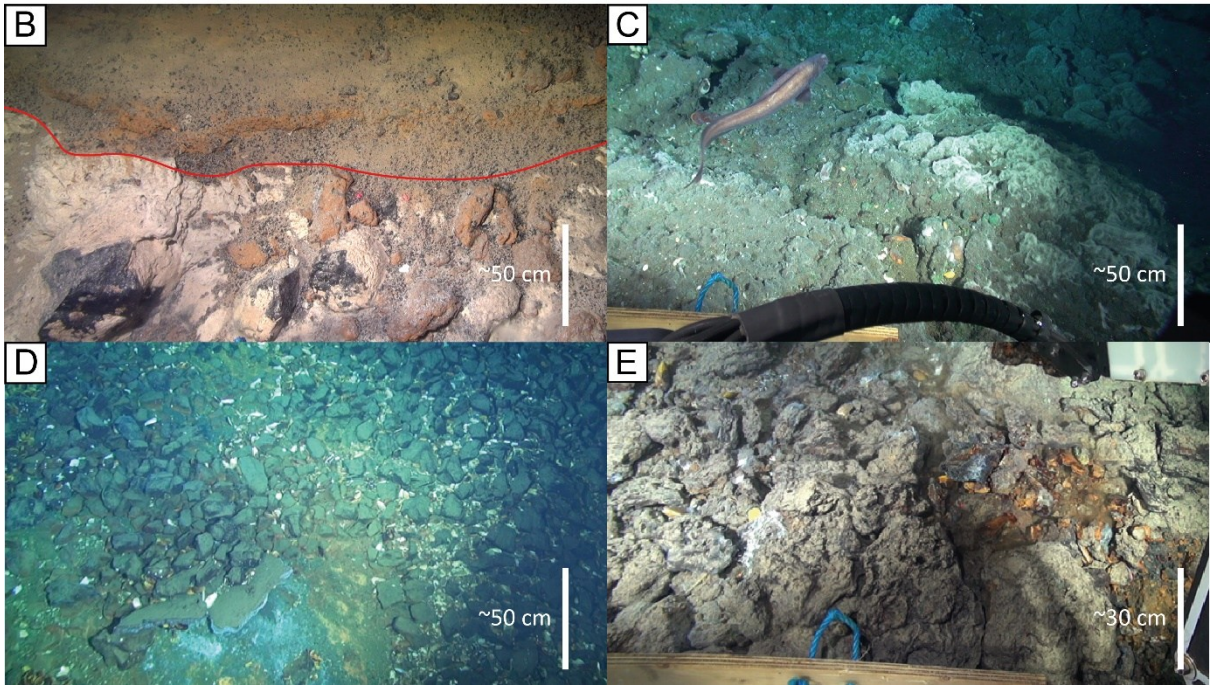
B
~50 cm
C
~50 cm
D
~50 cm
E
~30 cm

Figure 3.2. **(A)** Geological map of Semenov-2 with sample locations used in the study, geology interpreted from high-resolution bathymetry, surface samples and video surveys. **(B)** Hydrothermal sediment overlying bleached basalt talus. Boundary shown by red line. **(C)** Hydrothermal crust at Semenov-2 with small specks of atacamite mineralisation. **(D)** Basalt talus lying close to hydrothermal mound. **(E)** Sample location of 77_HY_02 and 77_HY_03 depicting FeOOH deposits.

3.3 Semenov-4

Semenov-4 represents the most geologically complex site within the Semenov hydrothermal field, characterised by extensive seafloor exposure of both volcanic and hydrothermal lithologies across a large mapped area spanning approximately 2500 meters east-west (Figure 3.3). The seafloor surface comprises predominantly basalt talus and igneous intrusive exposures covering approximately 40% of the mapped area, with talus exhibiting angular to subangular morphology.

Deposits of FeOOH, including admixtures with basalt and sulphide talus (Figure 3.3D), account for approximately 25% of the mapped seafloor area. These deposits display characteristic rough, crustal surface textures with variable manganese oxide coatings producing dark surface coloration (Figure 3.3C).

Sedimentary accumulations cover approximately 25% of the mapped area. The eastern part of Semenov-4 exhibits hydrothermal sediment accumulations with some overlying thinner pelagic sediment in areas (Figure 3.3B), suggesting recent hydrothermal activity consistent with proposed recent hydrothermal activity date at 1.7 ka (Kuznetsov et al., 2011). Conversely, the western area of Semenov-4 displays exclusively pelagic sedimentation without hydrothermal components, suggesting absence of recent hydrothermal influence in the western area, located on the footwall of the OCC.

Massive sulphide outcrops constitute approximately 10% of surface exposure, occurring primarily close to the summit of hydrothermal mounds and fault-controlled exposures. The largest concentration of sulphide material occurs atop a prominent sulphide mound measuring approximately 350 meters by 320 meters with 105 meters relief, where abundant relict chimney structures indicate previous high-temperature hydrothermal discharge.

Structural relationships of basalt talus overlying FeOOH deposits that indicates volcanic activity post-dating FeOOH formation and thus hydrothermal activity, while hydrothermal mounds surrounded by

basalt talus suggest simultaneous processes. These relationships indicate multiple phases of geological activity rather than simple sequential development.

Atacamite mineralisation occurs on both massive sulphide outcrops and FeOOH deposit surfaces, indicating widespread copper sulphide oxidation processes. The presence of atacamite on FeOOH deposits provides evidence for underlying sulphide mineralisation and suggests that surface FeOOH occurrences may overlie sulphide bodies (Hannington, 1993). Direct measurement of FeOOH deposit thickness using ROV imagery indicates approximately 30 cm thickness at one location, but difficult to obtain an accurate thickness estimate (Figure 3.3E).

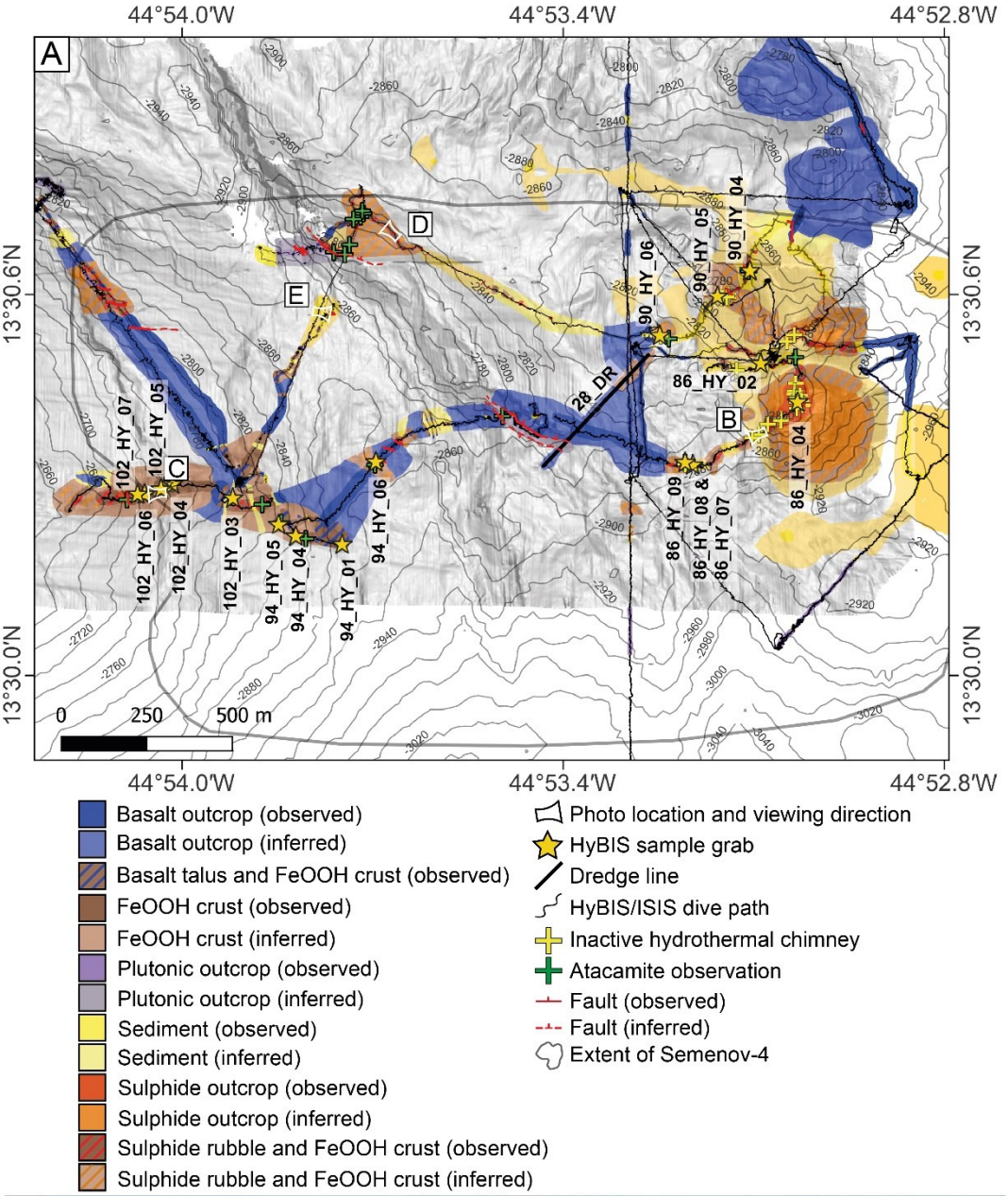
A
44°54.0'W
44°53.4'W
44°52.8'W
13°30.6'N
13°30.0'N
0
250
500 m
D
E
C
B
28_DR
102_HY_07
102_HY_05
102_HY_06
102_HY_04
102_HY_03
94_HY_05
94_HY_04
94_HY_01
94_HY_06
90_HY_06
90_HY_05
90_HY_04
86_HY_02
86_HY_04
86_HY_09
86_HY_08 &
86_HY_07
Basalt outcrop (observed)
Basalt outcrop (inferred)
Basalt talus and FeOOH crust (observed)
FeOOH crust (observed)
FeOOH crust (inferred)
Plutonic outcrop (observed)
Plutonic outcrop (inferred)
Sediment (observed)
Sediment (inferred)
Sulphide outcrop (observed)
Sulphide outcrop (inferred)
Sulphide rubble and FeOOH crust (observed)
Sulphide rubble and FeOOH crust (inferred)
Photo location and viewing direction
HyBIS sample grab
Dredge line
HyBIS/ISIS dive path
Inactive hydrothermal chimney
Atacamite observation
Fault (observed)
Fault (inferred)
Extent of Semenov-4

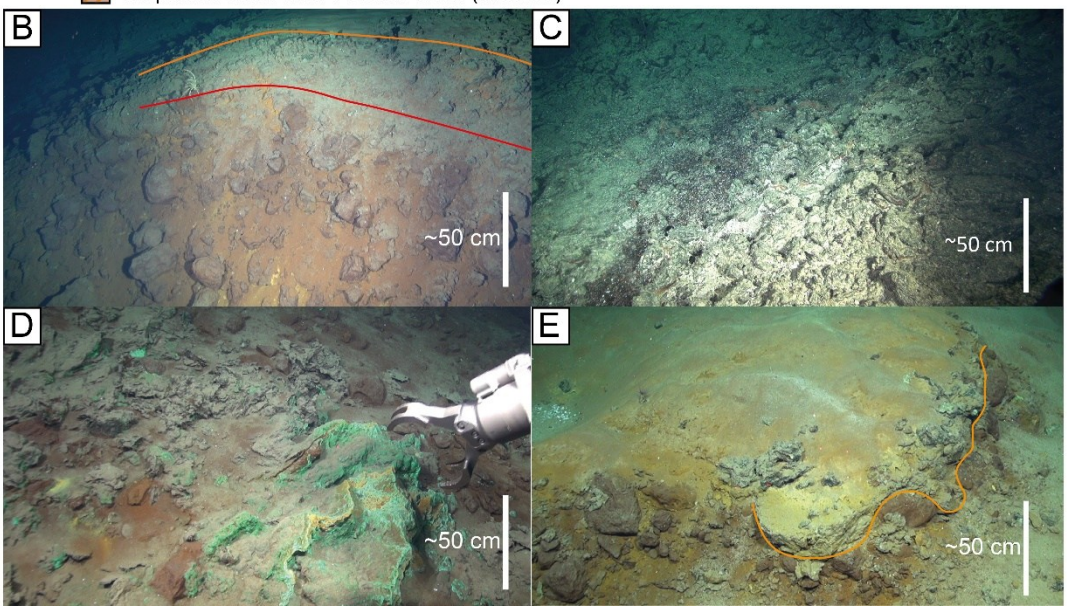
B
~50 cm
C
~50 cm
D
~50 cm
E
~50 cm

Figure 3.3 Geological map of Semenov-4 with sample locations used in the study, geology interpreted from high-resolution bathymetry, surface samples and video surveys. **(B)** Scarp located near the base of a large hydrothermal mound. Coloured lines indicate separation between pelagic to Fe rich sediment (orange) and Fe-rich sediment to sulphide rubble (red). **(C)** View of sample location at JC224_102_HY_04. Area is surrounded by FeOOH deposits with a coating of Mn-oxide (black). **(D)** Atacamite mineralisation (green) on massive sulphide and FeOOH deposits. **(E)** Boundary between sulphide and FeOOH deposits shown by the orange line. Approximate thickness of FeOOH is ~30 cm.

3.4 Semenov-5

Semenov-5 is characterised by exposure of massive sulphide as a result of faulting (Figure 3.4). Semenov-5 features a prominent east-west trending fault system extending approximately 130 meters across the seafloor (Figure 3.4D).

The seafloor surface comprises predominantly of FeOOH deposits with admixtures of sulphide talus covering approximately 50% of the mapped area, displaying typical rough, crustal morphologies and sheet like deposits (Figure 3.4E). Basalt talus and pelagic sediment collectively account for approximately 40% of the mapped area, with basalt talus concentrated around hydrothermal edifices and pelagic sediment accumulating in topographic depressions.

Massive sulphide exposures constitute approximately 10% of direct seafloor outcrop and are most visible through fault-controlled exposure (e.g., Figure 3.4B). The primary east-west trending fault system displaces surficial FeOOH deposits and reveals underlying massive sulphide bodies (Figure 3.4), demonstrating stratigraphic relationships between surface oxidation products and primary sulphide mineralisation. Additional fault exposures occur throughout areas otherwise dominated by basaltic terrain, and in one instance, reveals massive sulphide underlying basalt talus, indicating volcanic activity proceeding hydrothermal activity. Hydrothermal mounds surrounded by basalt talus suggest simultaneous volcanic activity with hydrothermal activity. These relationships indicate multiple phases of geological activity with varying temporal relationships between different areas of the site. Atacamite mineralisation occurs on the surface of sulphide outcrop, providing direct evidence for ongoing oxidation processes.

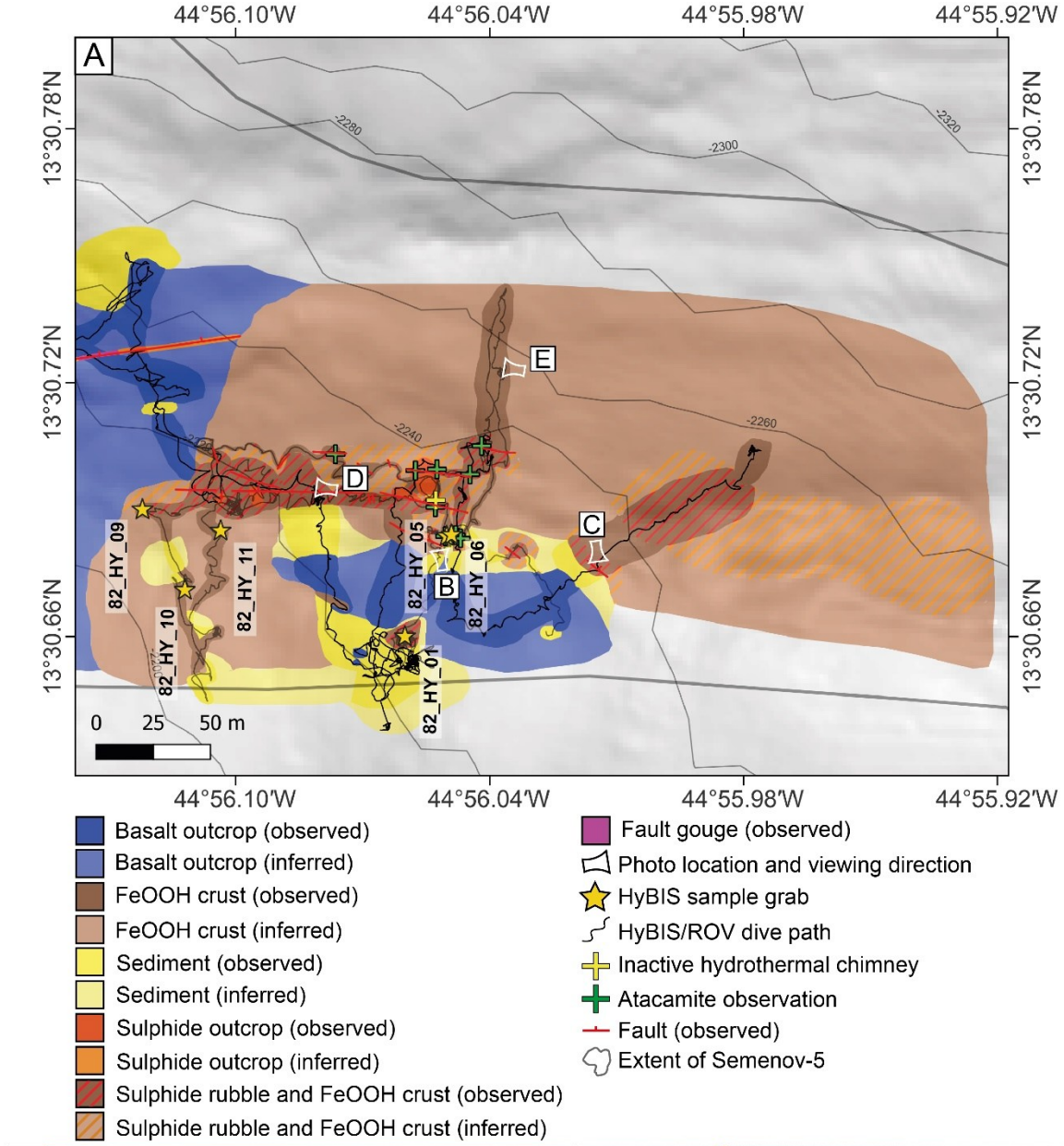
44°56.10'W
44°56.04'W
44°55.98'W
44°55.92'W
13°30.78'N
13°30.72'N
13°30.66'N
A
-2280
-2300
-2320
-2240
-2260
E
D
C
B
82_HY_09
82_HY_11
82_HY_10
82_HY_05
82_HY_06
82_HY_01
0 25 50 m
Basalt outcrop (observed)
Basalt outcrop (inferred)
FeOOH crust (observed)
FeOOH crust (inferred)
Sediment (observed)
Sediment (inferred)
Sulphide outcrop (observed)
Sulphide outcrop (inferred)
Sulphide rubble and FeOOH crust (observed)
Sulphide rubble and FeOOH crust (inferred)
Fault gouge (observed)
Photo location and viewing direction
HyBIS sample grab
HyBIS/ROV dive path
Inactive hydrothermal chimney
Atacamite observation
Fault (observed)
Extent of Semenov-5

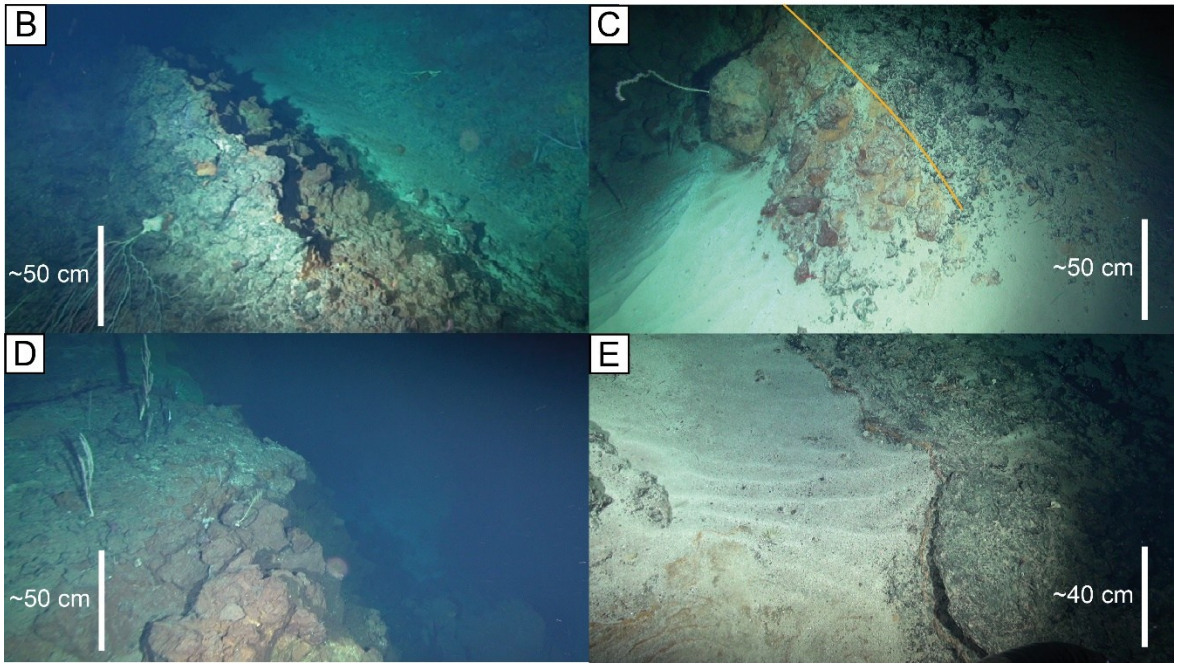
B
~50 cm
C
~50 cm
D
~50 cm
E
~40 cm

Figure 3.4 **(A)** Geological map of Semenov-5 with sample locations used in the study, geology interpreted from high-resolution bathymetry, surface samples and video surveys. **(B)** Large fault scarp oriented roughly E-W exposing massive sulphide (red) underlying FeOOH deposits (black). **(C)** Massive sulphide (red) underlying FeOOH deposits (black) with boundary shown by orange line. **(D)** Deposits of FeOOH (greyish black) overlying massive sulphide (red). Fault running approximately E-W creates a scarp exposing massive sulphide. **(E)** Deposits of FeOOH that form sheet like deposits.

Chapter 4 The Formation, Modification and Resource Potential of Fe-oxyhydroxides in Seafloor Massive Sulphide Systems

This chapter consists of a manuscript published in Mineralium Deposita. This chapter investigates FeOOH deposits and massive sulphide at Semenov hydrothermal field. The data acquired from this study is also used in the comparison of other similar studies in an attempt to explore the variation in metal content between FeOOH deposits at SMS systems and the reasons as to why. The objectives of this chapter are to discriminate metal-poor primary FeOOH versus metal-rich secondary FeOOH, quantify how seawater interactions modify Cu-Zn enrichment in secondary FeOOH, and assess the use of secondary FeOOH as an exploration guide for underlying sulphide.

The data within this Chapter is available within the Appendix of this thesis and the BODC database after Bishop et al. (2025a) and (Bishop et al., 2025b).

Bishop, C.S[1], Lichtschlag, A[2], Roberts, S., Lesage, M[3]., Murton, B.J.,[2] Fe-oxyhydroxide deposits at Semenov Hydrothermal Field (13°30'N), Mid-Atlantic Ridge: insights into formation, modification and resource potential. *Mineralium Deposita*, https://doi.org/10.1007/s00126-025-01376-6

[1]School of Ocean and Earth Science, University of Southampton, Southampton, UK,

[2]National Oceanography Centre, Southampton, UK,

[3]Haggaløkkveien 26, Asker, Viken 1383, Norway

Author contributions

Christian Bishop: Conceptualisation, data curation, formal analysis, investigation, methodology, writing. **Bramley Murton:** Conceptualisation, supervision, writing – review and editing. **Anna Lichtschlag:** Supervision, writing – review & editing. **Stephen Roberts:** Supervision, writing – review and editing. **Maxime Lesage:** Supervision, writing – review.

Abstract

Secondary Fe-oxyhydroxide (FeOOH) forms at seafloor massive sulphide (SMS) deposits through the oxidation of sulphide minerals by oxygenated seawater. Secondary FeOOH deposits are enriched in economically important metals, such as Cu and Zn, potentially representing an additional resource. However, how the metal content of secondary FeOOH evolves through post-formational modification at the seafloor, is poorly understood. Moreover, FeOOH can form as metal-poor primary precipitates, but our knowledge is insufficient to effectively discriminate between primary and secondary FeOOH at SMS deposits. At the Mid-Atlantic Ridge hosted Semenov hydrothermal field, primary FeOOH deposits are typically metal poor (<0.4 wt.% Cu + Ni + Zn, n=6) and form layered chimney structures with alternating Mn-oxide and FeOOH bands, with the fluid conduit lined with green smectite. In contrast, secondary FeOOH deposits have a high Cu content, averaging 2.4 wt.% (n=31), and exhibit diverse textural morphologies including chimney, brecciated, layered, ochre, ocherous and massive, inherited from the sulphide protolith. Secondary FeOOH behaves similarly to terrestrial gossans, acting as a metal trap through sorption or precipitation of metals released during underlying sulphide oxidation. A positive relationship between the Cu content of secondary FeOOH deposits and the Cu content of sulphide deposits across the field suggests that Cu-rich sulphide systems tend to produce Cu-rich FeOOH, highlighting the potential of FeOOH as a geochemical exploration indicator. Finally, the Cu content in the secondary FeOOH remains stable even under prolonged exposure to seawater at the seafloor, indicating that older, off-axis, buried and oxidised SMS deposits may still contain secondary FeOOH with appreciable amounts of Cu. Overall this study demonstrates the potential of secondary FeOOH as a potential metal resource and a tool to guide exploration at SMS deposits.

4.1 Introduction

Seafloor hydrothermal activity occurs in diverse tectonic settings, including Mid-Ocean Ridges (MOR), intra-oceanic volcanic arcs, back-arc spreading centres, ocean-continent transition and hotspots (Rona, 1988; Hannington et al., 1994; Patten et al., 2022). Hydrothermal fluids often precipitate metal-rich minerals at and below the seafloor that can develop into Seafloor Massive Sulphide (SMS) deposits, which are of international interest due to their high metal content (e.g. Cu; Hannington et al., 2010; Monecke et al., 2016; Juliani and Ellefmo, 2018). At SMS deposits, oxidation of sulphide minerals by oxygenated seawater produces secondary minerals such as Fe-oxyhydroxide (FeOOH), sulphates and atacamite (Herzig et al., 1991; Hannington, 1993; Hekinian et al., 1993). This oxidative weathering mobilises potentially economically valuable metals from the primary sulphides and this process could diminish the metal content of SMS

deposits over time. However, FeOOH also could retain these metals, potentially preserving the metal content of SMS deposits (Hannington et al., 1991; Melekestseva et al., 2020a; Hu et al., 2022; Hou et al., 2024).

At SMS deposits, FeOOH deposits can be present in the form of chimneys, mounds, or crust covering sulphide structures (Hekinian et al., 1991; Melekestseva et al., 2020a). FeOOH formation occurs through two processes: 1) as metal-poor primary precipitates from low-temperature (<~100°C), iron-rich hydrothermal fluids (Alt 1988; Hekinian et al., 1993; Gini et al., 2024), and 2) as metal-rich, secondary FeOOH, formed through the oxidation of sulphide by oxygenated seawater (Herzig et al., 1991; Hekinian et al., 1993). Despite extensive studies of SMS deposits, few studies investigate the variability of FeOOHs across a SMS deposit, and consequently, our understanding on their formation mechanisms and metal content is incomplete. It remains uncertain whether primary or secondary mechanisms of FeOOH formation dominate at SMS deposits (Hekinian et al., 1993). Clarifying this distinction is crucial because, similarly to terrestrial gossans (e.g., Constantinou, 1972), secondary FeOOH may indicate underlying sulphide and provide clues to the metal content of the sulphide, serving as a valuable tool for targeting exploration and as an additional resource. However, post-formational modification may alter the metal content of secondary FeOOH. For example, when secondary FeOOH is exposed to seawater, competing cations may displace adsorbed economic metals (Balistrieri & Murray, 1982; Calmano et al., 1988). Consequently, extensive seawater influence may reduce economic metal concentrations in secondary FeOOH, impacting the resource potential of these products. To address these questions, this study focuses on the Semenov hydrothermal field, an ultramafic-hosted SMS cluster located at 13° 30'N on the Mid-Atlantic Ridge (Beltenev et al., 2007). The Semenov field comprises of five hydrothermal areas each containing exposed sulphide and FeOOH material (Beltenev et al., 2007; Escartín et al., 2017, Murton & Shipboard Scientific Party, 2022). Our objectives are to: (1) discriminate primary and secondary FeOOH deposits across the Semenov hydrothermal field; (2) assess how seawater interaction can influence the economic metal content (i.e., Cu and Zn) of secondary FeOOH, and; (3) evaluate the potential of the secondary FeOOH as an exploration tool for identifying high-grade sulphide deposits.

4.2 Methods

4.2.1 Seafloor sampling

Forty-two samples were collected during the project "ULTRA" with the RRS James Cook (JC224; 2022; section 2.1). Samples from Semenov-1, Semenov-2, Semenov-4 and Semenov-5 were recovered at the seafloor using the Hydraulic Benthic Interactive Sampler (HyBIS) robotic underwater vehicle (Murton et al., 2012). Additional samples were acquired by dredging across Semenov-1 and Semenov-4. A full list of sample locations and descriptions can be found in Bishop et al., (2025a).

4.2.2 Reflective light microscopy

To help understand the formation mechanisms of the FeOOH and massive sulphide samples, I examined their mineralogy, textures and paragenesis using reflective light microphotography with a LEICA DM2700 P microscope. Images were captured by the LEICA DMC 4500 and processed with the Leica Application Suite X software (section 2.3.1).

4.2.3 XRD

To determine the crystalline phases, present in the FeOOH and massive sulphide samples, and thus infer their possible formation mechanisms, XRD analysis was conducted on 30 bulk samples. Samples were prepared by crushing and grinding with corundum internal standard, then analysed using a PANalytical X'Pert Pro diffractometer (full methodology in section 2.3.2)

4.2.4 Major and trace elemental analysis

Bulk geochemical analysis of FeOOH samples is essential to determine their formation history, tracking how metal contents may change during sulphide oxidation and seafloor alteration, and assessing the resource potential of FeOOH resulting deposits. Bulk elemental concentrations were obtained through acid digestion followed by ICP-MS/ICP-OES analysis of FeOOH samples (n=37) and massive sulphide samples (n=5). Samples underwent HF-HNO_3-HCl digestion in cleaned Teflon pots, with analysis performed on 4000-fold diluted solutions (detailed protocol in section 2.5.1).

Accuracy and precision were determined by triplicate measurements of CRM of JMn-1, RTS-1, GSPN-2, except for Fe, Ni, Mg and Ti, which were measured in duplicate for RTS-1 and GSPN-2. Further single measurements of GSPN-3, CH-4, Nod-A-1 and Nod-P-1 CRM were taken to ascertain accuracy. Of the elements discussed in the study, major and trace element

measurements exhibited good accuracy, the majority of elements were within 10% error of the expected values, except for Mg (± 13.0%), Ca (± 11.7%), Co (± 17.6%), Zn (± 10.0%) and La (± 11%). Precision exhibited good reproducibility with elements showing a standard deviation of ≤ 10.0%, except for As (± 14.5%). See section 2.5.1 for summary of accuracy and precision data and Appendix A.3 for full CRM list.

4.2.5 Sr-Nd-Pb isotope systematics

Radiogenic isotopic analysis provides information to the source of these elements within bulk samples and to interpret their origin and modification. Radiogenic Sr-Nd-Pb were extracted with a total of 19 samples for Pb and 16 samples for Nd and Sr analysis. Accuracy and precision of CRMs (Nod-A-1, Nod-P-1 and BHVO-1) and internal standards (JNdi-1, NBS 987 and NBS 981) fall within the range of published values for their respective isotope systematic (see full method in section 2.5.2)

4.2.6 End-member mixing

To account for the impact of pelagic sediment on the isotopic ratio of Pb within the FeOOH samples, the proportion of pelagic sediment in the FeOOH sample was assessed using binary mixing plots based on the Al/(Al+Fe+Mn) ratio as described by Boström (1973) to identify detrital input and Ca for carbonate within the pelagic sediment. This is done in order to create an accurate fluid-to-rock (F/R) ratio that accounts for the contamination of pelagic sediment within a given sample. By utilising massive sulphide samples from this study and North Atlantic carbonate ooze sediment composition after Menendez et al. (2017) as two endmembers, the resulting mixing curve allows to determine the percentage of the sedimentary component in a sample. The general form of a binary mixing equation adapted from Faure (1998) is used to quantify the contribution of pelagic sediment to each FeOOH sample using Eq. 4.1 and Eq. 4.2. Equation 4.1 estimates the proportion of detrital material using the Al/(Al+Fe+Mn) ratio, where PSDC and MSDS represent the Al/(Al+Fe+Mn) ratios of pelagic sediment and massive sulphide, respectively. PS_f and MS_f are the mixing fractions of pelagic sediment and massive sulphide, while Al, Fe, and Mn are the concentrations (in ppm) of each element in the respective endmembers.

$$\left(\frac{Al}{Al+Fe+Mn}\right)_{mix} = \frac{\left(PS_{DC} \times (Al_{PS} + Fe_{PS} + Mn_{PS}) \times PS_f\right) + \left(MS_{DC} \times (Al_{MS} + Fe_{MS} + Mn_{MS}) \times MS_f\right)}{\left(Al_{PS} + Fe_{PS} + Mn_{PS}\right) \times PS_f\right) + \left(Al_{MS} + Fe_{MS} + Mn_{MS}\right) \times MS_f\right)} \quad \textbf{Eq. 4.1}$$

To account for carbonate input, Ca concentrations are also evaluated in Eq. 4.2, based on Faure (1998). In this equation Ca_{PS} and Ca_{MS} are the Ca concentrations (ppm) in the pelagic sediment and massive sulphide endmembers, respectively, and PS_f represents the sediment fraction.

$$Ca_{mix} = PS_f \times Ca_{PS} + ((1 - PS_f) \times Ca_{MS}) \quad \textbf{Eq. 4.2}$$

4.2.7 Seawater mixing

Lead isotopic compositions in FeOOH can reflect the interaction between seawater and FeOOH and can be used to determine how this interaction may affect metal concentration. This interaction between FeOOH and seawater is expressed as the F/R ratio and represents the amount of seawater required to isotopically modify FeOOH from a massive sulphide signature toward a seawater-like composition. To estimate the F/R of secondary FeOOH, a binary mixing model is used, with massive sulphide and seawater as two endmembers. The position of the FeOOH sample along this mixing curve reflects the degree of Pb isotope exchange, and thus the F/R ratio required to shift the isotopic composition from that of the massive sulphide toward seawater. The concentration of Pb in seawater is acquired after Bridgestock et al. (2018) from a bottom water sample to the south-east of the Semenov field (station 16, 8.20°N, 28.20°W). The Pb isotopic ratios of seawater is derived from Abouchami et al. (1999).

Compilation of mixing models were developed using two component mixing equations from Faure (1998; Eq. 4.3 and Eq. 4.4). Equation 3.3 calculates the isotopic composition of a mixture between sulphide and pelagic sediment. Using $^{206}Pb/^{204}Pb$ as an example, $^{206}Pb/^{204}Pb_{MS}$ and $^{206}Pb/^{204}Pb_{PS}$ are the isotopic signatures of the sulphide and pelagic sediment endmembers, respectively; Pb_{MS} and Pb_{PS} are their Pb concentrations (ppm); and f_{MS} and f_{PS} are their respective mixing fractions. The fraction of sediment within each sample is obtained by the sulphide-pelagic sediment mixing line derived from Eq. 4.1 and Eq. 4.

$$\frac{206\text{Pb}}{204\text{Pb}_{MIX}} = \frac{\left(\frac{206\text{Pb}}{204\text{Pb}_{MS}} \times Pb_{MS} \times f_{MS}\right) + \left(\frac{206\text{Pb}}{204\text{Pb}_{PS}} \times Pb_{PS} \times f_{PS}\right)}{(Pb_{PS} \times f_{MS}) + (Pb_{MS} \times f_{PS})} \quad \textbf{Eq. 4.3}$$

The isotopic composition derived from Eq. 4.3 represents the Pb isotope ratio of a mixture between massive sulphide and pelagic sediment. This mixture is then treated as a single endmember, with seawater serving as the second endmember in subsequent mixing calculations. Eq. 4.4 is used to generate a final Pb isotopic ratio between the sulphide–sediment mixture and seawater to generate a binary mixing curve. In this equation, $^{206}Pb/^{204}Pb_{MIX}$ and $^{206}Pb/^{204}Pb_{SW}$ represents the isotopic ratios of sulphide-sediment and seawater, respectively; Pb_{MIX} and Pb_{SW} are the corresponding Pb concentrations; and f_{MIX} and f_{SW} are their respective mixing fractions. The position of the Pb isotope ratio of the FeOOH sample along the mixing curve from Eq. 4.4 will derive a quantitative F/R that accounts for the contamination of sediment.

$$\frac{206\text{Pb}}{204\text{Pb}_{Final}} = \frac{\left(\frac{206\text{Pb}}{204\text{Pb}_{MIX}} \times Pb_{MIX} \times f_{MIX}\right) + \left(\frac{206\text{Pb}}{204\text{Pb}_{SW}} \times Pb_{SW} \times f_{SW}\right)}{(Pb_{SW} \times f_{SW}) + (Pb_{MIX} \times f_{MIX})} \qquad \textbf{Eq. 4.4}$$

4.3 Results

4.3.1 Morphology, lithology and mineralogy of FeOOH deposits at Semenov

The FeOOH deposits samples at Semenov have various textural morphologies, including chimney, layered, ochre, brecciated, massive and ocherous material (Figure 4.1; Bishop et al. 2025a). Results of combined XRD, hand sample observations and reflective microscopy indicate that all FeOOH samples contain X-ray amorphous FeOOH and goethite (α-FeOOH) with the majority of samples containing a minor amount (<5% by volume) of quartz. Broad peaks of goethite in some samples (e.g., 82_HY_01) suggest over milling, but does not result in the formation of amorphous FeOOH. Atacamite is present in eight FeOOH samples, typically as veins (Figure 4.1B; see Bishop et al. 2025b for full XRD data).

FeOOH deposits with chimney textural morphologies are subdivided into two types; Type-I is only found at Semenov-1 and comprise pale brown to yellow alternating layers of FeOOH and Mn-oxide. Type-I chimney deposits also have a coating of clay-silt sized particles of green smectite on the inside of the fluid conduit (Figure 4.1A), which, based on visual observations, is likely nontronite (Murnane & Clague, 1983; Dekov et al., 2007). Type-I chimneys also contain minor amounts of quartz, barite and calcite. Reflected light microscopy reveals colloform Mn-oxide textures, rare relict pyrite surrounded by FeOOH and foraminifera tests replaced by FeOOH (Figure 4.1G, Figure 4.1H, Figure 4.1J). Pyrite remnants are typically found within specific FeOOH grains (Figure 4.1J), as such, the pyrite remnants are likely pyrite that have not yet been altered to FeOOH. Type-II chimneys at Semenov-4 comprise dark brown to dark red FeOOH that forms fluid conduit structures with minor amounts of atacamite, akageneite, calcite, barite and quartz (Figure 4.1D)

FeOOH deposits with layered textural morphologies are subdivided into two types with Type-I at Semenov-1 comprising <1 cm alternating horizontal layers of pale brown to yellow FeOOH and Mn-oxide with minor amount of talc. Type-II layered morphologies lack the Mn-oxide layers, but instead exhibit <1 cm layers of light orange to dark red FeOOH. Atacamite within type-II layered morphologies form as veins conformable to layering or as precipitates on the sample.

FeOOH deposits with ochre textural morphology are relatively soft compared with other textural morphologies and contain orange, granular FeOOH that is moderately sorted to well sorted with minor to trace amounts of quartz, barite, calcite, mackinawite and hematite. Ochre textural

morphologies exhibit either a homogenous texture (Type-I) or form alternating lamination of pale orange to orange FeOOH (Type-II; Figure 4.1C). While similar to ochre, ocherous textural morphologies are more consolidated and mechanically competent, often displaying a denser fabric and darker colouration ranging from dark brown to brownish orange. Ocherous textural morphologies are composed of granular FeOOH with minor quartz and pyrite, and exhibit internal veining. Ocherous samples may also exhibit subtle layering of orange to orange-brown FeOOH (Figure 4.1E)

Brecciated FeOOH deposits exhibit clasts set in a matrix of FeOOH and are subdivided into two types. Type-I with clasts of angular, dark red to orange FeOOH and veins of atacamite within the matrix with minor to trace amounts of Mn-oxide and akageneite acquired at Semenov-1 and Semenov-5. Type-II brecciated deposits at Semenov-2 occur as clasts of rounded to sub-angular clasts of barite, talc, quartz and FeOOH (Figure 4.1F). Brecciated deposits contain frequent pyrite with a single chalcopyrite crystal observed. Massive FeOOH deposits have no obvious textural morphology and are dominated by FeOOH with minor amounts of quartz, calcite, atacamite, Mn-oxide, paratacamite, and relict pyrite.

Massive sulphide samples contain pyrite (>50% by volume), followed by minor amounts of chalcopyrite, sphalerite, FeOOH ± barite ± atacamite, and trace quantities of covellite replacing chalcopyrite (Figure 4.1K, Figure 4.1L). Atacamite is observed within FeOOH and not in close association with sulphide minerals (Figure 4.1L).

One sample comprises both massive sulphide and FeOOH that forms as a crust on top of massive sulphide (Figure 4.1B). The massive sulphide is dominated by pyrite (>80% by volume), with minor amounts of chalcopyrite and FeOOH with trace amounts of sphalerite, atacamite and covellite. The contact between FeOOH and pyrite likely represents an oxidation front where sulphide has begun altering to FeOOH (Figure 4.1L). The FeOOH crust is dominated by FeOOH with atacamite making up approximately 10% by volume of the crust. Relict pyrite within grains of FeOOH are rare and have a similar appearance as relict pyrite observed in Figure 4.1I and Figure 4.1J.

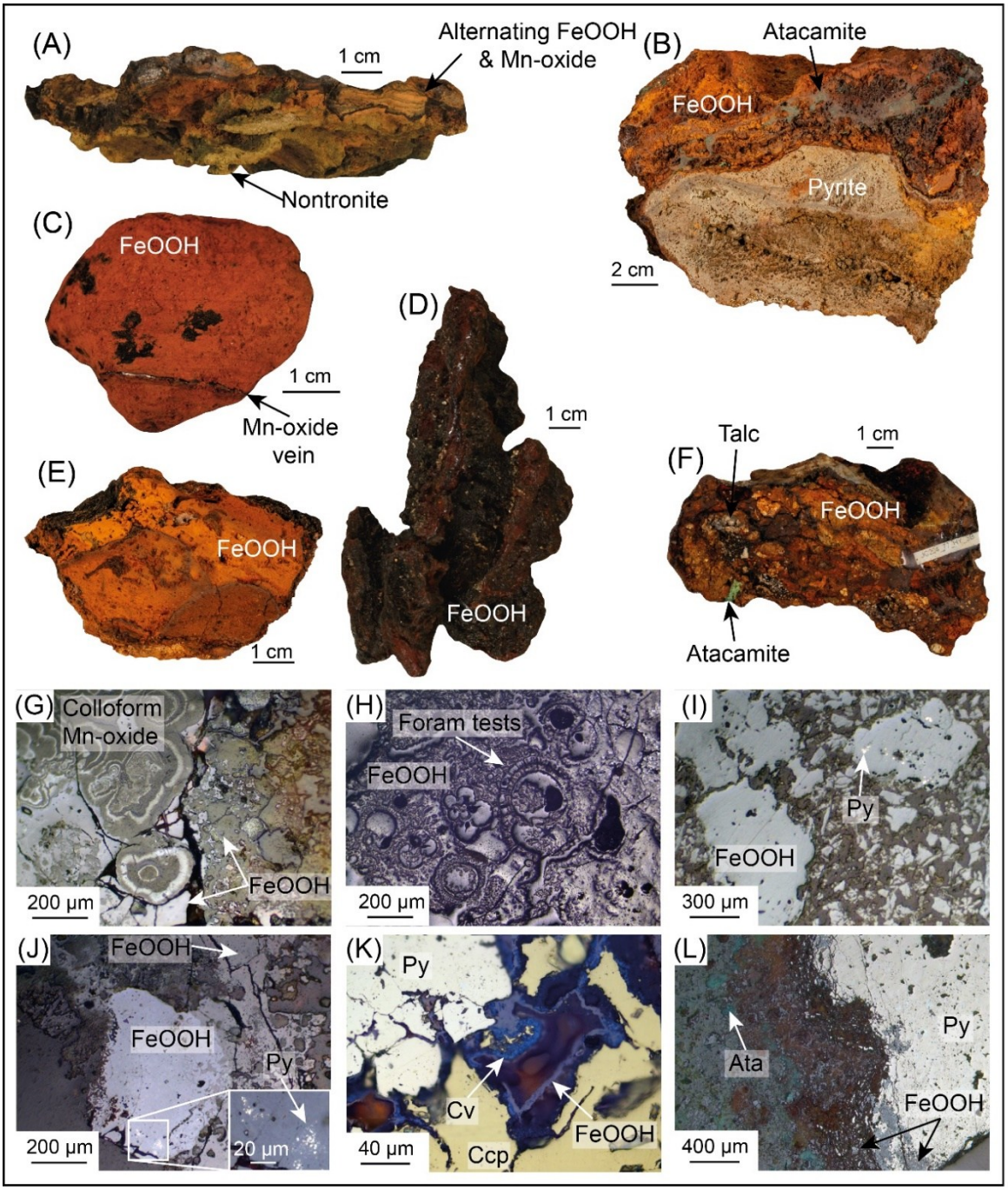

Figure 4.1. Representative hand specimen photos and reflected light photomicrographs of samples from Semenov hydrothermal field. **(A)** Type-I chimney FeOOH composed of nontronite with alternating layers of FeOOH and Mn-oxides (71_DR_01). **(B)** Massive FeOOH with actively weathering massive sulphide and an FeOOH crust comprising FeOOH and atacamite (82_HY_06). **(C)** Type-II ochre FeOOH comprise orange, soft, fine grains with thin layers (<1 mm) of alternating darker and lighter FeOOH (28_DR_18). **(D)** Type-II chimney with dark red to orange FeOOH and thin veins (~1 mm) of Mn-oxides (102_HY_04). **(E)** Ocherous FeOOH comprise fine grained FeOOH (82_HY_05). **(F)** Brecciated FeOOH of predominately FeOOH with minor quantities of atacamite, talc, quartz and barite (77_HY_03).

(G) Colloform Mn-oxides growth adjacent to FeOOH shown by the granular, subhedral–anhedral texture (71_DR_07**). (H)** Multiple foraminifera tests replaced by FeOOH (71_DR_03). **(I)** Grains of FeOOH with one grain containing relict pyrite indicating FeOOH grain is secondary. FeOOH form as pseudomorphs of pyrite crystals (82_HY_05). **(J)** Relict pyrite within large grain of FeOOH surrounded by FeOOH (71_DR_01). **(K)** Subhedral to anhedral pyrite set beside chalcopyrite. Covellite occurs adjacent to chalcopyrite and is typically encased by FeOOH (82_HY_06). **(L)** Redox front separating massive pyrite and FeOOH. Close to redox front, pyrite is replaced to FeOOH, at the redox front, pyrite forms as brecciated pyrite set in FeOOH. Atacamite vein within FeOOH (82_HY_06$_b$). Mineral abbreviations: Py – Pyrite, Cv – covellite, Ccp – chalcopyrite.

4.3.2 Bulk major and trace elemental composition

The geochemical composition of FeOOH deposits and sulphides from Semenov are summarised in Table 4.1, with details of each sample shown in Appendix B.1. The chemical composition of FeOOH deposits, regardless of morphology, is highly variable in Cu, Fe, and Mn with variations in Mg, Ca, Al, Zn, Ti, Li, Co and As (Table 4.1). The highest concentration of Cu is found in a massive FeOOH sample (82_HY_06$_a$) with a concentration of 16.8 wt.% with the lowest concentration at 0.04 wt.% (86_HY_08). Zn is less variable, with the highest measured concentration of 0.55 wt.% in an ochre sample (86_HY_09) and the lowest measured concentration of 0.01 wt.%.

Relative to other textural morphologies, Type-I chimney and Type-I layered deposits are enriched in Mn and Li, and depleted in Fe and Cu. Type-II chimney, Type-II layered brecciated, massive, ochre and ocherous deposits exhibit similar contents of Al, Ca, Cu, Ti and Zn (Table 4.1).

Massive sulphide samples exhibit greater variation in Cu concentrations compared to Zn and As concentrations (Table 4.1). Compared to barite-free massive sulphides, barite-rich massive sulphides have higher Cu (6.03–15.23 wt.% vs. 0.11–2.01 wt.%) and lower Fe (29.0–29.3 wt.% vs. 33.7–34.6 wt.%).

Table 4.1. Average contents of major and trace elements in FeOOH and massive sulphide. <LOD = below limit of detection. ± is 1 standard deviation. Where n = 2, the range of composition is given.

	Mg (wt.%)	Al (wt.%)	Ca (wt.%)	Mn (wt.%)	Fe (wt.%)	Cu (wt.%)	Li (ppm)	Ti (ppm)
Type-I chimney (n=5)	0.71 ± 0.04	0.17 ± 0.06	0.78 ± 0.15	7.76 ± 2.72	21.87 ± 1.84	0.14 ± 0.08	107 ± 29	100 ± 50
Type-II chimney (n=3)	0.33 ± 0.07	0.14 ± 0.12	0.58 ± 0.48	0.29 ± 0.39	35.04 ± 2.74	0.73 ± 1.11	1.2 ± 0.2	70 ± 70
Type-I layered (n=1)	1.06 ± 0.07	0.32 ± 0.03	0.67 ± 0.00	7.51 ± 0.01	20.48 ± 0.03	0.14 ± 0.00	102 ± 1.7	240 ± 10
Type-II layered (n=6)	0.50 ± 0.20	0.18 ± 0.11	0.72 ± 0.40	2.26 ± 2.72	33.40 ± 4.11	3.12 ± 4.40	11 ± 15	170 ± 130
Type-I brecciated (n=2)	0.61–0.75	0.24–0.15	1.00–0.72	0.62–0.19	30.00-34.68	2.48–1.84	3.9–3.6	120-330
Type-II brecciated (n=2)	0.89-2.05	1.00–0.46	1.53–0.56	1.38–2.48	18.65-24.64	6.90–0.87	7.1–3.0	180-510
Ocherous (n=3)	0.72 ± 0.15	0.22 ± 0.04	0.92 ± 0.44	0.21 ± 0.15	31.74 ± 2.62	1.56 ± 1.12	3.9 ± 2.9	80 ± 30
Type-I & II Ochre (n=6)	0.64 ± 0.34	0.57 ± 0.64	0.68 ± 0.45	0.63 ± 0.68	28.87 ± 4.70	2.42 ± 1.90	3.6 ± 3.6	420 ± 510
Massive FeOOH (n=9)	0.68 ± 0.29	0.38 ± 0.29	1.99 ± 1.65	2.12 ± 2.86	31.10 ± 3.54	2.46 ± 5.41	13 ± 21	360 ± 390
Massive sulphide (n=5)	0.03 ± 0.03	0.04 ± 0.05	0.08 ± 0.16	<0.01	32.64 ± 2.19	4.75 ± 6.73	0.2 ± 0.2	10 ± 10

	Co (ppm)	Zn (ppm)	As (ppm)	Sr (ppm)	Pb (ppm)	Bi (ppm)	U (ppm)	Al/(Al+Fe+Mn)
Type-I chimney (n=5)	35 ± 26	840 ± 330	87 ± 44	310 ± 100	19 ± 12	0.15 ± 0.21	2.0 ± 1.6	0.0055 ± 0.0016
Type-II chimney (n=3)	45 ± 36	2420 ± 990	207 ± 45	230 ± 150	293 ± 295	0.06 ± 0.02	25.6 ± 24.3	0.0039 ± 0.0020
Type-I layered (n=1)	111 ± 1	840 ± 10	199 ± 1	480 ± <10	51 ± 0.5	1.2 ± 2.0	19.3 ± 15.2	0.0113
Type-II layered (n=6)	240 ± 212	1620 ± 870	286 ± 262	240 ± 120	190 ± 175	1.12± 2.0	19.3 ± 15.2	0.0061 ± 0.0038
Type-I brecciated (n=2)	40–38	1060–310	329–241	270–210	190–16	15.1–0.2	16.7–5.3	0.0050-0.0068
Type-II brecciated (n=2)	139–59	290–130	171–159	1180–490	284–57	2.2–1.0	7.7–7.5	0.0168-0.0476
Ocherous (n=3)	29 ± 22	1940 ± 1750	469 ± 113	290 ± 50	351 ± 84	2.7 ± 3.7	13.6 ± 7.7	0.0067 ± 0.0008
Type-I & II Ochre (n=6)	82 ± 83	1900 ± 1920	423 ± 283	620 ± 240	265 ± 193	1.3 ± 1.0	10.4 ± 4.9	0.0212 ± 0.0273
Massive FeOOH (n=9)	95 ± 80	1300 ± 590	300 ± 128	440 ± 270	167 ± 143	2.1 ± 3.4	18.1 ± 12.9	0.0115 ± 0.0102
Massive sulphide (n=5)	111 ± 241	1900 ± 1010	214 ± 39	190 ± 260	156 ± 58	1.6 ± 2.4	4.1 ± 1.8	0.0013 ± 0.0013

4.3.3 REE concentration and correlation patterns

REE patterns of FeOOH from Semenov are categorised into three groups based on similar REE pattern regardless of textural morphologies or whether primary or secondary FeOOH deposits, and are shown in Table 4.2 and Figure 4.2 (full details in Appendix B.2 and Bishop et al. 2025b). REE FeOOH group 1 is defined by no or slightly negative Eu anomaly, weakly negative Ce anomaly and a considerable variation in ΣREE content (Table 4.2). REE FeOOH group 2 is characterised by a positive Eu anomaly, a weak negative Ce anomaly and lower average ΣREE concentration relative to REE FeOOH group 1. REE FeOOH group 3 has a strong positive Eu anomaly, a negative Ce anomaly and typically lower average ΣREE concentrations relative to REE FeOOH groups 1 and 2. The ΣREE concentrations of REE FeOOH group 1 exhibit a strong correlation with detrital elements such as Al, Al/(Al+Fe+Mn; Boström, 1973) and Ca (R^2 = 0.83, 0.67 and 0.81 respectively) and a moderate correlation with Ti (R^2 = 0.45; Bishop et al., 2025b). REE FeOOH group 2 show moderate positive correlations of ΣREE with Ti and Al/(Al+Fe+Mn; R^2 = 0.66 and 0.60 respectively) and a weak negative correlation with Fe/Ti ratio (R^2 = 0.42; Bishop et al., 2025b). Due to only three samples in REE FeOOH group 3, no correlation analyses were performed. However, relative to REE FeOOH group 2 and 1, REE FeOOH group 3 is strongly depleted in Ti (average of 30 ppm vs 160 ppm and 400 ppm) and the Al/(Al+Fe+Mn) ratio (0.0036 vs 0.0098 and 0.0122).

Massive sulphide samples (n=5) are also categorised into three REE groups with REE sulphide trend 1 exhibits neither an Eu anomaly or a Ce anomaly (Table 4.2; Figure 4.2). REE sulphide trend 2 characterised by a weakly positive Eu anomaly and no Ce anomaly. REE sulphide trend 3 show a strong positive Eu anomaly and no to weakly negative Ce anomaly.

Table 4.2. Contents of REEs in FeOOH and massive sulphides samples at Semenov. Both FeOOH and massive sulphide are categorised into three REE groups based on their REE trend. Sulphide group 1 and 3 only have two samples and the values depict the range. Ce and Eu anomalies (Ce* and Eu*) are calculated after McLennan (1989) using the following formula $Ce^* = Ce_n/(La_n*Pr_n)*0.5$. $Eu^* = Eu_n/(Sm_n*Gd_n)*0.5$. Elements with X_n indicate chondrite normalised.

	La (ppm)	Ce (ppm)	Pr (ppm)	Nd (ppm)	Sm (ppm)	Eu (ppm)	Gd (ppm)	Tb (ppm)	Dy (ppm)	Ho (ppm)
REE FeOOH group 1 (n=17)	20.7 ± 19.7	29.8 ± 25.8	5.0 ± 4.9	20.6 ± 19.8	4.4 ± 4.2	1.3 ± 1.1	4.9 ± 4.4	0.7 ± 0.6	4.7 ± 4.0	0.9 ± 0.8
REE FeOOH group 2 (n=17)	5.5 ± 3.2	8.3 ± 6.0	1.4 ± 0.8	5.8 ± 3.5	1.3 ± 0.8	0.7 ± 0.4	1.5 ± 0.9	0.2 ± 0.1	1.4 ± 0.9	0.3 ± 0.2
REE FeOOH group 3 (n=3)	2.3 ± 0.7	1.8 ± 0.7	0.4 ± 0.2	1.9 ± 1.0	0.6 ± 0.3	1.0 ± 0.3	0.6 ±-0.3	0.08 ± 0.05	0.5 ± 0.3	0.11 ± 0.06
REE Sulphide trend 1	0.1 ± 0.0	0.2 ± 0.0	0.02 ± 0.0	0.1 ± 0.0	0.01 ± 0.00	0.003 ± 0.000	0.01 ± 0.00	0.001 ± 0.000	0.01 ± 0.00	0.002 ± 0.000
REE Sulphide trend 2	0.9–0.2	1.4–0.5	0.14–0.05	0.5–0.2	0.07–0.03	0.03–0.02	0.05–0.02	0.008–0.003	0.01–0.01	0.009–0.003
REE Sulphide trend 3	0.5–0.2	0.6–0.2	0.03–0.01	0.1–<0.1	0.02–0.01	0.04–0.02	0.02–0.01	0.003–0.002	0.01–0.01	0.003–0.003

	Tm (ppm)	Yb (ppm)	Lu (ppm)	ΣLREE (ppm)	ΣHREE (ppm)	ΣREE (ppm)	Ce anomaly	Eu anomaly	La_n/Yb_n
REE FeOOH group 1 (n=17)	0.4 ± 0.3	2.5 ± 1.9	0.4 ± 0.3	80.5 ± 74.0	18.4 ± 15.3	98.9 ± 89.2	0.71 ± 0.21	0.90 ± 0.17	5.8 ± 1.3
REE FeOOH group 2 (n=17)	0.12 ± 0.08	0.8 ± 0.6	0.13 ± 0.10	25.2 ± 13.6	7.5 ± 3.7	32.8 ± 17.0	0.71 ± 0.27	1.68 ± 0.24	5.9 ± 2.9
REE FeOOH group 3 (n=3)	0.05 ± 0.03	0.4 ± 0.2	0.05 ± 0.03	7.0 ± 3.0	3.1 ± 1.4	10.1 ± 4.4	0.47 ± 0.05	8.31 ± 4.70	5.2 ± 1.4
REE Sulphide trend 1	0.001 ± 0.000	0.003 ± 0.000	0.001 ± 0.000	0.35 ± 0.000	0.04 ± 0.000	0.39 ± 0.000	0.97 ± 0.00	0.78 ± 0.00	18.7 ± 0.0
REE Sulphide trend 2	0.004–0.001	0.018–0.007	0.004–0.001	2.89–0.94	0.19–0.08	3.08–1.02	1.08–0.97	1.81–1.69	34.12–21.95
REE Sulphide trend 3	0.001–<0.001	0.005–0.004	0.002–0.001	1.25–0.46	0.20–0.06	1.45–0.52	1.14–1.01	34.85–5.60	86.23–29.19

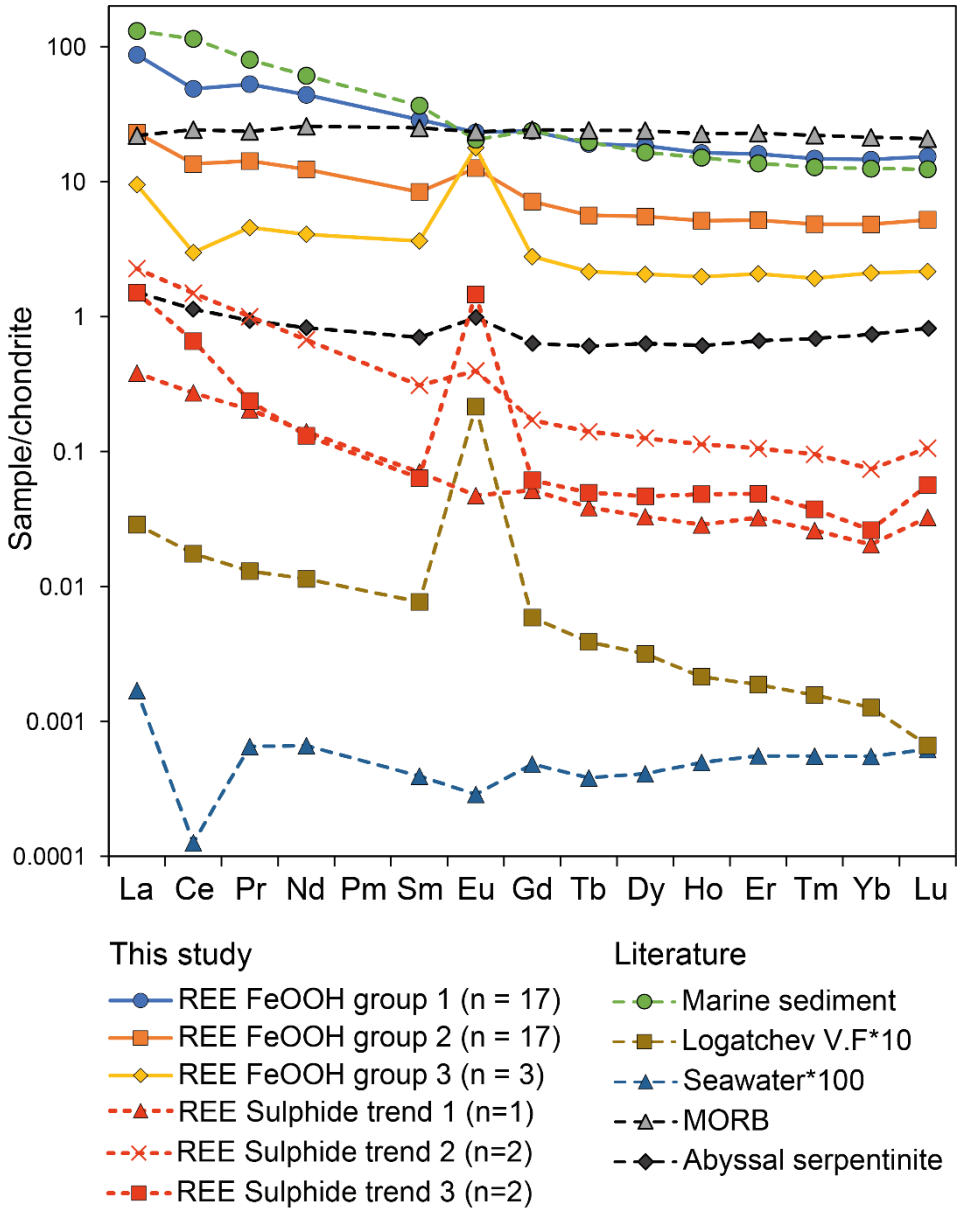

Figure 4.2. Chondrite-normalised (Barrat et al., 2012) REE distribution patterns of FeOOH and massive sulphide samples collected at Semenov. Seawater obtained from Douville et al. (1999), Logatchev vent fluid obtained from Schmidt et al. (2007), marine sediment obtained from Menendez et al. (2017), Mid Ocean Ridge Basalt (MORB) data from Gale et al. (2013) and abyssal serpentinite data after Debret et al. (2024). Note, the data from nearby ultramafic hosted Logatchev vent fluid are used as there is no published data on the composition of hydrothermal vent fluid at Semenov.

4.3.4 Sr-Nd-Pb isotope systematics

Strontium isotopic ratios of FeOOH deposits range from 0.70703 to 0.70922 (Figure 4.3A). While samples from Semenov-5 typically exhibit $^{87}Sr/^{86}Sr$ ratios indistinguishable from seawater, only a minority of samples (33%) at Semenov-4 share similar ratios to present day seawater or detrital sediment. Nd isotopic ratios vary from εNd = -12.39 to -5.02, resembling Western North Atlantic Deep Water (WNADW; Figure 4.3A; Abouchami et al. 1999). Combined Sr- εNd plots on Figure 4.3B show FeOOH samples of Semenov plotting towards seawater.

Lead isotopic ratios of FeOOH and massive sulphide samples are comparable to those found along the Northern Hemisphere Regression Line (NHRL; Hart 1984) and basalt samples measured at the 13°30′N OCC by Wilson et al. (2013). In each Semenov area, the Pb isotopic compositions of FeOOH samples plot along mixing lines that extend from the local massive sulphide signature toward WNADW; this trend is most pronounced at Semenov-5 (Figure 4.3C; Figure 4.3D). The exceptions to this trend are two samples from Semenov-1, of which one lies close to the FeOOH and massive sulphide samples at Semenov-4, while the other exhibits increased radiogenic Pb, closer to that of basalt derived from the Semenov OCC. Full details of isotopic data are found in Appendix B.3 and Bishop et al., (2025b).

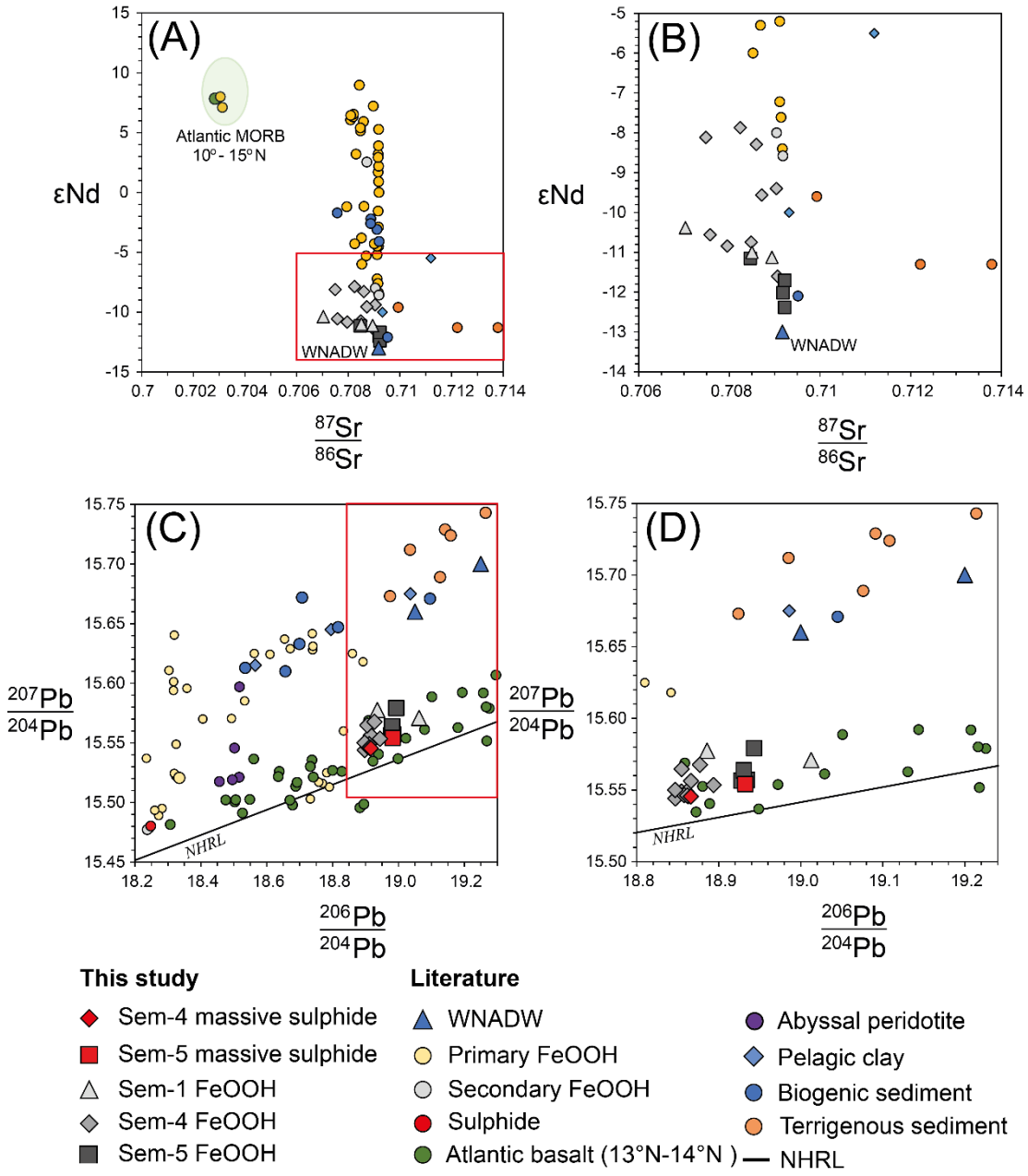

Figure 4.3. Summary of Pb-Nd-Sr isotopic data of the study. The data is compared with marine sediment (terrigenous, pelagic clay and biogenic) collected from Ben Othman et al. (1989), Western North Atlantic Deep Water (WNADW) collected from Abouchami et al. (1999), basalt derived from 13°N-14°N at the MAR after Wilson et al. 2013 and ultramafic rock after Burton et al. (2012). Primary FeOOH obtained after Dekov et al. (2010), Yang et al. (2015), Ta et al. (2021) and Li et al. (2024). The NHRL is the Northern Hemisphere Regression Line of Hart (1984). Additional data for Nd-Sr ratios includes Atlantic MORB obtained between 10°N and 15°N after Agranier et al. (2005). Panels (b), and (d) are magnified views of the red-boxed regions in (a) and (c) respectively.

4.4 Discussion

4.4.1 Mechanisms of FeOOH formation at seafloor massive sulphide deposits

FeOOH formation at SMS deposits occurs through either primary precipitation from hydrothermal fluids or via secondary oxidation of massive sulphide minerals (Alt 1988; Hekinian et al. 1993). At Semenov, both primary and secondary FeOOH are present, with varying textural morphologies, mineralogy, chemical composition and isotopic ratios.

Type-I chimney FeOOH deposits from Semenov-1 are likely coated with nontronite in the fluid conduit structure; nontronite typically precipitates from hydrothermal fluids at low temperatures (~30°C), overlapping with the temperature at which hydrothermal fluid can precipitate primary FeOOH and may represent a cooling trend from primary FeOOH to nontronite (≤100°C; Hekinian et al. 1993; Dekov et al. 207; Gini et al. 2024). Type-I chimney deposits also exhibit alternating layers of FeOOH and Mn-oxide; these minerals can precipitate from low temperature hydrothermal fluid and the layering could represent changes in fluid composition (i.e., Mn-rich to Fe-rich), pH, Eh or temperature fluctuations (Roy, 1992; Binns et al., 1993; Hekinian et al., 1993; Hein et al., 2008). Fe-oxyhydroxides precipitate more rapidly than Mn-oxides, so pulses of low-temperature, reduced hydrothermal fluid produce proximal FeOOH while more quiescent, oxygenated (higher-Eh) intervals favour Mn-oxide precipitation (Alt, 1988; Appendix B.4). Type-I chimney deposits are also poor in base/trace metals (<0.4 wt.% Cu + Ni + Zn). Combined with the characteristics of nontronite precipitation, alternating FeOOH and Mn-oxide layers, chimney-like morphologies and low base/trace metal contents, the Semenov-1 FeOOH deposits share characteristics similar to primary FeOOH deposits reported by Hekinian et al. (1993), which form chimney morphologies and mounds. This suggests that Type-I chimney deposits (n=5) are pre-dominantly primary FeOOH precipitates formed from low temperature Fe and Mn-rich hydrothermal fluids venting under fluctuating reducing conditions during the waning stage of hydrothermal activity or low temperature (<100 °C) hydrothermal venting (Hekinian et al. 1993; Alt 1988; Gini et al. 2024). The trace amounts of non-framboidal, disseminated pyrite within Type-I chimney deposits may reflect episodic input of higher-temperature, H_2S-rich hydrothermal fluids (Koski et al., 1994). The FeOOH associated with relict pyrite is likely to be secondary FeOOH, thus while Type-I chimney morphologies are pre-dominantly primary precipitates, secondary FeOOH does occur together with primary FeOOH. Type-I layered deposits at Semenov-1 are similar to Type-I chimney deposits (i.e., low metal content, alternating FeOOH and Mn-oxide) and as such, are also interpreted as primary FeOOH.

In contrast, Type-II FeOOH chimney deposits (Semenov-4) and other morphologies including brecciated, Type-II layered, ochre, ocherous and massive samples acquired at Semenov typically

have elevated Cu and Zn contents (>0.4 wt.%), with FeOOH forming pseudomorphs after primary sulphide textures such as subhedral or colloform pyrite. Relict pyrite, akageneite (a pyrrhotite weathering product) and/or atacamite (indicative of Cu-sulphide weathering; Nambu 1968; Hannington 1993) are observed in at least one or more of these textural morphologies and indicate high temperature (>240 ^{o}C) hydrothermal fluid capable of producing pyrite, Cu-sulphides and pyrrhotite (Koski et al. 1994).

Moreover, Pb isotope ratios of these FeOOH samples closely match those of co-located massive sulphides, so that FeOOH from Semenov-5 inherits the Pb signature of Semenov-5 sulphide, and similarly for those from Semenov-4. The exception of this includes 66_HY_05, which aligns with the Semenov-4 sulphide, suggesting a similar sulphide source to Semenov-4 and 71_DR_01 (Type-I chimney) whose radiogenic Pb indicates a distinct source. Taken together, the textural evidence (pseudomorphic textures and sulphide relics), mineralogy (akaganeite, atacamite, sulphide) and isotopic inheritance demonstrate that Type-II chimney, Type-II layered, brecciated, massive, ochre and ocherous deposits (84% of samples) are secondary FeOOH formed by sulphide oxidation, whereas the remaining Type-I chimney and Type-I layered deposits are predominately primary FeOOH precipitates.

Having shown that most of the FeOOH morphological types are pre-dominantly secondary, it is possible that they also preserve some of the characteristics of their sulphide protoliths (Figure 4.4). For example, based on their textural morphology and petrography, the protolith of a brecciated FeOOH samples are likely similar to brecciated massive sulphide, often found within the upper part of the SMS mound (Figure 4.4D; Humphris et al. 1996). Type-II chimney morphologies indicate focussed areas of fluid upwelling and are similar to black smoker chimneys located at the summit or close to the summit of SMS mounds (Figure 4.4C; Haymon 1983; Hekinian et al. 1993; Knott et al. 1998). Type-II layered morphologies could be the result of the oxidation of black smoker fragments where there are zonations of mineral phases (Haymon, 1983). The rhythmic layering of Type-II ochre indicates low energy levels and can be interpreted to form as plume fallout (Lilley et al., 1995; Gartman et al., 2024), or as products of gravity flow (Figure 4.4A; Dutrieux et al. 2023). While Type-I ochre does not exhibit lamination, we suggest that as they are also granular with similar mineralogy, that Type-I ochre forms under similar processes to Type-II ochre. Ocherous and massive textural morphologies lack discernible features that can be directly linked to a specific sulphide protolith. While their exact origins are uncertain, ocherous and massive textural morphologies are nonetheless pre-dominantly secondary FeOOH.

In summary, secondary FeOOH formation mechanisms are dominant at the Semenov hydrothermal field. Both, primary and secondary FeOOH formation mechanisms produce FeOOH

with varying textural morphologies with primary FeOOH identified by layering of FeOOH and Mn-oxide, low base metal contents (<0.4 wt.% Cu + Zn + Co) and the likely presence of nontronite. Secondary FeOOH are identified by high base metal content (>0.4 wt.% Cu + Zn + Co), Pb isotopic ratios inherited by massive sulphide, the presence of relict sulphide minerals (i.e., pyrite and chalcopyrite), sulphide weathering products (i.e., atacamite and akageneite) and FeOOH forming as pseudomorphs of sulphide minerals. The textural morphologies of secondary FeOOH can be used to infer their sulphide protolith and formation mechanisms (i.e., chimney-like secondary FeOOH are indicative of black smoker protolith). It is known that massive sulphides typically have varying metal contents depending on their texture (e.g., colloform vs. massive), which in turn relates to where they formed in the SMS mound (Fouquet et al., 1996; Martin et al., 2022). For example, black smoker chimneys that form at the summit of hydrothermal mounds are typically high in Zn and/or Cu (>10 wt.%) relative to massive sulphide found in other parts of the mound such as brecciated sulphide that has been modified within a mound (Fouquet et al. 1996; Hannington et al. 1998a). Thus, it is possible that secondary FeOOH inherit this variation of metal content based on textural morphology, similar to that of massive sulphide.

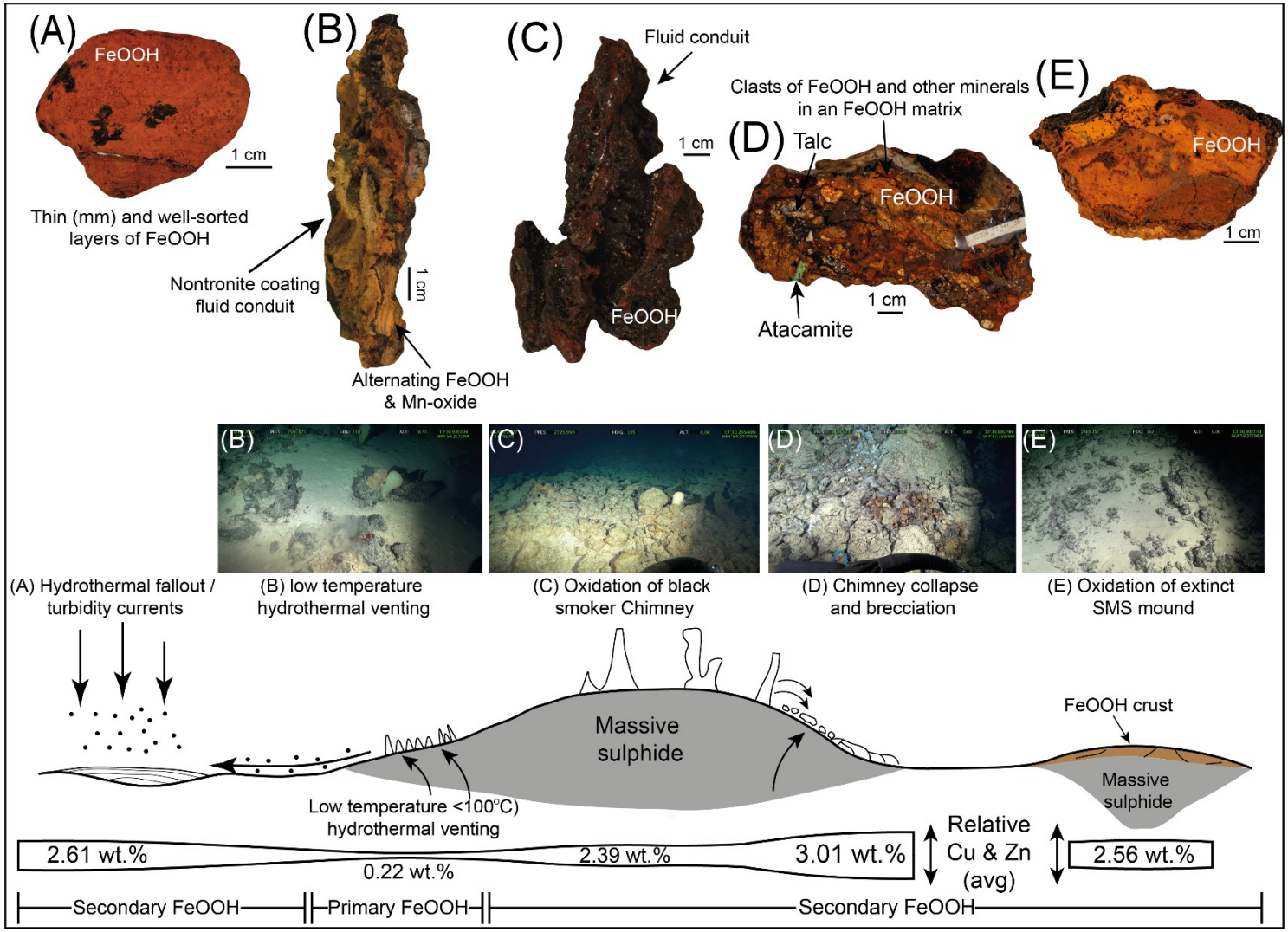
(A)
FeOOH
1 cm
Thin (mm) and well-sorted layers of FeOOH
(B)
Nontronite coating fluid conduit
1 cm
Alternating FeOOH & Mn-oxide
(C)
Fluid conduit
1 cm
FeOOH
(D)
Talc
Clasts of FeOOH and other minerals in an FeOOH matrix
FeOOH
1 cm
Atacamite
(E)
FeOOH
1 cm
(B)
(C)
(D)
(E)
(A) Hydrothermal fallout / turbidity currents
(B) low temperature hydrothermal venting
(C) Oxidation of black smoker Chimney
(D) Chimney collapse and brecciation
(E) Oxidation of extinct SMS mound
Massive sulphide
FeOOH crust
Massive sulphide
Low temperature <100°C) hydrothermal venting
2.61 wt.%
0.22 wt.%
2.39 wt.%
3.01 wt.%
Relative Cu & Zn (avg)
2.56 wt.%
Secondary FeOOH
Primary FeOOH
Secondary FeOOH

Figure 4.4. Formational mechanisms of FeOOH and their morphologies at Semenov with average of Cu & Zn contents. **(A)** Hydrothermal fallout precipitates as sulphides that are subsequently oxidised to secondary FeOOH. Alternatively, mass transport of metalliferous sediment and lithification may also result in the formation of ochre (e.g., 28_DR_18). Cu and Zn content is the average of type-I and type-II ochre morphologies (n=6). **(B)** Low-temperature hydrothermal venting precipitates primary FeOOH and relict pyrite which are oxidised to secondary FeOOH (e.g., 71_DR_01). Cu and Zn content is the average of type-I chimney and type-I layered morphologies (n=6). **(C)** Oxidation of black smoker hydrothermal chimneys to secondary FeOOH (e.g., 102_HY_04). Cu and Zn content is the average of type-II chimney and type-II layered morphologies (n=10). **(D)** Brecciation of chimney material that may be followed by diffuse hydrothermal venting that precipitates various minerals such as barite and talc result in brecciated secondary FeOOH like those found in Semenov-2 (e.g., 77_HY_03). Brecciated samples may also form via mass wasting of sulphide material. Cu and Zn content is the average of type-I and type-II brecciated morphologies (n=4). **(E)** Ambient seawater ingress into hydrothermal mound result in the oxidation of sulphide, forming secondary FeOOH. This mode of formation can produce massive, ocherous and ochre products (e.g., 66_HY_05). Cu and Zn content is the average of massive and ocherous morphologies (n=11).

4.4.2 Preservation of metal content in secondary FeOOH products

Textural morphologies of sulphide often correspond to distinct metal enrichments, for example, black smoker chimneys are typically enriched in Cu and Zn relative to massive sulphide within mound (Fouquet et al., 1998; Knott et al., 1998). In contrast, secondary FeOOH deposits at Semenov form three chemical distinct groups: (i) Fe-rich, (ii) Cu-rich and (iii) Zn-rich, without any association to their textural morphology (Figure 4.5). This decoupling suggests that the secondary FeOOH metal content does not reflect the metal content of the sulphide protolith, but may instead be altered by post-formational processes that modify Cu and Zn content within the crust. In order to prove so, a direct comparison must be made between the sulphides and weathering products. For this, 82_HY_06 is the only sample for which a direct comparison can be made between secondary FeOOH and the massive sulphide protolith. The massive sulphide ($82\_HY\_06_b$) contains 0.37 wt.% Cu and 0.44 wt.% Zn, with the texturally massive FeOOH

(82_HY_06$_a$) crust exhibiting considerable enrichment in Cu (16.79 wt.%) and depletion in Zn (0.09 wt.%; Figure 4.5), compared to the sulphide protolith. In this singular example, the metal content of secondary FeOOH does not reflect the metal content of the associated massive sulphide.

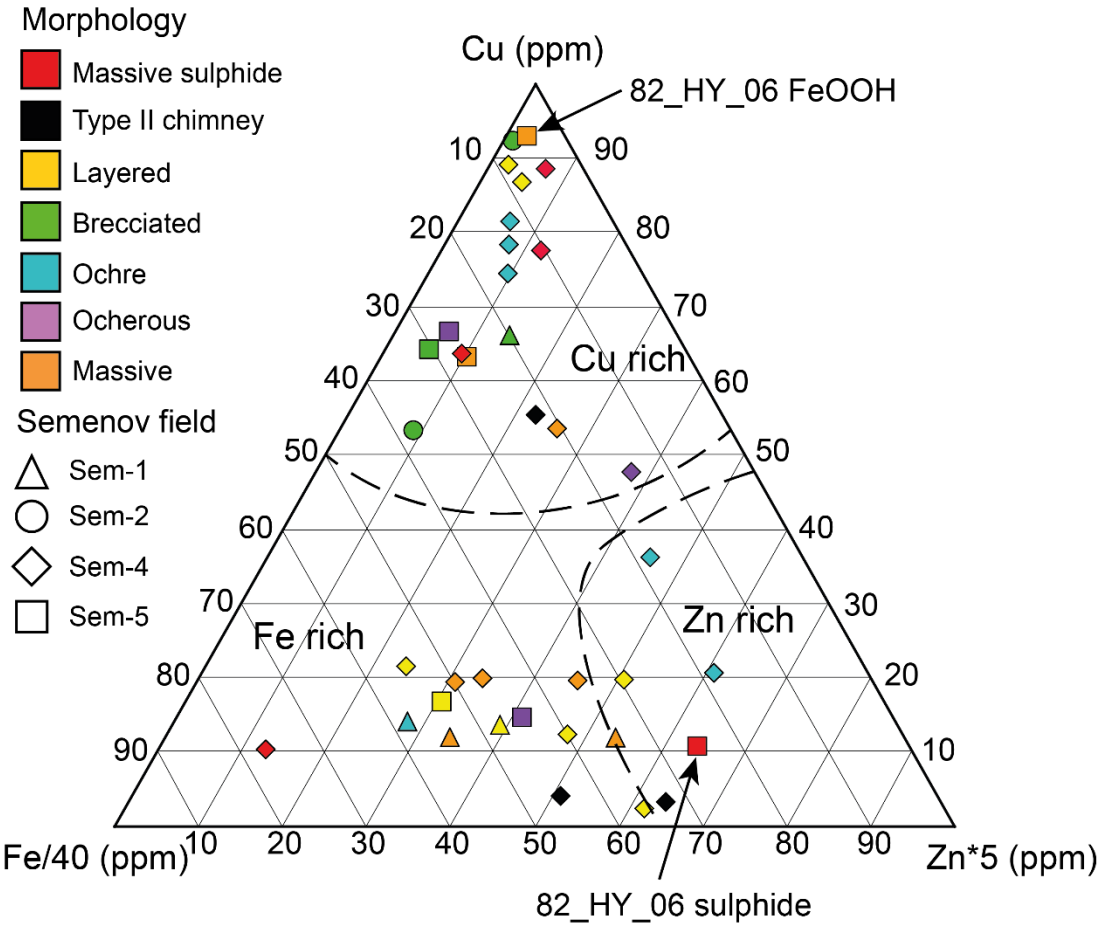

Figure 4.5. Ternary diagram of Cu, Zn*5 and Fe/40 illustrating secondary FeOOH of the study. The samples group into Fe rich (bottom left), Zn rich (bottom right) and Cu rich (top) regardless of morphology and Semenov area. Massive sulphide occupies each of these areas. 82_HY_06$_a$ (FeOOH) and 82_HY_06$_b$

The enrichment in Cu within the FeOOH crust can be partially attributed to the presence of atacamite that makes up approximately 10 wt.% by volume. Atacamite veins are present in eight samples of secondary FeOOH samples from Semenov and where they are found, they increase the bulk Cu content in the sample (average and standard deviation of 6.27 ± 5.30 wt.%, n=8) relative to secondary FeOOH samples with no atacamite (1.05 ± 1.20 wt.% Cu, n=23). Atacamite forms through the oxidation of Cu-sulphides and can be mobilised some distance from the sulphide protolith to form as atacamite veins (Hannington et al. 1993; Dekov et al. 2011) as observed in the samples of this study (Figure 4.1B). This observation indicates that secondary FeOOH do not necessarily reflect the metal content of the sulphide protolith as previous

observations suggest (Herzig et al. 1991; Hannington et al. 1991; Hu et al. 2022); instead, we propose that post-formational modification alters the composition of secondary FeOOH deposits over time. Due to the adsorptive qualities of FeOOH (Cornell & Schwertmann, 2003), FeOOH may act as a gossan by trapping metals released during the oxidation of underlying sulphide (Hu et al., 2022). For instance, atacamite veins are found to cross-cut the FeOOH crust in 82_HY_06$_a$ (Figure 4.1B), which indicates that metal mobilisation and reprecipitation can occur throughout the FeOOH crust, rather than confined to a single boundary. If secondary FeOOH acts as a gossan, the metal content of secondary FeOOH cannot be used to determine the metal content of the sulphide protolith, but may be used to infer the metal content of the underlying ore body. To test this, secondary FeOOH and massive sulphide reported from elsewhere have been compared with the results from this study (Figure 4.6).

This study identifies that Semenov has a higher average Cu content (average of 2.4 ± 3.5 wt. %, n=31) in secondary FeOOH relative to other reported studies (Figure 4.6). Although the Cu and Zn distributions include a few high-concentration outliers, we have chosen to report average values to capture the full range of metal enrichment within secondary FeOOH. These outliers are geologically meaningful because they may represent secondary FeOOH formed via weathering of high-grade sulphide or as effective gossan, capturing metals mobilised from the oxidation of underlying sulphide. We also find that the Cu content of secondary FeOOH correlates with the Cu content of massive sulphide; indicating that the average Cu grade of secondary FeOOH can reflect the Cu grade of massive sulphide. However, this correlation is not observed in Zn. Furthermore, relative to the average massive sulphide composition, secondary FeOOH are lower by up to 71% Cu and 99% Zn (Figure 4.6).

The observed decreased capacity of FeOOH to adsorb or incorporate Zn into its lattice relative to Cu may be a function of the pH of acidic pore fluids produced during sulphide oxidation, which are estimated to range from 3.6 to 5.5 (Hannington, 1993). Zinc adsorption onto FeOOH is more efficient at pH levels above 5.5, whereas Cu adsorption is effective above pH 4.5 (Benjamin & Leckie, 1981; Kooner, 1993). Given that goethite can precipitate at pH as low as 4.0 (Glasby & Schulz, 1999), Zn may not adsorb effectively onto FeOOH in environments where the pH remains below 5.5. This pH dependent adsorption behaviour may explain the increased loss of Zn within secondary FeOOH relative to massive sulphide as compared with Cu (Figure 4.6). Furthermore, the ionic radii of Zn^{2+} may not effectively be incorporated into the FeOOH lattice relative to Cu^{2+} (Hou et al., 2024). Zn is also more soluble than Cu and will have a higher probability of being mobilised into the overlying seawater (Rose, 1976; Hem, 1985; Haynes, 2016).

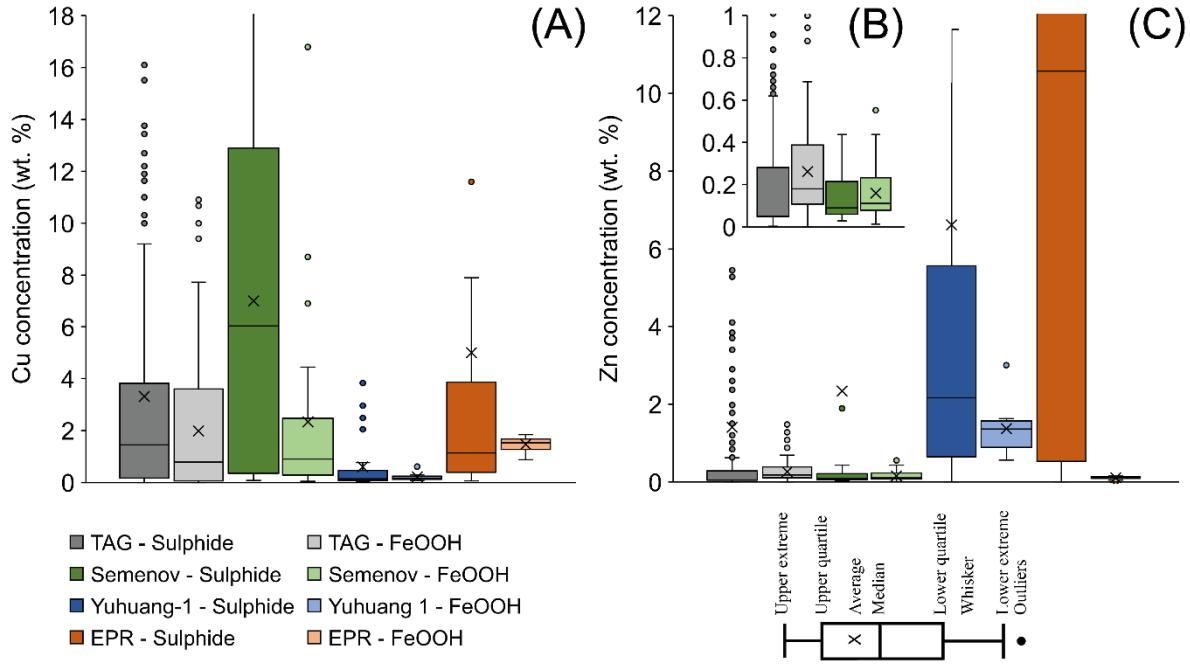

Figure 4.6. Average massive sulphide concentration and average FeOOH composition of Cu **(A)** and Zn **(B)** in box-whisker plots to visualise deviation and median of data. **(C)** Box-whisker plot displaying solely TAG and Semenov sulphide and FeOOH to better visualise Zn variation. TAG sulphide data (n=270) obtained from Fouquet et al. (1998; n=72), Hannington et al. (1998a; n=67), Miller, (1998; n=23), Pelleter et al. (2024; n=66) and Murton et al. (2019; n=42) with FeOOH data (n=210) obtained from Herzig et al. (1991; n=4), Hannington et al. (1998b; n=2), Petersen, (2000; n=163), Murton et al. (2019; n=7) and Pelleter et al. (2024; n=34). Semenov massive sulphide data (n=37) obtained from this study (n=5), Firstova et al. (2022; n=18), Melekestseva et al. (2014; n=2), Melekestseva et al. (2017b; n=7) and Melekestseva et al. (2018; n=5) with secondary FeOOH (n=31) obtained from this study. Yuhuang-1 massive sulphide (n=32) obtained from Liao et al. (2018; n =18), Yu et al. (2021; n=2) and Hu et al. (2022; n=12) with FeOOH (n=9) obtained from Hu et al. (2022). EPR massive sulphide (n=60) data obtained from Fouquet et al. (1996; n=44) and Zeng et al. (2010; n=16) with FeOOH data (n=17) from Zeng et al. (2008).

metals released as a result of sulphide oxidation. As the Cu content of secondary FeOOH correlates with Cu content of massive sulphide, secondary FeOOH deposits may be used as an exploration guide for identifying underlying Cu-rich massive sulphide. For example, during initial investigation, ROVs can collect grab samples of FeOOH deposits across the SMS deposit. These samples can be rapidly screened ship-board using portable X-ray fluorescence (pXRF;

Murton & Shipboard Scientific Party, 2022) to identify areas with anomalously high Cu (or Zn). By mapping Cu "on the fly" during site investigation, teams can focus subsequent geochemical or geophysical surveys (e.g., seismic surveys; Murton et al., 2019) on the most prospective sectors. By combining geochemical and geophysical models, this can create drilling targets or coring sites where secondary FeOOH deposits are most prospective with geophysical surveys guiding towards the larger sulphide bodies. Additionally, this study has shown that secondary FeOOH can contain appreciable quantities of Cu at on average 2.40 wt.% (n=31) and could be an additional resource at SMS deposits. This is more important when considering that metalliferous sediment (that has a component of secondary FeOOH; Dutrieux et al., 2023) at Semenov-4 is extensive and can reach >1 m in thickness (Murton & Shipboard Scientific Party, 2022), with one instance at TAG reporting metalliferous sediment >10 m thick (Murton et al. 2019). Despite this, secondary FeOOH deposits are still lower in both Cu and Zn compared with massive sulphide by up to 71% Cu and 99% Zn indicating that the weathering of massive sulphide results in a loss of both Cu and Zn (Figure 4.6).

4.4.3 FeOOH-seawater interactions: long term effects on Cu and Zn content

As secondary FeOOH accumulate on SMS deposits, they remain continually subjected to seawater flow. The interaction of seawater with FeOOH deposits is evidence by negative Ce anomalies (Debaar et al., 1985; Mills & Elderfield, 1995), enrichment of seawater-derived elements (e.g., Ni and Sc; Koschinsky and Hein, 2003; Hein et al., 2017) in FeOOH relative to massive sulphide and $^{87}Sr/^{86}Sr$ and εNd isotopic ratios trending towards seawater ratios (Figure 4.3). Seawater interaction with FeOOH may also be observed in Pb isotope ratios, where FeOOH ratios lie close to or on mixing lines between massive sulphide and seawater (Figure 4.7).

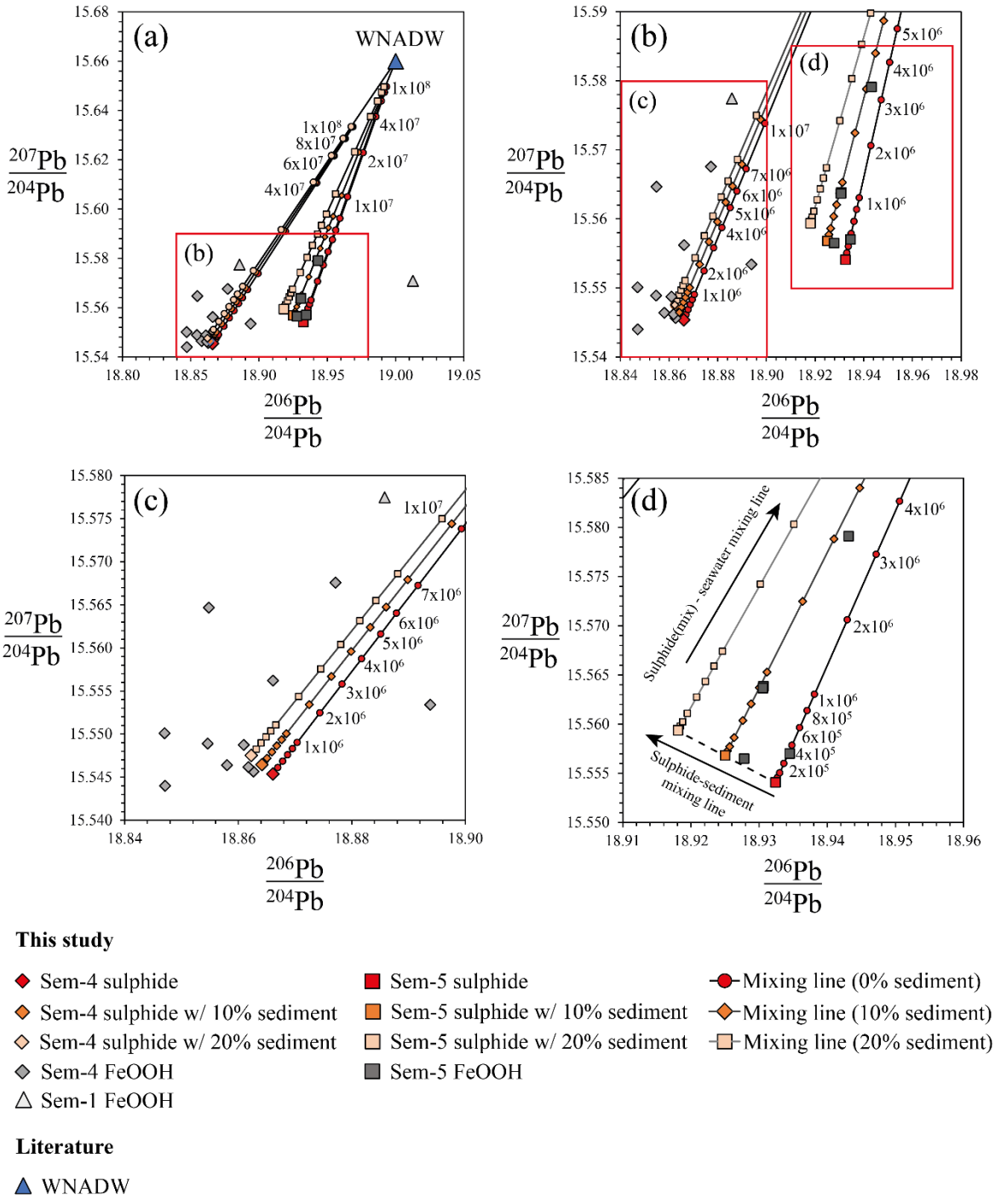

Figure 4.7. Lead isotope compositions of massive sulphide and FeOOH samples from this study, shown alongside a Western North Atlantic Deep Water (WNADW) reference at 3.57 ppt (Abouchami et al., 1999). Sulphide samples were modelled with 0%, 10%, and 20% sediment contribution to illustrate how sediment contribution impact mixing lines with seawater, and mixing curves illustrate the effect of increasing seawater input (higher F/R ratio) on Pb isotope signatures in FeOOH. **(A)** full isotope data showing Sem-4 and Sem-5 sulphide-seawater mixing lines. **(B)** magnified view of red box in panel (A) to highlight lower F/R values. **(C)** detailed

(D) detailed view of Sem-5 from region shown in panel (B) with labelled theoretical mixing lines of (1) sulphide-sediment mixing lines (Eq. 4.3) and (2) sulphide-seawater mixing lines (Eq. 4.4).

It is currently unclear how seawater interaction may affect the metal content of Cu and Zn, whether ions dissolved in seawater (e.g., Na^{+}, Mg^{2+}, Ca^{2+}) compete with sorbed metals on FeOOH, resulting in their depletion or if the content of Cu and Zn remain stable (Balistrieri and Murray, 1982; Calmano et al., 1988). Here, we quantify the degree of seawater exposure using a fluid-to-rock (F/R), defined as the cumulative mass of seawater that has percolated through FeOOH. Practically, as seawater is continuously replacing the interstitial fluid in the FeOOH pore network, thereby incrementally increasing the F/R ratio and providing new competing dissolved ions that compete with sorbed metals on the FeOOH surface. We derive F/R values by applying Pb isotope mixing models between massive sulphide and seawater endmembers (Figure 4.7; Abouchami et al., 1999; Bridgestock et al., 2018). However, pelagic sediment contamination within the FeOOH deposits is geochemically evident by similar REE trends as marine sediment (Figure 4.2) and a positive correlation exists between ΣREE and both Al/(Al+Fe+Mn) and Ca, suggesting that FeOOH samples could contain some pelagic sediment and hence impact the Pb isotopic ratios of the FeOOH. Pelagic sediment typically have lower $^{206}Pb/^{204}Pb$ and higher $^{207}Pb/^{204}Pb$ and $^{208}Pb/^{204}Pb$ ratios (Figure 4.3) and should be considered when looking at Pb isotope systematics of FeOOH samples. Pelagic sediments are primarily composed of biogenic material (i.e. carbonates) and clay-sized particles, and will, over longer term, settle on the seafloor and could get incorporated into the porous FeOOH minerals. Sediment studies at Semenov identify foraminiferal ooze common within the sediment, supporting the interpretation of pelagic sediment at Semenov (Rusakov et al., 2013). Using Eq. 4.1 and Eq. 4.2 (Appendix B.5) an average of 4% (n=17) sediment might be contained in our bulk FeOOH samples, and this was considered in when calculating the sulphide-seawater mixing (Eq. 4.3 and Eq. 4.4; Figure 4.7; Appendix B.6).

The calculated F/R ratios form positive correlations with seawater derived elements including Sc (R^2=0.79), REE (0.78) and Ni (0.66; Figure 4.8; Koschinsky and Hein, 2003; Hein et al., 2017). Consequently, the F/R ratio can serve as a proxy for assessing the interaction between seawater and FeOOH. Crucially, despite extensive F/R ratios observed in this study, Cu concentrations in secondary FeOOH remain stables at ~2 wt.% (Figure 4.8E). In contrast Zn behaviour is more variable and display no obvious trends except that not all Zn is depleted (Figure 4.8F).

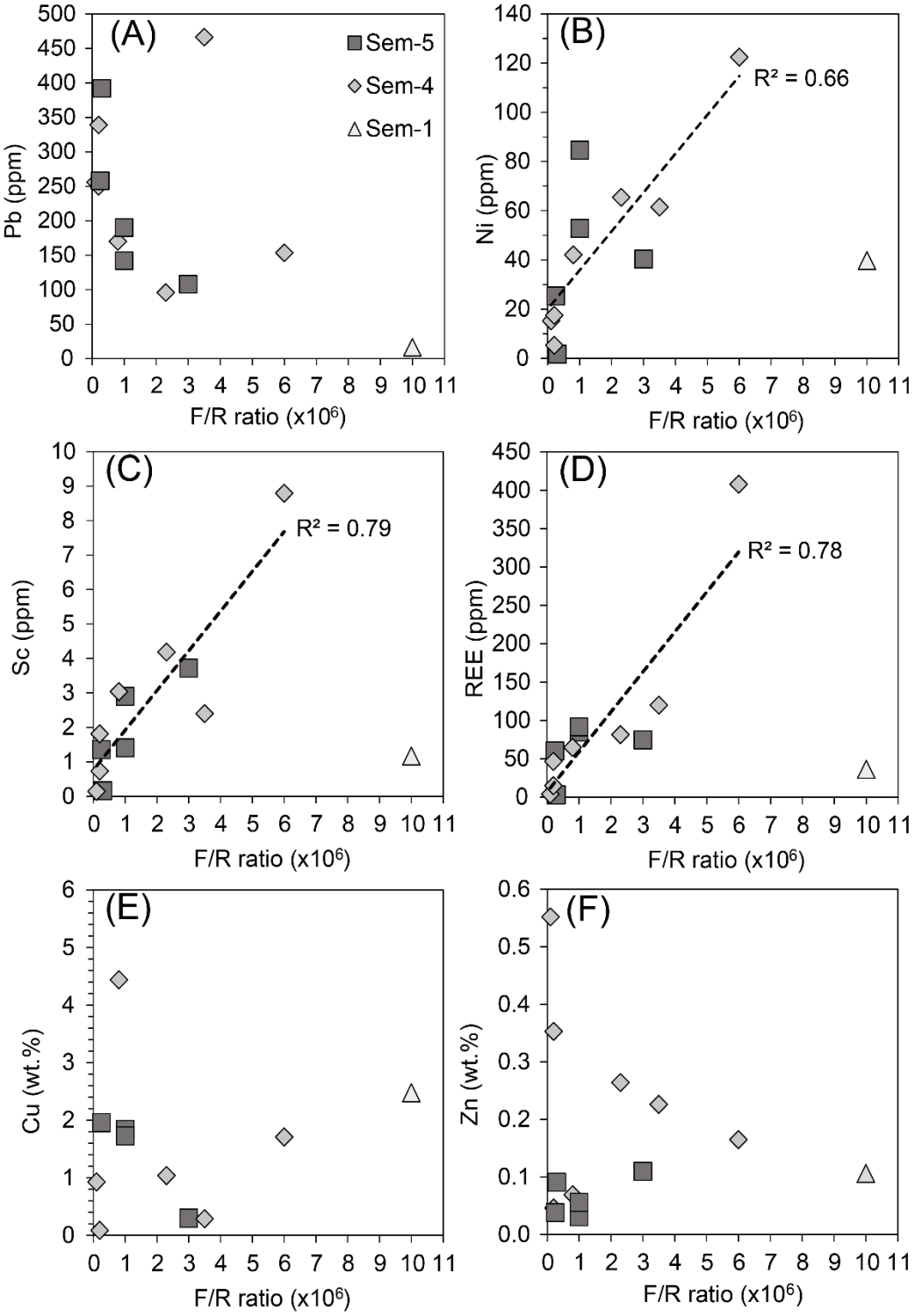

Figure 4.8. Bivariate plots comparing F/R ratios derived from Pb isotopic ratios against (A) Pb, (B) Ni, (C) Sc, (D) REE, (E) Cu and (F) Zn. Note, an outlier is not shown for (E) Cu at 16.79 wt.% Cu and 3.0×10^5 F/R ratio. Correlations visible on (B), (C) and (D) do not consider Sem-1 due to its low Pb content at 16.5 ppm making it highly susceptible to seawater influence resulting in an inflated F/R ratio.

In summary, increasing seawater exposure does not result in the depletion of Cu, which remains constant at approximately 2 wt.%, hence Cu is not released/desorbed from FeOOH and lost to seawater during FeOOH-seawater interactions. These findings suggest that secondary FeOOH are capable of retaining the adsorbed Cu and possibly Zn over time. This behaviour might be especially important at extinct, older, buried off-axis SMS deposits that have undergone increased oxidation and exhibit greater quantities of secondary FeOOH.

4.4.4 Implications for terrestrial analogues at VMS deposits

Ochre and gossanite deposits associated with VMS deposits, such as those from Skouriotissa in Cyprus (Constantinou, 1972) and Molodezhnoye in the Urals (Maslennikov et al., 2012), are regarded as ancient analogues of submarine sulphide weathering products (secondary FeOOH). By comparing modern secondary FeOOH from SMS deposits with terrestrial deposits, we can evaluate the genetic links and secondary alteration processes that affect metal content during seafloor oxidation and subsequent obduction. Although the Troodos ochres are hosted by mafic rocks and the Urals gossanites by ultramafic rocks, compared to the mixture of ultramafic and mafic influences in Semenov, all undergo seawater-driven oxidation.

In terms of morphology and mineralogy, secondary FeOOH at Semenov, exposed to seafloor conditions for up to ~130 ka (Kuznetsov et al., 2011), displays distinctive chimney, massive, ocherous, layered and brecciated textures. In contrast, the ochre deposits at Cyprus, exposed to continuous seafloor conditions for 5 million years (Ravizza et al., 2001), are pre-dominantly goethite and exhibit well-bedded, granular, graded textures (Constantinou, 1972), suggesting that in Cyprus the prolonged oxidation and gravity-driven reworking (e.g., mass-wasting) progressively erased the original textures that currently is still at Semenov. Gossanite deposits from the Urals are composed of oxidised sulphide clasts with varying components of hematised carbonate and/or hyaloclastic material replaced by silica, chlorite and hematite. Gossanite is formed by the oxidation of clastic sulphide in ore turbidites intermixed with sediment that has been later subject to metamorphism (150°-300°C; Maslennikov et al., 2012; Vikentyev et al., 2017). Although Urals gossanite experience sedimentary dilution and metamorphism, it retains primary oxidative weathering processes and can be used evaluate how alteration can modify the metal content of oxidative products.

Our geochemical analysis indicate that secondary FeOOH at Semenov exhibits higher average Cu and Zn concentrations at 2.55 wt.% (n=31), compared to Skouriotissa ochre at 0.81 wt.% (n=27) and Urals gossanite at 0.10 wt.% (n=20; Figure 4.9). The notably lower metal content in the gossanite may result from sedimentary dilution or metamorphic processes that can induce dehydration reactions in minerals like goethite to hematite and can lead to potential leaching of

Cu and Zn during fluid interactions (Jolly, 1974; Goss, 1987). The lower Cu and Zn concentration in Skouriotissa ochre relative to secondary FeOOH at Semenov may result from: (i) a metal poor sulphide protolith (Hannington et al., 1998b; Figure 4.9); (ii) enhanced metal leaching by meteoric groundwater circulation (Lydon, 1984); or (iii) dissolution of atacamite during obduction or meteoric alteration (Hannington, 1993). The data distribution (Figure 4.9) suggest minimal meteoric alteration in most Skouriotissa samples, likely preserving their original composition. However, the absence of atacamite and reduced Cu and Zn levels, compared to meteoric gossan from Kokkinoyia, suggest some influence of meteoric groundwater. Consequently, while secondary FeOOH retains Cu and Zn under submarine conditions, subaerial exposure may lead to their remobilisation. This is supported by F/R ratios indicating that older, off-axis SMS deposits likely preserve these metals.

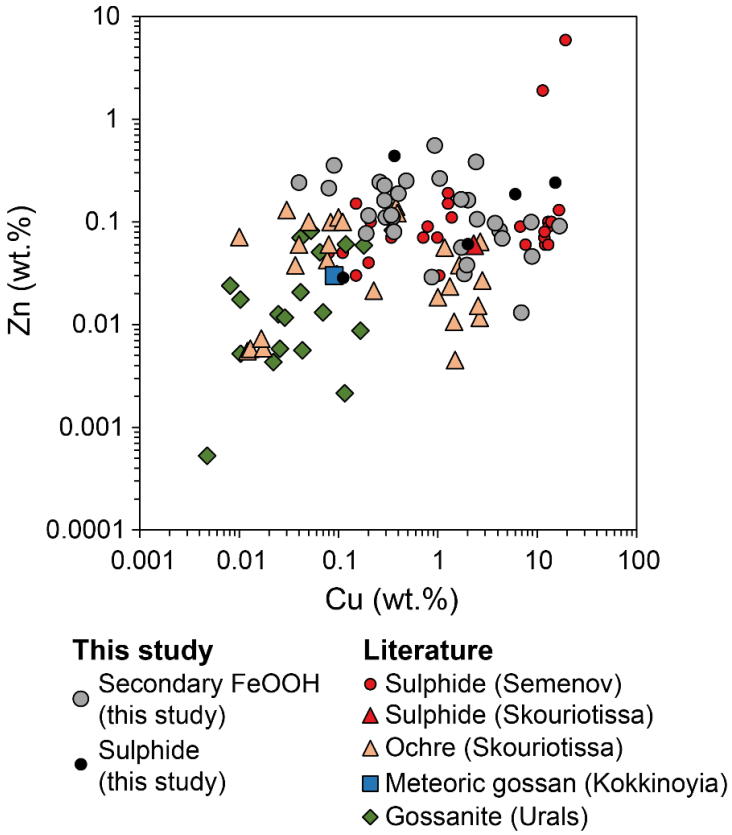

Figure 4.9. Bivariate plot comparing the content of Cu and Zn from secondary FeOOH at Semenov to ochre obtained at Skouriotissa, meteoric gossan material obtained at Kokkinoyia and gossanite material obtained from various VMS deposits in the Urals. Data for ochre obtained after Constantinou, (1972; n=17); Robertson and Fleet, (1976; n=3); Herzig et al. (1991; n=6) and Wells, (1998; n=4), with meteoric gossan after Herzig et al. (1991; n=1), gossanite after Maslennikov et al. (2012), sulphide at Skouriotissa after Hannington et al., 1998b and sulphide at Semenov (n=37) obtained from this study (n=5), Firstova et al. (2022; n=18), Melekestseva et al. (2014; n=2), Melekestseva et al. (2017b; n=7) and Melekestseva et al. (2018; n=5).

Comparing secondary FeOOH from SMS deposits with ochre/gossanite deposits from VMS systems demonstrates that seafloor FeOOH undergoes morphological alteration, losing its original textural morphology, likely due to continuous oxidation and gravity-driven flows. Despite these processes, the Cu and Zn content in secondary FeOOH may remain unaffected, indicating that older, off-axis SMS deposits likely also preserve their metal content. Furthermore, since ochre deposits, such as Skouriotissa, are constrained to overlying the sulphide orebody (Constantinou, 1972), the detection of secondary FeOOH deposits at the seafloor such as those at Semenov can serve as effective exploration marker to identify concealed massive sulphide mineralisation.

4.5 Summary and conclusions

At the Semenov hydrothermal field, primary FeOOH, characterised by low metal content, can be initially identified by its chimney-like textures, formed through alternating precipitation of FeOOH and Mn-oxide, accompanied by green smectite (nontronite) deposition within the fluid conduits. In contrast, secondary FeOOH constitutes the majority of FeOOH deposits at the Semenov hydrothermal field and displays a broader range of textural morphologies than previously reported at SMS deposits. Secondary FeOOH deposits inherit the textural morphology from the sulphide protolith (e.g., Type-II chimney and brecciated forms). We propose that secondary FeOOH can be chemically differentiated into distinct compositional groups of Fe-rich, Cu-rich and Zn-rich, resulting from the initially inherited metal content of the sulphide protolith and post-formational modification processes. For instance, atacamite veins may precipitate within FeOOH, as a result of the oxidation of underlying Cu-sulphides, enriching the secondary FeOOH crust in Cu. In this way, secondary FeOOH functions similarly to what has been shown in terrestrial gossan, i.e. acting as a trap for metals. Further to this, the average Cu-content of secondary FeOOH may provide an indication of the Cu-content of underlying sulphide and this can help to guide future exploration strategies to target areas of Cu-rich FeOOH crust that are likely identified by atacamite mineralisation. This may be especially useful in extinct SMS deposits where much of the sulphide has been oxidised to secondary FeOOH, resulting in limited sulphide exposure.

Secondary FeOOH at Semenov can retain appreciable quantities of Cu (average of 2.40 wt.%) that could be considered as an additional resource at SMS deposits. Derived F/R ratios and comparison with ochre/gossanite deposits from VMS deposits indicate that secondary FeOOH are likely to retain appreciable quantities of Cu at the seafloor. This suggests that secondary FeOOH in off-axis SMS deposits could contain increased quantities of Cu. Furthermore, as these off-axis SMS deposits are older, they are likely to have been subject to greater oxidation, and

thus, secondary FeOOH might be present in larger quantities and economic importance relative to younger SMS deposits close to the MOR, such as in Semenov. Overall, we suggest that secondary FeOOH at SMS deposits could represent both an additional resource and as valuable exploration guides in seafloor mineral exploration.

Chapter 5 Sulphides to weathering products: metal evolution in seafloor massive sulphide deposits at the Semenov hydrothermal field, Mid-Atlantic Ridge

This chapter consists of a manuscript submitted to Mineralium Deposita. This chapter examines the mobility of economic metals (Cu, Zn, Au, Ag) during sulphide oxidation and their incorporation into weathering products (FeOOH, atacamite). While Chapter 4 analysed FeOOH formation at the bulk sample scale, this chapter extends the analysis to the mineral scale to develop a comprehensive weathering model for SMS deposits.

The data within this Chapter is available within the Appendix of this thesis and the BODC database after Bishop et al. (2025d), Bishop et al. (2025e) and Bishop et al. (2025f).

Christian Bishop[1], Pierre Josso[2], Anna Lichtschlag[3], Stephen Roberts[1], Tom Belgrano[4], J. Andy Milton[1], Maxime Lesage[5] & Bramley J. Murton[2]., Sulphides to weathering products: metal evolution in seafloor massive sulphide deposits at the Semenov Hydrothermal Field, Mid-Atlantic Ridge. *Mineralium Deposita,* ***under review***

[1]School of Ocean and Earth Science, University of Southampton, Southampton, UK. [2]British Geological Survey, Keyworth, Nottingham, NG12 5GG, UK. [3]National Oceanography Centre, Southampton, UK. [4]University College Dublin, Belfield, Dublin 4, Ireland. [5]Nedre Slottsgate 8, 0157 Oslo, Norway

ORCiD - 0000-0003-0652-3008

Author contributions

Christian Bishop: Conceptualisation, data curation, formal analysis, investigation, methodology, writing. **Pierre Josso:** Conceptualisation, writing – review and editing. **Bramley Murton:** Conceptualisation, seagoing expedition leader, supervision, writing – review and editing. **Anna Lichtschlag:** Supervision, writing – review & editing. **Stephen Roberts:** Supervision, writing – review and editing. **Thomas Belgrano:** Resource provision, Writing – Review and editing. J. **Andy Milton:** Methodology, investigation. **Maxime Lesage:** Supervision, writing – review.

5.1 Abstract

Seafloor massive sulphide (SMS) deposits are potential sources of copper, zinc, gold and silver, however, how seafloor weathering affects the content of these metals in the deposits remains poorly understood. Key sulphide weathering products, i.e. Fe-oxyhydroxide and atacamite, can provide insight into metal mobilisation during and after oxidation of sulphides. Ten Fe-oxyhydroxide and three massive sulphide samples from the Semenov hydrothermal field (13°30′N, Mid-Atlantic Ridge) were studied; five Fe-oxyhydroxides and all sulphide samples were analysed by LA-ICP-MS with one sulphide sample analysed by LA-TOF-ICP-MS mapping. Additionally, a sequential leaching study comprising nine Fe-oxyhydroxide samples was performed. Copper is mainly sequestered into the sulphide weathering products atacamite (~60%) and Fe-oxyhydroxide (~30%). Initially, Fe-oxyhydroxide precipitates as ferrihydrite, inheriting the metal content of its sulphide precursor (e.g., pyrite or chalcopyrite). Concurrently, gold and silver are displaced from the sulphide and become concentrated along the oxidation front at the sulphide rims rather than being incorporated into the nascent Fe-oxyhydroxide. As oxidation proceeds, further breakdown of sulphides such as chalcopyrite, releases copper that initially adsorb onto existing Fe-oxyhydroxide. When sufficient mobilised copper reacts with oxygenated seawater, atacamite precipitates, sequestering the copper in a stable mineral form, serving as an exploration indicator for copper-rich Fe-oxyhydroxide deposits and underlying massive sulphide deposits. Complete sulphide oxidation leads to the loss of gold and silver from the solid system into seawater or their migration downwards toward a redox boundary. Additionally, the crystallisation of ferrihydrite into more stable goethite liberates substantial amounts of copper (92%) and zinc (57%). However, the metal loss caused by this process may be limited with released metals becoming re-adsorbed onto adjacent Fe-oxyhydroxide. These results reveal that Fe-oxyhydroxides are effective long-term traps for copper and zinc, suggesting that older, fully or partially oxidised off-axis SMS deposits retain considerable base metals, expanding exploration areas.

5.2 Introduction

Increasing global demand for metals crucial to the energy transition, such as Cu and Zn (Watari et al., 2021), drives the need for new sources to be discovered. As easily accessible terrestrial deposits are increasingly exhausted and difficult to discover (Ali et al., 2017), attention has turned to seafloor resources, particularly seafloor massive sulphide (SMS) deposits, driven by their enrichment in base (average of 4.3 wt.% Cu, 10.6 wt.% Zn) and precious metals (1.7 ppm Au and 107 ppm Ag; Hannington et al., 2010). The behaviour of base and precious metals during

sulphide oxidation is well-documented in terrestrial systems, where oxidation of sulphides with meteoric fluid generates acidic fluids, which mobilise redox-sensitive metals like Cu and Zn and can concentrate residual precious metals like Au and Ag to form supergene deposits (Emmons, 1917; Yesares et al., 2014). For submarine settings, where seawater provides an essentially unlimited source of fluid that buffers pH to near neutrality, studies of metal mobilisation are still rather limited. This is particularly true for research on the formation and subsequent modification of sulphide weathering products like Fe-oxyhydroxide (FeOOH) and atacamite ($CuCl_2(OH)_3$; Dekov et al., 2011; Fallon et al., 2017; Melekestseva et al., 2020a; Hu et al., 2022; Maslennikov et al., 2023; Hou et al., 2024). Atacamite is rich in Cu, while FeOOH can be enriched in Cu, Zn, Au and Ag through lattice substitution or adsorption, potentially acting as a trap for these metals following sulphide oxidation (Herzig et al., 1991; Cornell & Schwertmann, 2003; Dekov et al., 2011; Melekestseva et al., 2020a; Hu et al., 2022). Despite their economic relevance, the geochemical relationship between FeOOH and its sulphide precursor remains poorly understood (Blowes et al., 2003; Hu et al., 2023; Hou et al., 2024). If oxidised products retain the geochemical fingerprint of their sulphide precursors, they could serve as seafloor indicators of metal-rich sulphide at depth. While Au and Ag can be incorporated as sulphide inclusions in FeOOH, the fate of these metals after complete sulphide oxidation and whether they are lost to seawater or retained within FeOOH, remains uncertain (Melekestseva et al., 2020a; Maslennikov et al., 2023).

It also remains unclear how the geochemical composition of FeOOH evolves over time at the seafloor (Hu et al., 2022). Metastable ferrihydrite is the initially formed FeOOH minerals, which can dissolve and reprecipitate as more stable goethite crystals (α–FeOOH; Schwertmann and Murad, 1983; Grundl & Delwiche, 1993). This transformation could result in the loss of economic metals like Cu and Zn (Vu et al., 2013; Sajih et al., 2014), but this process has not been investigated using natural samples, requiring targeted geochemical analysis to understand metal partitioning during mineral transformation. Alternatively, post-formational modification may also enrich economic metals (i.e., Cu, Zn, Au, Ag) in FeOOH through atacamite veining or the adsorption of metals onto FeOOH derived from underlying sulphide weathering (Herzig et al., 1991; Hu et al., 2022). Finally, the deportment of Cu and Zn within these alteration products and whether they are mostly held in ferrihydrite, goethite or atacamite is unknown. Understanding the mobilisation of metals from sulphide and incorporation into weathering products, and the mechanisms of post-formational modification are essential to determine the long-term metal content of FeOOH and predict metal retention in older, extinct off-axis SMS deposits.

This study investigates sulphide weathering at the Semenov hydrothermal field, an ultramafic and mafic-hosted Mid-Atlantic Ridge SMS system, to understand whether complete oxidation of sulphides by seawater results in a metal-poor deposit or if alteration products, such as FeOOH

and atacamite, retain the economic metals. The specific objectives are: (1) to examine the oxidation pathways of different sulphide minerals and the accumulation of Cu, Zn, Au, and Ag in the weathering products; (2) to assess how post-formational modifications, such as seawater interaction and goethite crystallisation, alter the composition of FeOOH; and (3) the implications of SMS weathering products as a potential resource at SMS deposits.

5.3 Materials and methods

The following section provides a summary of the methods used in this study. Full methodological details of analyses are outlined in Chapter 2.

5.3.1 Sample collection

Ten samples of FeOOH and three massive sulphide samples collected from Semenov (see section 2.1) were used in this study. Samples of FeOOH were collected from Semenov-1, Semenov-4 and Semenov 5, with massive sulphide samples obtained at Semenov-4 and Semenov-5 (Figure 1.4). A full list of sample locations and description is summarised on Table 5.1 with their full descriptions shown in Bishop et al., (2025a).

Table 5.1. Summary data of samples used in the study with type of analyses used for this study. Depth refers to meters below sea level and the field refers to the hydrothermal field at Semenov. The coordinates (latitude and longitude) are presented in degrees and decimal minutes. Sample descriptions and morphology after Bishop et al. (2025a).

Sample	Morphology	Latitude	Longitude	Depth	Field	Analyses
66_HY_05	Type 1 Brecciated	13˚30.907 N	44˚59.374 W	2589	1	Sequential leaching
82_HY_01	Type 1 Brecciated	13˚30.660 N	44˚56.060 W	2222	5	Sequential leaching
82_HY_05	Ocherous	13˚30.687 N	44˚56.147 W	2230	5	LA-ICP-MS & Sequential leaching
82_HY_06$_a$ (FeOOH)	Massive	13˚30.684 N	44˚56.049 W	2230	5	LA-ICP-MS & Sequential leaching
82_HY_06$_b$ (sulphide)	Pyrite dominated massive sulphide	13˚30.684 N	44˚56.049 W	2230	5	LA-ICP-MS and LA-TOF-ICP-MS
86_HY_04	Ocherous	13˚30.430 N	44˚53.031 W	2798	4	Sequential leaching
86_HY_07	Pyrite dominated massive sulphide	13˚30.331 N	44˚53.196 W	2871	4	LA-ICP-MS
87_MC_01	Massive	13˚30.851 N	44˚59.453 W	2568	1	LA-ICP-MS
90_HY_04	Barite rich massive sulphide	13˚30.637 N	44˚53.106 W	2824	4	LA-ICP-MS
94_HY_04	Type I ochre	13˚30.219 N	44˚53.821 W	2841	4	Sequential leaching
94_HY_06	Type II layered	13˚30.336 N	44˚53.695 W	2865	4	LA-ICP-MS & Sequential leaching
102_HY_04	Type II chimney	13˚30.301 N	44˚59.015 W	2740	4	LA-ICP-MS & Sequential leaching
102_HY_05	Type II chimney	13˚30.293 N	44˚54.033 W	2725	4	Sequential leaching

5.3.2 Mineralogical characterisation

The samples were cut into polished blocks for reflected light microscopy (see section 2.3.1) and subsequent analysis. To provide mineral quantification, previously acquired XRD results after Bishop et al. (2025b) were processed using Siroquant v5.2 (supplied by Sietronics Pty Ltd©) with the methodology outlined in section 2.3.2. Nine polished blocks were selected for quantitative SEM-EDS analysis to provide major geochemical data (>0.1 wt.%) outlined in section 2.4.1. Major element compositions (>0.1 wt.%) were obtained by quantitative SEM-EDS analysis of X samples using a Carl Zeiss Leo 1450VP with Oxford Instruments X-Act detector. SEM-EDS is used for three purposes including: (1) provides quantitative major geochemical data of FeOOH phases otherwise unable to be obtained by LA-ICP-MS; (2) providing internal standard data for subsequent LA-ICP-MS calibration and; (3) providing targets for subsequent LA-ICP-MS and LA-TOF-ICP-MS.

5.3.3 Sequential leaching procedure

Leaching experiments were conducted to examine the deportment of Cu and Zn in sulphide weathering products (i.e., FeOOH and atacamite) and to how these metals are bound to FeOOH, whether sorbed or held in its lattice. In addition, sequential leaching can assess the metals bound in ferrihydrite and goethite to determine how the metal tenor of FeOOH changes during goethite crystallisation. Nine bulk FeOOH samples with varying compositions, morphologies, and atacamite content were used, following the methodology by Poulton and Canfield (2005). Samples (0.05 g) were leached sequentially using 1M magnesium chloride buffered to pH 7 (extracts easily adsorbed fraction), buffered 1M Na-acetate to pH 4.5 (carbonate and atacamite fraction), 1M hydroxylamine-hydrochloride with 25% acetic acid (amorphous FeOOH like ferrihydrite), and 0.5g/l Na-dithionite buffered with 0.2M Na-citrate and 0.35M acetic acid (crystalline FeOOH like goethite). Incomplete dissolution of crystalline FeOOH during leach 4 (Na-dithionite) were addressed by increasing the W/R ratio to 160 and extending the step to three hours (Claff et al., 2010). Problems with premodified FeOOH dissolution during the Na-acetate step, as noted by Hepburn et al. (2020), were mitigated by performing the experiment at room temperature instead of 50°C.

5.3.4 Geochemical analysis

5.3.4.1 LA-TOF-ICP-MS elemental mapping

Semi-quantitative elemental distribution maps at 2 μm resolution were obtained by LA-TOF-ICP-MS analysis of 82_HY_06$_b$, which visualise the spatial heterogeneity of base and precious metals

across weathering fronts, informing mechanisms of metal mobility. Elemental mapping was achieved using a Nu Instruments Vitesse TOF-ICP with 1-2 μm spot ablation, calibrated against NIST SRM 610 and GSD-2G reference materials (full methodology in Section 2.4.3). NIST SRM 612 was used as a secondary reference material for the elements presented in this study (Cd, Cu, As, Ag and Au) and are within uncertainty or within 10% of the reference values, with the exception of Cd (-54%), Au (-53%) and As (+35%), which are known to exhibit heterogeneity in this glass (Eggins & Shelley, 2002). During rastering of NIST SRM 612, most elements exhibit precision expressed as % relative standard deviation (RSD) better than 10.0 %, except for Cu (12.0%) and Au (11.1%).

5.3.4.2 LA-ICP-MS spot analysis

Quantitative trace element concentrations were determined by LA-ICP-MS spot analysis (30-50 μm) of 8 samples to obtain compositional data across the spectrum of fresh to weathered minerals. Measurements were achieved using an Agilent 8900 coupled to an ESL imageGEO 193 nm laser, with calibration against USGS, Geological Survey of Japan and OREAS reference materials (full methodology in Section 2.4.2). The majority of elements exhibit good precision and accuracy with concentrations within the reported uncertainty or within 10% of reference values with the exception are Si (±20.0%), Zn (7.6%) and Cd (±33.8%; Table 2.1). The majority of elements exhibit %RSD of < 10%, except for Au (17.1%; Appendix A.2).

5.3.4.3 Leachate analysis by ICP-MS and ICP-OES

The filtered solutions acquired from the sequential leaching experiments were analysed by ICP-MS and ICP-OES for their major and trace element concentrations (details in section 2.5.4). Accuracy and reproducibility of the analyses were assessed by analysing reference materials JMn-1, GSPN-2, RTS-1, in triplicate and further single analyses of Nod-P-1, GSPN-3, and CH-4.The majority of elements exhibit good accuracy within 10% of the CRM except for Zn (±48.7%), Mn (13.3%) and Ca (10.1%; Table 2.6; see Appendix A.9 for full details).

5.3.5 Statistical methods

5.3.5.1 Correlations and reporting

The majority of elemental data obtained by LA-ICP-MS and SEM-EDS for this study is non-linear, thus, Pearson correlation is not applicable to be used as this method assumes a linear relationship between the elements. Spearman correlation is used instead as this method assumes a monotonic (consistently increasing or decreasing) and a non-linear relationship. Another key advantage of Spearman correlation is that this method is robust to outliers. As these

values are non-linear with non-normal distribution, the median is used instead of the average for descriptive statistics. Sequential leaching data obtained by ICP-MS and ICP-OES were evaluated by Pearson correlation and described using their means.

5.3.5.2 Mann-Whitney U-test

A Mann-Whitney U-test (hereafter referred to as U-test) is a statistical method to determine if there is a significant difference between the distributions of two independent groups. The U-test differs to the conventional T-test as the U-test assumes a non-linear relationship between the tested variables and does not assume the data is normally distributed (Mann & Whitney, 1947; McKnight & Najab, 2010). The U-test compares the rank of values rather than the averages between the two groups, making it useful for non-normally distributed data. The U-test produces a p-value that indicates whether the difference in ranks between the two groups is statistically significant. P-values <0.05 indicate that there is a significant difference between the distribution of the two groups.

5.3.5.3 t-Distributed Stochastic Neighbour Embedding (t-SNE)

The t-SNE technique, a non-linear dimensionality reduction method, was used to analyse element interrelationships and identify potential sources influencing the composition of FeOOH in this study (van der Maaten & Hinton, 2008). Unlike principal component analysis (PCA), which assumes linearity and normally distributed data, t-SNE does not, making it more suitable for complex datasets. The elements included in the analysis were Na, Mg, Al, Si, S, Cl, Ca, Mn, Fe, Co, Ni, Cu, Zn, As, Mo, In, Sb, Pb, and REEs. Individual REEs were excluded to avoid skewing the data, and Ag and Au were omitted due to frequent measurements below the detection limit. Prior to t-SNE analysis, the data was normalized using Kaiser normalisation (Kaiser, 1974) to ensure each element contributed equally. Following t-SNE, K-means clustering was applied to group elements based on their similarities, revealing patterns and structures in the dataset (MacQueen, 1967). The t-SNE tests were conducted in RStudio with data visualisation with the ‘ggplot2’ package (Wickham, 2016), ‘dplyr’ package for data manipulation (Wickham et al., 2023), ‘Rtsne’ package to conduct the t-SNE test (Krijthe, 2015), ‘cluster’ for the cluster analysis of t-SNE (Maechler et al., 2023) and ‘readxl’ package to read Excel filed (Wickham & Bryan, 2023). Sequential leaching data obtained by ICP-MS and ICP-OES were evaluated by Pearson correlation and described using their means.

5.4 Results

5.4.1 FeOOH petrography and mineralogy

Textural morphologies of bulk FeOOH samples obtained from Semenov for this study include chimney, ocherous, brecciated and massive types (Figure 5.1; Bishop et al., 2025a). Sample 82_HY_06 is comprised massive sulphide (82_HY_06$_b$) mantled by a FeOOH weathering crust (82_HY_06$_a$). Poorly crystalline FeOOH interpreted as ferrihydrite (Jambor & Dutrizac, 1998) dominates the samples, comprising over 50 vol%, whereas crystalline FeOOH (goethite) accounts for approximately 8–20 vol%. Minor minerals detected in multiple samples include atacamite (<1 to ~10%) and its polymorph paratacamite (~3–4%), barite (~2–4%), akageneite (~3%), quartz (~1–2%), and calcite (<1 to ~2%; Appendix C.1). Reflective microscopy shows that FeOOH displays a range of mineral morphologies summarised in Figure 5.1 with a full description of each morphology in Appendix C.2. Sulphide inclusions within FeOOH were used to determine the FeOOH precursors. For example, FeOOH minerals with pyrite inclusions are classified as pyrite derived FeOOH (py-FeOOH; e.g., Figure 5.1H and Figure 5.1E) and FeOOH with chalcopyrite or covellite inclusions as chalcopyrite derived FeOOH (ccp-FeOOH; Figure 5.2D). Both py-FeOOH and ccp-FeOOH are mostly observed in massive sulphide samples and are defined as early-formed FeOOH phases that still contain relict sulphide precursor, in contrast to FeOOH with no sulphide. The latter, typically found in fully oxidised samples, likely exhibit advanced oxidation relative to py-FeOOH and ccp-FeOOH and are defined as modified FeOOH. Based on Chapter 4 of this thesis, all samples used in this Chapter are interpreted as secondary FeOOH (i.e., Cu and Zn >0.4 wt.%), with no observations of primary FeOOH formed through low temperature hydrothermal fluid or high-temperature hydrothermal plume fall-out (e.g., Hekinian et al., 1993; Mills et al., 1993). Atacamite occurs as a minor mineral within fully oxidised FeOOH samples and forms as anhedral crystals, vein, or euhedral crystals (Figure 5.1F and Figure 5.2E).

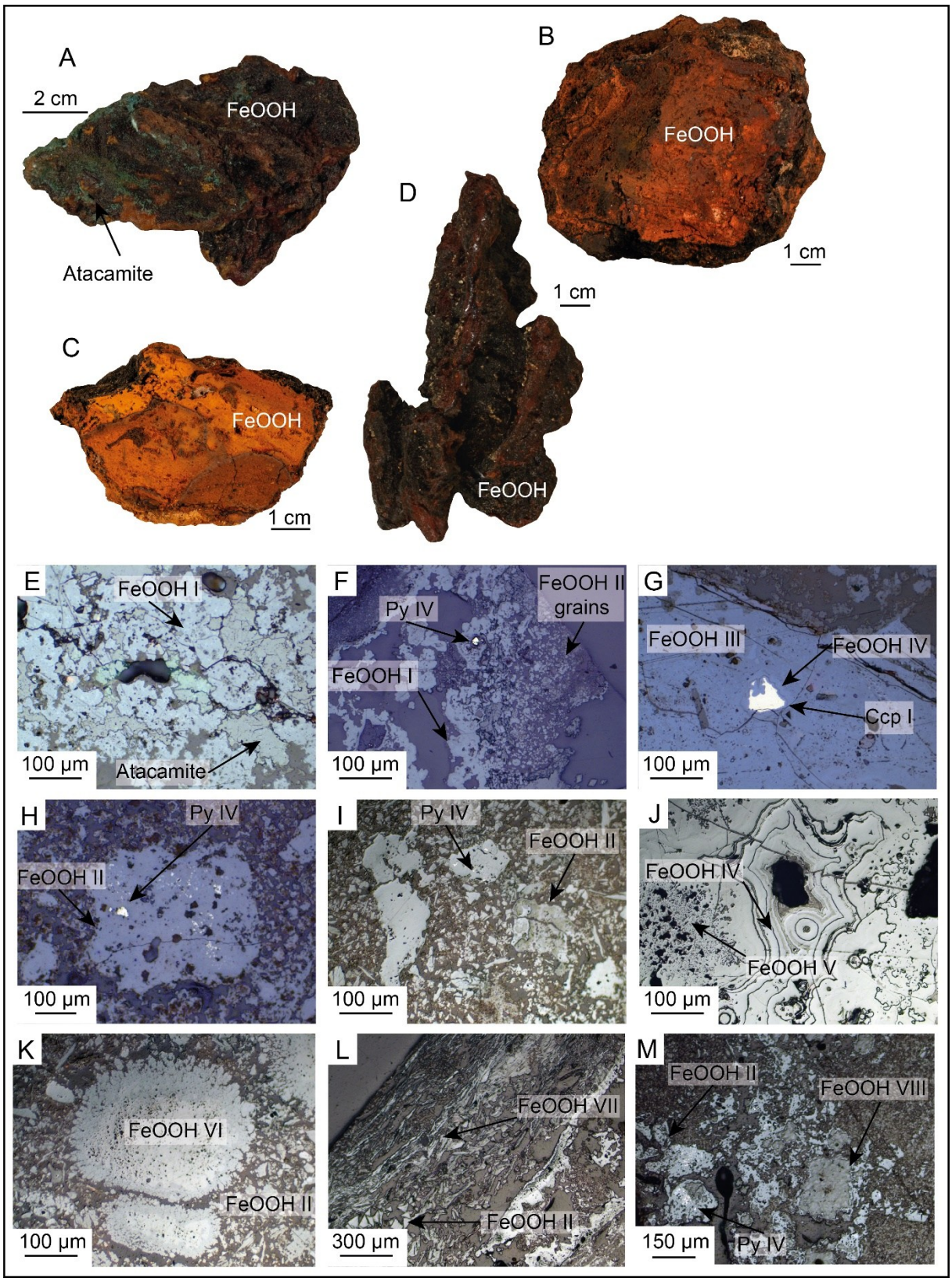

Figure 5.1. Images and reflected light photomicrographs of FeOOH samples from Semenov. **(A)** 94_HY_06: Reddish-brown FeOOH from Sem-4 with Mn-oxide crust and atacamite. **(B)** 87_MC_01: Reddish-brown FeOOH with Mn-oxide crust from Sem-1. **(C)**

Ocherous orange-brown FeOOH from Sem-5. **(D)** 102_HY_04: Dark reddish-brown FeOOH with chimney morphology from Sem-4. (**E)** 102_HY_04: Porous FeOOH I with atacamite. **(F)** 94_HY_06(i): Massive FeOOH I transitioning to FeOOH II grains. Relict pyrite within FeOOH I. **(G)** 87_MC_01: Relict chalcopyrite (ccp) in colloform FeOOH IV within FeOOH III. **(H)** 94_HY_06(ii): Py-FeOOH grain with pyrite inclusions. **(I)** 82_HY_05: FeOOH II with relict pyrite. **(J)** 82_HY_06$_b$: Dendritic FeOOH V enclosed by FeOOH IV. **(K)** 82_HY_05: Anhedral, porous FeOOH VI with FeOOH II. **(L)** 82_HY_05: Tabular, euhedral FeOOH VII with FeOOH II grains. **(M)** 82_HY_06$_a$: FeOOH II with pyrite inclusions overlain by FeOOH VIII.

5.4.2 Massive sulphide petrography

Massive sulphide samples are predominantly made of pyrite (>80 vol%), with minor amounts of chalcopyrite, barite, FeOOH, and atacamite (<20 vol%), as well as trace amounts of sphalerite and covellite (Figure 5.2). Pyrite displays four textural morphologies: colloform, porous, euhedral, and framboidal (Figure 5.2F). Chalcopyrite either forms as inclusions within both euhedral and porous pyrite, or as anhedral grains within texturally massive veins (Figure 5.2D). Sphalerite occurs as small inclusions (<10 μm) within euhedral and porous pyrite. Covellite typically forms at the rim or enclosing chalcopyrite (Figure 5.2D), indicating its formation through chalcopyrite oxidation.

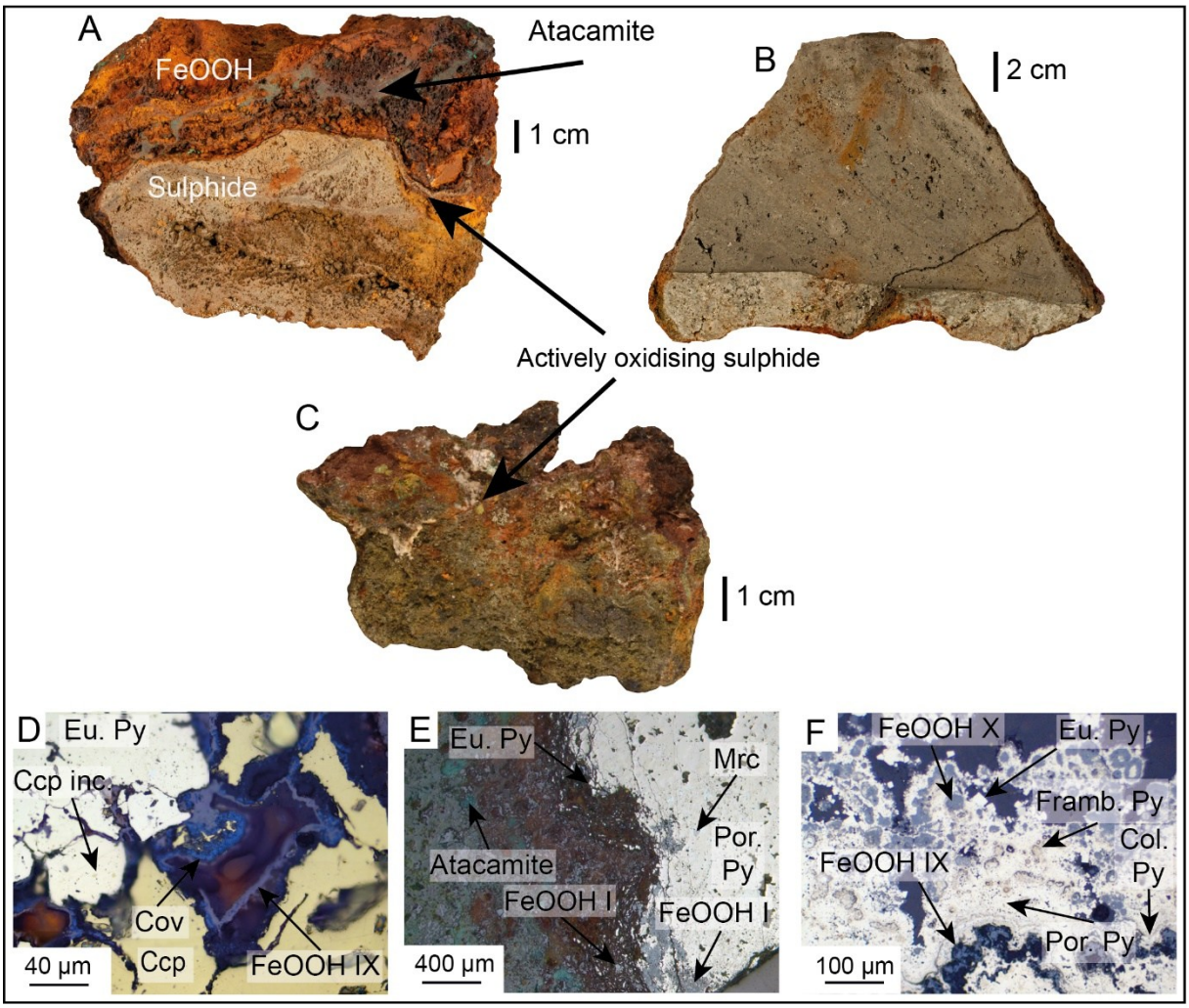

Figure 5.2. Representative images and reflective light photomicrographs of sulphide samples from the Semenov hydrothermal field. **(A)** 82_HY_06: Comprises FeOOH crust with atacamite veins (82_HY_06$_a$) mantled on massive sulphide (82_HY_06$_b$). **(B)** 86_HY_07: Pyrite-dominated massive sulphide. **(C)** 90_HY_04: Barite-rich massive sulphide with weathered Fe-oxide coatings. **(D)** 82_HY_06$_b$: Euhedral pyrite with chalcopyrite inclusions, anhedral, corroded chalcopyrite, and secondary covellite; FeOOH X linked to chalcopyrite alteration. **(E)** 82_HY_06$_b$: Porous and euhedral pyrite, replaced by FeOOH I and brecciated, with atacamite in oxidised areas. **(F)** 90_HY_04: Multiple pyrite morphologies (euhedral, framboidal, porous, colloform) with FeOOH X replacing framboidal pyrite, alongside bluish-grey FeOOH IX.

5.4.3 Geochemical composition of sulphides and their weathering products

5.4.3.1 Sulphides

Laser ablation ICP-MS was used to assess the major and trace metal composition of different mineral phases. Pyrite is enriched in As, Mo, Au, and Bi, but depleted in Ag relative to other sulphides (Appendix C.3; Figure 5.3). Key elements in pyrite include Cu (median: 0.36 wt.%, max: 5.65 wt.%), As (0.40 wt.%, max: 2.62 wt.%), Zn (0.12 wt.%, max: 1.10 wt.%), Ag (0.5 ppm, max: 153 ppm) and Au (median: 0.5 ppm, max: 9.4 ppm). Ablation depth profiles in pyrite exhibit spikes in Cu, Pb and Zn intensity, suggesting the presence of chalcopyrite, galena, and sphalerite inclusions (Figure 5.4). Elevated Ag generally coincides with elevated Au, Cu, or Pb (Figure 5.4A-C), with weak positive correlations between Ag and Pb (R = 0.41) and Au (R = 0.44) implying Ag is present in electrum, chalcopyrite, or galena inclusions (Appendix C.4). Flat, consistent intensity profiles suggest Au is hosted within the pyrite crystal lattice.

Compared to pyrite, chalcopyrite is enriched in the trace metals Ca, In, and Ag, but depleted in Zn, Co, and As (Appendix C.3; Figure 5.3). Statistical U-tests reveal significant differences in Ca, Zn, As, Mo, Sb between chalcopyrite and pyrite (Appendix 0). Ag in chalcopyrite correlates strongly with Zn (R = 0.82), Sb (R = 0.80), Au (R = 0.72), and In (R = 0.56), suggesting inclusions of sphalerite, galena, or tetrahedrite (Appendix C.6). Ablation depth profiles (Figure 5.4D) show Fe, Ag, Bi, Sb, Au, As, and Pb anomalies, indicating sulfosalt inclusions such as tetrahedrite (Johnson et al., 1986).

5.4.3.2 FeOOH and atacamite

Modified FeOOH are depleted in Au and Ag (median concentration of <0.1 ppm) compared to sulphides and py-FeOOH/ccp-FeOOH (Figure 5.3E and Figure 5.3F). Median Cu content is 2.86 wt.% (Figure 5.3C) and correlates positively with Pb (R = 0.53), S (0.45), and In (0.42), but negatively with Na (-0.56). Zinc is uncorrelated to other elements. Calcium correlates with Na (0.68) and Si (0.80) and inversely with Sb (-0.76), Mo (-0.71), As (-0.59), and Au (-0.44; Appendix C.7). Generally smooth ablation profiles for Si, Ca, Cu, Zn, Mo, As and Sb in 168/230 spots indicate lattice substitution or even distribution of adsorbed metals (Figure 5.4F; Bishop et al., 2025e).

On average, Py-FeOOH, is enriched in Si, Cu, Zn, As, Mo, In, Sb, REE and Au compared to pyrite across the dataset, but depleted in Co, Ag and Bi. Relative to chalcopyrite, ccp-FeOOH, is enriched in most elements except for Cu. A U-test reveals significant Si, Ca, Fe, Co, Ni, As, and Ag differences between py-FeOOH (n=6) and ccp-FeOOH (n = 9; Appendix 0). Correlations in py-FeOOH and ccp-FeOOH include Cu-Ag (R = 0.54) and inverse Cu-Zn (-0.69), whereas Zn

positively correlates with In (0.85) and Bi (0.57) but negatively with Na (-0.55) and Ca (-0.62; Appendix C.8). Depth profiles of ccp-FeOOH show Cu spikes correlate with Ag, suggesting relict Cu-sulphide inclusions (7/9 spots; Figure 5.4E). Some py-FeOOH profiles show Au and Ag concentrations together (e.g., 06iiS5-2), while others show opposing trends (e.g., 06iiS7-1) or spikes of Au alone (e.g., 06iiS5-6), indicating Au and Ag are not always co-enriched (Appendix C.9). Compared to modified FeOOH, both py-FeOOH and ccp-FeOOH are depleted in Si, Cl, Ca, Mn and REE but enriched in Cu, Mo, Ag, Au and Bi. Statistical U-tests show significant differences in most elements except Mg, Fe, and Ce (Appendix 0).

Atacamite is depleted in concentrations of most trace metals relative to FeOOH and chalcopyrite. Ablation depth profiles of most elements (e.g., As, Au, Ag, La, Sb, Mo) correlate with spikes and jumps of Fe suggesting the presence of FeOOH or possibly Fe-sulphides (e.g., 01S5-7 and 06FS5-9; Appendix C.9).

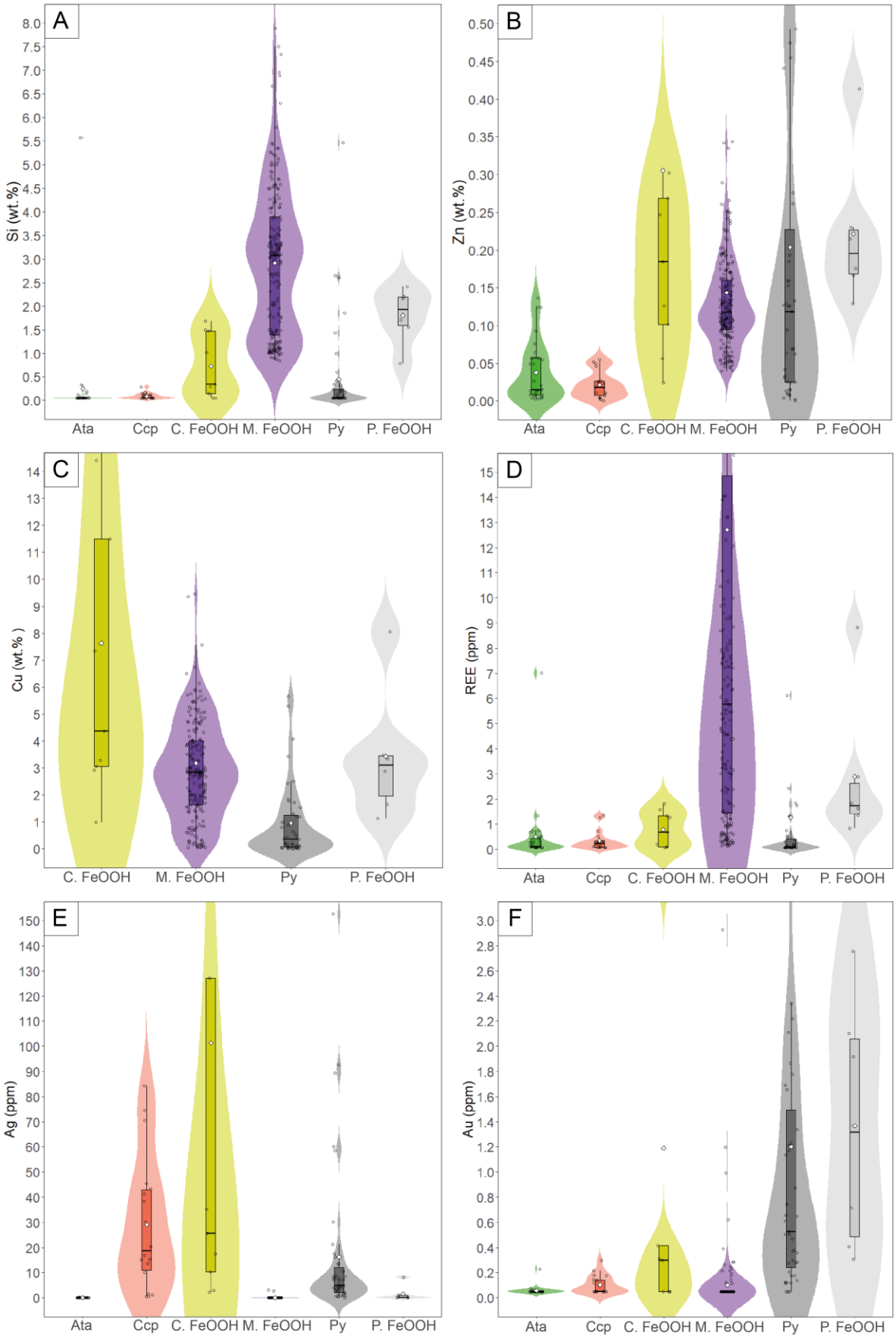
A
Si (wt.%)
Ata
Ccp
C. FeOOH
M. FeOOH
Py
P. FeOOH
B
Zn (wt.%)
C
Cu (wt.%)
D
REE (ppm)
E
Ag (ppm)
F
Au (ppm)

Figure 5.3. Combined box and violin plots showing the distribution of element concentrations in sulphide minerals and their weathering products for **(A)** Si (wt.%), **(B)** Zn (wt.%), **(C)** Cu (wt.%), **(D)** REE (ppm), **(E)** Ag (ppm) and **(F)** Au (ppm). The width of the violin reflects the frequency of values at a given concentration. Lower and upper fences are the 25th and 75th percentiles, the horizontal black bar in the box represents the median, the white diamond in the box is the average and the whiskers beyond the box plot represent the 10th and 90th percentiles. Individual data points are shown as dots. The horizontal black bar represents the median, and the white dot within the plot shows the mean. Abbreviations: Ccp – chalcopyrite, Ata – atacamite, Py – pyrite, C. FeOOH – chalcopyrite-derived FeOOH, P. FeOOH –

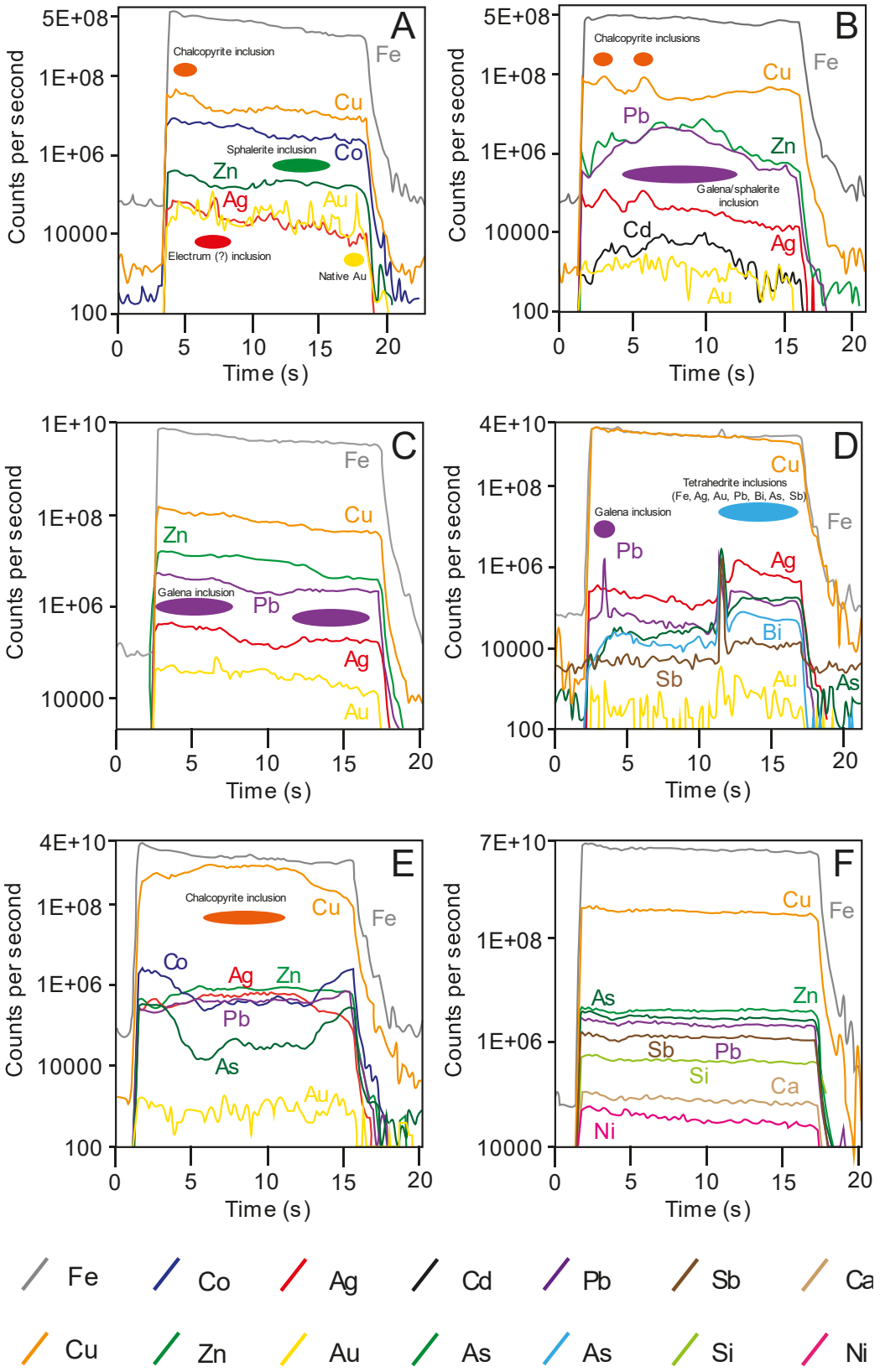

Figure 5.4. LA-ICP-MS ablation depth profiles for sulphides and FeOOH. **(A)** Porous pyrite (07S4-4, 86_HY_07): Smooth Co and Fe traces; jumps in concentration of Cu and Zn indicate chalcopyrite and sphalerite inclusions, while Au and Ag spikes suggest electrum or native Au. **(B)** Euhedral pyrite (07S7-3, 86_HY_07): Pb-bearing

Sphalerite or galena inclusions, with chalcopyrite and Ag spikes; Au trace suggests lattice substitution in pyrite. **(C)** Euhedral pyrite (06S6-5, 82_HY_06): Galena inclusions correlate with Ag spikes; stable Au, Zn, and Cu suggest solid substitution in pyrite. **(D)** Anhedral chalcopyrite (06S12-4, 82_HY_06): Galena and tetrahedrite inclusions with As, Au, Sb, Bi, Pb, Ag, and Fe spikes. **(E)** Ccp-FeOOH (07S6-1, 86_HY_07): Large Cu sulphide inclusion with correlating Ag. **(F)** Modified FeOOH (05S2-2, 82_HY_05): Smooth elemental profiles, indicating solid substitution or even adsorption of Fe, Cu, Zn, As, Sb, Pb, Si, Ca, and Ni in FeOOH.

5.4.3.3 REE concentrations

Rare earth element (REE) concentrations, and in particular the presence of negative Ce anomalies, are useful indicators of interaction with oxygenated seawater (Debaar et al., 1985; Mills & Elderfield, 1995). While FeOOH and atacamite are expected to exhibit a partly seawater-like REE signature (Dekov et al., 2011; Maslennikov et al., 2023), they may also retain the signature of the sulphide precursor (Bishop et al., 2025d).

Fe-oxyhydroxide are enriched in the sum of rare earth element concentrations (ΣREE) compared to pyrite and chalcopyrite by approximately one or two orders of magnitude, respectively (Figure 5.3D), and have a negative Ce anomaly (median of -0.55; Table 5.2). The REE content in FeOOH has a weak negative correlation with In (R = -0.49), Sb (-0.36), S (-0.52) and weak positive correlation with Ca (0.50), Ni (0.43) and Si (0.41; Appendix C.7). Early formed Py-FeOOH and ccp-FeOOH are depleted in ΣREE relative to modified FeOOH, but enriched in LREE compared to their respective sulphide precursor (Figure 5.3D). Atacamite is depleted in REE elements relative to FeOOH and chalcopyrite and exhibits negative Ce anomalies with a median of 0.67.

Table 5.2. Median REE concentration of sulphide minerals and weathering products. Where data is below the limit of detection (LOD), the LOD/2 value is used and included in the calculations. The Ce and Eu anomaly is calculated as a geometric mean interpolation defined as $Ce^* = Ce_n/((La_n \times Pr_n) \times 0.5)$ and $Eu^* = Eu_n/(Sm_n*Gd_n)*0.5$ after McLennan, (1989). Note, Ce anomalies alongside La_n/Yb_n were compiled using data above limit of detection. See Bishop et al., 2025d for full details. Bold values denote that the median grade is the LOD/2. Normalised values (X_n) obtained from chondrite values after Sun and McDonough (1989).

REE (ppm)	Pyrite	Chalcopyrite	Py-FeOOH	Ccp-FeOOH	Modified FeOOH	Atacamite
La	0.08	0.04	0.35	0.21	1.59	0.006
Ce	0.04	0.06	0.49	0.16	0.71	**0.003**
Pr	**0.003**	**0.003**	0.08	0.04	0.25	**0.003**
Nd	0.05	0.02	0.36	0.14	1.12	**0.010**
Sm	**0.005**	**0.005**	0.07	0.01	0.20	**0.005**
Eu	**0.005**	**0.005**	0.03	0.02	0.07	**0.005**
Gd	**0.005**	**0.005**	0.11	0.04	0.32	**0.005**
Tb	**0.005**	**0.005**	0.01	0.01	0.05	**0.005**
Dy	0.01	**0.005**	0.08	0.07	0.29	**0.005**
Er	0.01	0.003	0.05	0.02	0.24	**0.003**
Yb	0.010	**0.005**	0.04	**0.005**	0.19	**0.005**
La_n/Yb_n	6.18	2.15	6.19	6.10	6.25	3.83
Ce*	0.64	0.85	0.82	0.46	0.41	0.67
Eu*	0.88	N/A	0.86	1.37	0.77	0.80

5.4.4 Geochemical data by SEM-EDS

Sample 82_HY_06 (Figure 5.2) allows direct for comparison of precursor massive sulphide ($82\_HY\_06_b$) with early formed ccp-FeOOH, py-FeOOH and modified FeOOH from the oxidised crust ($82\_HY\_06_a$). Since $82\_HY\_06_b$ contains FeOOH too small for LA-ICP-MS, SEM-EDS measurements are used (Bishop et al., 2025d). Modified FeOOH ($82\_HY\_06_a$) is enriched in Si, Cu, Cl, and Ca but depleted in S, Fe, and Zn compared to FeOOH in $82\_HY\_06_b$ (Table 5.3). A U-test confirms statistically significant differences in S, Si, Fe, Cu, Zn, Cl, and Ca concentration between modified FeOOH in $82\_HY\_06_a$ and early formed FeOOH in $82\_HY\_06_b$ (Appendix C.5). Spearman's correlations show Cu negatively correlates with S (-0.43), Fe (-0.71), and Zn (-0.48), but positively with Si (0.40), Cl (0.46), and Ca (0.50; Appendix C.10).

Table 5.3. Summary major geochemical data of FeOOH obtained from $82\_HY\_06_a$ and $82\_HY\_06_b$ by SEM-EDS showing median concentration. The first number of sample size for each element (n=X,X) is the measurement number for $82\_HY\_06_b$ with the latter number the number of measurements for $82\_HY\_06_a$.

	S (wt.%) n=174,73	Si (wt.%) n=174,74	Fe (wt.%) n=174,74	Cu (wt.%) n=172,74	Zn (wt.%) n=119,3	Cl (wt.%) n=167,74	Ca (wt.%) n=73,74
$82\_HY\_06_b$ (recent FeOOH)	0.58	1.74	49.51	2.52	0.86	0.21	0.10
$82\_HY\_06_a$ (modified FeOOH)	0.29	1.82	46.63	4.78	0.28	0.78	0.24

5.4.5 Elemental mapping of active sulphide weathering sites

To assess trace element mobility during the conversion from sulphide to FeOOH, LA-TOF-ICP-MS elemental mapping was performed on sample 82_HY_06$_b$ (Figure 5.5). At the first site, pyrite oxidation at a redox front is marked by brecciation of the pyrite and replacement by FeOOH (Figure 5.5A). Where py-FeOOH is observed within pyrite, py-FeOOH is enriched in Cd and Cu, but depleted in Ag relative to pyrite. Gold and Ag exhibit concomitant enrichment at the redox front, particularly on pyrite rims, but are depleted in FeOOH (Figure 5.5D).

At the second site, chalcopyrite oxidation leads to its replacement by covellite and FeOOH (Figure 5.5G). Covellite shows the highest enrichment in Cu, Au, and Ag among all of the sulphides studied, while sphalerite is rich in Cd. Chalcopyrite derived FeOOH forms as pseudomorphs of chalcopyrite and is enriched in Cd but depleted in Cu, Ag, and Au relative to its chalcopyrite protolith. Au and Ag are typically concentrated along chalcopyrite rims and in covellite.

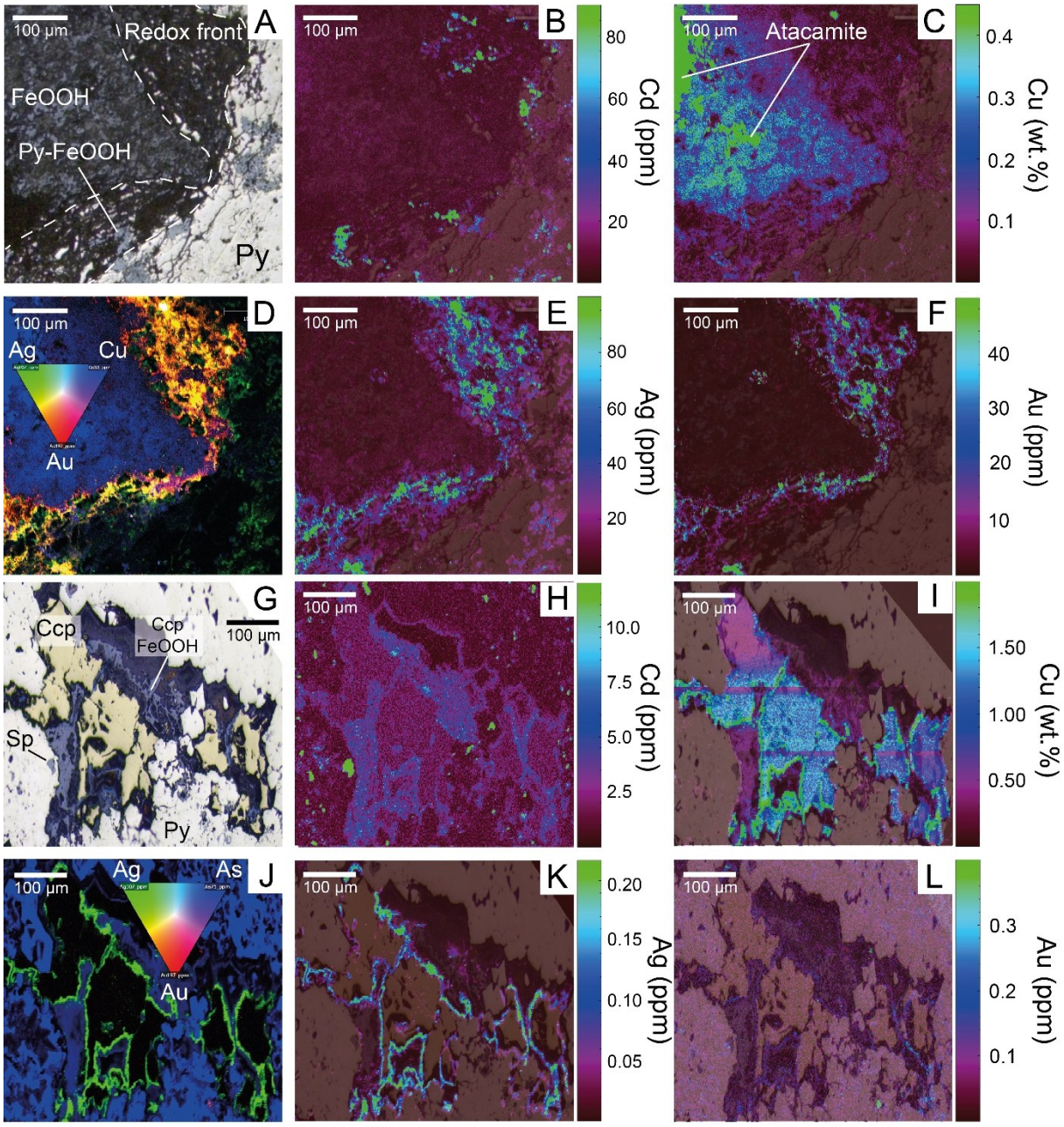

Figure 5.5. Semi-quantitative LA–TOF–ICP–MS trace elemental maps for two sites of actively weathering sulphide within 82_HY_06$_b$. **(A)** Reflective microphotograph image of site 1 and trace elemental maps for **(B)** Cd, **(C)** Cu, **(E)** Ag and **(F)** Au. **(D)** shows a red-green-blue image for Au, Ag and Cu respectively to illustrate their correlation. **(G)** Reflective microphotograph image of site 2 with element maps of **(H)** Cd, **(I)** Cu, **(K)** Ag and **(L)** Au. **(J)** illustrates a red-green-blue image for Au, Ag and As respectively to show their correlation. Ccp – chalcopyrite, py – pyrite, sp - sphalerite

5.4.6 Sequential leaching procedure

Sequential leaching studies with bulk samples of FeOOH isolate the compositions of atacamite (leach 2), ferrihydrite (leach 3), and goethite (leach 4) to understand metal distribution among these phases and their influence on FeOOH composition. Leach 1 removes sorbed metals, with >99% of Cu, Zn, and Fe not sorbed (Figure 5.6). Leach 2 effectively extracts atacamite, indicated by low Fe recovery (0.5% of total Fe) and high Cu recovery (43%). Leach 3 targets ferrihydrite and reducible FeOOH phases, extracting ~63% of Fe and ~38% of Cu. Leach 4 attacks crystalline FeOOH such as goethite, extracting ~12% of Fe and ~6% of Cu (Figure 5.6, Appendix C.11). Leach 2 recovers the most Cu (~2.9 wt.%), followed by leach 3 (~1.4 wt.%; Figure 5.6B). Bulk Cu content strongly correlates with Cu dissolved in leach 2 (R^2 = 0.99) and leach 3 (R^2 = 0.77), but not leach 4 (R^2 = 0.23). Leach 3 extracts the most Fe (~30 wt.%), followed by leach 4 (~5.8 wt.%). Zn is primarily extracted in leach 3 (~57%) and leach 4 (20%).

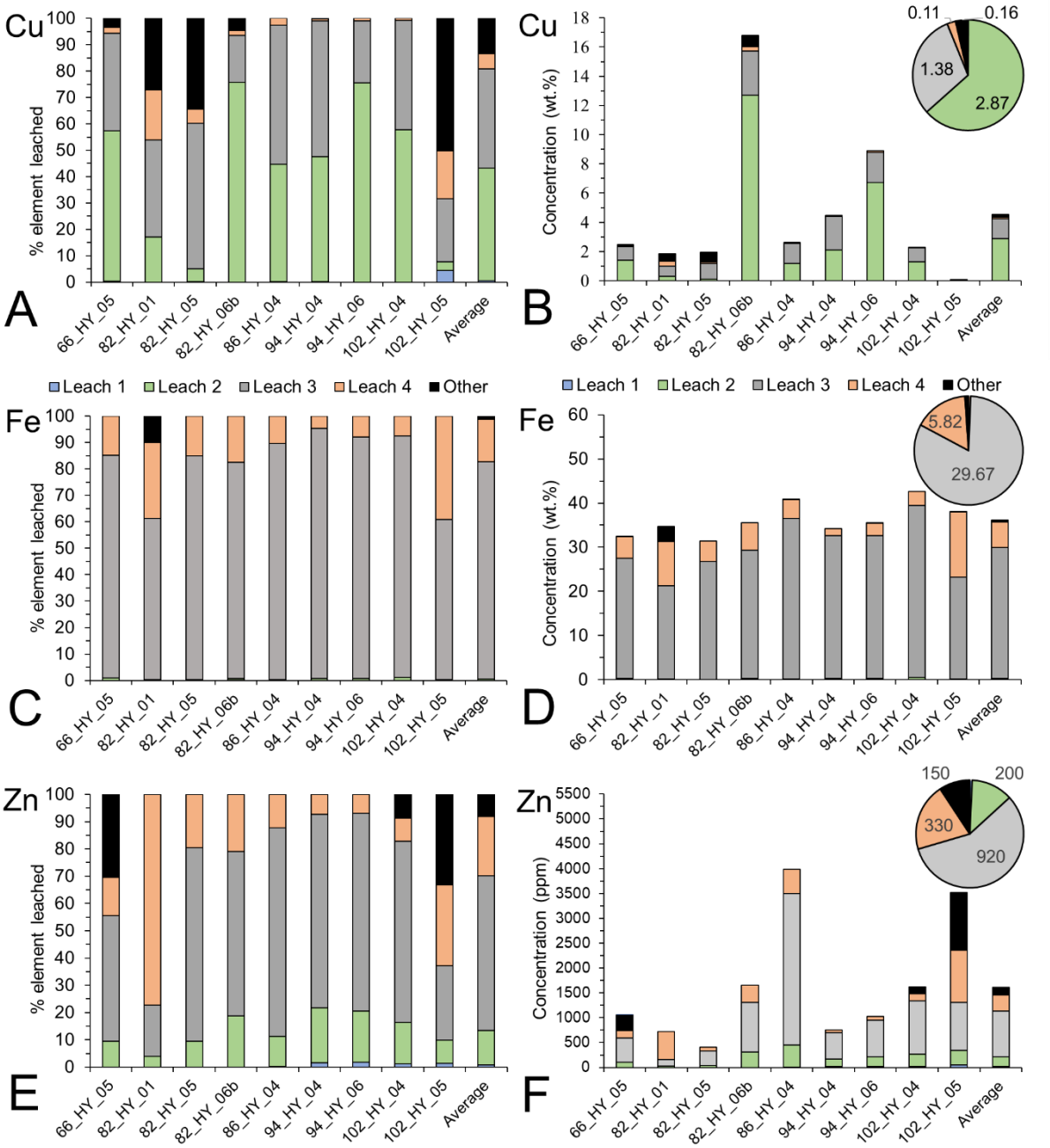

Figure 5.6. Percentage element leached and concentration of Cu (**A**,**B**), Fe (**C**,**D**) and Zn (**E**,**F**) in the leaches of the nine samples of secondary FeOOH from Semenov with the average. The pie chart in the total concentration depicts the average concentration of the nine samples. Leach 1 extracts adsorbed metals. Leach 2 dissolved carbonates and atacamite. Leach 3 extracts easily reducible Fe-oxide and FeOOH such as ferrihydrite. Leach 4 targets crystalline phases of Fe-oxides and FeOOH such as goethite. Note, for average calculation, outliers are removed.

5.4.7 t-SNE analysis

To test elemental interrelationships and identify potential sources modifying FeOOH composition, a t-SNE analysis was performed on FeOOH using the quantitative LA-ICP-MS spot data. K-means clustering of the t-SNE results produced five clusters (Figure 5.7), with each occupying a distinct quadrant, except clusters 3 and 4 that share the same quadrant.

Cluster 1 groups together Mo-As-In-Sb-Pb-Al and likely represents the original sulphide derived elements. Cluster 2 (Ca-Na-Si-Mg-Fe) represents seawater derived elements with Fe associated, with FeOOH that precipitates during seawater oxidation of sulphide material. Clusters 1 and 2 are diametrically opposed and highlight the two endmembers of FeOOH formation, which inherit the metal tenor from the original sulphide protolith (cluster 1) and modified by seawater derived elements (cluster 2). Cluster 3 (Cu-S-Cl) occupies an intermediate position between the sulphide (cluster 1) and seawater (cluster 2) clusters, suggesting it may represent a pathway of Cu-sulphide (Cu-S) oxidation by seawater (Cl) with subsequent incorporation into FeOOH. Clusters 4 and 5 also show mixed associations with seawater and sulphide signature, but likely represent a different interaction pathway between sulphide and seawater compared to cluster 3. Clusters 4 and 5 may result from hydrothermal fluid-seawater mixing, precipitating Mn-oxides that correlate with Co (cluster 5) and Ni and REE (cluster 4; Elderfield et al., 1981). Though similar in origin, cluster 5 may also stem from other processes, such as seawater (REE-Ni) interaction with FeOOH or sulphide oxidation (Zn).

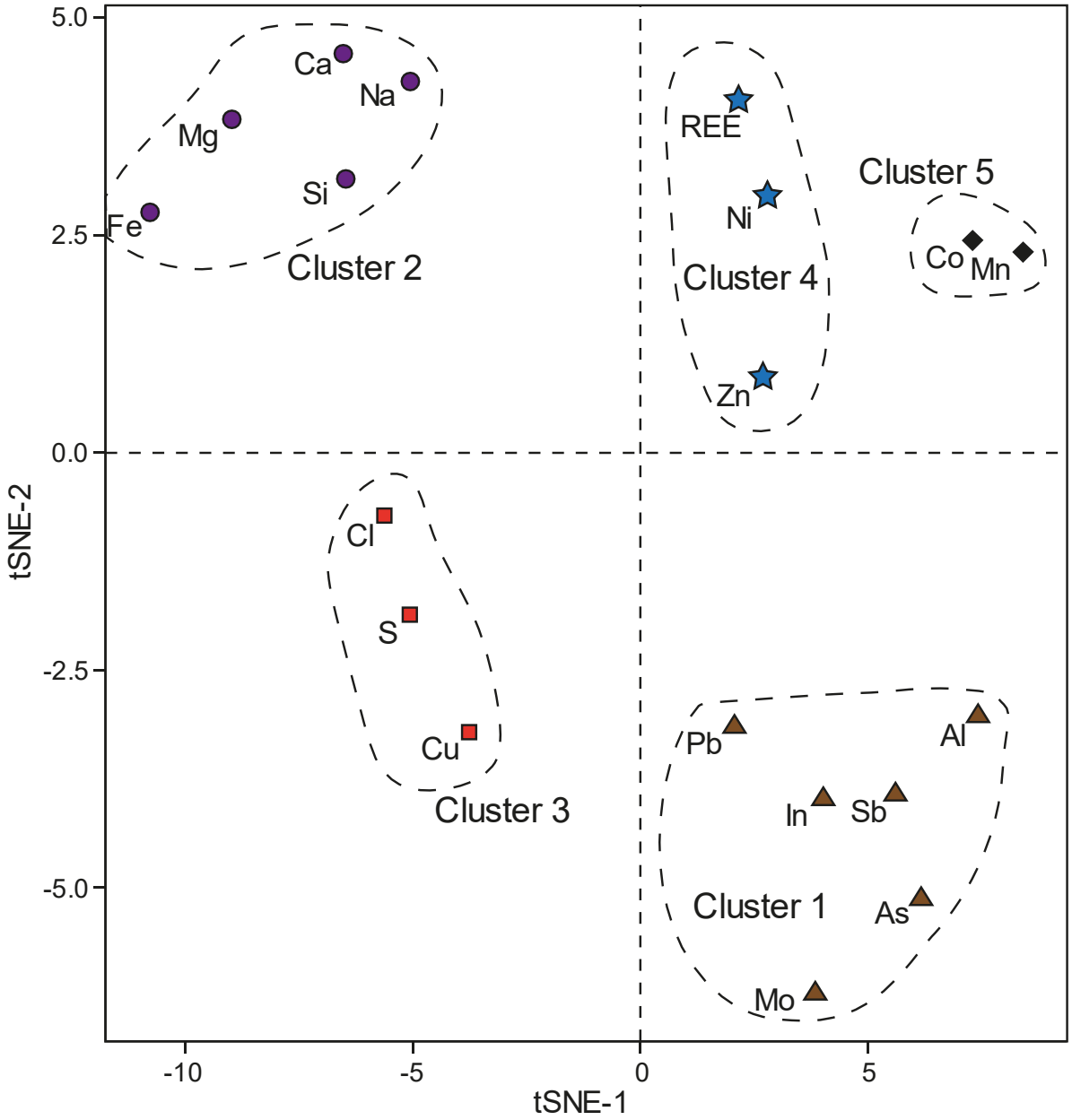

Figure 5.7. t-SNE and k-means clustering analysis on FeOOH measurements by LA-ICP-MS (n=195). Five clusters are compiled including; (1) Cu-S-Cl, (2) Mo-As-In-Pb-Sb-Al, (3) Mn-Co and (4) Na-Ca-Si-Mg-Fe and (5) REE-Ni-Zn.

5.5 Discussion

5.5.1 The mobility and behaviour of metals during sulphide weathering

Understanding the behaviour of economic metals (e.g., Cu, Zn, Au and Ag) during seafloor weathering is critical to assess whether ageing SMS deposits preserve their economic potential. At Semenov, the FeOOH derived from the oxidation of pyrite and chalcopyrite initially inherit their composition, i.e., py-FeOOH are enriched in As, Fe, Au and depleted in Ca, Cu and Ag relative to ccp-FeOOH (Appendix C.3). However, metal concentrations in FeOOH often deviate from stoichiometric expectations. For example, consider pyrite that contains a median concentration of 0.36 wt.% Cu that transforms to py-FeOOH. During this transformation, approximately 26% of the original mineral mass is lost. In the absence of Cu mobilisation, this mass loss alone should concentrate the Cu to ~0.5 wt.%. However, 3.1 wt.% Cu is observed, indicating that additional Cu is captured from external sources. Moreover, metals such as Zn, Mo and Sb show similar concentrations in both py-FeOOH and ccp-FeOOH, irrespective of the concentration of these metals in the sulphide precursor and thus, their concentrations are not inherited solely from the precursor and may be modified during or post-formation. The FeOOH identified in this study include early formed, minimally modified py-FeOOH and ccp-FeOOH, with visible relict sulphide, and modified FeOOH without relict sulphide in fully oxidised bulk samples (Figure 5.1). Relative to both py-FeOOH and ccp-FeOOH, modified FeOOH are significantly enriched in elements such as Si, Cl, Ca and REE, and depleted in Cu, Zn, Mo, Ag, Sb and Au, indicating a compositional evolution of FeOOH (Hu et al., 2022).

In summary, while the sulphide precursor mineral influences FeOOH composition (e.g., Cu, As, Au, Ag), external inputs also control modified FeOOH composition (e.g., Ca, Cu, Si, REE). Without knowing the protolith of modified FeOOH, it is challenging to trace the geochemical evolution of FeOOH and thus, assess its role as a metal trap and a potential additional resource in SMS systems.

5.5.2 The evolution of FeOOH composition

5.5.2.1 Identifying the sulphide protolith

To trace the sulphide protolith and the geochemical evolution of modified FeOOH, two ternary diagrams were constructed using LA-ICP-MS data (Figure 5.8A and Figure 5.8B). Both py-FeOOH and ccp-FeOOH closely associate with their protolith (Figure 5.8A), with most FeOOH derived from pyrite, reflecting its dominance in the system (Maslennikov et al., 2023; Figure 5.8C). The majority of modified FeOOH plot between pyrite and chalcopyrite end-members (Figure 5.8A),

suggesting a mixed sulphide composition. Furthermore, outliers of py-FeOOH and ccp-FeOOH also fall into this mixed composition field (Figure 5.8A) that display similar morphologies with modified FeOOH (Figure 5.1 and Figure 5.2), implying that their hybrid signature arose through post-formational modification (e.g., sulphide oxidation). Data reduction T-SNE analysis of FeOOH indicates that post-formational modification sources include seawater interaction (Mg-Ca-Na-Si) and metals derived from sulphide oxidation (i.e., Cu-S-Zn). This is further supported by SEM-EDS of 82_HY_06, showing that relative to py- and ccp-FeOOH, modified FeOOH are enriched in Cu and seawater elements (i.e., Ca-Si-Mg), but depleted in other sulphide derived elements (e.g., S and Zn). Seawater interaction is further evidenced by modified FeOOH showing an increased negative Ce anomaly relative to py-FeOOH and ccp-FeOOH. Seawater modification can be observed on Figure 5.8B and Figure 5.8D whereby minimally modified FeOOH occupy areas of low seawater influence (high As/Ca, Fe/Cu and low Si/Mo), while modified FeOOH trend towards high seawater modification (i.e., high Si/Mo, low As/Ca and Fe/Cu).

These findings suggest FeOOH inherits its initial composition from the protolith, but undergoes post-formational modification, becoming enriched in Na, Mg, Ca, Cl, Si, REEs, and Cu while losing Zn, Sb, Mo, and As and obscuring the original geochemical inheritance from the sulphide protolith. At this stage it is unclear if the lower content of trace metals of the hydrothermal samples carrying the strongest seawater signature relates to an effective loss of Zn, Sb, Mo and As to an open system, or a dilution of the geochemical content of the sulphide weathering product by addition of seawater-derived elements. As geochemical analysis is weight-normalised, both options explain the data. Unfortunately, an isocon analysis (Gresens, 1967; Grant, 1986) could not be conducted due to a lack of clear relationship between samples' stages of alteration successions. However, seawater addition alone cannot explain the observed enrichment of Cu in FeOOH. The t-SNE analysis reveals a Cu-Cl-S association, potentially linked to chalcopyrite oxidation or atacamite precipitation, which may account for the observed Cu enrichment.

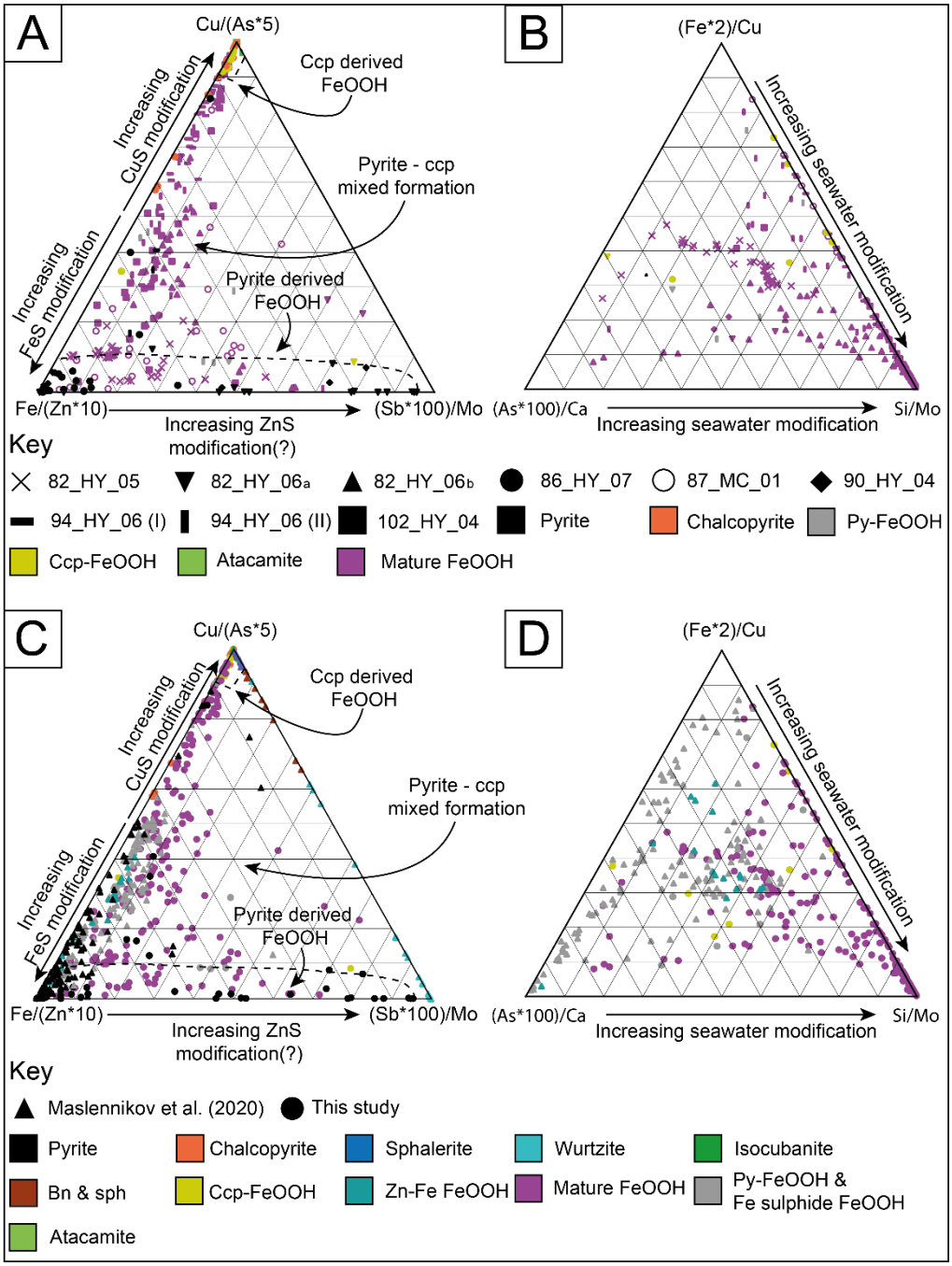

Figure 5.8. Ternary discrimination diagrams of FeOOH precursors at Semenov, showing potential sources of post-formational modification. Diagrams **(A)** and **(C)** depict areas of pyrite (py) and chalcopyrite (ccp) derived FeOOH, a mixed signature, and possible ZnS modification. Diagrams **(B)** and **(D)** illustrate the modification of seawater interaction with FeOOH. (A) and (B) show data from this study, while (C) and (D) compare with LA-ICP-MS measurements of FeOOH from Pobeda vent field (Maslennikov et al., 2023). Fe sulphide FeOOH replaces py-FeOOH, indicating origins from Fe-sulphide (pyrite, pyrrhotite, marcasite), and Zn-Fe-FeOOH suggests derivation from Zn-Fe sulphide (e.g., wurtzite). Bn – bornite, sph – sphalerite. FeOOH with relict sulphide ablation omitted from diagrams.

5.5.2.2 The influence of atacamite on the composition of FeOOH

The Cu extracted from ferrihydrite in the leaching experiment has a moderate positive correlation with the quantity of (par)atacamite in the sample (R^2 = 0.52; Figure 5.9A) and the Cu extracted from (par)atacamite (R^2 = 0.69; Figure 5.9B), suggesting that increasing (par)atacamite precipitation leads to Cu enrichment in ferrihydrite. However, this may also reflect (par)atacamite dissolution during leach 2, followed by adsorption of Cu onto ferrihydrite and subsequent release during leach 3 (Moon & Peacock, 2012), which could underestimate the Cu in (par)atacamite and overestimate it for ferrihydrite. Regardless, these observations highlight the capacity of FeOOH to adsorb Cu from low-pH solutions (e.g., pH 4.5 in leach 2), similar to processes occurring during weathering of natural SMS systems. For instance, during chalcopyrite oxidation, Fe precipitates as FeOOH (Glasby & Schulz, 1999) whereas Cu is mobilised in chloride complexes (Rose, 1976; Hannington, 1993). At low pH (e.g., 4.5), (par)atacamite may precipitate (Sharkey & Lewin, 1971); however, Cu likely migrates in solution through the FeOOH and then reprecipitate as (par)atacamite upon interaction with seawater (Hannington, 1993). As such, the Cu will instead adsorb onto FeOOH, enriching it in Cu as well as Cl. This is supported by t-SNE (Cu–Cl–S) analysis and by the higher Cu and Cl contents in modified FeOOH (82_HY_06$_a$) relative to minimally modified FeOOH (82_HY_06$_a$). Eventually, when cuprous chloride complexes mix with seawater, buffering pH, Eh, and Cl^- activity, (par)atacamite precipitates in voids within FeOOH crust veins (Figure 5.2A) or on surfaces directly exposed to seawater (Figure 5.1A; Woods and Garrels, 1986; Pollard et al., 1989; Hannington, 1993).

These observations highlight the role of FeOOH as a metal trap, retaining Cu that might otherwise be lost to seawater. For seafloor exploration, areas of atacamite precipitation likely also indicate Cu enrichment within the surrounding and underlying FeOOH crust. In contrast, goethite contains only ~2.5% of the total Cu (0.11 wt.%) in the bulk FeOOH samples and shows no correlation with atacamite (Figure 5.9). This suggests that atacamite formation can concentrate Cu in ferrihydrite, whereas the transformation of ferrihydrite to goethite promotes Cu and Zn loss to seawater during crystallisation, thereby reducing the metal tenor of FeOOH at SMS systems (Grundl & Delwiche, 1993; Blowes et al., 2003; Vu et al., 2013; Sajih et al., 2014).

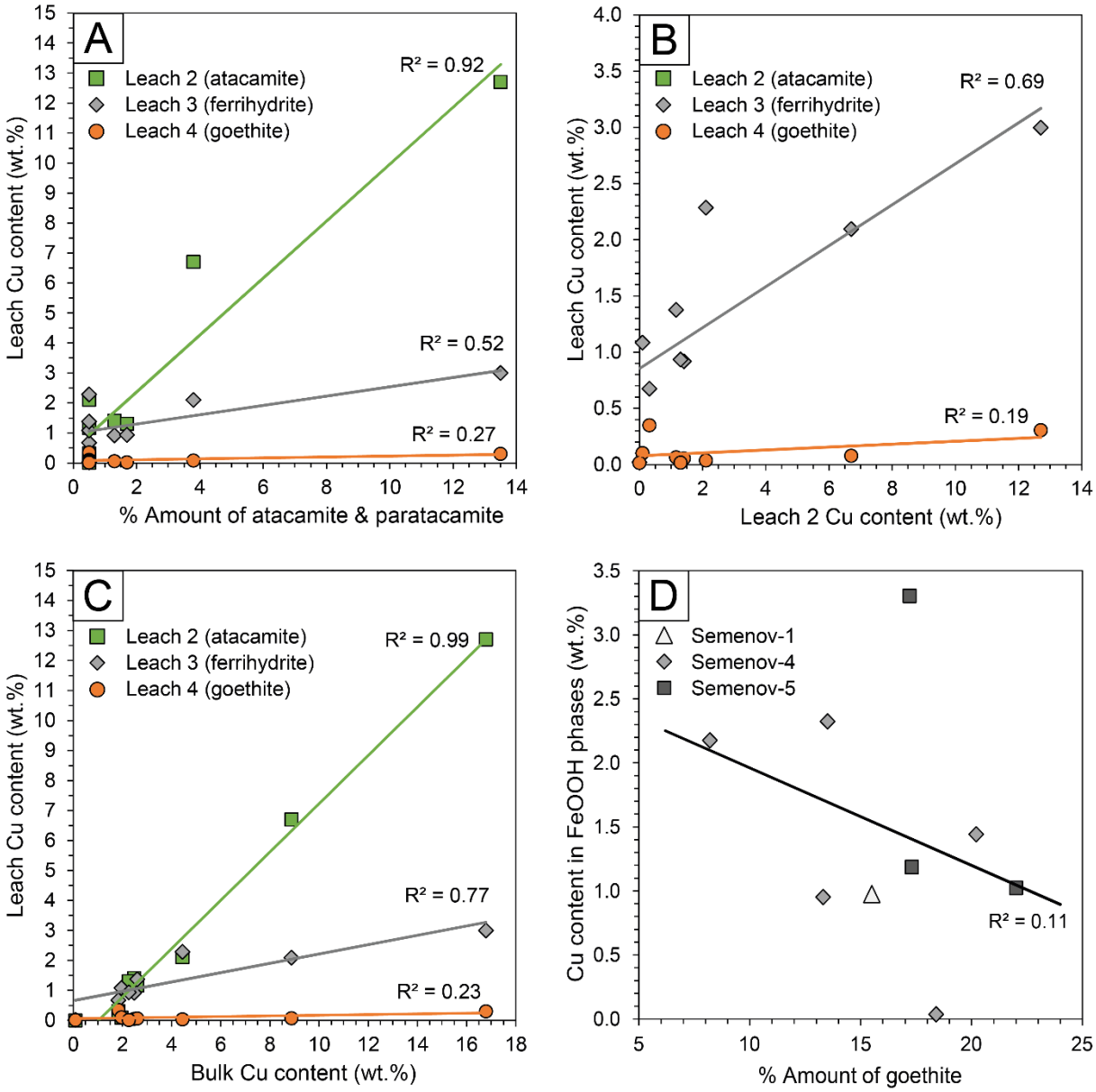

Figure 5.9. Bivariate plots illustrating relationships relevant to Cu deportment in the samples. **(A)** Leached Cu content against the % amount of (par)atacamite by quantitative XRD. **(B)** Leached Cu content of leach 3 and leach 4 against the leached Cu content of leach 2. **(C)** Leached Cu content against the bulk Cu content of the sample and. **(D)** The Cu content within FeOOH phases (i.e., goethite and ferrihydrite) against the % amount of goethite in the sample by quantitative XRD.

5.5.2.3 The crystallisation of ferrihydrite

Sequential leaching studies show that if ferrihydrite fully crystallises into goethite, the Cu content in FeOOH drops from 1.4 wt.% to 0.11 wt.% (92% loss), and the Zn content decreases from 0.09 wt.% to 0.03 wt.% (57% loss; Figure 5.6). As such, it would be expected that an increasing proportion of goethite would correlate with Cu and Zn depletion. However, correlations between goethite percentage and metal content in the total FeOOH fraction (leaches 3 and 4) yield statistically weak relationships, with R^2 values of 0.11 for Cu (Figure 5.9D) and 0.14 for Zn. These low correlation coefficients indicate that the proportion of goethite does not reflect the Cu or Zn content within the FeOOH. Within natural systems, at an SMS deposit, the metals released during goethite crystallisation may re-adsorb onto adjacent FeOOH phases, thereby limiting net metal loss from the system despite increasing goethite formation (Vu et al., 2013). However, since goethite has lower metal adsorption capacity than ferrihydrite, extensive goethite crystallisation could exceed the system's ability to retain released Cu and Zn, ultimately leading to metal depletion (Sajih et al., 2014; Görn et al., 2021). The extent of metal loss would therefore depend on the crystallisation rate of goethite, available adsorption sites and local geochemical conditions.

The half-life of ferrihydrite crystallisation to goethite under seafloor conditions (ridge-flank) has been estimated at ~100 ka (Dunk & Mills, 2006), based on sequential leaching extraction data combined with sediment age (i.e., sedimentation rates). This implies that off-axis SMS deposits exposed to seawater >100 ka should be dominated by goethite and poor in Cu and Zn. Using the Semenov hydrothermal field as a test case, we assess whether goethite content in FeOOH correlates with deposit age. The goethite content of FeOOH samples varies considerably within and across deposits of different primary sulphide ages. Semenov-4 (1.7-123.8 ka) contains 8-20% goethite, Semenov-5 (8-14 ka) contains 17-22% goethite and Semenov-1 (12.9-37.4 ka) contains 16% goethite (Figure 5.10; Kuznetsov et al., 2011; Cherkashov et al., 2017). Hence there is no clear correlation between the age of the deposit and goethite content. Notably, the oldest samples from Semenov-4 (up to 123.8 ka) contain generally less goethite compared to the younger Semenov-5 samples (up to 14 ka), contradicting the time-dependent crystallisation model. The absence of age-related goethite enrichment suggests that factors other than time control the extent of ferrihydrite crystallisation. Adsorption of Fe^{2+} catalyses goethite formation, but competes with adsorbed or lattice-bound metals (e.g., Cu, Zn, As; Tronc et al., 1992; Jambor and Dutrizac, 1998). Additionally, bacterial interactions may stabilise ferrihydrite (Kennedy et al., 2004). As such, lattice bound metals and bacterial interactions may inhibit complete goethite crystallisation, limiting metal loss.

In summary, the metals released during goethite crystallisation from ferrihydrite can re-adsorb onto nearby ferrihydrite, provided there are sufficient adsorption sites available in ferrihydrite. Biogeochemical factors may inhibit extensive goethite crystallisation from ferrihydrite. Consequently, FeOOH deposits at older off-axis SMS deposits may not be goethite-dominated or metal-depleted. However, our conclusions are limited by sampling bias (exposed surface material) and a small dataset. Future work should target off-axis, older SMS deposits and investigate goethite crystallisation kinetics under realistic biogeochemical conditions.

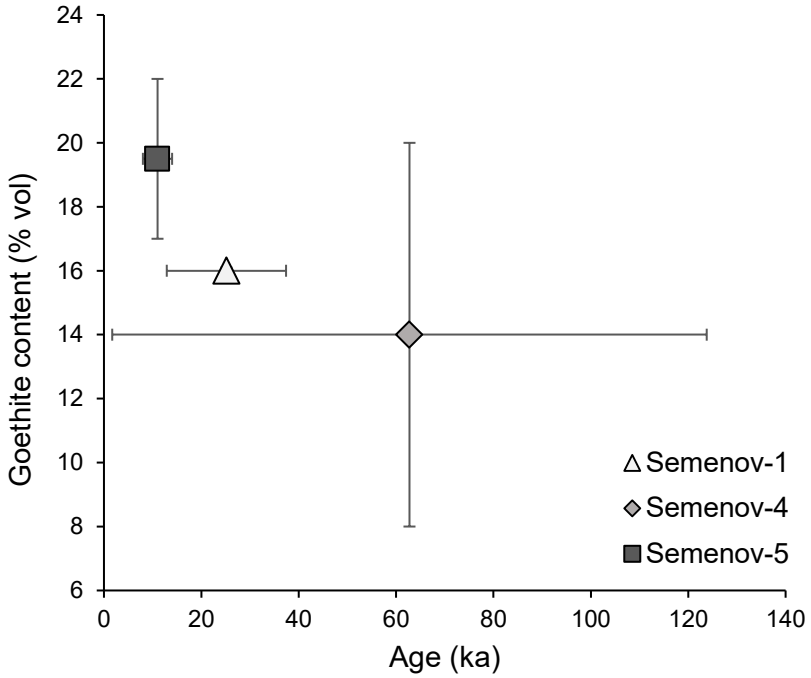

Figure 5.10. Estimated age of Semenov hydrothermal field and goethite content in bulk samples of FeOOH from the Semenov hydrothermal field. Horizonal bars represent the age range of each area, while vertical bars represent the range of goethite content estimated within bulk FeOOH samples of this study. Age data are after Kuznetsov et al. (2011) and Cherkashov et al. (2017).

5.5.3 The fate of Au and Ag

Elevated concentrations of Au and Ag in SMS deposits may enable their valorisation as by-products of Cu and Zn extraction (Herzig & Hannington, 1995; Hannington et al., 2010). Previous studies report native gold in FeOOH with bulk samples up to 28.4 ppm Au (Fouquet et al., 1993; Herzig et al., 1991; Maslennikov et al., 2023). While this study observes Au enrichment in py-FeOOH (median of 1.3 ppm) and Ag in ccp-FeOOH (25.6 ppm), correlations and ablation depth profiles show these enrichments are hosted by sulphide inclusions (Figure 5.4E). Measurements of FeOOH with no sulphide inclusions or their association contain <0.1 ppm Au and Ag (Figure 5.3F). Depletion of Au and Ag in FeOOH cannot be explained by a Au-Ag-poor sulphide protolith, as sulphides in 82_HY_06 and 94_HY_06 (e.g., 06iiS5-7; Appendix C.9) have Au and Ag concentrations similar to this study's median. In contrast, modified FeOOH in 82_HY_06$_a$ and 94_HY_06 are depleted in both Au and Ag. Combined with the sharp contrast of Au and Ag between the sulphide phases and their alteration products (Figure 5.5E and Figure 5.5L), this suggests that precious metals are not sequestered within FeOOH phases during seafloor weathering in our samples. The spatial association of Au and Ag with pyrite and chalcopyrite rims suggests that they precipitate rapidly at pH/Eh gradients caused by seawater mixing at the oxidation front (Figure 5.5D and Figure 5.5J). As sulphides shrink during oxidation, Au and Ag remain bound to the sulphide rim. After complete oxidation, both Au and Ag are absent within FeOOH, implying mobilisation after sulphide oxidation.

To understand these observations, it is essential to consider how SMS weathering differs from terrestrial systems. In terrestrial deposits, Au and Ag are mobilised from oxidising sulphides by acidic meteoric waters (pH < 5.5) as chloride complexes or under near-neutral conditions as thiosulphate complexes (Webster & Mann, 1984). Thiosulphate/chloride complexes are transported downward through weathering profiles and precipitate at redox boundaries where oxidised fluids encounter reducing conditions, such as at the interface between oxidised gossans and underlying reduced lithologies (e.g., fresh sulphide; Mann, 1984; Webster and Mann, 1984; Yesares et al., 2014). In contrast, SMS deposits are influenced by seawater, buffering pH to ~8, limiting the development of highly acidic conditions favourable for efficient Au and Ag mobilisation as chloride complexes. While initial sulphide oxidation may generate locally acidic pore fluids capable of forming chloride complexes (Rose, 1976; Mann, 1984; Hannington, 1993), the buffering capacity of seawater likely restricts sustained acidic conditions, potentially favouring the formation of less mobile thiosulphate complexes instead (Webster, 1986; Benedetti & Boulëgue, 1991).

The absence of Au and Ag in fully oxidised FeOOH samples at Semenov, despite previous findings of residual Au seafloor samples of FeOOH elsewhere (Herzig et al., 1991) may reflect sampling

within zones where seawater-buffered conditions were unsuitable for Au and Ag precipitation, suggesting their mobilisation after complete sulphide oxidation. The data from this study do not provide definitive insights into the ligands responsible for Au and Ag remobilisation in SMS deposits. Therefore, the following discussion explores potential transport mechanisms that may occur under seawater-dominated conditions and explain the observations of this study. During the final stages of sulphide oxidation, seawater dominated, near neutral and oxidising conditions likely dominate within FeOOH crust pore space. Under these conditions, intermediate thiosulphate ions produced by sulphide oxidation (Eq. 5.1) could mobilise Au or Ag as thiosulphate complexes (e.g., Eq. 5.2; Goldhaber, 1983; Webster, 1986). Thiosulphate complexes are stable under the pH and Eh conditions corresponding to goethite stability in seawater (Becking et al., 1960; Glasby & Schulz, 1999; Appendix C.12), allowing their coexistence and mobilisation from FeOOH. Production of thiosulphate ions may also be facilitated by sulphide oxidising bacteria at hydrothermally inactive SMS systems (Schippers et al., 1996; Reith et al., 2007; Sylvan et al., 2012). Thiosulphate complexes have reduced capacity to adsorb onto goethite relative to chloride complexes and this may explain the absence of Au (and likely Ag) within FeOOH phases (Ran et al., 2002).

$$FeS_2\,(s) + 6Fe^{3+} + 3H_2O\ = S_2O_3^{2-} + 7Fe^{2+} + 6H^+ \qquad Eq.\,5.1$$

$$4Au + 8S_2O_3^{2-} + O_2 + 2H_2O = 4[Au(S_2O_3^{2-})_2]^{3-} + 4OH^- \qquad Eq.\,5.2$$

The fate of mobilised Au-Ag thiosulphate complexes likely depends on fluid flow patterns within SMS deposits. In terrestrial massive sulphide deposits, Au and Ag mobilise through gravity-driven downward migration of fluids (Mann, 1984), whereas SMS deposits experience complex fluid flow patterns influenced by hydrothermal convection, fractures, and permeability variation (Rona, 1984). The direction of fluid flow within the weathering system could determine the decomposition of thiosulphate complexes and subsequent Au-Ag precipitation (Webster, 1986). Upward migration into oxic seawater should lead to thiosulphate oxidation and Au-Ag precipitation (Eq. 5.3; Kalinin et al., 2019), while downward migration and reduction within the SMS mound could also result in thiosulphate decomposition and Au-Ag precipitation (Webster, 1986).

$$Au(S_2O_3)_2^{3-} + 2.5H_2O + 3.75O_2 = Au(s) + 4SO_4^{2-} + 5H^+ \qquad Eq.\,5.3$$

While the fate of Au and Ag during sulphide weathering at SMS deposits remains an open question, the near complete absence of Au and Ag in FeOOH suggests that surface sampling of oxidised SMS deposits underestimate precious metal content of underlying sulphide. Moreover, downward migration of Au and Ag could result is supergene enrichment zones at the FeOOH-

sulphide boundary. Future studies should aim to acquire preserved drill cores of FeOOH and underlying sulphides, capturing both oxidised and fresh sulphides to enable a more detailed analysis of Au and Ag mobilisation, precipitation and possible supergene processes, particularly at redox boundaries and pH buffer interfaces.

5.5.4 Model for sulphide weathering, FeOOH formation and post-formational modification

This study presents a conceptual model illustrating the mineralogical and geochemical evolution of sulphides and their weathering products at SMS deposits (Figure 5.11). Stage 1 shows primary, unaltered sulphides typical of young SMS systems. Stage 2 depicts initial weathering, where chalcopyrite oxidises before pyrite (Figure 5.2D), likely driven by galvanic interactions (Mehta & Murr, 1983; Fallon et al., 2017; Knight et al., 2018). Chalcopyrite oxidation forms covellite, with expelled Fe precipitating as ccp-FeOOH and inheriting chalcopyrite's geochemical signature. Mobilised Ag becomes enriched in covellite or binds to the grain boundaries of chalcopyrite. Stage 3 involves pyrite oxidation, forming py-FeOOH, with Au and Ag bound at pyrite rims. Continued Cu-sulphide oxidation releases Cu^{2+} ions that are later precipitated as atacamite or incorporated into FeOOH. In Stage 4, sulphides are fully oxidised. Seawater-dominated interaction depletes sulphide-derived elements (e.g., Zn, As, Sb) and enriches seawater-derived elements (e.g., Na, Si, Ca, REEs). Goethite crystallisation from ferrihydrite re-releases Cu and Zn which may adsorb onto neighbouring FeOOH. Py-FeOOH with lower Cu and higher Fe may crystallise to goethite more rapidly than ccp-FeOOH (Jambor and Dutrizac, 1998). By Stage 5, the FeOOH has been modified by continued seawater interaction and has adsorbed metals released from nearby oxidising sulphides. This results in a modified FeOOH phase that obscures the original sulphide-derived composition. The long-term fate of Cu and Zn beyond this stage remains unresolved (Figure 5.11).

While this model advances our understanding of the compositional evolution of SMS deposits, several limitations exist. Data on other sulphides (e.g., sphalerite, marcasite, pyrrhotite) is limited, and their weathering may uniquely affect FeOOH formation and modification (Firstova et al., 2016; Lehrmann et al., 2022; Maslennikov et al., 2023). Some alteration products, such as jarosite and hematite, are not included due to their absence in our sample set (Herzig et al., 1991; Dutrieux, 2020). Microbial influences, including recently discovered “cable” bacteria forming galvanic coupling, also impact weathering dynamics (Toner et al., 2009; Meysman, 2018). The rate of goethite crystallisation and its impact on FeOOH metal content is also yet to be fully considered. Finally, we have shown that the fate of Au and Ag during seafloor weathering of SMS is more complex than previously thought (e.g., Herzig et al., 1991). Whether these precious metals are retained or lost depends on whether fluids migrate downward to the

sulphide-FeOOH boundary or upwards into seawater, and will require sub-surface sampling and more detailed hydrodynamic consideration of SMS mounds to solve.

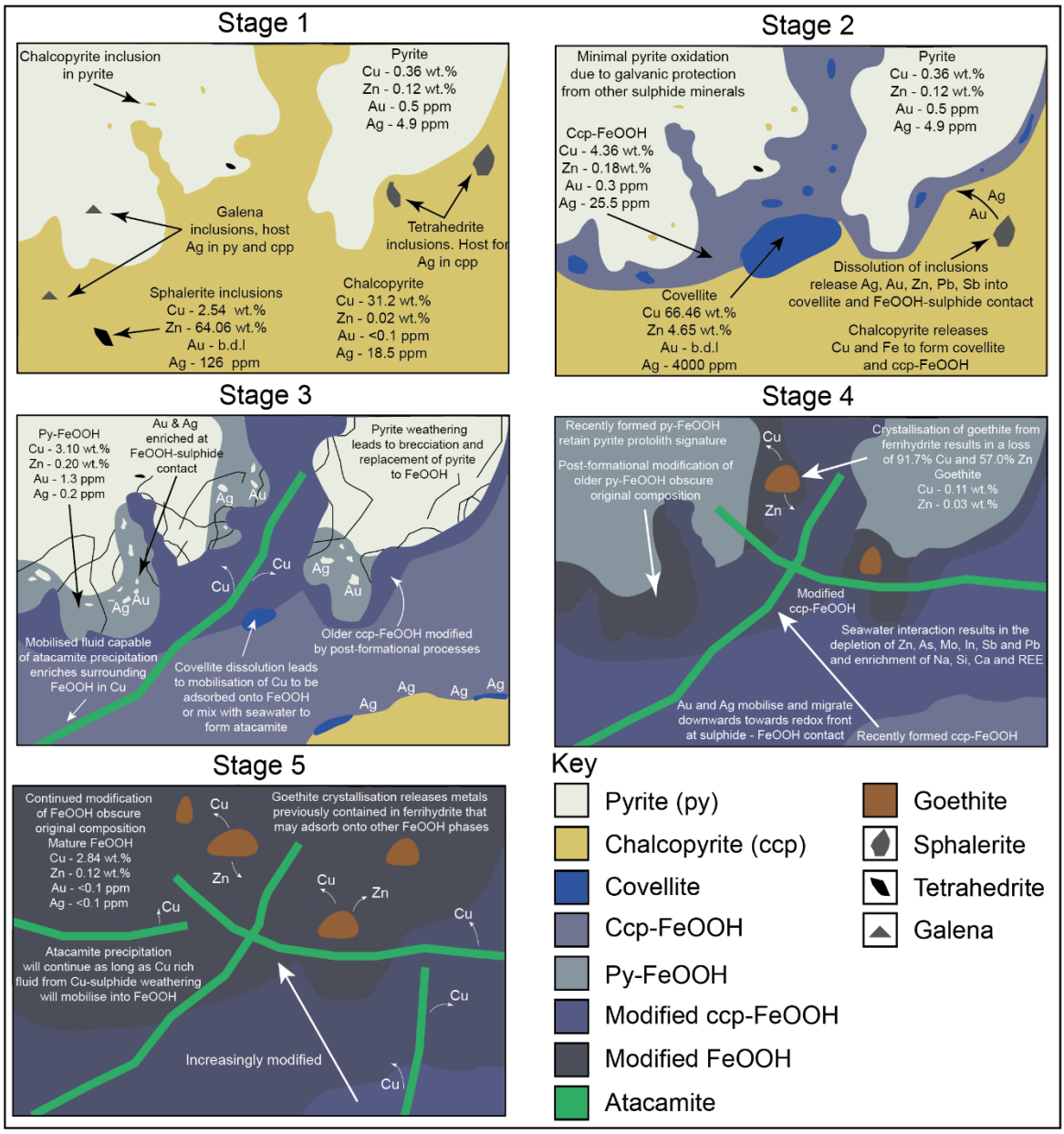

Figure 5.11. Schematic illustration of SMS deposit evolution and associated geochemical changes. **Stage 1:** Formation of unoxidised sulphides. **Stage 2:** Minor oxidation of chalcopyrite forms covellite and ccp-FeOOH. **Stage 3:** Pyrite oxidation forms py-FeOOH, with Cu-sulphide weathering releasing Cu and enriching FeOOH via adsorption and atacamite precipitation. **Stage 4:** Complete sulphide oxidation drives Au and Ag migration, while seawater interaction enriches FeOOH in Na, Si, Ca, and REEs and depletes sulphide derived Zn, As, Mo, In, Sb and Pb. **Stage 5:** Post-formational processes obscure the sulphide protolith, with ongoing goethite crystallisation releasing Cu and Zn that may adsorb onto surrounding FeOOH.

5.5.5 Implications of FeOOH and atacamite as an additional resource or exploration tool at SMS deposits

The average Cu content in bulk FeOOH with and without atacamite observed in this study (4.53 wt.%, n=9) and others (e.g., Herzig et al., 1991; Melekestseva et al., 2018; Hu et al., 2022) is comparable to those of VMS deposits (1.10-2.04 wt.%; Barrie and Hannington, 1999). Although atacamite comprises only a minor fraction of our samples compared to FeOOH (typically <10%), its abundance shows the strongest correlation with bulk Cu content (R^2 = 0.99; Figure 5.9C) where it also hosts the majority (60%) of the total Cu, averaging 2.87 wt.% (Figure 5.6). The presence of atacamite veins demonstrates mobilisation of Cu-rich fluids, and our leaching experiments show a positive correlation between atacamite abundance and Cu content in ferrihydrite (R^2 = 0.69), indicating that FeOOH adsorbs Cu from acidic solutions before atacamite precipitation occurs at higher pH when these fluids mix with seawater. Therefore, atacamite mineralisation serves as a strong indicator of Cu-enriched FeOOH deposits in the surrounding crust, as FeOOH acts as a metal trap that retains Cu during the oxidation process before atacamite formation. Although not guaranteed to indicate fresh sulphide below, atacamite marks Cu-rich areas worth focusing on for exploring ageing, weathered SMS deposits (Figure 5.12). Zinc content in bulk FeOOH is low (average of 0.16 wt.%), but other SMS deposits, such as Yuhuang-1 (1.37 wt.% Zn; Hu et al., 2022), show comparable Zn levels to VMS deposits (1.82-5.63 wt.%; Barrie and Hannington, 1999). Sequential leaching also demonstrates Zn is better retained than Cu during goethite crystallisation, losing only 57.0% Zn compared to 91.7% for Cu. As such, suggesting older SMS systems may retain Zn-rich goethite.

In summary, samples of FeOOH and atacamite at Semenov exhibit Cu and occasionally Zn grades comparable to those found at VMS. However, the economic potential of FeOOH and atacamite remains uncertain due to limited knowledge of their grade and tonnage at SMS deposits. Nonetheless, atacamite may also serve as an exploration vector, providing targets for Cu-rich FeOOH and as a possible indicator for underlying Cu-rich massive sulphide.

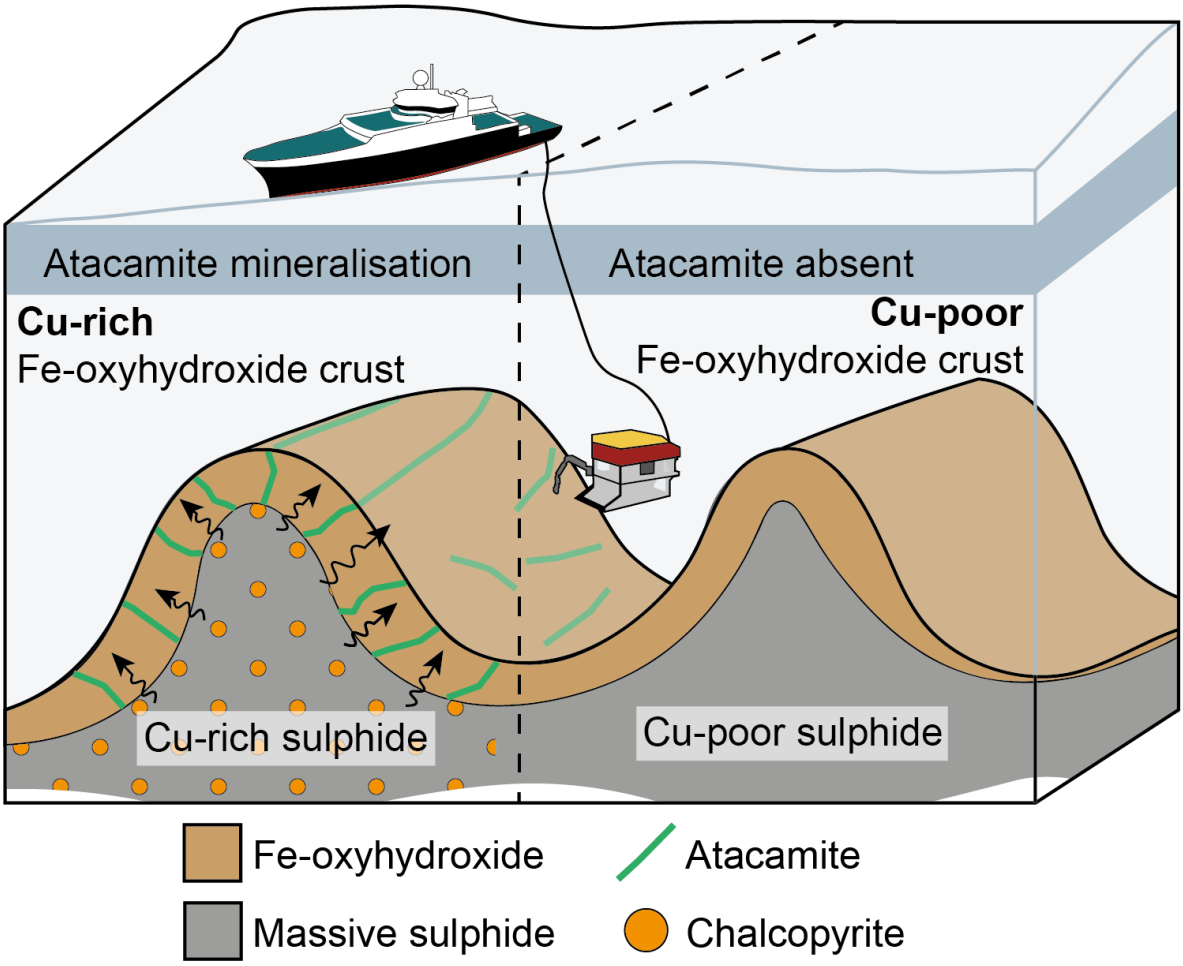

Figure 5.12. Schematic diagram illustrating Cu-rich FeOOH deposits and atacamite mineralisation form by the weathering of Cu-rich sulphide and may indicate the underlying presence of Cu-rich sulphide in contrast to Cu-poor sulphide resulting in the formation of Cu-poor FeOOH deposits and a lack of atacamite mineralisation.

5.6 Summary and conclusions

This study examined both minimally modified FeOOH in actively oxidising sulphide and modified FeOOH in fully oxidised sulphide to track their geochemical evolution. Initially, FeOOH inherits the elemental signature of its sulphide precursor, but seawater interaction later depletes sulphide-derived elements (e.g., As, Mo, Sb) while enriching it with seawater-derived elements (e.g., Si, Ca, REEs). As sulphides oxidise, economic metals like Cu are released and adsorbed onto FeOOH, enriching it in Cu before (par)atacamite precipitation. The mineralisation of (par)atacamite can be used for a dual purpose: as a possible exploration tool for underlying Cu-rich massive sulphide and to highlight surrounding Cu-rich oxidised FeOOH crust. Although our data indicates that ferrihydrite crystallisation to goethite may lower metal tenor (with losses of 91.7% Cu and 57.0% Zn from ferrihydrite), goethite crystallisation may not be extensive and the released Cu and Zn may re-adsorb onto adjacent FeOOH phases, limiting metal loss at the deposit scale.

In contrast to the behaviours of Cu and Zn, LA-TOF-ICP-MS reveal that Au and Ag are bound to sulphide rims during oxidation and are absent in both FeOOH and atacamite. While the fate of these precious metals after complete sulphide oxidation remains an open question, we propose that Au and Ag may be mobilised via thiosulphate complexes to either seawater or to the FeOOH-sulphide boundary deeper within the SMS system. If the latter occurs, our data predict Au and Ag supergene enrichment at these boundaries.

Our schematic model summarises the geochemical evolution of SMS deposits, highlighting seafloor FeOOH crusts as long-term base metal traps, acting as a ‘marine gossan’. These findings imply that older, extinct, off-axis SMS deposits may still host economic metals locked within their alteration products. Consequently, our research not only advances the understanding of metal mobility during sulphide oxidation and the geochemical evolution of FeOOH, but also provides a basis for the exploration of SMS deposits off-axis. Further research is needed on the fate of Au and Ag, goethite recrystallisation kinetics, tonnage estimates of weathering products, and processing methods for FeOOH and atacamite to fully assess their resource potential.

Chapter 6 Metal release during oxidative dissolution of sulphide minerals at the seafloor: environmental and economic implications for deep-sea mining

This chapter investigates how naturally occurring polymineralic sulphide samples oxidise under simulated seafloor conditions. The experimental approach examines the relationship between mineral characteristics (composition, texture, morphology) and oxidation rates, while determining how secondary FeOOH formation affects metal release and retention.

The data within this Chapter is available within the Appendix of this thesis and the BODC database after Bishop et al. (2025c).

Christian S. Bishop[1], Anna Lichtschlag[2], Stephen Roberts[1], Maxime Lesage[3] & Bramley J. Murton[2]

[1]School of Ocean and Earth Science, University of Southampton, Southampton, UK, [2]National Oceanography Centre, Southampton, UK, [3]Nedre Slottsgate 8 - 0157 Oslo, Norway

ORCiD - 0000-0003-0652-3008

Author contributions

Christian Bishop: Conceptualisation, data curation, formal analysis, investigation, methodology, writing. **Bramley Murton:** Conceptualisation, supervision, writing – review and editing. **Anna Lichtschlag:** Supervision, writing – review & editing. **Stephen Roberts:** Conceptualisation, sample collection, supervision, writing – review & editing. **Maxime Lesage:** Supervision, writing – review.

Abstract

Seafloor Massive Sulphide (SMS) deposits are rich in Cu and Zn and present a potential future resource for these metals. However, both the oxidation kinetics and the fate of metals released during sulphide weathering, whether they remain dissolved in seawater or become trapped in secondary sulphide alteration products, are still poorly constrained, limiting our understanding of the ecological and economic risks. To address these uncertainties, leaching studies on polymetallic sulphides simulated SMS oxidative dissolution under seafloor conditions (~2.1°C, pH 8.2) over two weeks to investigate metal release patterns and environmental implications. Our results demonstrate that As, Sb and Cd showed slow release rates allowing for natural dilution and dispersion, while Cu, Zn and Pb dissolved rapidly, reaching concentrations up to two orders of magnitude above background levels in synthetic seawater. The majority of experiments demonstrate that metal release from sulphide oxidation effectively ceases within two weeks due to Fe-oxyhydroxide precipitation, suggesting that sulphide plumes generated during SMS mining may not continuously release metals. However, a minority of samples exhibited sustained linear metal release; extrapolation of these rates indicate that stockpiling 1,000 tonnes of sulphide ore could annually release up to 7.1% Zn and 0.2% Cu. Our findings reveal that bulk metal content alone does not predict metal release; instead, reactive surface area governed by sulphide mineral morphology is critical. Black smoker hydrothermal chimney material, characterised by finer grain sizes and higher porosity, exhibits considerably greater surface areas than massive sulphide, leading to enhanced Cu and Zn release potential. Importantly, up to 23% of Cu released into seawater may be captured by secondary Fe-oxyhydroxide formation, minimising both environmental damage and economic metal loss. This study highlights the need for environmental impact assessments to include sulphide ore variability and FeOOH precipitation as a natural attenuation mechanism for proposed mining operations involving seafloor ore stockpiling.

6.1 Introduction

Seafloor Massive Sulphide (SMS) deposits have garnered global interest because of their reportedly high average grades of 4.3 wt.% Cu, 10.6 wt.% Zn, 1.7 ppm Au and 107 ppm Ag. This has led to the prospect of mining these deposits in the near future (Hannington et al., 2010). However, seafloor mining will expose unaltered sulphide minerals to seawater, which can result in their oxidative dissolution. This process can leach economic base metals (i.e., Cu and Zn) and trace metals (e.g., As, Cd, Sb and Pb), potentially leading to both economic losses and toxic impacts to marine ecosystems (Van Dover, 2011; Baker & Beaudoin, 2013; Boschen et al., 2013; Stauber et al., 2022).

Experimental studies show that sulphide oxidation kinetics are governed by mineralogy, galvanic interactions, temperature, and redox conditions, with minerals like chalcopyrite, sphalerite, and pyrite dissolving at different rates and releasing heavy metals (Abraitis et al., 2004; Bilenker et al., 2016; Fallon et al., 2018; Knight et al., 2018; Hu et al., 2023). Secondary Fe-oxyhydroxide (FeOOH) formation has been shown to lead to Zn adsorption, released during sphalerite oxidation, potentially reducing dissolution rates and toxic metal release, while itself acting as a metal trap (Fallon et al., 2018; Knight et al., 2018; Hu et al., 2023). However, these studies were relatively short (up to three days) and may not capture the temporal patterns of metal release and oxidation behaviour that could occur during mining operations, where uplifted sulphide material can remain exposed at the seafloor for extended periods (Morato et al., 2022). Additionally, these studies did not examine the release of toxic trace elements such as Sb and As, nor did they address whether FeOOH formation can capture metals beyond Zn (e.g., Cu) or metals released from neighbouring sulphide particles (Fallon et al., 2018; Hu et al., 2023; Long et al., 1995). Natural variations in sulphide composition and texture (e.g., micro-surface morphology, surface and porosity) are likely to influence oxidation kinetics, yet these parameters remain largely unexplored. Limiting our understanding of how the environmental and economic implications of seafloor mining may vary across a deposit (Gwyther, 2008; Baker & Beaudoin, 2013; Morato et al., 2022). FeOOH formation on sulphide particles can impede oxidation and sequester metals released during oxidative dissolution, and when combined with galvanic interactions between sulphide phases, this makes the calculation of oxidation rates challenging (Benjamin and Leckie, 1981; Knight et al., 2018). Despite this, accurate oxidation rate measurements are needed to estimate metal release into seawater over time and to provide quantitate environmental and economic impacts of oxidative sulphide dissolution during mining operations.

This study investigates how variations in sulphide morphology and composition influence oxidative dissolution kinetics, and explores the process by which FeOOH precipitation may sequester those mobilised metals. By understanding these factors, we can evaluate how mining operations of SMS deposits at the seafloor could impact the local marine ecosystem as well as the potential economic impacts of the dissolution and loss of valuable metals during the mining operations. The specific aims of this work are to: (1) quantify the oxidation rate of polymetallic sulphide samples and their economic implications; (2), determine how oxidation dissolution kinetics differ with different sulphide morphologies, surface areas and compositions and; (3) investigate the role of FeOOH formation in retaining metals released during sulphide dissolution and hence, assess its potential to act as a metal trap and impede further oxidative processes.

6.2 Materials and methods

6.2.1 Sample materials

Whole-rock polymineralic seafloor massive sulphide samples were collected from three hydrothermal systems, i.e. the Moytirra vent field (45°N, Mid-Atlantic Ridge) during the CE11009 VENTuRE survey (2011; Wheeler et al., 2013), the Trans-Atlantic Geotraverse (TAG) hydrothermal system during the JC138 research expedition (26°N, Mid-Atlantic Ridge) of the Blue Mining project (2017; Murton and Shipboard Scientific Party, 2018) and the Beebee hydrothermal vent field (Mid Cayman Rise, Caribbean) during the research expedition JC82 (2013; Webber et al., 2015). In addition, terrestrial sulphide samples were provided from the Wetar Island VMS deposit in Indonesia (Scotney, 2002). A detailed description of the samples can be found on Table 6.1 and Figure 6.2

6.2.2 Sample preparation and mineralogical analyses

The sulphide samples were crushed with an agate mortar and pestle and sieved to obtain grain sizes of 38-100 µm, optimising the surface area to facilitate measurable oxidation reactions. The sieved grains were cleaned, following the procedure from Knight et al. (2018). The samples were initially cleaned in an ultrasonic bath in methanol for five minutes to remove dust particles from grain surfaces and to remove microbes resistant to acid cleaning. Followed by repeated five-minute acetone washes until the supernatant fluid ran clear, indicating all dust was removed. After overnight drying under vacuum, the samples were agitated in 1 M HCl for 30 seconds and then soaked for a further five minutes to remove carbonates and oxidation products such as FeOOH. They were then rinsed with Milli-Q de-ionised water, acetone, dried and stored in a sealed, nitrogen filled chamber to prevent oxidation. A sub-sample was taken and visually inspected by reflective microscopy to ensure no visible FeOOH is present within the sample.

To characterise sample properties for interpreting oxidation kinetics, mineral proportions of the cleaned material was analysed by XRD using a PANalytical X'Pert Pro diffractometer with the mineral proportions quantified as described in section 2.3.2. The surface areas of the cleaned grains were determined by BET surface area analysis as described in section 2.3.3. To investigate the sulphide mineralogy, their associations and textures, the six samples used in this study were cut and mounted on polished blocks. A LEICA DM2700 P microscope was used to produce reflective light microphotography, with images captured by the LEICA DMC 4500 processed by the Leica Application Suite Z software (section 2.3.1).

Table 6.1. Sample locations, morphologies and mineralogy of cleaned and sieved samples, including BET measurements of surface area, semi-quantitative mineral data (% vol) and average bulk contents (wt.%) of Fe, Cu, Zn, As, Sb, Cd and Pb. ± indicates the error of mineralogical analyses. Py – pyrite, Mrc – marcasite, Ccp – chalcopyrite, Sp – sphalerite, Cv – covellite, Qtz – quartz, Gn – galena.

Location	Sample	Latitude/ longitude	Morphology	Surface area m^2/g	Mineralogy (% volume)						
					Py	Mrc	Ccp	Sp	Cv	Qtz	Gn
Wetar Island	DE-02 (VMS)	7°47.62 S 126°30.68 E	Massive sulphide	0.041	44.3 ± 0.6		50.5 ± 0.7			5.1 ± 0.5	
Moytirra	DE-03 (SMS)	45°28.400 N 33°50.851 W	Black smoker	0.256	94.2 ± 0.9		2.3 ± 0.3			3.3 ± 0.4	
Wetar Island	DE-05 (VMS)	7°47.62 S 126°30.68 E	Massive sulphide	0.067	37 ± 0.7		6.8 ± 0.4	24.4 ± 0.4		25 ± 0.6	<1.0
Wetar Island	DE-06 (VMS)	7°47.62 S 126°30.68 E	Massive sulphide	0.090	92.1 ± 4.7		0.5 ± 0.3		0.1 ± 0.3	7.3 ± 0.5	
Beebe	DE-07 (SMS)	18°32.720 N 81°43.250 W	Black smoker	0.730	36.6 ± 0.4	43.5 ± 0.5	8.4 ± 0.2	6.8 ± 0.2		2.2 ± 0.3	
TAG	DE-10 (SMS)	26°09.345 N 44.49.017 W	Massive sulphide	0.046	95.4 ± 0.7		1.5 ± 0.2			3.2 ± 0.4	

Location	Sample	Bulk Fe wt.%	Bulk Cu wt.%	Bulk Zn wt.%	Bulk As ppm	Bulk Sb ppm	Bulk Cd ppm	Bulk Pb ppm
Wetar Island	DE-02	35.57	16.65	0.07	127	3	486	83
Beebe	DE-03	11.54	9.69	0.01	1.5	0.7	0.24	3.3
Wetar Island	DE-05	28.30	1.46	10.89	12.7	370	1.8	2749
Wetar Island	DE-06	44.81	0.43	0.01	250	0.3	39	125
Moytirra	DE-07	39.51	2.24	5.62	399	202	20	794
TAG	DE-10	45.47	1.30	0.01	19.1	0.1	1.1	13.4

6.2.3 Experimental setup and procedure

The experimental setup is identical to that of Knight et al. (2018) with the addition of a dissolved oxygen (DO) probe to detect variations in oxygen saturation (%) during the experiment. The experimental set-up comprised a 1-litre polyfluoroalkyl reaction jar, modified with three ferrule fittings, used for semi-batch reactor experiments. The fittings accommodated a pH electrode, the DO probe, and a sample input/sampling port. The pH electrode and DO probe were connected to an Orion Star™ A213 Dissolved Oxygen Benchtop Meter to display and record measurements. The pH electrode was calibrated against standard solutions of pH 7.0 and 9.2 before each experiment. The reaction jar was filled with 700 mL of synthetic seawater (ASTM-D1141-98), placed in a temperature-controlled bath at 2.1 ± 0.2 °C, and stirred (Figure 6.1). The pH of the seawater was maintained at ~8.2 (seawater scale; Dickson 1984; Hunter, 1988) using 1 M sodium hydroxide or 1 M HCl.

To determine the initial concentration of metals in the solution, two to three 1 mL synthetic seawater sub-samples were collected prior to the start of the experiment. Then ~2 g of sieved and cleaned sulphide grains were added into the synthetic seawater and sampling started. Sampling intervals were staggered, beginning with 10-minute intervals for the first hour and progressively lengthening to intervals of up to 16 h by the end of the experiment (i.e., 336 hours; for details see Bishop et al., 2025c). During each sampling, 1 mL of seawater was collected, minimising the volume change during the experiment to < 5%. The samples were then filtered through a 0.45 μm polytetrafluoroethylene membrane to remove sulphide particles and diluted with 3% nitric acid spiked with Re, In, and Be to 22x dilution for further analyses by ICP-MS. The pH and DO measurements were obtained during the collection of each sample and the pH was adjusted as required (Bishop et al., 2025c). Dissolved oxygen saturation (%) was not actively adjusted with measurements at an average of 75 ± 17 % throughout our experiments (Bishop et al., 2025c). After the experiment, the reacted sulphide surfaces for each sample were analysed by semi-quantitative SEM-EDS to characterise the alteration of the minerals and determine what weathering products had precipitated (section 2.4.1; Bishop et al., 2025c).

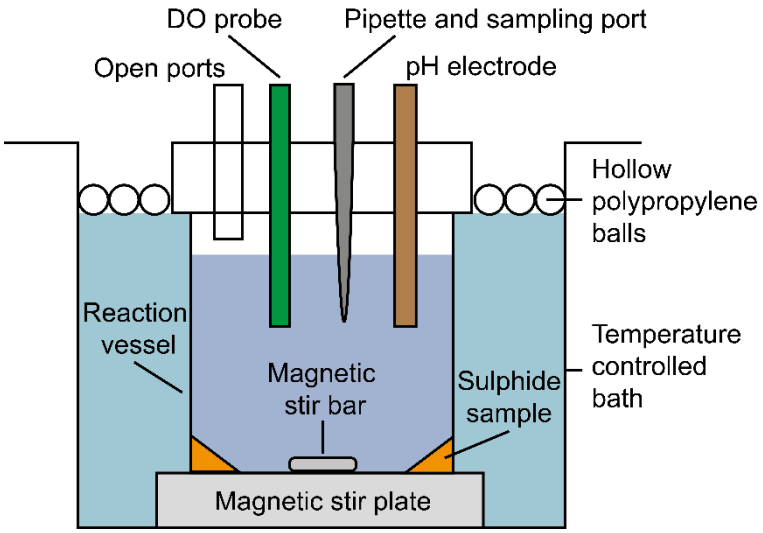

Figure 6.1. Schematic diagram of the experimental setup, modified after Knight et al. (2018) to include a DO probe.

6.2.4 Analysis of synthetic seawater and bulk samples

6.2.4.1 Synthetic seawater samples

Metals dissolved in the synthetic seawater (Fe, Cu, Zn, As, Sb, Cd, Pb) were measured using ICP-MS and ICP-OES with the methods outlined in section 2.5.3. Accuracy and reproducibility were assessed by three separate spiked seawater CRM. All elements showed good accuracy (within 10% of CRM values) except for Fe (±142%). Reproducibility was generally good with %RSD ≤ 8%, except Fe (24.5%; Appendix A.7). Duplicate experiments of DE-02 exhibit similar compositional trends but with median %RSD values of 26.7-45.8% which are considered when discussing the environmental and economic implications of the data presented in this study (Appendix A.8).

To calculate the absolute changes of a metal concentrations during the experiment, metal concentrations of the initial seawater solution were subtracted from each sample result. To enable a comparison of the samples, corrections are applied using the surface area of each sample powder, the relative proportion of sulphide minerals (%), the mass (g) of material used and the volume of seawater (L). The corrected values are expressed as cumulative metal release (μmol/m^2; Bishop et al., 2025c).

6.2.4.2 Bulk samples

Bulk geochemical analysis of the samples provides a foundation for which to interpret the release of metals and oxidation kinetics within the experiments. For this, approximately 50 mg of material were crushed using an agate mortar and pestle and digested in a mixture of hydrofluoric acid, nitric acid and HCl as outlined in section 2.5.1. Bulk geochemical analysis on six samples were measured by ICP-MS and ICP-OES and exhibited good accuracy (within 7% of CRM values) and reproducibility (within 7 %RSD) with the exception of As in OREAS-620 that showed a 65% error regarding its accuracy and Zn in CH-4 with an error of 72% (Appendix A.4).

6.2.5 Influence of DO on sulphide oxidation kinetics

Metal speciation and oxidation is influenced by the DO concentration (Holmes & Crundwell, 2000). To evaluate whether DO variations influenced sulphide oxidation kinetics in this study, we generated bivariate plots comparing DO concentration with metal release for all studied elements (Cu, Zn, As, Sb, Cd, Pb) and conducted correlation analyses between DO, time, and metal concentrations (Appendix D.1). The bivariate plots reveal no systematic relationships between DO levels and metal concentrations across the observed DO range (40-95% saturation). High metal concentrations occur across the entire DO spectrum, and low metal concentrations are similarly distributed across all DO levels. This lack of consistent DO-dependent patterns is observed across all experiments (DE-02 through DE-10) and all metals analysed. Correlation analysis between DO and time shows generally poor statistical relationships ($R^2 < 0.30$ for most experiments), indicating that sulphide oxidation does not consume oxygen faster than it can be replenished through air-seawater equilibration in the open reaction vessel. The exceptions are experiments DE-03 and DE-07, which show DO actually increasing over time ($R^2 = 0.89$ and 0.95, respectively) rather than being depleted by oxidation reactions. These findings demonstrate that DO variations (%RSD = 17%) represent natural fluctuations around equilibrium rather than systematic depletion from sulphide oxidation or control over dissolution kinetics. It is clear that the DO concentration remained above conditions that would limit sulphide oxidation reactions. Therefore, metal release was primarily controlled by intrinsic factors such as dissolved Fe^{3+}, mineral composition, bulk composition, surface area, galvanic interactions, and temperature (Benjamin and Leckie, 1981; Moses et al., 1987; Fallon et al., 2018; Knight et al., 2018), rather than by DO concentrations observed in this study.

6.3 Results

6.3.1 Morphology, mineralogy and composition of sulphides

The three polymetallic sulphide samples from the Wetar Island VMS deposit in Indonesia, primarily consist of coarse (>100 μm), euhedral crystals of pyrite, chalcopyrite, and sphalerite, with sample DE-05 containing minor amounts of galena (Figure 6.2). Each sample is dominated by a different sulphide phase: chalcopyrite in DE-02, sphalerite in DE-05, and pyrite in DE-06 (Table 6.1).

The three samples obtained from modern day SMS deposits include a massive sulphide sample from the TAG mound (DE-10, Figure 6.2F) that contains fine to medium euhedral pyrite crystals with anhedral chalcopyrite crystals, and with crystal sizes and surface areas similar to those observed in the VMS samples from Wetar Island under reflective microscopy (Table 6.1 and Figure 6.2). The black smoker hydrothermal chimney samples (DE-03 and DE-07) exhibit considerably finer grained (<100 μm) and more porous mineral assemblages compared to the massive sulphide sample (DE-10) and the VMS samples (Figure 6.2). Distinctive textures within black smoker hydrothermal chimney samples, such as colloform pyrite (Figure 6.2K), are present which, along with smaller (<100 μm) and porous mineral phases, results in a greater surface area relative to the VMS sulphide samples (Table 6.1). The black smoker hydrothermal chimney sample DE-03 is characterised by a Cu-rich composition, whereas DE-07 has a Zn-rich composition, reflected by a higher proportion of sphalerite (Table 6.1). Compared to the massive sulphide sample (DE-10), the black smoker hydrothermal chimney samples (DE-03 and DE-07) comprise less pyrite and increased amounts of chalcopyrite and sphalerite, which is reflected by their relatively high Cu and Zn content (Table 6.1).

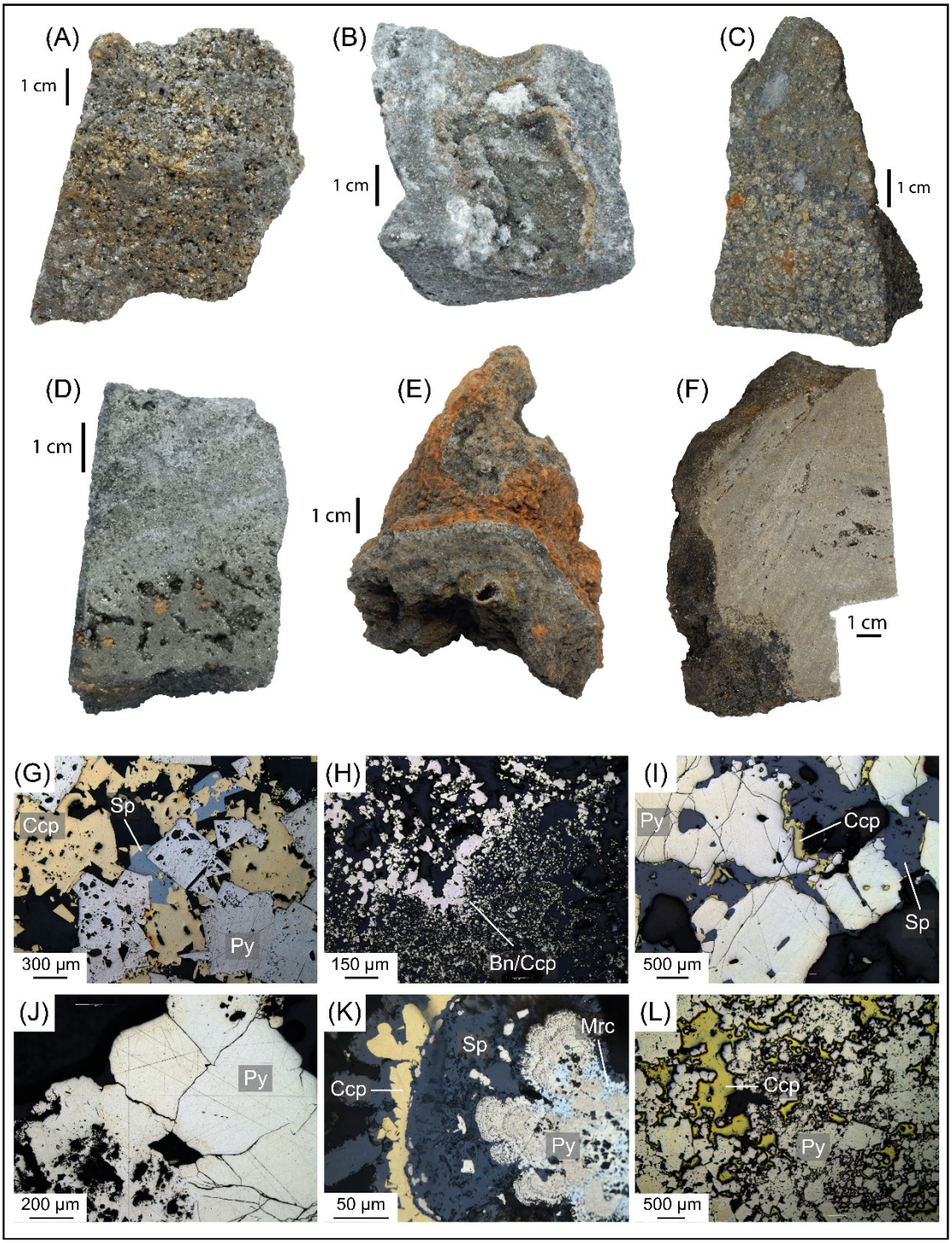

Figure 6.2. Representative hand specimen photos and reflective light microphotographs of the samples used in the study. **(A)** Massive sulphide comprised of chalcopyrite, pyrite and sphalerite (DE-02). **(B)** Black smoker hydrothermal chimney with the fluid conduit lined with chalcopyrite and pyrite. Gangue material consists of anhydrite and quartz (DE-03). **(C)** Massive sulphide of chalcopyrite, sphalerite and pyrite (DE-05). **(D)** Massive sulphide mainly comprised of pyrite with minor amounts of quartz and chalcopyrite (DE-06). **(E)** Weathered black smoker hydrothermal chimneys dominated by pyrite and FeOOH with minor amounts of chalcopyrite and

sphalerite (DE-07). **(F)** Massive sulphide dominated by pyrite with minor amounts of chalcopyrite (DE-10). **(G)** Euhedral pyrite with subhedral chalcopyrite overgrown over euhedral sphalerite (DE-02). **(H)** Chalcopyrite altering to bornite with smaller crystals on the outside of the fluid conduits with larger crystals on the inside (DE-03). **(I)** Subhedral-euhedral pyrite with anhedral sphalerite and small amounts of anhedral chalcopyrite (DE-05). **(J)** Euhedral pyrite and porous, subhedral pyrite (DE-06). **(K)** Porous, colloform pyrite and marcasite with anhedral sphalerite overgrown with euhedral pyrite and anhedral chalcopyrite. **(L)** Euhedral to subhedral pyrite with anhedral chalcopyrite.

Although all samples were subsequently ground to a uniform particle size range (38–100 μm) for analysis, the inherent textural differences observed in the polished blocks prior to grinding are likely to persist in the powdered material. The black smoker samples, with their finer-grained, porous, and colloform textures, have higher surface areas compared to the coarser-grained, non-porous massive sulphide samples. These intrinsic textural features contribute to a greater number of grain boundaries and micro-porosities, which are not entirely eliminated by the grinding process. Therefore, despite possible standardisation of particle size through grinding, the textural differences between the black smoker material and massive sulphide samples retain different surface areas (Table 6.1).

6.3.2 Leaching of metals from massive sulphide

Cu release from the different samples show four chemical trends during the experiments including: (1) initial rapid release of metals that slowly decreases (DE-05), with one sample (DE-03) showing a decrease of Cu after approximately 230 hours; (2) Rapid leach of Cu with an immediate rapid drop in concentrations after 0.8 h, followed by a continuous Cu release for up to two weeks (DE-02); (3) Initial leach followed by slow continual decrease of Cu concentration in the experimental vessel (DE-10) and; (4) a chaotic pattern of leaching (DE-06; Figure 6.3). In terms of absolute dissolved Cu concentrations in seawater, most Cu was leached from sample DE-03 into seawater, reaching 327 ± 23 ppb. However, when normalized for surface area, sample mass, proportion of sulphide phases, and seawater volume, sample DE-02 released the highest amount of Cu, with a maximum of 26.7 ± 1.8 μmol/m^2, likely due to the greater proportion of chalcopyrite and Cu relative to the other sulphide samples (Table 6.1). In addition, sample DE-02 is the only sample that exhibited a constant oxidation rate ($R^2 > 0.91$) after initial rapid leaching (at approximately 20 hours) at a rate of 0.065 μg/hour (3.19×10^{-6} % loss of Cu per hour).

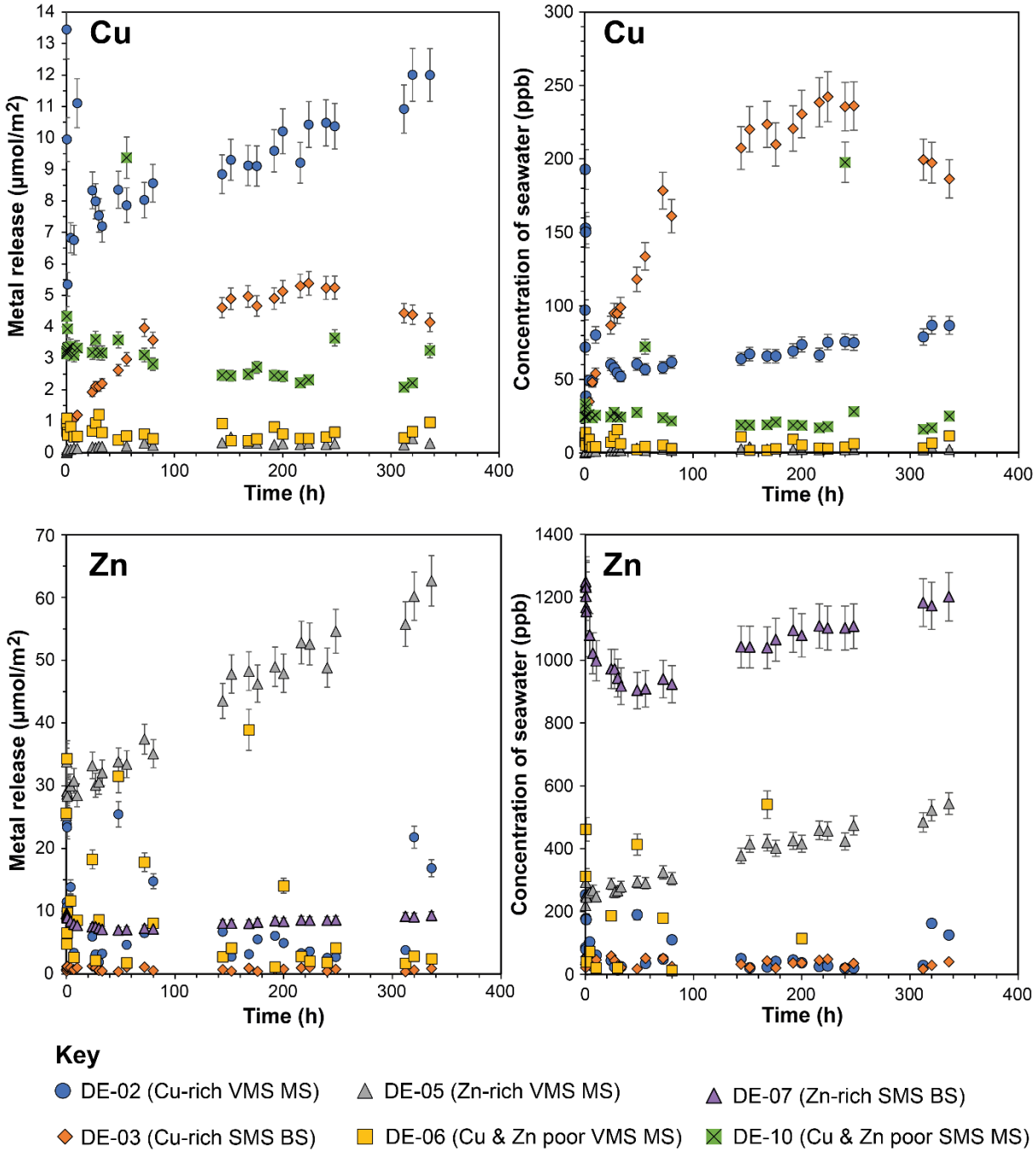

Figure 6.3. Cu (top) and Zn (bottom) release in µmol/m² (left) and ppb (right). Concentrations have been corrected for the initial metal concentration of seawater. Error bars represent the %RSD of the CRM with a concentration most similar to that of the samples. VMS – sample from a volcanogenic massive sulphide deposit. SMS – sample from a seafloor massive sulphide deposit. BS – black smoker chimney material. MS – massive sulphide sample. Full details found on Appendix D.3.

Zinc shows three different chemical trends including: (1) Initial rapid release of Zn and subsequent drop in concentration, followed by a continuous increase throughout the rest of the experiment (DE-05 and DE-07); (2) Initial leach of metals followed by a generally chaotic trend (DE-02 and DE-03) and; (3) Similar to (2) but with large outliers with considerably high release of metals (e.g., 302 ± 4 μmol/m^2; DE-06; Figure 6.3). Using linear chemical trends (R^2 >0.92) fitted to the data observed for DE-05 and DE-07 after 24 hours, calculated oxidation rates are at approximately 0.60 and 0.62 μg/hour respectively. Sample DE-07 released the most Zn into seawater according to its absolute concentration, reaching 1249 ± 80 ppb. However, normalised values show that sample DE-05 released the highest amount, with a maximum of 302 ± 25 μmol/m^2.

While Fe exhibits poor accuracy and precision, spikes in concentrations may still be used as indicators for significant metal release into, or depletion from, seawater. Typically, poor accuracy and precision are reflected by generally chaotic patterns of iron in seawater (Appendix D.2).

6.3.2.1 Toxic trace metals (As-Sb-Cd-Pb)

Arsenic displays three types of chemical trends including: (1) Rapid initial leaching with subsequent decrease, followed by a continuous increase in the metal concentration (DE-02); (2) Rapid leaching followed by flattening of As (DE-05, DE-06 and DE-07) and; (3) Flat trend (DE-03; Figure 6.4).

For Sb, four of the sulphide samples show values above the limit of detection (LOD) during the experiment. All four sulphides exhibit different geochemical trends including: (1) Initial rapid leaching followed by flattening of the trend (DE-05); (2) Initial rapid leaching followed by depletion and continuous release throughout the experiment (DE-02); (3) Initial rapid leaching followed by slowing increase throughout the experiment (DE-06) and; (4) Flat trend (DE-03; Figure 6.4).

Cadmium leaching with concentrations above the LOD is detected for five sulphide samples and exhibit four geochemical trends including: (1) Initial rapid leaching followed by continual release (DE-05 and DE-07); (2) Initial rapid leaching followed by depletion and a flat trend (DE-02); (3) Chaotic trend (DE-03) and; (4) Flat trend (DE-06; Figure 6.4). Samples DE-05 and DE-07 exhibit continuous metal release trends similar to Zn, with DE-05 showing a greater release of Cd and Zn into the seawater than DE-07 (Figure 6.3 and Figure 6.4).

For Pb, four sulphide leaching experiments showed trends with concentrations above the LOD and exhibit three geochemical trends including: (1) Initial rapid release of Pb followed by a slow

flattening of the trend (DE-05); (2) Initial rapid leach followed by considerable depletion and slow subsequent decrease (DE-02 and DE-06) and; (3) Flat trend (DE-03; Figure 6.4).

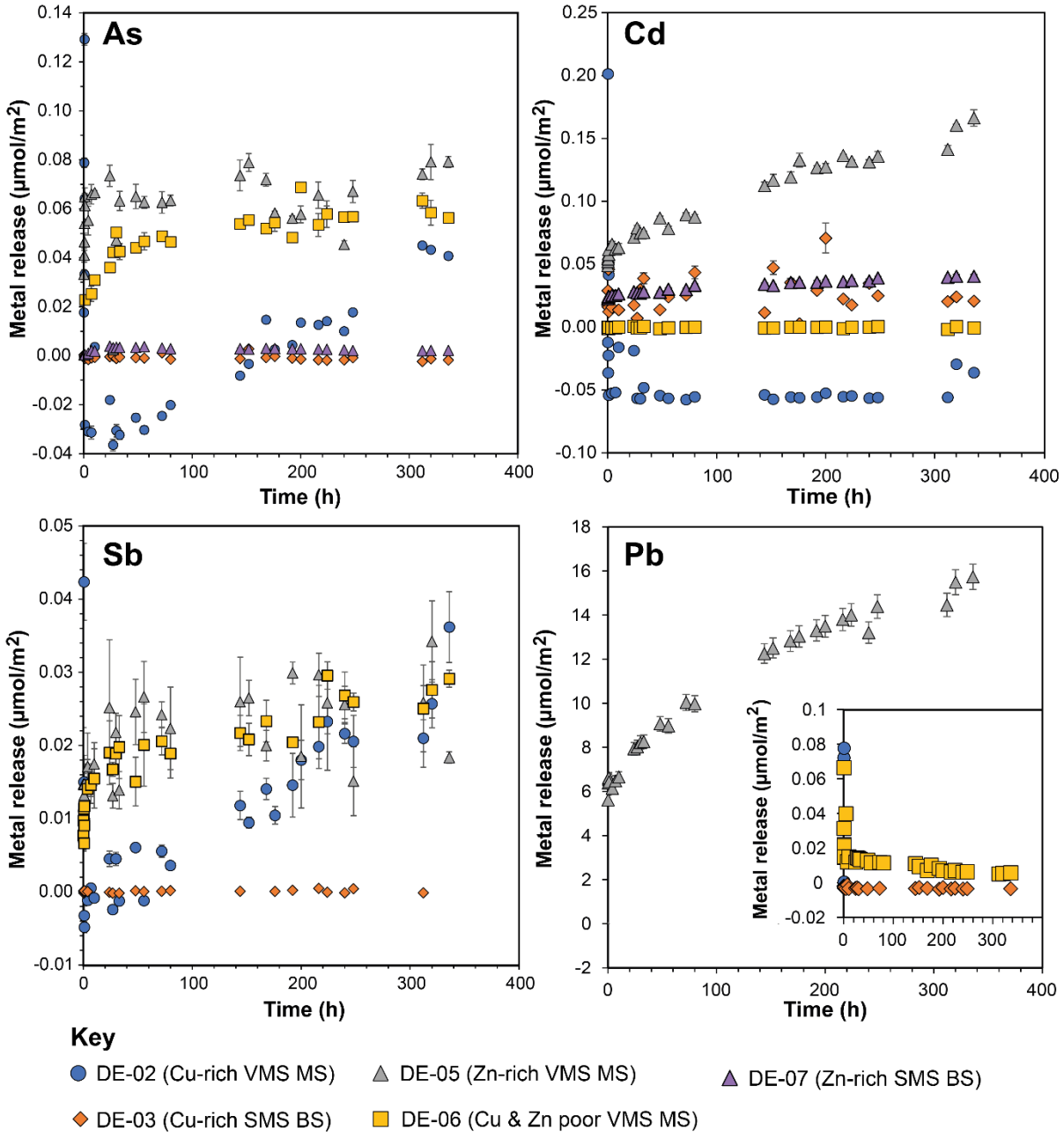

Figure 6.4. Trace metals leached over time for all samples with results above the limit of detection. Concentrations have been corrected for initial seawater concentration. Error bars for As, Cd and Sb are based on the %RSD of sample measurements. Error bars for Pb represent the %RSD of the CRM with a concentration most similar to that of the samples (Bishop et al., 2025c). VMS – sample from a volcanogenic massive sulphide deposit. SMS – sample from a seafloor massive sulphide deposit. BS – black smoker chimney material. MS – massive sulphide sample. Full details found on Appendix D.3.

6.3.3 Morphology of oxidised sulphide particulates

Upon completion of the oxidative dissolution experiments, the surfaces of reacted sulphide grains were again analysed by SEM-EDS. On all samples, with the exception of DE-03, the presence of FeOOH or hydrous ferric oxides was observed (HFOs; Figure 6.5). Reflective microscopy and XRD measurements confirmed the absence of FeOOH in the cleaned sulphide powders before our experiments, indicating that all Fe-oxide (FeOOH and HFO) precipitated during the experiments. Typically, Fe-oxide minerals are observed covering sulphide crystals (e.g., Figure 6.5D) or within aggregates of sulphide crystals (Figure 6.5A) and only one occurrence of FeOOH is observed as a grain (Figure 6.5E). The metal content of Cu and Zn within Fe-oxide is associated with the sulphide adjacent to or covering it, for example, in Figure 6.5A, Fe-oxide occurring within and around grains of chalcopyrite contain Cu concentrations between 2.80-5.30 wt.%. Similarly, Fe-oxide on sphalerite grains (Figure 6.5B) contain Zn concentrations of approximately 13 wt.%. However, when Fe-oxide occurs together with pyrite grains (i.e., Figure 6.5C, Figure 6.5D; Figure 6.5F), the Fe-oxides typically contain increased quantities of Zn or Cu relative to the pyrite grains that are depleted in these metals (Bishop et al., 2025c).

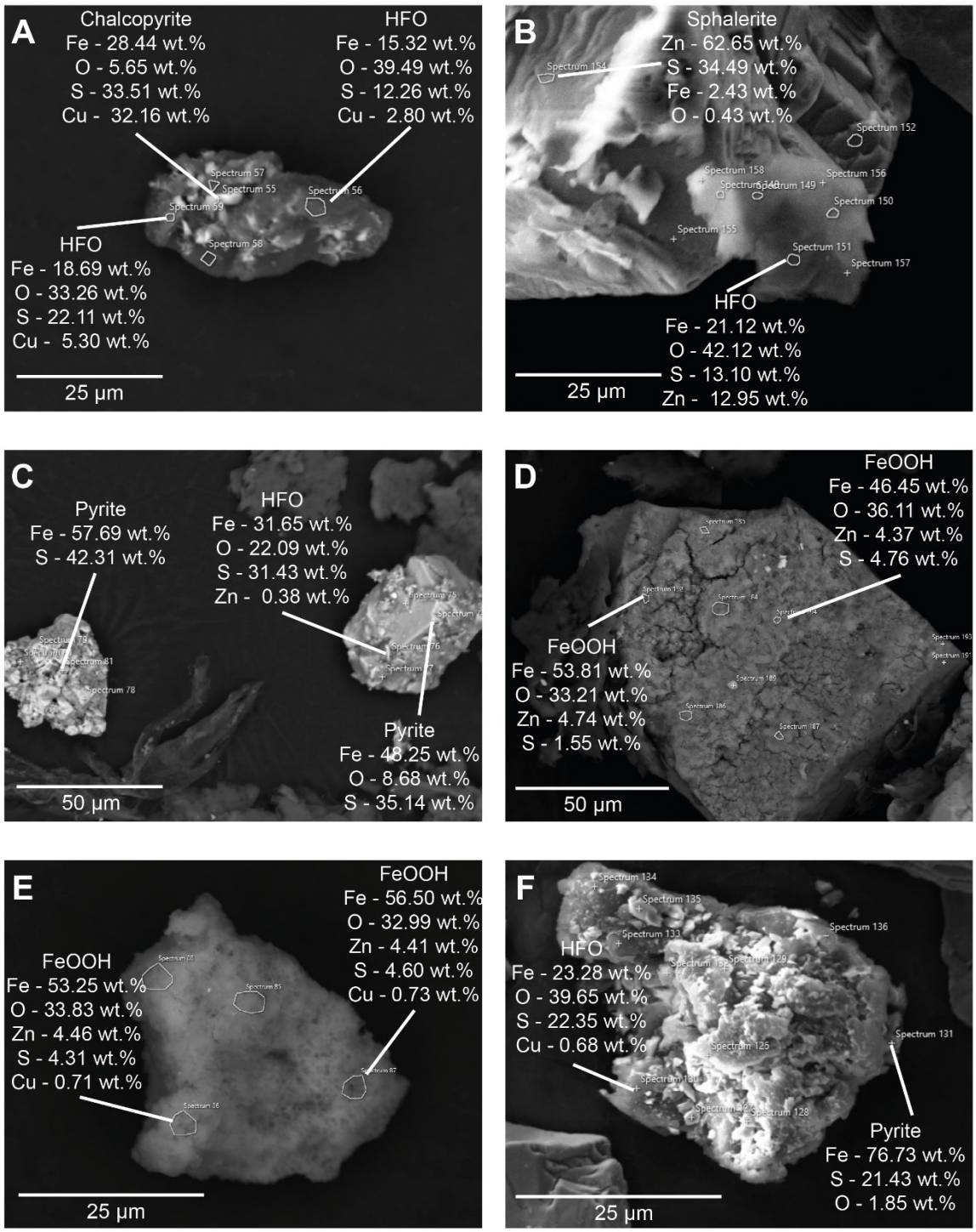

Figure 6.5. Semi-quantitative SEM-EDS images of sulphide material proceeding experiment. (A) Chalcopyrite and oxidation product comprising of hydrous ferric oxides (HFO) containing Cu between 2.80-5.30 wt.% (DE-02). (B) Sphalerite crystal with some coating of HFOs comprising of approximately 12.95 wt.% Zn (DE-05). (C) Aggregate of pyrite crystals with HFO in areas coating sulphide with approximately 0.38 wt.% Zn (DE-06). (D) FeOOH coating on probable pyrite crystal. FeOOH product contains approximately 4.50 wt.% Zn. (DE-07). (E) Singular grain of FeOOH containing both Zn and Cu at approximately 4.43 and 0.72 wt.% respectively (DE-07).

6.4 Discussion

6.4.1 Mineralogical influences on the reaction kinetics of sulphide oxidation

The sulphide samples used in this study have varying concentrations of Cu (0.43-16.65 wt.%) and Zn (0.01-10.89 wt.%; Table 6.1). If the metal concentration in the sulphide samples would be main driver for the release of Cu and Zn (e.g., Hu et al., 2023), then highest release rates would be expected from DE-02 and DE-05 (Table 6.1). However, a comparison of both median and average dissolved Cu and Zn concentrations in the synthetic seawater exhibit poor correlations with the bulk sample concentration (R^2 = 0.43-0.52 for Cu; R^2 = 0.26-0.36 for Zn; Appendix D.4 and Appendix D.5), indicating that other factors might be more important for metal release into seawater. A known key factor that can influence oxidation is the sample surface area (Fallon et al., 2018; Fuchida et al., 2018). In this study black smoker hydrothermal chimneys (i.e., DE-03 and DE-07), have an order of magnitude higher surface area at 0.256-0.726 m^2/g relative to massive sulphide samples (e.g., DE-10) at 0.041-0.099 m^2/g. Even after grinding the sulphide to the 38–100 µm size fraction, black smoker material retains abundant fine grains, intergranular porosity and colloform textures that multiply reactive surfaces, which are common in black smoker hydrothermal chimneys (Wang et al., 2022). By contrast, massive sulphide powders originate from coarser, non-porous subhedral to euhedral grains, yielding fewer micro-crevices and grain boundaries. Because our grinding protocol necessarily narrows the natural size distribution, the true surface-area contrast in unprocessed chimney versus massive sulphide samples would be even more pronounced than these powdered measurements indicate.

To investigate how surface area impacts the release of metals into seawater, the absolute concentration of metals in seawater (ppb) is normalised by the sulphide surface area to calculate $\mu mol/m^2$ (See section 6.2.4.1; Bishop et al., 2025c). Effectively, this removes the impact surface area has on the release of metals during oxidation. Here, the bulk Cu concentration in the sulphide samples exhibit a strong positive correlation (R^2 = 0.76-0.82; Appendix D.4) with both the average and median Cu release ($\mu mol/m^2$). Similarly, the bulk Zn concentration across the sulphide samples exhibit a strong correlation with the median Zn release (R^2 = 0.82; Appendix D.5). While bulk Zn concentration shows a weak correlation with average Zn release (R^2 = 0.29), this relationship is influenced by sample DE-06, which has low bulk Zn content (0.01 wt.%) but exhibits episodically elevated Zn concentrations in seawater. These high values disproportionately affect the mean, resulting in a weaker correlation compared to that observed using median Zn release. The weak correlations between bulk sulphide metal concentrations (Cu and Zn) and dissolved concentrations in seawater (R^2 = 0.26-0.52) demonstrate that bulk metal

content alone does not control metal release rates. However, when metal release is normalised by surface area (μmol/m^2), strong correlations emerge with bulk concentrations (R^2 = 0.76-0.82 for Cu, R^2 = 0.82 for median Zn), indicating that surface area is the dominant control on oxidation kinetics.

While increasing the reactive surface area has been previously shown to increase sulphide oxidation and thus metal release (Gwyther, 2008; Fallon et al., 2018), we demonstrate that surface area is linked to the morphology of the bulk sulphide sample. In particular, black smoker hydrothermal chimneys found at the surface of SMS mounds likely represent the most reactive sulphide morphologies due to their high surface area relative to massive sulphide morphologies, typically found within SMS mounds. The high reactivity of surface black smoker sulphide in SMS deposits means seafloor mining could rapidly release metals into the marine environment, causing toxicity to local fauna and economic losses as metals oxidise.

6.4.2 Fe-oxide precipitation, implications to metal release

Iron-oxide commonly forms as weathering products during the oxidative dissolution of sulphide minerals and have been shown to contain metals of economic interest such as Cu and Zn (Dekov et al., 2011; Fallon et al., 2017; Hu et al., 2022; Maslennikov et al., 2023). As no Fe-oxide were found before the experiment, Fe-oxide formation observed by SEM-EDS (Figure 6.5) after the experiment formed directly as a result of sulphide oxidation. In most instances, Fe-oxide forms as a coating on sulphide grains, with one instance of Fe-oxide encapsulating a sulphide grain (Figure 6.5D) or forming as an isolated grain indicating complete sulphide oxidation (Figure 6.5E). Our SEM-EDS analysis shows that Fe-oxide formed during sulphide oxidation contains Zn (0.38–12.95 wt.%) and Cu (0.68–5.30 wt.%; Figure 6.5), extending previous studies that demonstrated only Zn uptake (Hu et al., 2023) and confirming predictions by Fallon et al. (2018) and Knight et al. (2018).

When Fe-oxide forms as a product of sphalerite (Figure 6.5B) or chalcopyrite (Figure 6.5A) oxidation, Zn and Cu concentrations in Fe-oxide are approximately 80-90% lower than in their sulphide protoliths (e.g., chalcopyrite with 32.16 wt.% Cu is coated by Fe-oxide containing 2.80-5.30 wt.% Cu). This partial metal uptake indicates that Fe-oxide formation does not fully balance metal release, and together with the observed increase of Cu and Zn concentrations in seawater (Figure 6.3), indicates that Fe-oxide formation retains only a minority of metals released during initial sulphide oxidation (Fallon et al., 2018).

However, the temporal trends show that dissolved Cu concentration in sample DE-03 begins to decrease after ~230 hours, while Cu concentrations in samples DE-02 and DE-05 and Zn concentrations in samples DE-05 and DE-07 decline following their initial rapid increase (Figure

6.3). This time-series decline in dissolved metals is consistent with previous studies by Fallon et al. (2018) and Knight et al. (2018), predicting this to be the result of Cu and Zn adsorption from solution onto Fe-oxide. The temporal decrease in dissolved Cu and Zn concentrations in our experiments, concurrent with continued Fe-oxide formation, suggests that the rate of metal sequestration into Fe-oxides can exceed the rate of net metal release to solution, creating self-limiting oxidation systems. This effect likely results from Fe-oxide formation both adsorbing dissolved metals and physically impeding sulphide oxidation by reducing contact between sulphide surfaces and seawater (Knight et al., 2018).

Notably, Fe-oxides precipitated on pyrite grains (Figure 6.5C and Figure 6.5F) contain Zn (~0.38 wt.%) and Cu (~0.68 wt.%), despite the pyrite protolith lacking these metals. This demonstrates aqueous adsorption of metals from solution, as any Cu and Zn leached from neighbouring chalcopyrite or sphalerite can diffuse and adsorb onto Fe-oxide surfaces regardless of their original source location. Thus, Fe-oxide might also be able to trap metals originating from sulphide phases that are not in direct contact with the Fe-oxide, highlighting the broader role of Fe-oxide as metal sinks.

This study provides a semi-quantitative assessment of both Cu and Zn concentrations in Fe-oxides formed during seafloor sulphide oxidation experiments, demonstrating that these phases can simultaneously adsorb multiple metals through both direct incorporation during sulphide oxidation and subsequent aqueous adsorption from seawater. The temporal decrease in dissolved Cu and Zn concentrations, coupled with Fe-oxide formation, suggests that metal sequestration into Fe-oxide phases can exceed net release rates, creating self-limiting oxidation systems. The implication of this is that natural Fe-oxide formation may mitigate metal release into the surrounding marine environment while retaining the metal content, reducing economic losses caused by sulphide oxidation that would otherwise be lost to seawater.

6.4.3 Oxidation kinetics and metal-specific release patterns

Understanding how sulphide oxidation varies over time is important to determine the potential geochemical impacts of seafloor mining. Similar to previous studies (Benjamin & Leckie, 1981; Knight et al., 2018), sulphide oxidation rates were not constant over time. Temporal trends typically followed one of two patterns: (1) initial metal release followed by concentration decline (e.g., Cu in DE-03 after ~230 hours, DE-10 after ~1 hour), attributed to Fe-oxide precipitation and metal sequestration, or (2) rapid initial release followed by stabilisation (e.g., As in DE-05 after ~33 hours, Cd in DE-02 after ~1 hour), suggesting equilibrium between metal release and sequestration onto Fe-oxides or minimal sulphide oxidation.

However, samples DE-02 (Cu-rich massive sulphide, 16.65 wt.% Cu, 0.041 m^2/g), DE-05 (Zn-rich massive sulphide, 10.89 wt.% Zn, 0.067 m^2/g), and DE-07 (Zn-rich black smoker material, 5.62 wt.% Zn, 0.73 m^2/g) exhibited sustained, near-linear release rates for almost the entire two-week experimental period. Linear extrapolation of these sustained rates, while simplified (assuming constant oxidation, uniform metal content and surface area), provides an approximate framework for long-term metal release. Using observed oxidation rates of 0.065 ± 0.031 μg/h for Cu in DE-02, complete Cu release would require approximately 225-450 years. For Zn, using rates of 0.851 ± 0.390 μg/h (DE-05) and 0.89 ± 0.407 μg/h (DE-07), complete release would require 29-78 years (DE-05) and 7-19 years (DE-07). The two-fold difference in the complete loss of Zn between DE-05 and DE-07, despite similar Zn concentrations, likely reflects morphological control where black smoker material exhibits considerably higher surface area.

Complete Cu loss is approximately an order of magnitude longer than Zn release. While increased Zn loss could be partially attributed to surface area, we suggest that galvanic interactions between different sulphide minerals could explain both the preferential Zn release and the sustained linear oxidation rates observed in some samples (i.e., DE-02, DE-05, DE-07). Sphalerite has a lower rest potential (0.46 V) than chalcopyrite (0.56 V; Majima, 1969), indicating sphalerite would be galvanically oxidised preferentially in mixed sulphide assemblages, leading to enhanced Zn release relative to Cu. Additionally, the extensive mineral intergrowths and contacts between different sulphide phases (Figure 6.2; Bishop et al., 2025c) may facilitate continuous galvanic coupling that could result in linear oxidation rates despite Fe-oxide formation that would otherwise cause rate decline. Whilst galvanic interactions are likely to influence the oxidation rates observed in this study, due to numerous inseparable variables (e.g., varying mineralogy, sulphide textures and FeOOH precipitation), the importance of galvanic interactions for metal release was difficult to quantify

This study extends beyond shorter-term investigations (e.g., Knight et al., 2018; Fallon et al., 2018; Hu et al., 2023) and demonstrates that most polymineralic sulphide samples reach oxidation equilibrium or self-limiting behaviour within two weeks in oxygenated seawater due to Fe-oxide formation. However, samples, possibly due to galvanic interactions may have linear oxidation rates beyond this timeframe. The observed oxidation kinetics have direct implications for both environmental impact assessments and economic viability calculations in seafloor mining operations, as they determine the extent and rate of metal loss to seawater.

6.4.4 Implications for the mining of SMS deposits

6.4.4.1 Economic

Oxidation and the release of metals within stockpiled sulphide ore or during transport within the riser may lead to economic losses. In this study, we evaluate two scenarios: first, metal loss during riser transport; and second, metal loss during seafloor stockpiling.

To estimate economic loss during slurry-riser transport, we use pilot data after Ishiguro et al. (2018): 16 t of ore lifted in 23 minutes, with a 7-minute ascent from the seafloor. By extrapolating our oxidation rates, this yields annual losses of ~0.9–1.8 kg Cu and ~6.8–27.7 kg Zn per riser, equating to a loss of <0.1% Cu and Zn during transport (Appendix D.6). As such, the annual metal loss expected during transport in the slurry riser is likely minimal. If stockpiling sulphide ore on the seafloor becomes necessary during mining, the contact of fresh sulphide with oxygenated seawater will be continuous and over longer times, possibly resulting a higher loss of economic metals. For this scenario, assuming a worst-case scenario with grain sizes and surface areas similar to our experimental sulphide mix, stockpiling 1,000 t of ore could lead to a loss of 180-370 kg of Cu and 1,400-4,000 kg of Zn annually. Translating to an annual loss of 0.1–0.2% Cu for Cu-rich (16.65 wt.%) massive sulphide (DE-02), 1.3–3.5% of Zn loss in Zn-rich (10.89 wt.%) massive sulphide (DE-05), and 2.6–7.1% of Zn in Zn-rich (5.62 wt.%) black smoker chimney material (DE-07). Black smoker chimney material (DE-07) releases Zn at nearly twice the rate of massive sulphides despite lower Zn content, implying greater economic loss from black smoker chimney material. The amount of Cu loss equates to an annual monetary loss of approximately US$1900-3800 with the amount of Zn loss between US$4500-12700 per 1,000 tonnes of stockpiled ore annually (Trading Economics, 2024; Appendix D.7). These estimates represent maximum potential losses, since our experiments use 38–100 μm powders, whereas real-world ore fragments (~30 mm; Ishiguro et al., 2018) have lower reactive surface area and will oxidise more slowly.

Considering the net present value of Solwara 1 (~US$56 million; Lipton et al., 2018) the metal loss from oxidation in the slurry riser or within stockpiles is not economically considerable. However, the morphology-dependent nature of these losses creates opportunities for optimisation through strategic mining approaches. Prioritising extraction of high-surface-area chimney materials early in mining operations would minimise their exposure time to seawater, while massive sulphides could be stockpiled with lower economic risk. Additionally, the self-limiting oxidation behaviour driven by Fe-oxide formation, coupled with the non-constant oxidation rates observed in most samples, suggests that long-term stockpiling losses are likely to be lower than linear extrapolations indicate.

The morphological controls of metal release during oxidation identified in this study could be used as "weathering factor" to improve resource recovery predictions. Areas dominated by black smoker chimney structures should be assigned higher oxidation risk factors in economic block models, while massive sulphide zones can be modelled with lower anticipated losses (Lesage et al., 2018). This morphology-informed approach could reduce overall metal losses by integrating spatial heterogeneity of sulphide textures into mine planning and extraction sequencing.

In summary, while absolute economic losses from sulphide oxidation during SMS mining are relatively small compared to predicted project values, the morphology-dependent nature of these losses provides a framework for economic optimisation. Understanding the spatial distribution of sulphide morphologies within deposits enables improved resource modelling, optimised stockpile management, and enhanced mine planning that can minimise oxidation-related economic impacts while maximising resource recovery efficiency.

6.4.4.2 Environmental

Dissolved metals, which are released through oxidative dissolution, are likely more bioavailable than the sulphide phases themselves, and thus, may pose a toxicity risk (Simpson & Spadaro, 2016). While fauna at active SMS deposits often are adapted to metal-rich conditions (Simpson et al., 2007; Gwyther, 2008), mining at extinct SMS deposits may expose local fauna to hazardous metal concentrations. We use the Australian and New Zealand Guidelines (ANZG) for shallow coastal environments to benchmark metal concentrations, as specific seawater toxicology standards for extinct SMS deposits are unavailable. Although the design of our experiments is not directly applicable to real-world scenarios, the average concentration of metals in seawater likely represents longer-term exposure, justifying its use in our study. All samples leached in this experiment generate leachate that exceed the ANZG for 95% fauna protection for Cu (0.4 µg/L) and Zn (8 µg/L; ANZG, 218; ANG, 2023). Moreover, compared to massive sulphide samples, black smoker hydrothermal chimney samples, due to their greater surface area, release the highest amounts of metals into the seawater, averaging 96 µg/L for Cu (DE-03) and 751 µg/L for Zn (DE-07). Potentially toxic trace metals such as As, Cd, Sb, and Pb fell below ANZG guidelines except for one experiment (DE-05), where Pb was measured at an average of 198 µg/L relative to the ANZG guidelines at 4.4 µg/L. SMS deposits from other tectonic settings, such as rifted arcs, have been reported to contain higher bulk concentrations of As, Cd, Sb and Pb than MOR-hosted SMS deposits, including the MOR-hosted SMS samples examined in this study (Monecke et al., 2016). Thus, while toxic trace metals (As, Sb, Cd and Pb) of this study are unlikely to exceed ANZG guidelines, this may not be the case for SMS deposits within other tectonic settings. It should be emphasised that these results are influenced by both the mass and exposed surface area of

sulphide particles, both these factors will differ in full-scale operations with exposed surface area driving oxidation and subsequent metal release.

Our two-week experiments reveal that most sulphide particles lose their reactivity within this period: either oxidation tapers off or Fe-oxide formation outpaces metal release. Consequently, even if particles remain suspended for days to months in mining plumes (Fallon et al., 2018; Morato et al., 2022), they may not continue to liberate metals at high rates. Seawater dilution and ongoing Fe-oxide precipitation would further drive Cu and Zn levels toward or below guideline thresholds (ANZG, 2018, 2023; Gwyther et al., 2008). However, even when dissolved metal concentrations remain below guideline thresholds, local fauna may still be harmed by increased sedimentation and the physical scour of fine particles from mining plumes (Morato et al., 2022). Furthermore, samples DE-03 (Cu) and DE-05/DE-07 (Zn) exhibit sustained oxidation beyond two weeks, indicating that under certain mineralogies and morphologies, suspended sulphides could continually leach metals while elevating local sediment loads, both of which pose additional risks to seafloor communities (Boschen et al., 2013; Carreiro-Silva et al., 2022).

In summary, while our results indicate that oxidative sulphide dissolution can initially elevate metal concentrations in seawater above ANZG guideline limits, natural processes are likely to reduce these concentrations over time. Seawater dilution will dilute released metals, while Fe-oxide formation both impedes further sulphide oxidation and sequestering metals that are released from sulphide oxidation. Nevertheless, localised toxicity, particularly under stagnant conditions (e.g., within ore stockpiles) and increased local sedimentation rates (Morato et al., 2022), remains a concern. Moreover, the variability in metal release observed across samples highlights the importance of accounting for differences in sulphide morphology (i.e., black smoker hydrothermal chimney and massive sulphide), ore grade and Fe-oxide formation in future environmental impact assessments for deep-sea mining. Currently, toxicology guidelines for deep sea, extinct SMS deposits do not exist and without them we are unable to conclusively determine the environmental impacts of mining SMS deposits at the seafloor.

6.5 Summary and conclusions

Our study demonstrates that sulphide morphology and reactive surface area drive oxidation kinetics. Black smoker hydrothermal chimney material, with its finer grains and higher porosity, exhibits considerably greater surface area than massive sulphide morphologies, leading to enhanced leaching of Cu and Zn, even when massive sulphide contains higher bulk metal concentrations. Consequently, metal release is most pronounced at SMS surfaces dominated by black smoker hydrothermal chimney material. We propose incorporating this behaviour as a "weathering factor" to be integrated into future economic block models for SMS deposits,

thereby improving predictions of resource recovery (Lesage et al., 2018). Moreover, our data indicate that economic metal losses during ore stockpiling or slurry riser transport are minimal relative to overall deposit value.

The concentration of dissolved Cu, Zn (and one occurrence of Pb) exceeds the ANZG shallow-water regulatory thresholds. Although our experiments are not applicable to real world scenarios, our data suggests that this may form localised toxicity in stagnant areas. However, this will likely be diluted by fresh seawater. While toxic trace metals such as As, Sb, and Cd remain below ANZG guideline limits, our MOR-derived samples are relatively depleted compared to those from other tectonic settings (e.g., arc rift settings), emphasising the need for site-specific risk assessments tailored to local geochemical conditions (Monecke et al., 2016).

A critical aspect of our study is the role of Fe-oxide precipitation in influencing metal release. Our experiments show that the majority of sulphide samples effectively cease oxidation within two weeks due to Fe-oxide formation that can mitigate further sulphide oxidation and adsorb Cu and Zn from seawater. This suggests that sulphide particles in suspension for extended periods of time may not continuously release their contained metals, thereby reducing long-term ecological risks of mining plumes (Van Dover, 2011; Weaver et al., 2018). Nevertheless, increased sedimentation from these plumes may still impact background fauna (Boschen et al., 2013; Carreiro-Silva et al., 2022).

In summary, our work advances the understanding of SMS oxidation by demonstrating that ore morphology, reactive surface area, and Fe-oxide formation are critical determinants of metal release (Figure 6.6). These insights should be integrated into future environmental impact assessments to enhance sustainable deep-sea mining practices. We advocate for monitored pilot studies to refine these parameters and for the development of toxicology guidelines tailored to deep-sea, extinct hydrothermal systems, ensuring that environmental impacts are accurately addressed in regulatory frameworks.

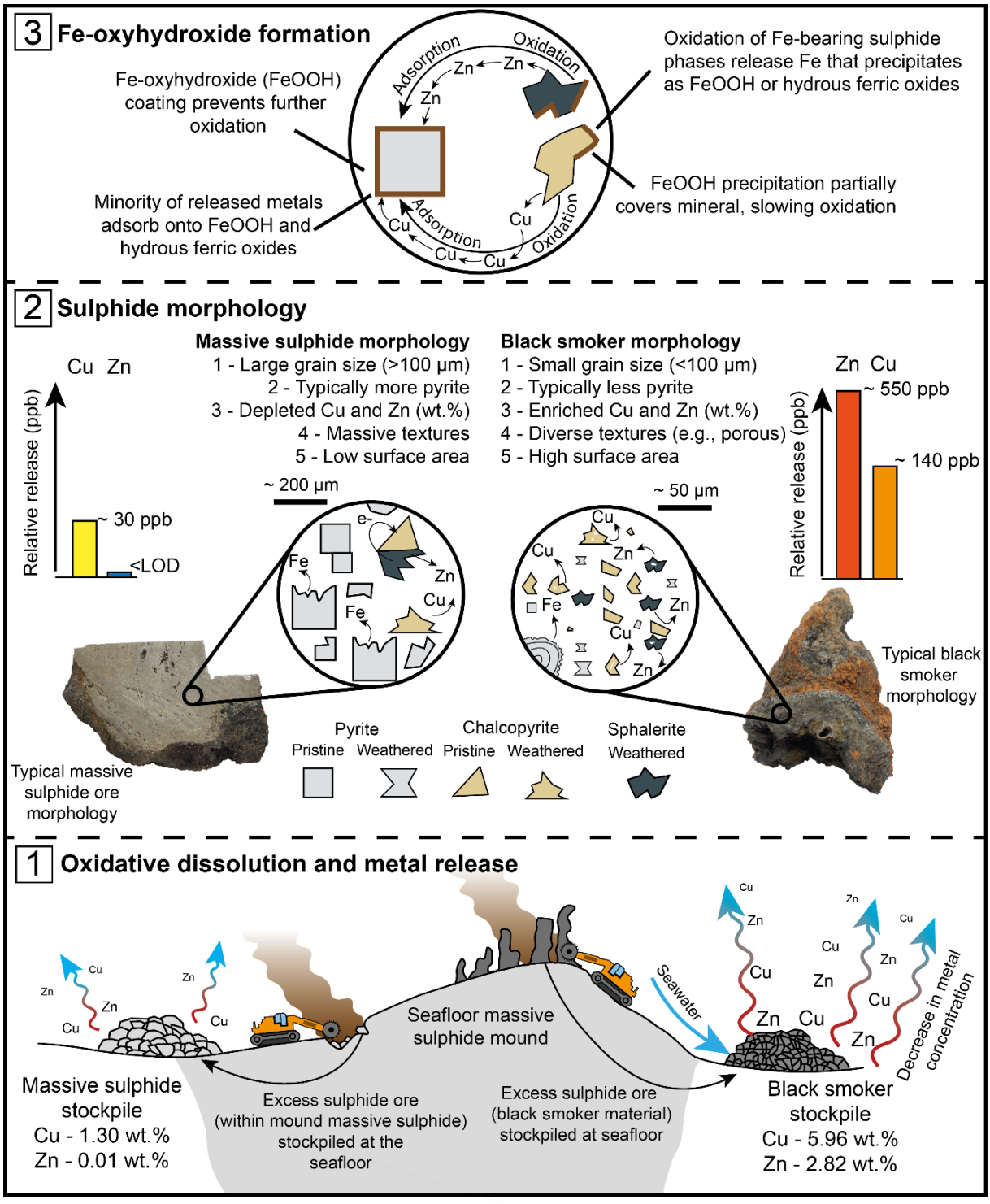

Figure 6.6. Schematic summary of the study. (1) Oxidative dissolution of massive sulphide ore typically found in the mound of SMS deposits (i.e., DE-10) are relatively depleted in Cu and Zn when compared with black smoker hydrothermal chimney material. The amount of Cu and Zn released is lower in these massive sulphide samples relative to black smoker hydrothermal chimney material and require less dilution for the concentration of Cu and Zn to fall below ANZG guidelines. (2) The morphology and mineralogy of sulphide ore impacts the release of metals. In this study, massive

sulphide ore typically has a larger grain size, increased pyrite content, depleted Cu and Zn and lower surface area relative to black smoker material. Combined, this results in massive sulphide ore to release less Cu and Zn relative to black smoker material. (3) The precipitation of Fe-oxide typically form on the sulphide rims assumed to be the protolith. Here, they trap metals (i.e., Cu and Zn) released from oxidation, generally from the sulphide protolith. However, Fe-oxide also trap metals released from the oxidation of neighbouring sulphide particles, mitigating the release of these metals in the surrounding marine environment.

Chapter 7 Discussion

Following the years since their discovery, SMS deposits have attracted commercial interest owing to their rich content of base metals (i.e., Cu and Zn) and precious metals (i.e., Au and Ag), and future resource potential (Lonsdale, 1977; Francheteau et al., 1979; Hannington et al., 2010; Hannington et al., 2011; Juliani & Ellefmo, 2018). However, sulphides exposed at the seafloor are subject to oxidation and alteration by oxygenated seawater, transforming into secondary minerals like FeOOH and (par)atacamite (Hannington, 1993; Fallon et al., 2018; Knight et al., 2018; Hu et al., 2023). Understanding these weathering pathways is critical, both for assessing whether economic metals released from sulphide oxidation are sequestered in solid alteration products or are lost to seawater. Understanding whether sulphide weathering products can retain economic metals is critical to evaluate whether larger, off-axis extinct systems, that have experienced prolonged exposure to seawater, could potentially retain economic quantities of metals or are barren. Complicating this picture, FeOOH may also form as metal-poor primary precipitates directly from low-temperature (<~100°C), iron-rich hydrothermal fluids (Alt 1988; Hekinian et al. 1993; Gini et al. 2024). Although earlier work demonstrates that secondary FeOOH can retain metals otherwise lost to seawater during sulphide oxidation (e.g., Herzig et al., 1991; Hannington, 1993; Melekestseva et al., 2020; Hu et al., 2022; Maslennikov et al., 2022; Hou et al., 2024), key questions remain:

1. How can the mineralogical and textural morphologies of FeOOH deposits at hydrothermal fields, such as Semenov, be used to distinguish variations in metal content, and how does the metal content of secondary FeOOH vary across Semenov hydrothermal field?
2. What are the mechanisms governing the mobilisation, redistribution and retention of Cu, Zn, Au and Ag during sulphide oxidation, and how do post-formational modifications alter the composition of secondary FeOOH over time?
3. What are the kinetics and timescales of sulphide oxidation, how does secondary FeOOH formation impact sulphide oxidation rates, and how do these interactions dictate the fate of metals at SMS systems?
4. Can secondary FeOOH and atacamite serve as additional resources or exploration vectors for critical/strategic metals in SMS deposits?

This chapter constructs a three-part narrative, from formation of sulphide weathering products and their geochemical evolution to fate and economic implications. Section 7.1 traces the geochemical evolution of secondary FeOOH, from its initial formation through post-formational modification, to its long-term fate. Section 7.2 assesses whether FeOOH deposits and atacamite

could represent viable resources. Finally, section 7.3 considers whether secondary FeOOH and atacamite can serve as effective exploration vectors for SMS deposits.

7.1 Discussion on the geochemical evolution of secondary FeOOH at Semenov hydrothermal field

Here, I provide an extended geochemical evolution of secondary FeOOH, from its initial precipitation during sulphide oxidation, to its ultimate fate, based on mineralogical, geochemical, isotopic and experimental analyses performed for this thesis combined with previous knowledge.

7.1.1 Formation of secondary FeOOH

During laboratory experiments the oxidation of mixed sulphide assemblages was tested, to simulate oxidative dissolution of sulphide at the seafloor. In these experiments exclusively secondary FeOOH coatings were produced and the presence of Fe–Mn oxyhydroxides or atacamite was not detected (Chapter 6). This secondary FeOOH nucleates directly on pyrite, chalcopyrite, and sphalerite grains, forming thin laminar films and, in some cases, fully encrusting angular sulphide fragments (Figure 6.5). An isolated FeOOH fragment suggests complete sulphide oxidation under marine conditions (Maslennikov et al., 2022; Hou et al., 2024). Petrographic studies in Chapter 5 show that secondary FeOOH can form ten types of morphologies that are observed in this thesis, that range from light grey to bluish-grey, porous to non-porous with textures including dendritic, tabular, framboidal and massive (Appendix C.2; Figure 5.1). The different morphologies of secondary FeOOH are inherited from the sulphide protolith (e.g., framboidal pyrite, colloform pyrite, massive chalcopyrite; Figure 5.2).

7.1.1.1 Mobilisation of Cu and Zn during sulphide oxidation

In Chapter 6, I describe how coatings of secondary FeOOH on sphalerite (ZnS) can contain high contents of Zn at 0.4–13 wt.%, while chalcopyrite derived FeOOH (ccp-FeOOH) on grains of chalcopyrite ($CuFeS_2$) carries highest Cu content at 0.7–5.3 wt.%; in contrast, pyrite derived FeOOH (py-FeOOH) on pyrite (FeS_2) is depleted in both Cu (0.68 wt.%) and Zn (0.38 wt.%), suggesting the absence of both these metals from the pyrite protolith. As such, the Cu and Zn content of initially formed secondary FeOOH is primarily inherited from the sulphide protolith. Supporting this, in Chapter 5, LA-ICP-MS analyses show that both pyrite and py-FeOOH are enriched in As and Fe, but depleted in Cu relative to chalcopyrite and ccp-FeOOH respectively. The capacity of FeOOH to adsorb metals in aqueous systems is due to their large specific surface area, resulting in effective scavenging of elements by FeOOH (Cornell and Schwertmann, 2003).

However, geochemical profiles of cumulative Cu release measured during the oxidative dissolution experiments in Chapter 6 (Figure 6.3) show that secondary FeOOH sequestered only ~23% of the Cu released over the course of the experiment; the remaining ~77% escaped to the surrounding seawater. A similar pattern is observed for Zn, where the majority of released Zn is also found in seawater solution (Figure 6.3), indicating that nascent FeOOH capture is limited under our experiments.

7.1.1.2 Mobilisation of Au and Ag during sulphide oxidation

Where FeOOH traps Cu and Zn, Au and Ag show a different behaviour as shown in Chapter 5. Ablation depth-profiles (nominal depth of 25 μm) measured with LA-ICP-MS reveal that Au and Ag reside within sulphide inclusions, not in the FeOOH matrix itself. Whereas sulphide inclusion-free FeOOH is effectively barren in both Au and Ag (median <0.1 ppm). Trace elemental maps measured with LA-TOF-ICP-MS show that Au and Ag are concentrated at the sulphide-FeOOH boundary. This pattern suggests that, unlike Cu and Zn, precious metals are not trapped by secondary FeOOH during sulphide weathering. Under locally acidic, reducing microenvironments at the sulphide–seawater interface, Au and Ag likely form chloride complexes (e.g. $AuCl_3$, $AgCl_3$; Rose, 1976; Mann, 1984) and subsequently precipitate at the sulphide rim, which is effectively a redox front (Figure 5.5). As sulphide grains continue to oxidise, Au and Ag are liberated and as pH/Eh gradients shift to circumneutral and oxic, these metals then precipitate at the rim of the shrinking sulphide phase in contact with secondary FeOOH. It is currently unclear what happens to the Au and Ag after complete oxidation. Previous studies suggest that native Au forms within secondary FeOOH (Herzig et al., 1991), however the observations of this study indicate that this is not always the case. One possible mechanism that may explain absence of Au and Ag in secondary FeOOH observed in this thesis is thiosulphate complexation of Au and Ag under near-neutral, oxidising porewaters within the stability field of goethite (Becking et al., 1960; Goldhaber, 1983; Webster, 1986; Glasby and Schulz, 1999). Thiosulphate complexes have a reduced capacity to adsorb onto goethite relative to chloride complexes (Ran et al., 2002), potentially enhancing the mobility of Au and Ag. As a result, these metals may migrate either upwards into overlying seawater or downwards towards the sulphide–FeOOH boundary deeper within the SMS mound. Upward migration through fractures into oxic seawater should lead to thiosulphate oxidation and Au/Ag precipitation (Kalinin et al., 2019). Alternatively, downward migration and reduction within the SMS mound could result in decomposition into bisulphide or hydrogen sulphide, also leading to Au/Ag precipitation (Webster, 1986). If the latter is dominant, this would result in a Au and Ag-rich layer at the boundary between FeOOH and sulphide deeper within the SMS deposit.

Consequently, while secondary FeOOH acts as a metal trap for some metals like Cu and Zn, it does not seem to capture the precious-metals. This highlights the need to investigate redox- and ligand-controlled pathways to evaluate Au and Ag mobilisation during sulphide weathering.

7.1.2 Post-formational modification at the seafloor

Secondary FeOOH deposits can remain exposed on the seafloor for millennia, where they can interact with seawater, are exposed to dissolved metals released from underlying sulphide oxidation (Hu et al., 2022) or experience goethite crystallisation from ferrihydrite (Schwertmann and Murad, 1983; Grundl and Delwiche, 1993). Together, these competing processes drive a geochemical evolution, altering both trace-element signatures and base-metal contents over time as shown in Chapter 4 and Chapter 5.

7.1.2.1 Modification of FeOOH by oxygenated seawater

Bulk-rock REE data (Chapter 4) show that secondary FeOOH is enriched in REEs relative to massive sulphide and carry a clear negative Ce anomaly. Mineralogical analyses of secondary FeOOH by LA-ICP-MS (Chapter 5) complement this data, with early formed py-FeOOH and ccp-FeOOH enriched in REE relative to their respective sulphide protolith and modified FeOOH in fully oxidised samples enriched in REE and stronger negative Ce anomalies relative to both py-FeOOH and ccp-FeOOH. This demonstrates a clear compositional evolution of the REE signatures in FeOOH, with the progressive strengthening of the negative Ce anomaly reflecting the increasing incorporation of seawater-derived REE into the FeOOH structure (Debaar et al., 1985). Statistical analysis discussed in Chapter 5 reduced via t-SNE cluster analysis produce five clusters of elements from FeOOH analyses by LA-ICP-MS. For this, one cluster, Mg-Ca-Na-Si, corresponds to seawater-FeOOH interaction; two clusters include REE-Ni-Zn and Co-Mn mark zones of hydrothermal-seawater mixing with Cl-S-Cu cluster suggesting oxidation of Cu-sulphides by seawater (Figure 5.7). Finally, SEM-EDS analysis of FeOOH on 82_HY_06$_a$ exhibit significant enrichment (determined by U-tests) in Si, Cl, Ca and depletion of S relative to early formed py-FeOOH and ccp-FeOOH in 82_HY_06$_b$. The aforementioned evidence indicates that seawater influence increases the concentration of Mg, Ca, Na, Si, REE and depletion of S within both bulk samples of FeOOH and mineralogical analysis of FeOOH phases. Seawater interaction may also compete with other sulphide derived, sorbed elements like Cu and Zn on secondary FeOOH, possibly removing these metals over time (Balistrieri & Murray, 1982; Calmano et al., 1988). However, fluid-rock ratios, calculated from Pb-isotope systematics, show no correlation with either Cu or Zn concentrations, suggesting that the contents of Cu and Zn remain stable in secondary FeOOH over time (Chapter 4).

Taken together, these lines of evidence demonstrate that oxygenated seawater progressively imprints FeOOH with seawater-derived major and trace elements, leading to increasingly negative Ce anomalies, enriching REE, and adsorbing high-abundance ions, while removing or diluting residual sulphur content. Crucially, however, the content of Cu and Zn indicate that once base metals are sequestered onto FeOOH, they remain stable within FeOOH.

7.1.2.2 Cu enrichment processes

Chapter 6 demonstrates that the initial Cu content of newly formed FeOOH directly reflects the composition of the underlying sulphide mineral: ccp-FeOOH, derived from the oxidation of chalcopyrite is Cu-rich, whereas py-FeOOH, derived from the oxidation of pyrite is relatively depleted in Cu. However, Chapter 5 mass-balance calculations reveal a systematic enrichment beyond inheritance. For example, oxidising a sulphide grain containing 0.36 wt.% Cu (e.g., pyrite) should yield ~0.5 wt.% Cu in py-FeOOH under closed-system conditions (following a 26 % Fe loss), yet analyses record a median exceeding 3.0 wt.% Cu, which is evidence of Cu uptake from external sources.

Chapter 6 illustrates that nascent FeOOH formation does not trap all the Cu and Zn released during sulphide oxidation, resulting in their ultimate dispersion into seawater. The subsequent removal of Cu and Zn from oxic seawater is attributed to the adsorption of these metals onto secondary FeOOH, resulting in their enrichment (Figure 6.5). Together, this indicates that metals, not trapped by initial FeOOH formation, may become trapped by adjacent FeOOH phases at seawater pH (~8.2), such as what may occur within an FeOOH deposit overlying massive sulphide. Sequential leaching experiments (Chapter 5) extend this picture, demonstrating the capacity for FeOOH to adsorb Cu from low-pH solutions (4.5), highlighting the effectiveness of FeOOH to adsorb Cu through a range of pH (4.5 to ~8.2) that can occur at SMS deposits. For instance, during chalcopyrite oxidation, Fe transitions into FeOOH (Glasby and Schulz, 1999), whereas Cu is mobilised in chloride complexes (Rose, 1976; Hannington, 1993). At low pH (e.g., 4.5), (par)atacamite may precipitate (Sharkey & Lewin, 1971); however, Cu likely migrates in solution through the FeOOH and then reprecipitate as (par)atacamite upon interaction with seawater (Hannington, 1993). As such, the Cu will instead adsorb onto FeOOH, enriching it in Cu as well as Cl. The aforementioned processes are supported by t-SNE (Cu–Cl–S) analysis and by the higher Cu and Cl contents in modified FeOOH (82_HY_06$_a$) relative to minimally modified FeOOH (82_HY_06$_b$) shown in Chapter 5. Eventually, when cuprous chloride complexes mix with seawater, (par)atacamite ($Cu_2Cl(OH)_3$) may precipitate as veins cross-cutting FeOOH or on the surface of the sample exposed to seawater (Figure 5.1A and Figure 5.2A; Woods and Garrels, 1986; Pollard et al., 1989; Hannington, 1993). Together, these findings support a four-stage enrichment pathway (Figure 7.1):

1. **Initial protolith inheritance:** Secondary FeOOH precipitation acquires the initial Cu content directly from its sulphide protolith, i.e., metal-rich for ccp-FeOOH or metal-poor for py-FeOOH.
2. **Early-stage Scavenging at low pH:** Chapter 5 demonstrates that secondary FeOOH adsorbs dissolved Cu^{2+} at low pH, mimicking the oxidative dissolution of sulphide within mounds with limited mixing of seawater.
3. **(Par)atacamite precipitation:** Oxic conditions at approximately circumneutral conditions (~7) likely dominate within secondary FeOOH crust and given sufficient mixing with seawater, Cu is likely to precipitate as (par)atacamite within FeOOH deposits. This precipitation enriches the bulk deposit in Cu through the formation of a separate mineral phase rather than adsorption onto FeOOH (Chapter 5).
4. **Late-stage scavenging at high pH:** Dissolved Cu^{2+} in oxic seawater is scavenged by secondary FeOOH, a process that may occur in secondary FeOOH deposits close to the seafloor with circulation of seawater (Chapter 6).

This retention efficiency at both high and low pH demonstrates secondary FeOOH role as an active scavenger of Cu, functioning as a "marine gossan" similar to terrestrial gossan (e.g., Herzig et al., 1991; Yesares et al., 2014) and act long-term trap for Cu and Zn.

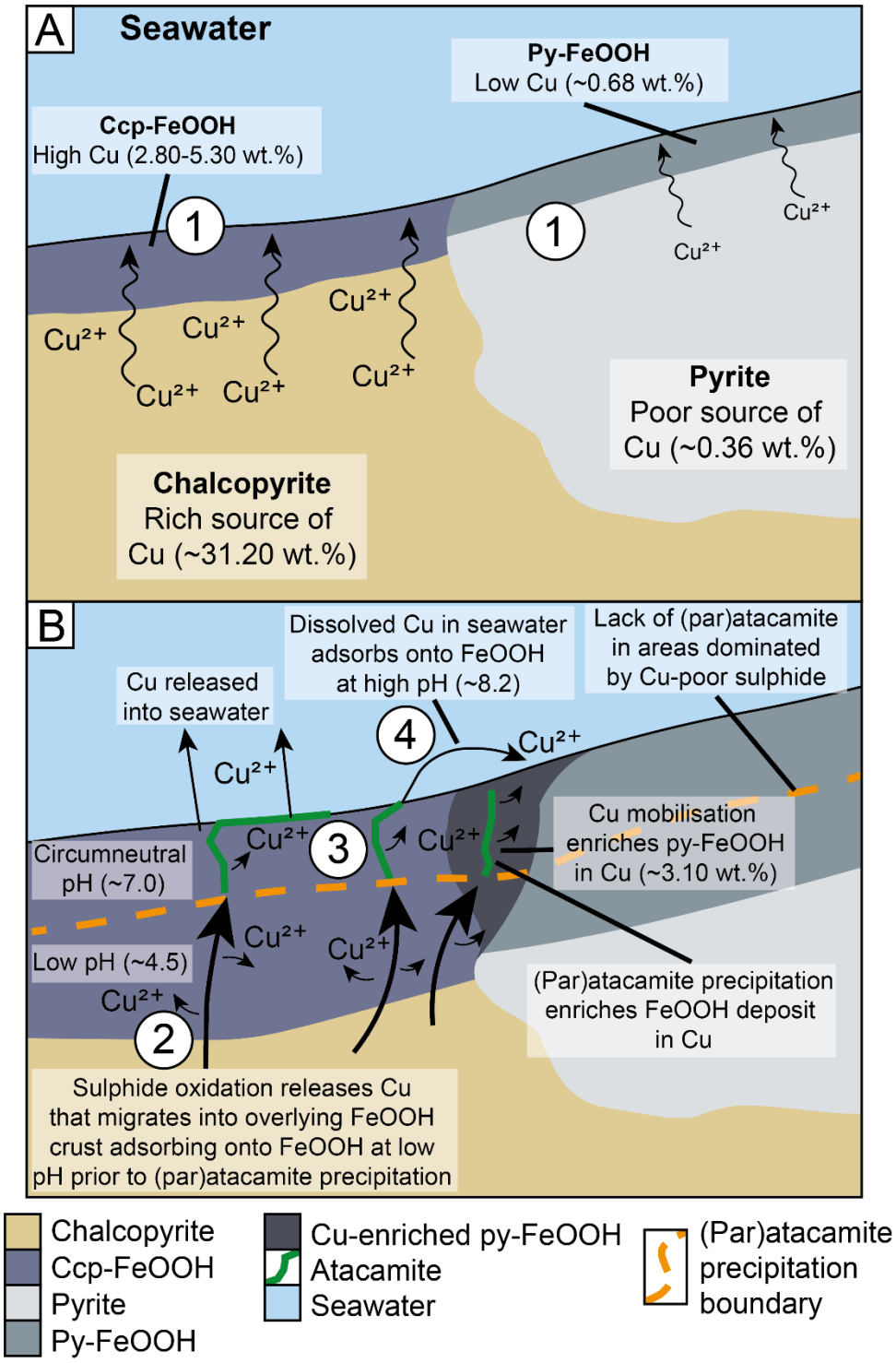

Figure 7.1. Cu-enrichment processes for secondary FeOOH. **(A)** Illustrates the initial inheritance (1) of Cu from chalcopyrite (ccp-FeOOH; high Cu) and pyrite (py-FeOOH; low Cu). **(B)** shows how Cu is enriched within secondary FeOOH by the adsorption of Cu at low pH (2), high pH (4) and with the precipitation of (par)atacamite (3) enriching the FeOOH deposit in Cu. Boundary between low- and high-pH zones for (par)atacamite precipitation is schematic; arrows indicate dominant Cu transport and uptake pathways.

7.1.2.3 Cu and Zn depletion processes

Sequential leaching studies reported in Chapter 5 show that the crystallisation of goethite from ferrihydrite results in a substantial depletion of Cu from 1.4 wt.%, to 0.11 wt.% (92% loss) and Zn from 0.09 wt.% to 0.03 wt.% (57% loss). Yet, the expected metal coupling between goethite abundance and metal depletion is not observed as shown by poor correlations between these components (R^2 ~0.1). This decoupling may arise as Cu and Zn liberated during goethite crystallisation can re-adsorb onto adjacent FeOOH phases or Cu may precipitate as atacamite, buffering against considerable loss. Still, goethite's lower affinity to adsorb Cu and Zn compared to ferrihydrite means that, once neighbouring adsorption sites saturate, further crystallisation will strip more Cu and Zn from the system and their subsequent release into seawater (Vu et al., 2013; Sajih et al., 2014).

7.1.3 Fate of SMS deposits and their weathering products

Exposed sulphides at the seafloor undergo oxidative weathering, however, it is unclear as to how deep the oxidation goes within an extinct SMS deposit. Furthermore, burial of sulphide weathering products by sediment may induce reducing conditions, resulting in the dissolution of both FeOOH and atacamite and stripping their contained Cu and Zn (Woods and Garrels, 1986; Pollard et al. 1989; Sulzberger et al., 1989; Schwertmann, 1991). Together, the ultimate fate of SMS deposits is governed by oxidative and reductive processes, influenced by environmental conditions and geological settings. Understanding these processes is crucial for assessing the longevity of metal enrichment within both sulphide and their weathering products. While the ultimate fate of SMS deposits and their weathering products is not ascertained within this thesis, the surrounding literature and the results of this study provide several hypotheses summarised on Figure 7.2.

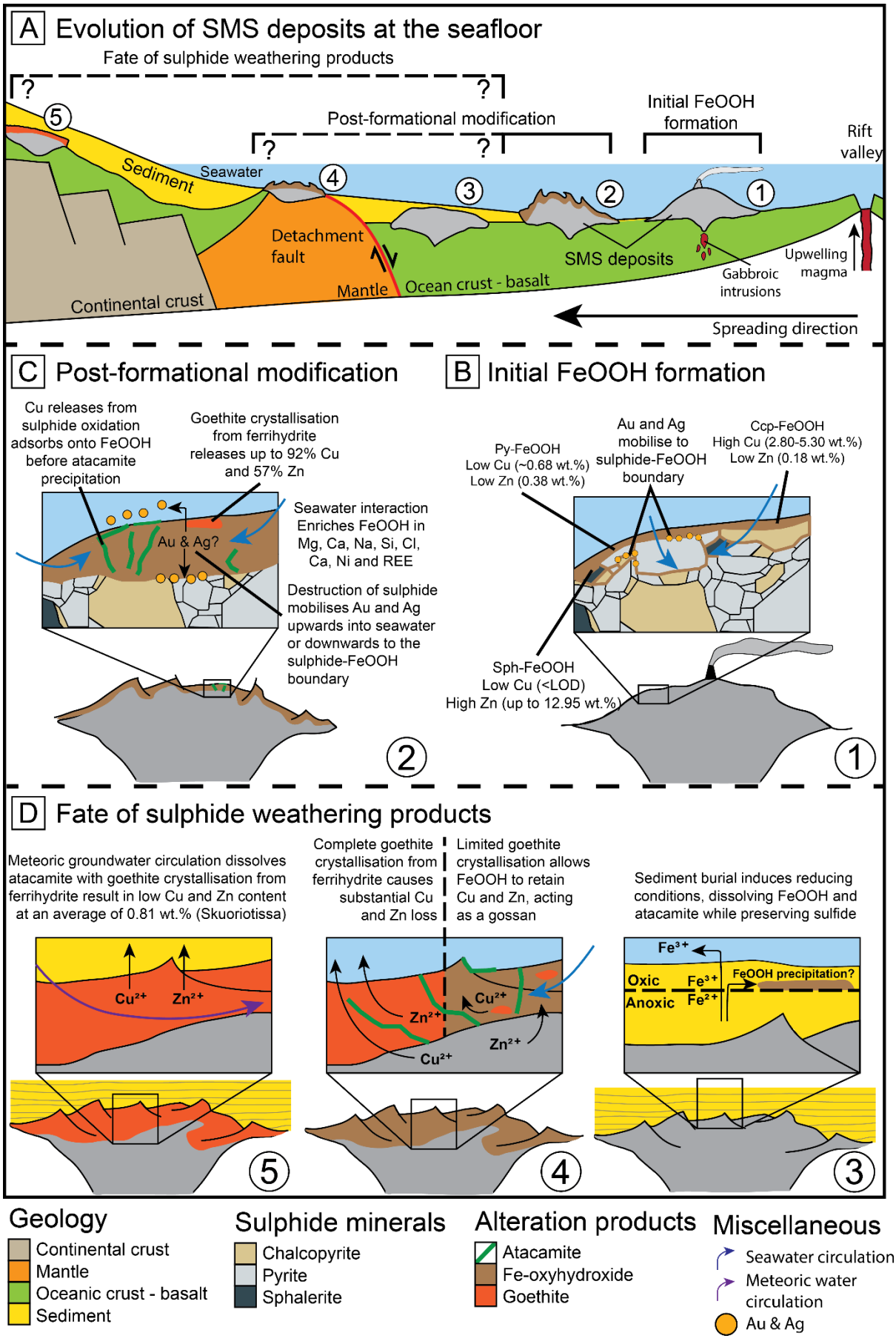
A Evolution of SMS deposits at the seafloor
Fate of sulphide weathering products
?
?
5
Post-formational modification
? ?
Initial FeOOH formation
Rift valley
Sediment
Seawater
4
3
2
1
Detachment fault
SMS deposits
Upwelling magma
Gabbroic intrusions
Continental crust
Mantle
Ocean crust - basalt
Spreading direction
C Post-formational modification
Cu releases from sulphide oxidation adsorbs onto FeOOH before atacamite precipitation
Goethite crystallisation from ferrihydrite releases up to 92% Cu and 57% Zn
Au & Ag?
Seawater interaction Enriches FeOOH in Mg, Ca, Na, Si, Cl, Ca, Ni and REE
Destruction of sulphide mobilises Au and Ag upwards into seawater or downwards to the sulphide-FeOOH boundary
2
B Initial FeOOH formation
Py-FeOOH
Low Cu (~0.68 wt.%)
Low Zn (0.38 wt.%)
Au and Ag mobilise to sulphide-FeOOH boundary
Ccp-FeOOH
High Cu (2.80-5.30 wt.%)
Low Zn (0.18 wt.%)
Sph-FeOOH
Low Cu (<LOD)
High Zn (up to 12.95 wt.%)
1
D Fate of sulphide weathering products
Meteoric groundwater circulation dissolves atacamite with goethite crystallisation from ferrihydrite result in low Cu and Zn content at an average of 0.81 wt.% (Skuoriotissa)
Complete goethite crystallisation from ferrihydrite causes substantial Cu and Zn loss
Limited goethite crystallisation allows FeOOH to retain Cu and Zn, acting as a gossan
Sediment burial induces reducing conditions, dissolving FeOOH and atacamite while preserving sulfide
Cu2+
Zn2+
Fe3+
Oxic
Anoxic
Fe2+
FeOOH precipitation?
5
4
3
Geology
Continental crust
Mantle
Oceanic crust - basalt
Sediment
Sulphide minerals
Chalcopyrite
Pyrite
Sphalerite
Alteration products
Atacamite
Fe-oxyhydroxide
Goethite
Miscellaneous
Seawater circulation
Meteoric water circulation
Au & Ag

Figure 7.2. Schematic diagram illustrating the **(A)** evolution of SMS deposits at the seafloor**. (B, 1)** Initial secondary FeOOH formation through sulphide oxidation, with compositional variation driven by primary sulphide mineralogy. **(C, 2**) Post-formational modification, including goethite crystallisation, seawater interaction, and atacamite precipitation. **(D)** Potential fates of weathering products: **(3)** sediment burial and dissolution, **(4)** retention as metal-rich gossans or complete goethite crystallisation stripping Cu and Zn and **(5)** uplift and metal loss in ophiolite terrane by meteoric water circulation. Geochemical data of Skouriotissa after Constantinou, (1972).

7.1.3.1 Oxidation at the seafloor

When SMS deposits are exposed to oxygenated seawater, they begin to oxidise and release their constituent metals via oxidative dissolution. Laboratory experiments (Chapter 6) demonstrate that oxidation rates scale with particle surface area related to sulphide morphology: black smoker hydrothermal chimneys, characterised by high surface area, may lose its contained metal content in 10–20 yr g^{-1}, whereas massive sulphide, with an order of magnitude lower surface area, requires on the order of 300 yr g^{-1} under similar conditions to fully oxidise. These linear rates, however, only occur in a minority of the samples; most natural samples show non-linear kinetics, with slower oxidation. In some cases, Cu and Zn concentrations in seawater decrease over time, indicating either that sulphide oxidation (and metal release) has ceased, or that metal adsorption onto FeOOH exceeds the rate of metal release from ongoing sulphide oxidation (Figure 6.3). Terrestrial analogues demonstrate that sulphide oxidation remains incomplete even over geological timescales. The Skouriotissa VMS in Cyprus possesses up to 4 m of ochre crust above a 52 m sulphide body after ~5 Ma of seafloor exposure (Constantinou, 1972; Ravizza et al., 2001). Despite prolonged oxidative potential, the majority of the sulphide orebody remains relatively unaltered, implying that mechanisms such as secondary FeOOH formation effectively mitigate and prevent further oxidation.

Secondary FeOOH formation as a result of sulphide oxidation can completely encapsulate the sulphide, reducing oxidation, leading to the observed non-linear metal release in Chapter 6. Moreover, the density of initially precipitated ferrihydrite (3.80-4.15 g/cm^3; Hiemstra and Van Riemsdijk, 2009; Hiemstra, 2018) is less relative to that of chalcopyrite (4.10-4.30 g/cm^3) and pyrite (5.02 g/cm^3), and as such, the formation of secondary FeOOH will lead to volumetric expansion upon formation (Anthony et al., 2025).

While sulphide oxidation can initially create fractures (e.g., Figure 5.2E) permitting increased circulation of seawater into the sulphide, enhancing oxidation, the formation of extensive FeOOH deposits may eventually reduce sulphide-seawater contact and limit further oxidation (Figure 7.3B; Yin et al., 2025).

While not considered within this thesis, burial of sulphide beneath pelagic sediment can attenuate oxidation by preventing oxygen penetration to the sulphide (Cai & Sayles, 1996). Within the sediment, oxygen is consumed through the oxidation of organic carbon (Jørgensen et al., 2022). While the depth of oxygen penetration will depend on multiple factors including the amount of organic carbon and type of sediment (Reimers et al., 1984). Nonetheless, sedimentation will restrict effective oxygen circulation to the sulphide and hence, limit sulphide oxidation that results in the formation of a thin FeOOH crust (Figure 7.3C). However, in areas where gravity driven flows cause rapid burial, sulphide oxidation may be minimal (Figure 7.3D; Dutrieux et al., 2023).

Together, these lines of evidence (Figure 7.3) suggest that off-axis SMS deposits may not fully oxidise. Instead, they retain unaltered sulphide cores overlain by secondary FeOOH ± atacamite, potentially preserving Cu and Zn at the seafloor.

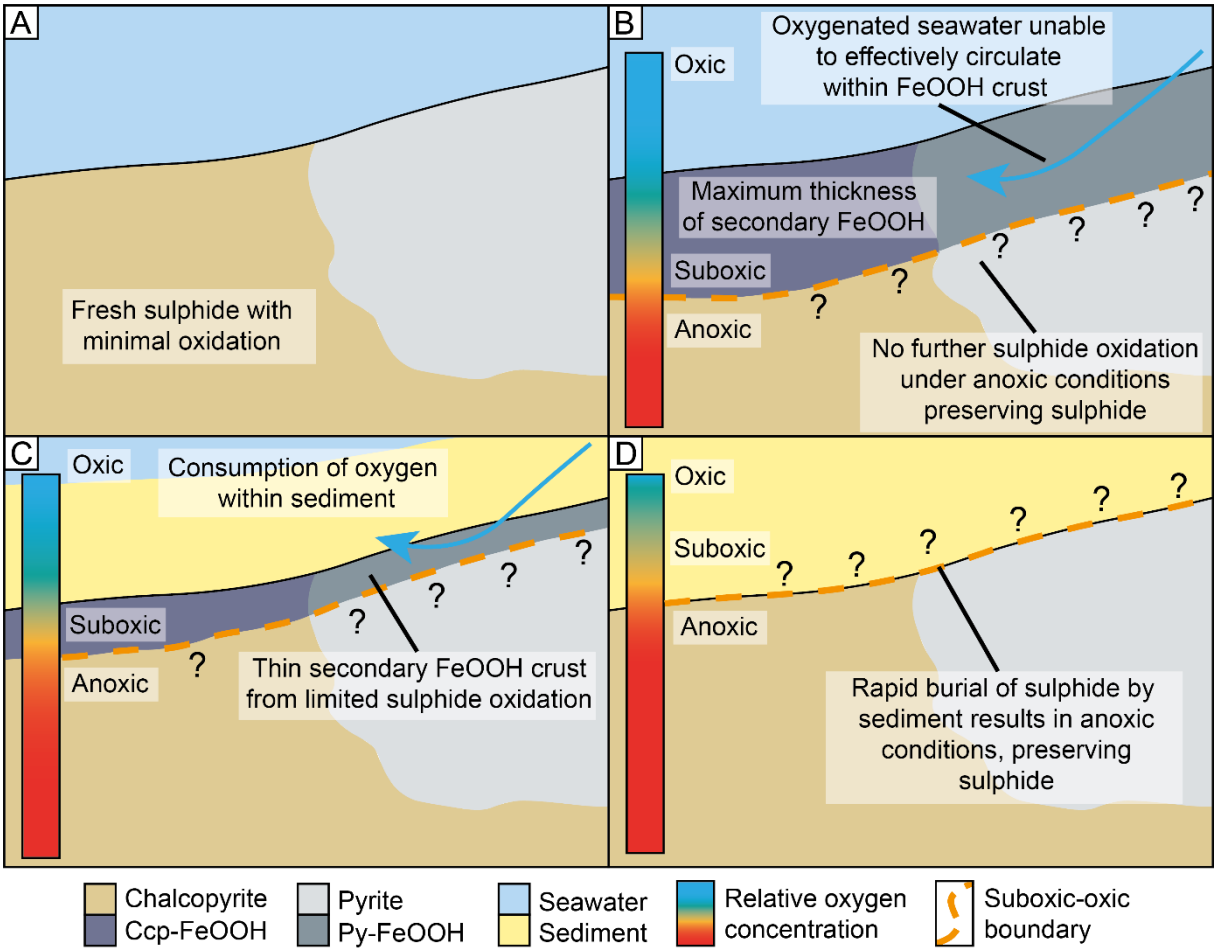

Figure 7.3. Schematic cross-sections illustrating three preservation scenarios for SMS deposits. **(A)** illustrates relatively fresh sulphide exposed at the seafloor, prior to oxidation or sediment burial. **(B)** Secondary FeOOH formation: secondary FeOOH deposits forms volumetrically expansive coatings that block seawater circulation, hindering sulphide oxidation. Secondary FeOOH may altogether prevent oxygen penetration to the sulphide, preserving sulphide. **(C)** Combined burial and secondary FeOOH formation: partial burial under sediment and FeOOH sealing jointly maintain suboxic-anoxic conditions, preventing sulphide oxidation. **(D)** Sediment burial: rapid infill by pelagic sediment limits oxygen penetration, halting oxidation and preserving sulphide.

7.1.3.2 Reduction at the seafloor

When reducing conditions prevail, secondary FeOOH and atacamite can undergo reductive dissolution, releasing their contained metals (Woods and Garrels, 1986; Pollard et al. 1989; Sulzberger et al., 1989; Schwertmann, 1991). At the seafloor, pelagic sediment can contain organic carbon that undergoes oxidation through a sequence of diagenetic processes. This decomposition follows a predictable order of electron acceptors: O_2 > nitrates > manganese oxides > FeOOH > sulphates (Froelich et al., 1979).

The depth of oxygen penetration is primarily controlled by the organic carbon content within the sediment. Organic carbon-rich sediment results in rapid oxygen consumption and its penetration limited to just a few millimetres (Cai & Sayles, 1996). In contrast, areas of organic carbon-starved sediment can have oxygen penetrating to depths up to metres (Middelburg, 2019). This suggests that depending on the geographic location of the SMS deposit, this could result in prevailing reducing conditions under a thin blanket of sediment causing FeOOH dissolution (Figure 7.2D). Applying this to the Semenov hydrothermal field, its location in the North Atlantic deep ocean likely indicates very low organic-carbon sediment (Parameswaran et al., 2025). With sedimentation rates in the North Atlantic deep ocean of 1-10 mm/ka (Restreppo et al., 2020), burying FeOOH deposits below the oxic zone to reach reducing conditions could take approximately 100 ka to 1 Ma. Additionally, SMS deposits typically form steep slopes where bottom currents and gravity driven sediment flows could continuously strip pelagic sediment. While this will impact permeability and thus oxygen diffusion (Spinelli et al., 2004), it may also result in a thinner sediment cover, maintaining oxic conditions. The Semenov hydrothermal field's location on a topographically elevated OCC promotes sediment stripping, preventing the prolonged burial necessary for reducing conditions to develop.

Reductive processes can dissolve metal-rich secondary FeOOH and atacamite, stripping their contained metals and potentially lost from the system. However, given the correct conditions (i.e., organic carbon poor sediment and situated topographically high), reductive dissolution may take considerably longer (up to 1 Ma) or may not occur at the seafloor, maintaining oxic conditions and preserving both FeOOH and atacamite.

7.1.3.3 Goethite crystallisation

While oxic conditions preserve FeOOH, extensive transformation to goethite from ferrihydrite could strip Cu (up to 90%) and Zn (up to 57%) from the system. Model half-lives of ~100 ka for the crystallisation of goethite from ferrihydrite (Dunk and Mills, 2006) imply that off-axis SMS deposits older than this could be dominated by goethite. This process reverses the initial role of FeOOH as a metal trap, unless impeded. For instance, Fe^{2+} catalyses goethite crystallisation, but

competes with other metals, both adsorbed or lattice-bound (e.g., Cu and Zn), onto ferrihydrite that slows its maturation into goethite (Tronc et al., 1992; Jambor and Dutrizac). Additionally, microbial biofilms have been shown to stabilise poorly crystalline oxyhydroxides (Kennedy et al., 2004). If goethite crystallisation remains minimal, secondary FeOOH deposits will continue to act as long-term traps for metals (section 7.1.2.3; Figure 7.2D).

7.1.3.4 Uplift onto land

When oceanic lithosphere, hosting seafloor massive sulphide (SMS) deposits, is uplifted onto continental crust, the resulting ophiolite complex contains these deposits, are then classified as VMS deposits. Under terrestrial conditions, the sulphide enters a different weathering regime than at the seafloor. Meteoric groundwater can generate variably reducing, acidic fluids (pH <6; Emmons, 1917; Yesares et al., 2014) that can infiltrate the FeOOH deposit, promoting reductive dissolution of FeOOH and atacamite, releasing Cu and Zn. Terrestrial weathering effects vary with subsequent metamorphic and hydrological histories. For example, some ochre deposits in the Troodos Ophiolite, such as those at Skouriotissa, Mathiatis, and Mousoulos, were not subjected to metamorphism or extensive meteoric fluid circulation, thereby preserving goethite-dominated ochres that retain ~0.8 wt.% Cu+Zn (Constantinou, 1972). By contrast, the gossanite deposits in some of the Urals' ophiolites have been subject to greenschist-facies metamorphism, during which goethite dehydrated to hematite and magnetite (Jolly 1974; Goss 1987), restructuring the gossan, and stripping Cu and Zn (average combined grade ~0.10 wt.% Cu and Zn; Maslennikov et al., 2012; Vikentyev et al., 2017). Both pathways during ophiolite uplift and/or obduction suggest complete goethite crystallisation from ferrihydrite and the absence of atacamite indicate its dissolution.

While unclear whether atacamite dissolution and full goethite crystallisation occurs at the seafloor or during ophiolite emplacement and uplift, it nonetheless indicates that Cu and Zn becomes depleted in goethite relative to the ferrihydrite dominated secondary FeOOH deposits at the Semenov hydrothermal fields (average of 2.55 wt.% Cu and Zn). Without resolving this issue, we cannot predict what happens to secondary FeOOH deposits and atacamite on the seafloor. This is an important question given the possibility that the majority of SMS deposits are buried by sediment off-axis. Determining marine versus terrestrial contributions to metal loss or preservation has direct implications for expanding exploration efforts to discover off-axis SMS deposits.

7.2 Are sulphide weathering products a source of critical or strategic metals at SMS deposits?

At this preliminary stage, with only 37 bulk samples of sulphide weathering products (FeOOH and atacamite) and no drilling data, the evaluation presented here is qualitative, based on grade and tonnage estimates. To date, the only National Instrument 43-101 (NI 43-101) compliant resource estimate for an SMS deposit is the Solwara 1 Project in Papua New Guinea, which defined a cut-off grade at 2.6 wt.% Cu equivalent at an indicated tonnage of 1.03 Mt (Lipton et al., 2018). Although Solwara 1 focuses on primary sulphide ore, its grade and tonnage provides a valuable benchmark for evaluating the economic potential of sulphide weathering products. If secondary FeOOH and atacamite deposits can approach or supplement such metal concentrations and tonnages, they may represent a complementary, if not standalone, resource.

7.2.1 Concentration

At the Semenov hydrothermal field, the concentration of critical[1] and strategic[2] metals within secondary and primary FeOOH deposits is generally lower than in those extracted at terrestrial deposits (Table 7.1). The Fe content itself is relatively low, consistent with what is considered low-grade for iron deposits (Clout and Manuel, 2015). However, the secondary FeOOH deposits at the Semenov hydrothermal field show enrichment in Cu compared to VMS deposits (Barrie and Hannington, 1999), which positions Cu as the primary economic driver for extracting these deposits. In contrast, other metals like Zn or Co may become more relevant at SMS deposits where the protolith contains higher abundances of these elements, such as Zn-rich systems like Yuhuang-1 (Hu et al., 2022), or Co-rich ultramafic-hosted hydrothermal systems like Rainbow, Ashadze-1, and Fåvne (Fouquet et al., 2010; Sahlström et al., 2023).

[1] Metals that are deemed essential for modern technology and societal needs but their supply is potentially at risk.
[2] Metals that are vital for industrial and energy infrastructure but are not currently supply constrained.

Table 7.1 Comparison of the average concentration of critical and strategic metals in the FeOOH deposits at Semenov and the approximate economic grade of those metals found in terrigenous deposits. BIF – Banded iron formation, GIF = granular iron formation. List of critical metals after Mudd et al. (2024) with the addition of Cu as a strategic metal after European Commission (2023) and Australian Government (2024). References for the approximate economic grade and deposit type are as follows; [1]Mondillo et al. (2021), [2]Hein and Tshibubudze (2016), [3]Clout and Manuel (2015), [4]Barrie and Hannington (1999), [5]Fanka and Tadthai (2023), [6]Mudd et al. (2013), [7]Mudd and Jowitt (2014), [8]Mitchell (2015), [9]Seal et al. (2017), [10]Weng et al. (2015), [11]Green et al. (2020), [12]Deady et al. (2022). [a] approximate economic grade for REE data includes yttrium.

Critical metals	Avg. grade in secondary FeOOH	Avg. grade in primary FeOOH	Approximate economic grade	Deposit type
wt.%				
Al	0.35	0.19	50[1]	Bauxite
Mn	1.37	7.72	40[2]	Sedimentary Mn, BIF
Fe	31.1	21.63	>30[3]	BIF and GIF
Zn	0.15	0.08	1.83-5.63[4]	VMS
ppm				
Li	7.3	106.4	2800-18600[5]	Pegmatites
Co	106	48	1000[6]	Magmatic sulphide,
Ni	49	145	18000-25000[7]	Hydrous Mg silicate
Nb	2	1	1400-3500[8]	Carbonatites
Sb	16	8	34000-42000[9]	Stibnite-quartz
REE	65	31	5400[a][10]	Carbonatite
W	3	2	2400-8800[11]	Skarn
Bi	2	<1	1000-1900[12]	Skarn
Strategic metal	Avg. grade in secondary	Avg. grade in primary FeOOH	Approximate economic grade	Deposit type
wt.%				
Cu	2.4	0.13	1.10-2.04[4]	VMS

7.2.2 Tonnage

A critical limitation in evaluating the economic potential of these weathering products is the uncertainty around their tonnage. Estimating tonnage first requires establishing both surface extent and deposit thickness. The surface extent of FeOOH deposits at Semenov-1, Semenov-2, Semenov-4 and Semenov-5 has been mapped through ROV dives using HyBIS during cruise JC224 and ISIS during JC254 with respect to Semenov-4. The geological maps in Chapter 3 yield an observed FeOOH deposit surface area of approximately 116,000 m^2 and an inferred minimum extent of up to 420,000 m^2. It is important to note that these are estimates and much of Semenov hydrothermal field remains unexplored suggesting that the actual coverage of FeOOH may be greater. Thickness remains our greatest uncertainty in estimated FeOOH tonnage. Previous studies have suggested FeOOH deposits may reach several tens of centimetres (Hannington & Jonasson, 1992), with observations in this study indicate a conservative average of approximately 30 cm (Figure 3.3E). In the absence of three-dimensional imaging or core samples, our tonnage figures must be viewed as first-order approximations, nonetheless, they provide a baseline for evaluating resource potential.

To convert these thickness and area estimates into mass, we must know the density of the FeOOH deposits. Bulk density (ρ_{bulk}) represents the mass per unit volume of the solid, and it directly links our estimated crust volume to an equivalent tonnage. We calculate ρ_{bulk} using Eq. 7.1 with the volumetric proportions (V_i) of each mineral phase (i) determined by quantitative XRD (Appendix C.1). The grain densities of each mineral phase (ρ_i) is acquired after Hiemstra and Van Riemsdijk (2009), Lyle et al. (2002) and Anthony et al. (2025)

$$\rho_{bulk} = \sum_i \left(\frac{V_i}{100} \times \rho_i \right) \qquad Eq. 7.1$$

Applying Eq. 7.1 to measured mineral fractions yields an average bulk density of 3.75 g/cm^{-3}. Because the FeOOH deposits contain open pore space, the bulk density must be adjusted for porosity (φ) to find the dry bulk density (ρ_{dry}) as shown on Eq. 7.2.

$$\rho_{dry} = \rho_{bulk} \times (1 - \varphi) \qquad Eq. 7.2$$

The tonnage of FeOOH deposits can be approximated using Eq. 7.3 where A is the surface area (m^2) and T is the thickness (m). For this, a scenario-based approach using a thickness of 30 cm and 70 cm with a porosity of 20% and 60% of which the upper porosity bound is noted in ferromanganese crusts after Hein (2004), which may demonstrate similar porosities with FeOOH deposits.

$$Tonnage\ (t) = \rho_{dry} \times A \times T \qquad Eq. 7.3$$

The scenario-based approach leads to a considerable range of the approximate tonnage in FeOOH deposits at Semenov, ranging from 0.05-0.88 Mt (Table 7.7.2).

Table 7.7.2 Approximate calculation of the total tonnage of FeOOH deposits at Semenov using a scenario-based approach.

Surface area (m^2)	Thickness (m)	Density (t/m^3)	Tonnage (t)
Observed: 116,000	0.30	2.99	104052
116,000	0.30	1.50	52200
116,000	0.70	2.99	242788
116,000	0.70	1.50	121800
Inferred: 420,000	0.30	2.99	376740
420,000	0.30	1.50	189000
420,000	0.70	2.99	879060
420,000	0.70	1.50	441000

Combining grade and tonnage, the total contained Cu and Zn within the weathering products at Semenov is estimated using Eq. 7.4, producing a metal content range of approximately 1,300 to 22,400 tonnes (Table 7.7.3). Although these carry considerable uncertainty, they are valuable to gauge whether secondary FeOOH deposits may meaningfully contribute to the overall metal resource.

$$Metal\ content\ (t) = Tonnage\ (t) \times \left(\frac{Grade\ (wt.\%)}{100}\right) \qquad Eq.\ 7.4$$

Table 7.7.3 Calculated tonnage of Cu and Zn using the average grade of secondary FeOOH deposits at Semenov and the highest and lowest calculated tonnage based on Table 7.7.2.

Metal	Grade (wt.%)	Tonnage (t)	Metal content (t)
Cu	2.4	52200	1253
Cu	2.4	879060	21097
Zn	0.15	52200	78
Zn	0.15	879060	1319

7.2.3 Implications for sulphide weathering products as a resource at SMS deposits

The average Cu and Zn concentration contained within sulphide weathering products at Semenov of 2.55 wt.% falls just below the Solwara-1 cut-off grade at 2.6 wt.% Cu equivalent, which also accounts for metallurgical processes, transportation and royalty losses (Lipton et al., 2018). However, sulphide weathering products may offer environmental and economic advantages over sulphide ore processing that may offset that deficient grades of Cu and Zn.

Atacamite and FeOOH do not generate acid mine drainage during transportation or when stored, and FeOOH can act as a natural sink for metals mobilised during sulphide oxidation (Tabelin et al., 2020; Chapter 5 and Chapter 6). The mineral hardness of sulphide weathering products is lower than that of primary sulphides (e.g., Mohs hardness: atacamite 3.0–3.5, goethite 5.0–5.5, ferrihydrite <2.5 vs. pyrite 6.0–6.5, chalcopyrite 3.5-4.0 and sphalerite 3.5-4.0), suggesting reduced energy costs for grinding (Berquó et al., 2007; Anthony et al., 2025). The lower sulphur content (FeOOH median ~0.25 wt.%, atacamite below detection; Chapter 5) implies decreased sulphur emissions and related treatment costs during processing. Moreover, these materials can be treated hydrometallurgically, avoiding the high energy demands and emissions of pyrometallurgical methods used for sulphides (Abkhoshk et al., 2014). These attributes of sulphide weathering products suggest that the economic threshold for processing these secondary minerals may be lower than that for sulphide ores, which could make these products viable to extract under the right conditions.

However, even under optimistic scenarios, the metal content (up to 22,400 tonnes Cu and Zn) remains lower than Solwara 1's estimated 78,000 tonnes. Consequently, sulphide weathering products are unlikely to serve as primary drivers for SMS mining, but could represent a

supplementary resource that boosts overall recovery. For instance, the additional Cu and Zn from weathering products could enhance total metal yields at SMS sites by as much as 22% relative to Solwara 1's reserve.

In summary, while sulphide weathering (i.e., FeOOH and atacamite) products at Semenov do not yet meet the grade-tonnage thresholds to justify standalone extraction, they offer promising supplemental value. Their potential for environmentally sustainable, lower-cost processing, combined with their capacity to enhance metal recovery from primary SMS ores, positions them as a valuable secondary resource. This thesis highlights the need for future work focused on defining the three-dimensional morphology, distribution of FeOOH deposits and processing techniques, which could lead to the integration of sulphide weathering products into broader SMS resource strategies.

7.3 Sulphide weathering products as exploration vectors

Secondary FeOOH deposits are formed by the alteration of sulphide and are observed overlying sulphide (Figure 3.4A) and are analogous to ochre deposits found at Cyprus-type VMS systems (e.g., Skouriotissa), as such, secondary FeOOH deposits are likely spatially constrained to zones of sulphide mineralisation (Constantinou, 1972; Herzig et al., 1991). In contrast, primary FeOOH deposits can form on the fringes of hydrothermal systems and do not guarantee underlying sulphide (e.g., Dekov et al., 2007). As demonstrated in Chapter 4, primary FeOOH deposits at Semenov are identified by chimney-like morphologies formed through alternating precipitation of FeOOH and Mn-oxide, often accompanied by green smectite (nontronite) within the conduit system. Secondary FeOOH deposits display a darker hue, lack of Mn-oxide banding, and the occurrence of atacamite relative to primary FeOOH deposits. Moreover, secondary FeOOH deposits have more varied suite of textural morphologies, including brecciated and relict chimney textures, inherited from the sulphide protolith (Figure 4.4).

However, the limited comparative studies of primary versus secondary FeOOH deposits mean these distinguishing features require validation across multiple SMS deposits. For example, Hekinian et al. (1993) documented primary FeOOH deposits with purple-red colouration and can form as layered or mound like deposits, suggesting that colour or textural morphology alone may not be universally diagnostic. Despite these limitations, the mineralogical and morphological differences of primary and secondary FeOOH deposits at Semenov can aid in identifying secondary FeOOH to help guide future exploration of SMS deposits to mark potential areas of underlying sulphide. Secondary FeOOH deposits also act as a marine gossan, trapping metals released from the oxidation of underlying sulphide (section 7.1.2.2). This trend implies that Cu enrichment in secondary FeOOH may be used to infer the concentration of Cu within the underlying sulphide. Chapter 4 illustrates a correlation between average Cu concentrations in secondary FeOOH and bulk sulphide concentrations at SMS deposits (Figure 4.6), suggesting that Cu-enriched secondary FeOOH could guide exploration even if the correlation is imperfect.

Atacamite forms at the seafloor from the oxidative weathering of Cu-sulphides (Hannington, 1993). Chapter 4 shows that secondary FeOOH deposits with visible atacamite tend to be more Cu-rich than those without. Chapter 5 suggests that Cu mobilised during sulphide weathering may initially sorb onto FeOOH before atacamite precipitation, thereby increasing the Cu content of the FeOOH. Atacamite, therefore, both enriches FeOOH in Cu and acts as a visual indicator of Cu-rich zones within FeOOH deposits and may indicate Cu-rich sulphide underlying. It often forms conspicuous green coatings that can extend over large areas of sulphide or FeOOH outcrop, aiding in ROV surveys and reconnaissance (Chapter 3; Figure 3.3D).

In summary, secondary FeOOH deposits and associated atacamite mineralisation could provide a framework for guiding exploration at SMS deposits. Grab samples of secondary FeOOH collected during ROV dives can be quickly screened on board using pXRF to identify Cu-enriched zones. This allows mapping of metal distributions in near-real-time and prioritise targets for more detailed geochemical, geophysical surveys and drilling targets.

7.4 Conclusions of the study

Bulk samples of sulphide weathering products (FeOOH and atacamite) at the Semenov hydrothermal field contain Cu concentrations comparable to mined terrestrial VMS deposits. These concentrations, combined with their estimated 0.05-0.88 Mt at Semenov containing 1,200-21,000 t of Cu. This thesis demonstrates that sulphide weathering products may constitute a supplementary resource alongside primary sulphide across SMS deposits, thereby expanding the metal inventory and economic potential of SMS deposits.

Investigating the geochemical evolution of secondary FeOOH reveals a multi-stage process of metal enrichment and retention. Initially secondary FeOOH inherits Cu and Zn directly from the sulphide protolith and is subsequently modified at the seafloor. Despite potential loss of Cu and Zn during ferrihydrite crystallisation to goethite, this mechanism may not be extensive. Neighbouring FeOOH phases can re-adsorb metals released goethite crystallisation, reducing their loss. Overall, Cu and Zn do not become depleted and instead can become enriched in Cu. Together, this thesis demonstrates that secondary FeOOH functions effectively as a "marine gossan", trapping base metals over extended periods, similar to terrestrial gossan (Herzig et al., 1991; Yesares et al., 2014).

The behaviour of Au and Ag differs from that of Cu and Zn. Gold and Ag are not fixed within FeOOH or atacamite, but instead are concentrated at the rims of the sulphide during oxidation. After complete oxidation of the sulphide, Au and Ag are lost from the secondary FeOOH, suggesting their mobilisation as complexes such as thiosulphate and transport away from the FeOOH matrix. While their ultimate fate remains an open question, these metals may migrate to the FeOOH-sulphide boundary deeper within the SMS deposit. Such migration could create previously unrecognised zones of precious-metal enrichment, offering new exploration targets and insights into precious metal mobility in SMS deposits.

The long-term preservation of metal content within sulphide weathering products depends on burial conditions, sedimentation rates and tectonic history. Given the correct conditions, the sulphide weathering products may remain in an oxic environment at the seafloor, preserving Cu and Zn for potentially millions of years. This longevity is demonstrated by VMS deposits in Cyprus where, even after 1-5 Ma of seafloor exposure and subsequent uplift, ochre deposits (Skouriotissa) still retain an average of 0.80 wt.% Cu and Zn. Together these findings establish that older, off-axis SMS deposits may preserve their contained Cu and Zn inventory within their weathering products, expanding the potential of prospective areas for exploration at the seafloor.

Finally, secondary FeOOH deposits also serve as valuable exploration vectors. Their capacity to trap Cu provides insight into the metal content of underlying sulphide mineralisation. While not perfect indicators of primary orebody metal tenor, the presence of atacamite enriches surrounding FeOOH in Cu, marking Cu-rich zones and potentially pinpointing underlying Cu-rich sulphide bodies. Visual identification of atacamite during ROV surveys, combined with rapid onboard pXRF screening, can facilitate in-situ mapping of Cu anomalies, directing focused drilling toward high-potential targets.

This thesis delivers a model of sulphide weathering and FeOOH evolution at an SMS deposit, integrating geological mapping, mineralogy, bulk and in-situ geochemistry, isotopic tracing, and laboratory oxidation experiments. The findings enhance our understanding of metal cycling on the seafloor while establishing secondary FeOOH and atacamite as both valuable metal sinks and potential exploration guides. Future research directions include investigating goethite crystallisation kinetics in marine environments, determining the three-dimensional morphology of secondary FeOOH deposits, and tracking the fate of Au and Ag to fully assess the long-term metal retention and economic potential of these weathering products.

7.5 Future work and directions

7.5.1 The fate of gold and silver

Chapter 5 demonstrates that, unlike earlier work (e.g. Herzig et al., 1991; Dekov et al., 2011), Au and Ag are not sequestered within secondary FeOOH or atacamite. High-resolution LA-TOF-ICP-MS data indicate that precious metals remain associated with diminishing sulphide phases but are absent once oxidation is complete. I hypothesise that both Au and Ag are mobilised as thiosulphate complexes; whether they are ultimately retained or lost likely depends on fluid flow direction, downward toward the sulphide–FeOOH interface or upward into the overlying seawater. Resolving this requires subsurface sampling, ideally drill cores intersecting the weathered FeOOH crust and underlying sulphide. Such an approach would eliminate potential sampling biases inherent to surface grabs and allow direct comparison with terrestrial sulphide systems, thereby clarifying how tectonic setting, fluid pathways, and sampling methodology influence observed mineralogy, grain size, and metal grades (Herzig et al., 1991; Yesares et al., 2014).

7.5.2 Resource assessment of sulphide weathering products

This thesis lays the foundation for evaluating the resource potential of sulphide weathering products, with preliminary tonnage estimates at Semenov suggesting considerable secondary FeOOH material. However, a complete resource assessment requires defining the three-dimensional morphology of secondary FeOOH deposits, particularly their thickness and lateral extent; parameters that remain poorly constrained. Addressing this knowledge gap will require integrated mapping and sampling: high-resolution ROV surveys to delineate FeOOH deposit continuity, targeted drilling (or alternatively, using an ROV-mounted saw to recover intact box samples), and complementary geophysical methods to image subsurface architecture. Only through such a multidisciplinary campaign can we accurately quantify the volume, continuity, and metal content of these deposits and thereby assess their viability as a primary resource.

7.5.3 Off-axis exploration

Despite decades of study, no truly off-axis, extinct SMS deposit has yet been documented. This thesis, however, highlights the potential of secondary FeOOH and atacamite weathering products as mineral resources, providing further motivation to extend exploration beyond close to the axial valley (Petersen et al., 2018; Jamieson & Gartman, 2020). Off-axis targets, areas where hydrothermal activity has ceased and deposits have undergone prolonged alteration, are the logical next step in testing the models developed here (section 7.1.3). By sampling these off-

axis SMS deposits, we can evaluate whether secondary FeOOH retain the content of Cu and Zn (Chapter 4), confirm the capacity of FeOOH layers to act as gossans (Chapter 5). Ultimately, off-axis exploration will either validate or challenge our understanding of metal retention and mineral transformation in extinct SMS deposits.

7.5.4 Goethite crystallisation

The kinetics of goethite crystallisation from ferrihydrite are well constrained under laboratory conditions, conducted at room temperature and lower pH (Schwertmann et al., 2004). However, the transformation kinetics of ferrihydrite to goethite under seafloor conditions remain poorly constrained, particularly within SMS deposits. Theorised predictions by Dunk and Mills (2006) calculated a time to half conversion of ~100 ka. While this provides a useful framework, it implies that secondary FeOOH deposits older than 100 ka would predominantly consist of goethite. Based on findings from this thesis, goethite crystallisation from ferrihydrite could strip Cu and Zn from FeOOH deposits, potentially rendering them barren in these metals. Therefore, it is essential to investigate secondary FeOOH deposits older than 100 ka to assess their mineralogical composition and metal content. Alternatively, controlled laboratory experiments that replicate SMS conditions can accurately determine the kinetics of ferrihydrite to goethite crystallisation and understand the factors influencing this process. These studies should also consider the effects of incorporating metals like Cu and Zn as they may influence both the rate and extent of crystallisation. Investigating goethite crystallisation kinetics is important in understanding the long-term geochemical evolution of SMS deposits and their capacity to sequester metals in marine environments.

Appendix A **Supplementary to methods**

A.1 BET surface area analysis

Table A.1. Summary of BET surface area measurements for samples presented in Chapter 6.

Sample	Surface area (m^2/g)	Error (m^2/g)	Mass (g)	C value
DE-02 (I)	0.037	0.0002	2.768	239.8
DE-02 (II)	0.0455	0.0015	1.9209	206.4
DE-03	0.256	0.0026	2.519	366.7
DE-05	0.0671	0.0017	1.6171	1031
DE-06 (I)	0.1091	0.0006	3.3487	155.8
DE-06 (II)	0.0881	0.002	2.6542	186.9
DE-07 (I)	0.6719	0.0074	2.3855	1318
DE-07 (II)	0.7796	0.0087	1.7208	2656
DE-10	0.046	0.0003	3.1845	181.8

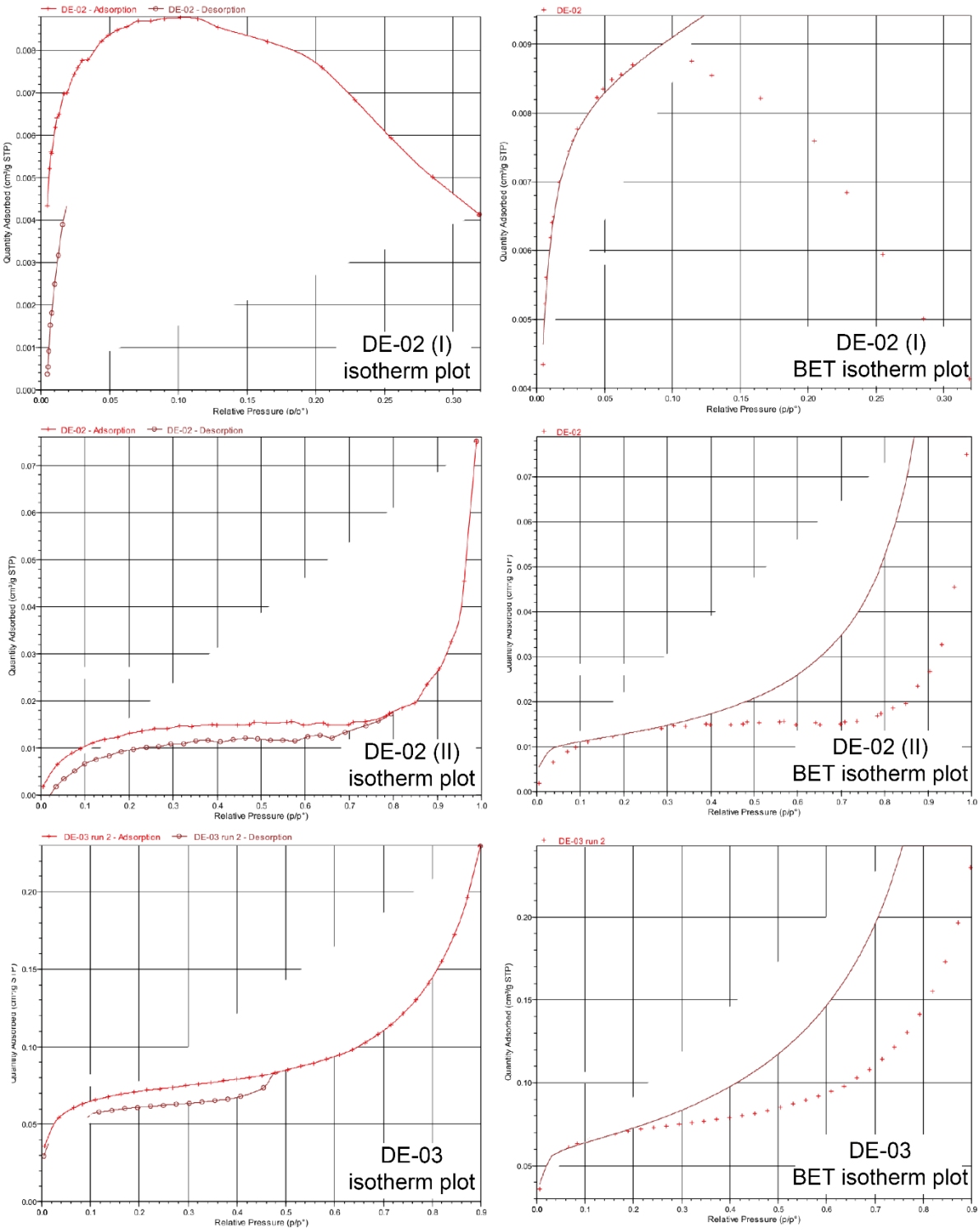

Figure A.1. Isotherm and BET isotherm plots of DE-02 (I), DE-02 (II) and DE-03. Figure 1 of 3.

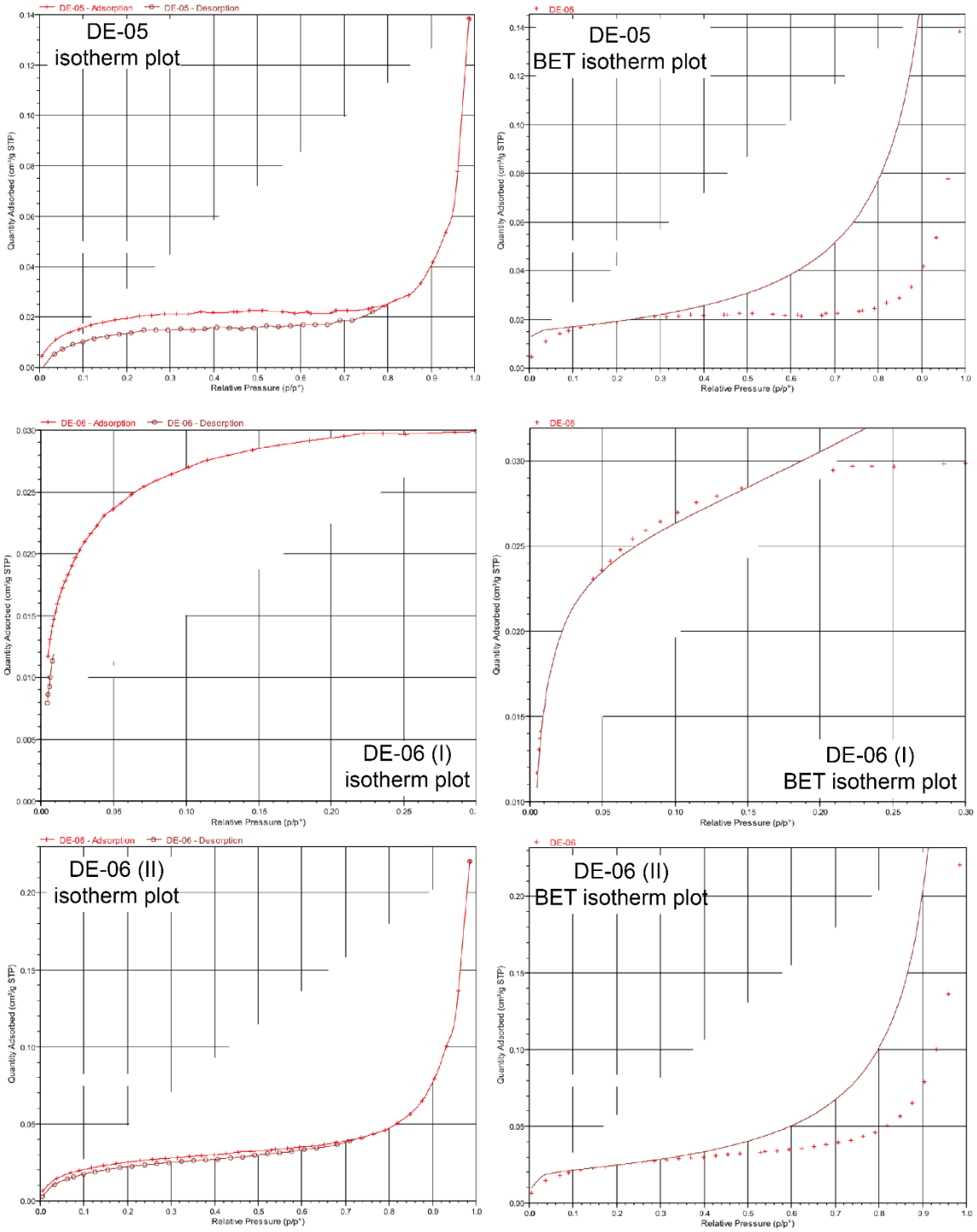

Figure A.2. Isotherm and BET isotherm plots of DE-05, DE-06 (I) and DE-06 (II). Figure 2 of 3.

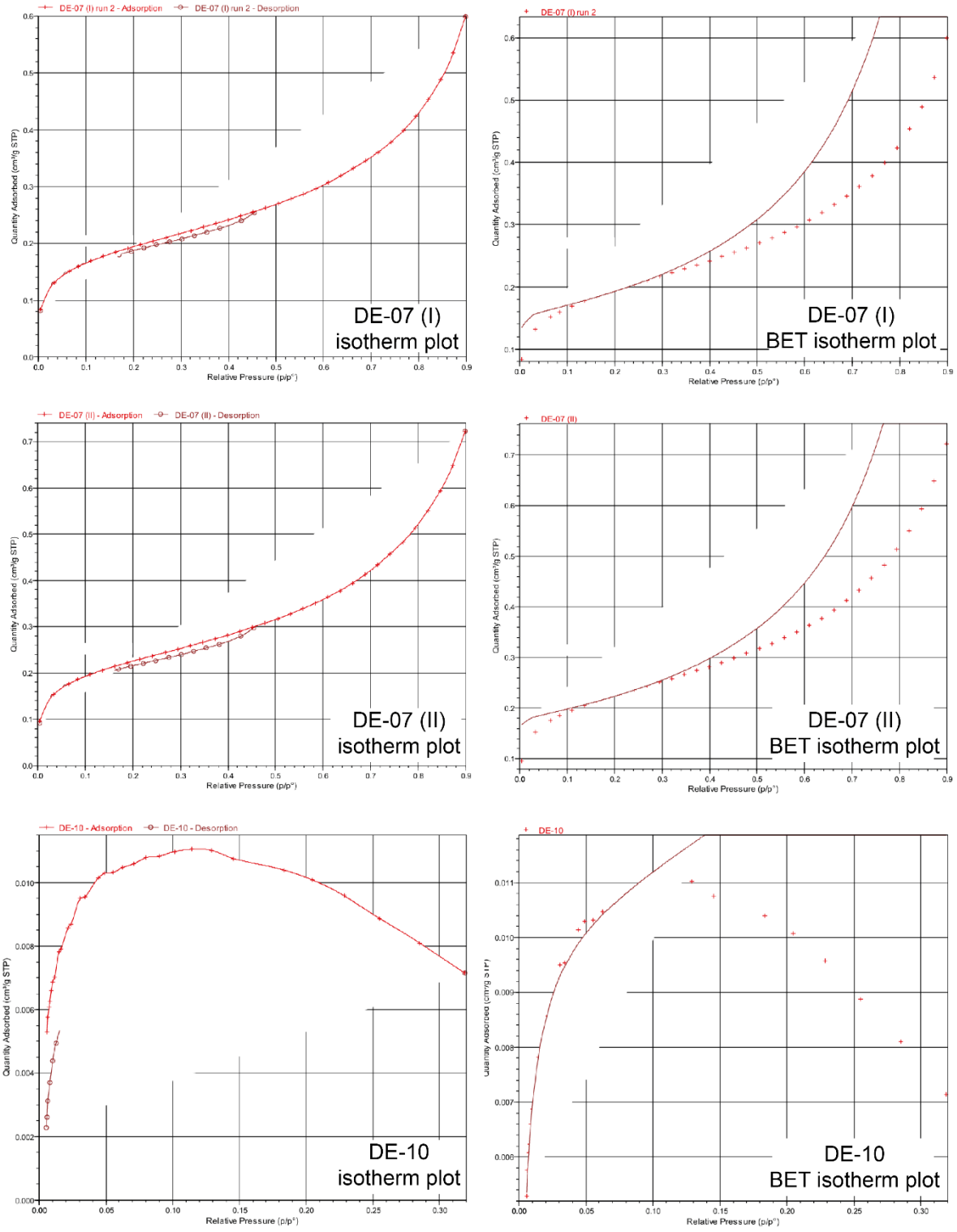

Figure A.3. Isotherm and BET isotherm plots of DE-07 (I), DE-07 (II) and DE-10. Figure 3 of 3.

A.2 LA-ICP-MS quality control

Table A.2 Average element concentrations of rock standards GSD-1G and OREAS-993. Five measurements were taken at the beginning and end of every run. Note GSD-1G is used as a calibration standard, with OREAS-993 used as an external standard for accuracy and reproducibility for Si, Se, Mo, Ag, Cd, In, Au, Pb and Bi. %RE – percentage relative error with respect to recommended published values. ± indicates one standard deviation.

wt.%	Average (n=30)	GSD-1G	%RE	Average (n=30)	OREAS-993	%RE
Al	7.16 ± 0.07	7.09 ± 0.11	-0.93	1.66 ± 0.08	1.60 ± 0.03	-3.74
Si	23.0 ± 1.4	24.9 ± 0.2	7.48	6.6 ± 0.3	4.9 ± 1.0	-33.27
Ca	5.19 ± 0.04	5.15 ± 1.03	-0.95	0.8 ± 1.0	0.7 ± 0.1	-13.36
Cu				21.9 ± 0.9	23.9 ± 0.5	8.57
ppm	**Average (n=30)**	**GSD-1G**	**%RE**	**Average (n=30)**	**OREAS-993**	**%RE**
Mn	209 ± 9	197 ± 43	-6.08	120 ± 10	77 ± 15	-57.61
Co	41 ± 1	39 ± 1	-4.04	95 ± 4	95 ± 19	-0.28
Ni	59 ± 2	55 ± 5	-8.68	54 ± 4	52 ± 10	-4.51
Cu	41 ± 1	41 ± 1	1.05			
Zn	49 ± 1	54 ± 5	8.76	1100 ± 100	885 ± 177	-25.81
As	25 ± 1	27 ± 4	7.00	138 ± 7	143 ± 29	3.31
Se	3 ± 2	2 ± 0	-42.07	198 ± 9	194 ± 39	-1.85
Mo	40 ± 2	37 ± 2	-6.58	2400 ± 200	2512 ± 251	2.77
Ag	25 ± 2	23 ± 2	-7.29	46 ± 3	42 ± 1	-9.83
Cd	22 ± 1	17 ± 3	-26.91	10 ± 1	6 ± 1	-60.98
In	38 ± 1	37 ± 2	-3.83	1.57 ± 0.04	1.54 ± 0.31	-1.81
Sb	33 ± 1	40 ± 4	18.81	54 ± 7	55 ± 6	1.27
Te	N/A	N/A	N/A	11 ± 1	13 ± 3	16.86
La	39.2 ± 0.4	40.5 ± 1.5	3.12	10 ± 2	10 ± 1	-1.57
Ce	41.7 ± 0.4	41.7 ± 0.3	0.11	18 ± 3	18 ± 2	1.92
Pr	45.3 ± 0.4	45.5 ± 0.5	0.36	1.9 ± 0.4	2.0 ± 0.2	3.44
Nd	44.7 ± 0.6	44.4 ± 0.4	-0.81	7 ± 2	8 ± 1	0.99
Sm	47.7 ± 0.5	46.9 ± 0.9	-1.72	1.5 ± 0.3	1.5 ± 0.2	4.17
Eu	41.2 ± 0.4	42.1 ± 2.0	2.11	0.4 ± 0.1	0.4 ± 0.0	2.20
Gd	50.3 ± 0.6	49.4 ± 1.4	-1.81	1.3 ± 0.2	1.3 ± 0.1	2.53
Tb	48.4 ± 0.8	47.5 ± 0.5	-1.89	0.17 ± 0.03	0.17 ± 0.02	-1.90
Dy	51.3 ± 0.5	51.1 ± 0.1	-0.43	1.0 ± 0.2	1.0 ± 0.1	1.12
Er	39.4 ± 0.6	38.1 ± 2.1	-3.49	0.6 ± 0.1	0.5 ± 0.1	-6.01
Yb	50.7 ± 0.6	50.6 ± 0.6	-0.21	0.54 ± 0.07	0.53 ± 0.05	-1.17
Au	6.3 ± 0.4	4.4 ± 0.7	-42.76	51 ± 9	55 ± 1	7.06
Pb	41 ± 1	50 ± 2	17.92	250 ± 10	230 ± 23	-8.34
Bi	24 ± 1	33 ± 2	28.75	23 ± 2	24 ± 2	2.09

Table A.3. Average element concentrations of rock standards JMn-1 and NOD-A-1. Five measurements were taken at the beginning and end of every run. Note Nod-A-1 is used as a calibration standard, with JMn-1 used as an external standard for accuracy and reproducibility for Al, Ca, Mn, Ni, Cu, Co, Cu, Zn, As, Sb, Te and REEs. %RE – percentage relative error with respect to recommended published values. ± indicates one standard deviation.

wt.%	Average (n=30)	JMn-1	%RE	Average (n=30)	Nod-A-1	%RE
Al	2.18 ± 0.02	2.27 ± 0.23	3.77	2.01 ± 0.03	2.05 ± 0.03	1.87
Si	9.5 ± 0.2	6.6 ± 0.7	-44.13	3.5 ± 0.6	1.8 ± 0.0	-94.61
Ca	2.09 ± 0.02	2.08 ± 0.21	-0.50	11.2 ± 0.1	11.0 ± 0.0	-1.47
Mn	23.1 ± 1.3	25.4 ± 0.4	9.05	16.6 ± 1.7	18.3 ± 0.4	9.20
Ni	1.26 ± 0.02	1.26 ± 0.08	0.62	0.62 ± 0.01	0.64 ± 0.00	9.20
Cu	1.11 ± 0.03	1.11 ± 0.10	0.10			
ppm	**Average (n=30)**	**JMn-1**	**%RE**	**Average (n=30)**	**Nod-A-1**	**%RE**
Co	1710 ± 32	1730 ± 70	1.32	3060 ± 60	3110 ± 11	1.62
Cu				1140 ± 30	1100 ± 10	-4.07
Zn	1270 ± 30	1070 ± 110	-18.61	610 ± 20	590 ± 5	-3.64
As	78 ± 2	75 ± 4	-2.92	270 ± 20	310 ± 8	12.14
Mo	370 ± 21	320 ± 20	-17.58	420 ± 20	448 ± 9	6.96
Ag				0.03 ± 0.04	0.17 ± 0.02	81.03
Cd	10.4 ± 1.2	16.7 ± 3.3	37.58	5.0 ± 0.8	6.8 ± N/A	26.75
Sb	39 ± 1	38 ± 2	-3.05	36 ± 1	34 ± 0	-6.83
Te	4.3 ± 0.3	4.3 ± 0.2	0.50	32 ± 1	31 ± 0	-2.78
La	120 ± 2	122 ± 3	1.79	116 ± 2	112 ± 3	-3.67
Ce	266 ± 4	277 ± 12	3.82	747 ± 16	743 ± 21	-0.60
Pr	30.4 ± 0.6	31.4 ± 1.4	3.22	24.3 ± 0.3	24.3 ± 0.7	0.07
Nd	130 ± 2	137 ± 8	5.44	103 ± 3	93 ± 4	-10.94
Sm	29.4 ± 0.6	30.2 ± 1.1	2.57	22.6 ± 0.7	21.0 ± 2.1	-7.53
Eu	7.2 ± 0.2	7.6 ± 0.3	4.43	5.5 ± 0.2	5.0 ± 0.5	-9.37
Gd	30.3 ± 0.7	29.8 ± 2.5	-1.62	25.7 ± 0.5	24.9 ± 0.8	-3.35
Tb	4.5 ± 0.1	4.8 ± 0.4	5.50	3.9 ± 0.1	3.9 ± 0.1	1.19
Dy	27.2 ± 0.6	28.3 ± 1.9	4.06	23.5 ± 0.5	23.5 ± 0.7	-0.10
Er	14.8 ± 0.3	14.6 ± 1.9	-1.42	14.4 ± 0.9	14.6 ± 0.4	1.05
Yb	13.7 ± 0.4	13.8 ± 0.6	1.03	13.9 ± 0.3	13.7 ± 0.3	-1.26
Pb	500 ± 20	430 ± 25	-15.50	910 ± 30	850 ± 10	-7.26
Bi	4.6 ± 0.1	4.3 ± 0.1	-6.14	9.6 ± 0.3	10.2 ± 0.1	5.40

Table A.4. Average element concentrations of rock standard FeMnOx-1 compared with published values. Five measurements were taken at the beginning and end of every run with the exception of run one when only three measurements were taken. Note, FeMnOx-1 is used as a calibration standard and should not be used for accuracy and reproducibility checking. %RE – percentage relative error with respect to recommended published values. ± indicates one standard deviation.

wt.%	**Average (n=27)**	**FeMnOx-1**	**%RE**
Al	1.91 ± 0.01	1.95 ± 0.04	2.35
Si	9.8 ± 0.2	9.8 ± 0.3	0.04
Ca	2.82 ± 0.09	2.88 ± 0.15	2.15
Mn	18.8 ± 1.1	20.6 ± 1.0	8.82
ppm	**Average (n=27)**	**FeMnOx-1**	**%RE**
Zn	1400 ± 100	1508 ± 153	5.00
La	690 ± 14	666 ± 42	-3.64
Ce	650 ± 11	630 ± 39	-3.15
Pr	680 ± 15	660 ± 33	-2.98
Nd	652 ± 7	616 ± 40	-5.82
Sm	589 ± 7	565 ± 34	-4.21
Eu	568 ± 12	537 ± 26	-5.84
Gd	557 ± 8	535 ± 27	-4.20
Tb	558 ± 8	538 ± 33	-3.69
Dy	584 ± 7	568 ± 34	-2.77
Er	600 ± 8	584 ± 40	-2.74
Yb	589 ± 9	565 ± 37	-4.27
Pb	1800 ± 100	1624 ± 280	-10.04

A.3 ICP-MS and ICP-OES quality control for Chapter 4

Table A.5. Average of measured trace element concentrations of rock standard RTS-1. These were run as triplicates and their recommended published values for accuracy and reproducibility checking. Elements with an asterisk (*) were obtained from a separate run on the ICP-OES where there were only duplicates of RTS-1. Values with (**) are indicative and not certified. %RE – percentage relative error with respect to certified/recommended published values. ± indicates one standard deviation.

wt.%	Average (n = 3)	RTS-1	%RE
Na**	0.66 ± 0.14	0.50	-31.9
Mg*	2.69 ± 0.08	2.67 ± 0.07	-0.7
Al	3.80 ± 0.10	4.26 ± 0.15	9.7
Ca	3.20 ± 0.20	2.70 ± 0.09	-19.7
Mn**	0.26 ± 0.02	0.20 ± 0.00	-36.6
Fe*	18.05 ± 0.44	19.6 ± 0.71	8.1
ppm	Average (n = 3)	RTS-1	%RE
Cu	719 ± 64	600 ± 20	-20.8
Co	12 ± 3	16.6 ± 3.9	20.8
Ni	17 ± 6	22 ± 7.0	20.8
Ti*	4140 ± 540	4000	-3.5
Zn	520 ± 80	550 ± 30	6.1
As	10 ± 3	8.2 ± 1.6	-20.3
Sr**	72 ± 13	60	-20.2
Cd**	0.4 ± 0.3	2	78

Table A.6. Average of measure trace element concentrations of rock standard CH-4 & NOD-A-1. These were run as unknowns and their recommended published values for accuracy checking. Elements with an asterisk (*) were not able to be measured for CRM CH-4 due to no sample remaining during ICP-OES run. Elements with two asterisks (**) are indicative. ± indicates one standard deviation.

Wt.%	Measured	CH-4	%RE	Measured	NOD-A-1	%RE
Na	3.69 ± 0.02	0.86 ± 0.02	-	0.88 ± 0.01	0.74 ± 0.01	-19
Mg*	N/A	N/A	N/A	2.87 ± 0.17	2.87 ± 0.01	0.1
Al	8.40 ± 0.60	7.73 ± 0.45	-8.5	2.00 ± 0.20	2.05 ± 0.03	0.8
Ca	2.19 ± 0.02	1.96 ± 0.13	-12	11.66 ± 0.02	11.01 ± 0.04	-5.9
Mn	0.046 ±	0.043 ± 0.050	-6.8	18.99 ± 0.06	18.30 ± 0.40	-3.8
Fe*	N/A	N/A	N/A	11.14 ± 0.06	10.90 ± 0.04	-2.0
Ni*	N/A	N/A	N/A	0.70 ± 0.06	0.60 ± 0.00	-6.2
Cu	0.22 ± 0.01	0.20 ± 0.01	-12.3	0.117 ± 0.000	0.110 ± 0.001	-6.0
ppm	Measured	CH-4	%RE	Measured	NOD-A-1	%RE
Li	12.8 ± 0.08	12 ± 2	-6.9	63.6 ± 0.5	76.1 ± 0.8	16.3
Sc	10.9 ± 0.6	13 ± 1	16	10.8 ± 0.5	12.4 ± 0.3	13
Ti*	N/A	N/A	N/A	2920 ± 8	3177 ± 42	8.0
Co	21 ± 0.4	26 ± 2	19.0	2567 ± 25	3110 ± 11	17.5
Ni	49 ± 3	51 ± 4	3.9			
Mn	860 ± 10	430 ± 50	-			
Zn	191 ± 5	200 ± 20	4.7	509 ± 6	590 ± 5	13.8
As	8.8 ± 0.1	8.8 ± 1.7	0.1	258 ± 3	310 ± 8	16.9
Sr	222 ± 0.9	209 ± 20	-6.7	1560 ± 18	1750 ± 14	10.9
Nb	3.5 ± 0.1	4.0 ± 0.5	12.3	38.2 ± 0.5	43.1 ± 1.1	11.4
Cd	1.03 ± 0.04	1.14 ± 0.15	9.9	6.7 ± 0.1	6.8**	1.2
Sb	0.9 ± 0.1	0.77 ± 0.6	-12.5	33.3 ± 0.7	33.8 ± 0.1	1.4
Ba	450 ± 9	425 ± 60	-7	1393 ± 7	1670 ± 31	16.5
La	14.9 ± 0.1	16 ± 3	6.7	100.2 ± 0.5	112 ± 3.4	10.5
Ce	31.1 ± 0.3	35 ± 5.0	11.2	680 ± 9.9	743 ± 20.8	9.0
Pr	3.72 ± 0.04	4.0 ± 0.3	6.9	22.6 ± 0.1	24.3 ± 0.7	6.8
Nd	14.59 ± 0.1	16 ± 1	8.8	94.1 ± 0.9	93 ± 4.5	-1.2
Sm	2.97 ± 0.04	3.0 ± 0.2	1.1	21.1 ± 0.1	21.0 ± 0.0	-0.4
Eu	0.65 ± 0.04	0.7 ± 0.1	6.6	5.0 ± 0.1	5.0 ± 0.0	-0.1
Gd	2.70 ± 0.02	3.0 ± 0.2	10.0	24.9 ± 0.1	24.9 ± 0.8	0.0
Tb	0.37 ± 0.01	0.4 ± 0.1	7.3	3.62 ± 0.02	3.9 ± 0.1	7.1
Dy	2.33 ± 0.04	2.0 ± 0.2	-16.4	23.7 ± 0.1	23.5 ± 0.7	-0.7
Ho	0.45 ± 0.01	0.40 ± 0.03	-11.3	4.82 ± 0.02	4.9 ± 0.2	1.6
Er	1.25 ± 0.01	1.2 ± 0.1	-4.4	14.1 ± 0.1	14.6 ± 0.4	3.3
Tm	0.19 ± 0.01	0.20 ± 0.01	7.0	2.06 ± 0.02	2.1 ± 0.1	1.3
Yb	1.21 ± 0.04	1.0 ± 0.1	-21.4	13.3 ± 0.3	13.7 ± 0.3	2.8
Lu	0.19 ± 0.00	0.20 ± 0.02	4.8	2.17 ± 0.02	2.2 ± 0.1	1.2
W	5.8 ± 0.07	3 ± 1	-93	93 ± 1	87 ± 0.8	-7.4
Pb	17.5 ± 0.2	14 ± 7	-25.1	850 ± 15	846 ± 8	-0.4
Bi	0.61 ± 0.02	0.6 ± 0.2	-1.7	10.7 ± 0.2	10.2 ± 0.1	-5.2
Th	2.47 ± 0.05	2.0 ± 0.2	-23.3	23.9 ± 0.4	23.4 ± 0.5	-2.1
U	0.85 ± 0.02	0.7 ± 0.3	-21.7	7.9 ± 0.1	7.0 ± 0.2	-12.7

Table A.7. Average of measure trace element concentrations of rock standard NOD-P-1 & GSPN-3. These were run as unknowns and their recommended published values for accuracy checking. %RE – percentage relative error with respect to certified/recommended published values. ± indicates one standard deviation.

	Measured	NOD-P-1	%RE	Measured	GSPN-3	%RE
Na	1.78 ± 0.01	1.71 ± 0.02	-4.0	3.20 ± 0.03	2.25 ± 0.1	-42.2
Mg	2.00 ± 0.20	2.00 ± 0.07	0.2	2.00 ± 0.1	2.10 ± 0.08	7.2
Al	2.50 ± 0.23	2.46 ± 0.10	-1.0	2.20 ± 0.21	2.49 ± 0.16	11.1
Ca	2.38 ± 0.02	2.24 ± 0.01	-6.1	2.22 ± 0.03	1.60 ± 0.10	-38.5
Mn	27.68 ± 0.04	29.60 ± 0.10	6.5	29.21 ± 0.05	32.2 ± 0.50	9.3
Fe	6.10 ± 0.40	5.90 ± 0.04	-4.1	4.50 ± 0.28	4.70 ± 0.19	4.4
Ni	1.40 ± 0.16	1.30 ± 0.01	-5.4	1.60 ± 0.13	1.60 ± 0.07	-1.3
Cu	1.19 ± 0.01	1.15 ± 0.00	-3.3	1.40 ± 0.01	1.36 ± 0.05	-3.1
	Measured	NOD-P-1	%RE	Measured	GSPN-3	%RE
Li	130 ± 4	140 ± 1	6.9	196 ± 3	205 ± 17	4.2
Sc	10.0 ± 0.7	9.7 ± 0.1	-3.5	9.6 ± 0.5	9.4 ± 1	-1.8
Ti	2720 ± 70	2720 ± 40	0.0	2950 ± 8	3237 ± 240	8.9
Co	1940 ± 32	2240 ± 11	13.4	1375 ± 36	1700 ± 100	19.1
Zn	1410 ± 31	1600 ± 6	11.6	1400 ± 36.3	1600 ± 200	12.2
As	76.7 ± 0.6	88.50 ± 3.9	13.4	52.8 ± 0.4	53 ± 5	0.4
Sr	665 ± 2.1	680 ± 3.0	2.3	613 ± 3.8	561 ± 62.0	-9.3
Nb	18.3 ± 0.5	21.30 ± 0.1	14.0	17.1 ± 0.3	21.0 ± 3.0	18.8
Cd	20.6 ± 0.3	22.6 ± 0.3	8.7	19.9 ± 0.2	23 ± 3	13.4
Sb	49.4 ± 0.9	49.40 ± 1.4	0.1	46.2 ± 1.2	46.0 ± 9.0	-0.5
Ba	2460 ± 55	3350 ± 28	26.7	2220 ± 37	2400 ± 200	7.6
La	98 ± 1.5	104.0 ± 0.0	6.1	84.6 ± 0.8	96.0 ± 10.0	11.8
Ce	294 ± 4.8	290.0 ± 0.0	-1.5	232 ± 2.5	249.0 ± 21.0	6.9
Pr	30.2 ± 0.4	31.0 ± 0.2	2.5	27.7 ± 0.2	29.0 ± 2.0	4.3
Nd	127 ± 1.5	120.0 ± 0.0	-5.6	116 ± 1.1	121.0 ± 15.0	4.2
Sm	31.2 ± 0.4	30.0 ± 0.3	-4.0	29.3 ± 0.2	31.0 ± 2.0	5.4
Eu	7.4 ± 0.1	7.5 ± 0.1	1.7	7.0 ± 0.1	7.6 ± 0.7	7.5
Gd	30.4 ± 0.2	28.0 ± 0.5	-8.7	28.6 ± 0.2	28.0 ± 4.0	-2.2
Tb	4.53 ± 0.03	4.90 ± 0.0	7.6	4.4 ± 0.03	4.6 ± 0.5	4.3
Dy	27.3 ± 0.2	27.0 ± 0.0	-1.1	26.7 ± 0.2	27.0 ± 3.0	1.0
Ho	4.95 ± 0.04	5.0 ± 0.0	1.0	4.8 ± 0.1	5.1 ± 0.3	5.9
Er	13.4 ± 0.2	13.6 ± 0.1	1.3	13.0 ± 0.1	13.0 ± 1.0	-0.1
Tm	1.93 ± 0.01	1.90 ± 0.0	-1.5	1.89 ± 0.03	1.9 ± 0.1	0.3
Yb	12.6 ± 0.3	13.0 ± 0.0	3.2	12.3 ± 0.3	12.0 ± 1.0	-2.6
Lu	1.93 ± 0.03	1.80 ± 0.0	-7.3	1.87 ± 0.03	1.8 ± 0.2	-4.0
W	66 ± 1	57.8 ± 1.1	-15	74 ± 1	61 ± 5	21.7
Pb	460 ± 4.0	56 ± 6	17.9	307 ± 1.1	328.0 ± 33.0	6.5
Bi	0.61 ± 0.02	0.6 ± 0.2	-1.7	10.7 ± 0.2	10.2 ± 0.1	-5.2
Th	2.47 ± 0.05	2.00 ± 0.2	-23.3	23.9 ± 0.4	23.4 ± 0.5	-2.1
U	4.60 ± 0.1	4.00 ± 0.04	-14.9	4.25 ± 0.03	3.8 ± 0.7	-11.9

A.4 ICP-MS and ICP-OES quality control for bulk analyses in Chapter 6

Table A.8. Average and one standard deviation (±) of measure trace element concentrations of CRMs for bulk sample analysis in ppm. %RE – percentage relative error with respect to certified/recommended published values. ± indicates one standard deviation. Sb* and Cd*, these values are informational for RTS-1. Zn[a] – Data shows two measurements of RTS-1 as the third measurement was anomalous at a reported measurement of 755 ppm.

	OREAS 620			**OREAS 908**		
ppm	Average (n=3)	Reported	%Error	Average (n=3)	Reported	%Error
Cu	1670 ± 20	1730 ± 40	3.7	12450 ± 70	12600 ± 290	1.2
Fe	28900 ± 400	29400 ± 1440	1.6	147000 ± 1000	146400 ± 7050	-0.4
Pb	7150 ± 70	7740 ± 220	7.7	61 ± 0.2	65 ± 3.4	6.7
Zn	28700 ± 200	31500 ± 970	8.7	280 ± 20	285 ± 10	1.4
Sb	71 ± 1	76 ± 8	6.0	4.94 ± 0.07	5.2 ± 0.35	4.9
Cd	150 ± 2	163 ± 8	8.2	0.784 ± 0.003	0.79 ± 0.08	0.8
As	17.7 ± 0.4	50 ± 4.4	64.6	60.9 ± 0.3	65 ± 2.1	6.3
	RTS-1			**CH-4**		
ppm	Average (n=3)	Reported	%Error	Measured	Reported	%Error
Cu	610 ± 20	595 ± 18	2.1	1980 ± 15	2000 ± 100	1.2
Fe	190000 ± 3000	196400 ± 7100	3.4	51600 ± 300	54200 ± 1800	4.8
Pb	83 ± 1	105 ± 18	20.6	17.0 ± 0.3	14 ± 7	21.5
Zn[a]	556 ± 20	553 ± 31	0.6	340 ± 13	200 ± 20	-71.5
Sb	1.21 ± 0.01	N/A		0.8 ± 0.9	0.77 ± 0.58	-2.5
Cd*	0.29 ± 0.02	2	85.6	1.090 ± 0.009	1.14 ± 0.15	4.4
As	9.2 ± 0.3	8.2 ± 1.6	12.7	9.05 ± 0.05	8.8 ± 1.7	-2.9

A.5 Duplicate bulk geochemical analysis for Chapter 4

Table A.9. %RSD of each element by duplicate measurements of listed samples. Where %RSD is shown as 0, this indicates that the duplicates measured the same relative to the accuracy/precision of each element. Full data of each sample shown in Bishop et al., 2025b.

Element	28_DR_03	28_DR_04	66_HY_05	71_DR_07	82_HY_05	82_HY_06a	82_HY_06b	102_HY_03	102_HY_05	Average
Li	0	0	28.57	6.99	0	0	0	40	0	8.40
Na	3.01	2	4.88	0.62	94.25	1.83	0	28.57	2.9	15.34
Mg	4.88	3.51	3.97	2.56	2.3	0	0	7.06	3.39	3.07
Al	0	0	13.33	8	4.44	0	0	29.41	0	6.13
Ca	3.92	4.44	4.14	16.39	110.64	4.65	0	31.58	0	19.53
Sc	8.7	0	8.7	0	7.41	0	0	16.67	0	4.61
Ti	13.33	0	0	0	0	0	66.67	10.26	0	10.03
Mn	3.55	0	25.64	6.75	0	0	0	20.08	15.38	7.93
Fe	4.31	0.24	0.27	0.49	1.94	4.93	4.21	5.91	2.79	2.79
Co	3.06	0	0	11.76	0	0	0	14.72	1.8	3.48
Ni	0	0	18.18	0	40	0	0	33.33	66.67	17.58
Cu	2.06	39.71	5.65	0	3.06	0.89	2.74	27.59	11.76	10.38
Zn	6.4	2.44	2.82	6.67	8	1.1	2.75	27.05	1.99	6.58
As	3.08	3.44	1.66	5.13	0.28	0.61	22.78	26.22	4.12	7.48
Sr	2.74	1.12	3.64	5.13	36.07	0	0	25	4.88	8.73
Nb	0	0	0	0	0	0	0	24.56	0	2.73
Cd	9.52	66.67	0	22.22	76.92	7.41	0	28.57	22.22	25.95
Sb	7.49	2.53	1.23	10.91	0.59	0	4.04	27.54	4.12	6.49
Ba	2.04	4.18	11.36	23.73	4.91	22.22	0	25.93	13.56	11.99
La	2.53	7.14	2.6	3.51	3.66	0	0	20.58	3.17	4.80
Ce	1.42	10	2.67	3.08	1.8	0	0	20.13	0	4.34
Pr	1.1	7.41	2.87	1.57	1.89	0	0	20.67	2.56	4.23
Nd	0	4.26	2.78	3.77	0.74	0	0	20.88	0	3.60
Sm	0	0	6.45	0	0	0	0	23.42	0	3.32
Eu	0	3.15	5.61	6.45	0	28.57	0	23.5	2.11	7.71
Gd	0.53	2.86	3.41	3.17	0.56	0	0	22	1.07	3.73
Tb	0	10.53	0	0	0	40	0	25	7.41	9.22
Dy	1.14	3.17	1.77	3.51	1.03	5.71	0	23.49	1.08	4.54
Ho	0	0	2.82	0	1.17	0	0	24.07	5.13	3.69
Er	2.87	4.88	3.88	2.9	1.13	0	0	23.26	1.71	4.51
Tm	0	0	6.9	0	0	0	0	23.81	0	3.41
Yb	1.03	7.06	1.01	6.45	3.39	28.57	200	23.4	1.74	30.29
Lu	0.67	4.58	5.86	0	0.68	11.76	0	24.26	2.17	5.55
W	12.77	7.41	5.41	15.38	0	22.22	16.67	22.73	0	11.40
Pb	3.17	3.29	6.06	8.7	0.39	0.51	2	31.08	6.4	6.84
Bi	0	8	0	0	10.22	3.55	5.71	0	200	25.28
Th	0	0	0	0	0	0	0	28.57	0	3.17
U	0	0	0	0	0	0	0	34.48	5.61	4.45

A.6 Duplicate bulk geochemical analysis for Chapter 6

Table A.10. Measurements of bulk sulphide sample duplicates in ppm by ICP-MS and ICP-OES showing average and %RSD.

ppm	Cu	Fe	Pb	Zn	Sb	Cd	As
DE-03 (I)	92810	111200	3.30	135	0.24	0.65	1.45
DE-03 (II)	100910	119600	3.30	138	0.24	0.75	1.52
Average	96860	115400	3.30	140	0.24	0.70	1.49
%RSD	**5.9**	**5.1**	**0.8**	**1.5**	**0.1**	**10.3**	**3.4**
DE-05 (I)	14560	283000	2750	108900	1.78	370	12.7
DE-05 (II)	13690	323200	2870	105300	1.62	351	14.9
Average	14120	303100	2810	107100	1.70	360	13.8
%RSD	**4.4**	**9.4**	**3.0**	**2.4**	**6.4**	**3.6**	**11.5**
DE-06 (I)	2170	459700	86	66	29.7	0.280	400
DE-06 (II)	1960	451200	86	63	30.2	0.281	273
Average	2060	455500	86	65	30.0	0.280	337
%RSD	**7.3**	**1.3**	**0.1**	**3.1**	**1.3**	**0.2**	**26.7**
DE-07 (I)	22260	394000	807	56600	19.7	204	412
DE-07 (II)	22540	396300	781	55800	20.2	201	387
Average	22400	395100	794	56200	19.9	202	399
%RSD	**0.9**	**0.4**	**2.3**	**0.9**	**1.9**	**1.1**	**4.3**
DE-10 (I)	12790	457300	13.6	75	1.28	0.104	20.2
DE-10 (II)	13210	452100	13.2	71	0.90	0.098	18.0
average	13000	454700	13.4	73	1.09	0.10	19.1
%RSD	**2.3**	**0.8**	**2.2**	**4.3**	**24.2**	**4.3**	**8.1**
Average %RSD	4.2	3.4	1.7	2.4	6.8	3.9	10.8

A.7 ICP-MS quality control for seawater analysis in Chapter 6

Table A.11. Average of measure trace element concentrations of spiked seawater CRM (High-Purity) in ppm. These were run as triplicates for each run. In total there were six runs on the ICP-MS resulting in a total of 18 measurements for each spiked CRM. The calculated concentration of the spiked CRM are presented for accuracy and reproducibility checking. %RE – percentage relative error with respect to certified/recommended published values. ± indicates one standard deviation.

	Sp.1 CRM			Sp.2 CRM			Sp.3 CRM		
ppb	Average (n=18)	Theoretical	%Error	Average (n=18)	Theoretical	%Error	Average (n=18)	Theoretical	%Error
Fe	490 ± 180	258	-90.58	1500 ± 140	1238	-21.70	280 ± 70	68	-313.04
Cu	255 ± 14	234	-9.01	1170 ± 50	1152	-1.68	54 ± 3	55	1.97
Zn	23 ± 2	23	-1.62	93 ± 7	92	-1.05	370 ± 20	357	-4.21
Sb	18.7 ± 0.6	17.7	-5.65	93 ± 4	88	-5.90	360 ± 10	355	-2.11
Pb	183 ± 6	192	4.59	870 ± 40	961	9.21	42 ± 2	41	-1.56
As	75 ± 4	67	-12.86	275 ± 15	257	-6.63	31 ± 2	29	-7.75
Cd	19.0 ± 0.7	17.8	-6.72	92 ± 4	87	-4.49	350 ± 20	355	1.44

A.8 Duplicate experiment seawater analysis for DE-02 in Chapter 6

Table A.12. Measurements of sulphide-seawater experiment of DE-02 for four days.

ppb	Fe	Cu	Zn	Sb	Pb	As	Cd	ppb	Fe	Cu	Zn	Sb	Pb	As	Cd
DE-02 R1 SW 1	18	10	15	0.1	2.4	0.1	0.5	DE-02 R1 - 9	17	34	37	0.1	1.1	0.3	0.4
DE-02 R2 SW 2	74	22	20	0.2	2.5	0.6	1.0	DE-02 R2 - 9	18	89	73	0.2	2.0	0.6	0.8
%RSD	**88**	**54**	**21**	**61.8**	**1.1**	**90.0**	**44.7**	**%RSD**	**5.3**	**63**	**47**	**28.9**	**39**	**58.5**	**52.3**
DE-02 R1 - 1	661	304	17	1.6	3.9	1.5	0.5	DE-02 R1 - 10	-15	43	23	0.2	1.2	0.3	0.4
DE-02 R2 - 1	145	106	266	0.4	5.7	0.7	0.9	DE-02 R2 - 10	35	69	57	0.3	1.5	0.4	0.8
%RSD	**90**	**68**	**124**	**88.5**	**26.6**	**48.4**	**39.6**	**%RSD**	**355**	**33**	**60**	**11.9**	**15**	**34.5**	**42.4**
DE-02 R1 - 2	10	29	29	0.1	1.7	0.1	0.8	DE-02 R1 - 11	58	43	35	0.2	1.5	0.3	0.7
DE-02 R2 - 2	153	202	98	0.3	4.3	1.3	3.6	DE-02 R2 - 11	36	67	36	0.2	0.8	0.3	0.3
%RSD	**125**	**106**	**76**	**83.1**	**61.9**	**114.9**	**89.1**	**%RSD**	**33**	**30**	**1.3**	**13.3**	**45**	**11.9**	**55.5**
DE-02 R1 - 3	38	27	21	0.1	1.6	0.1	1.4	DE-02 R1 - 12	109	44	28	0.3	1.2	0.4	0.4
DE-02 R2 - 3	162	81	190	0.4	4.4	0.9	0.6	DE-02 R2 - 12	22	63	27	0.3	0.7	0.3	0.3
%RSD	**88**	**72**	**113**	**107.1**	**67.5**	**100.7**	**58.1**	**%RSD**	**95**	**26**	**4**	**3.7**	**32**	**9.3**	**13.5**
DE-02 R1 - 4	250	43	90	0.1	1.5	0.3	0.6	DE-02 R1 - 13	36	53	20	0.3	1.2	0.6	0.4
DE-02 R2 - 4	508	162	92	0.8	3.3	1.7	0.8	DE-02 R2 - 13	24	61	37	0.2	0.9	0.3	0.4
%RSD	**48**	**82**	**1.8**	**106.4**	**54.0**	**93.2**	**19.5**	**%RSD**	**30**	**10**	**42**	**34.4**	**24**	**46.2**	**2.3**
DE-02 R1 - 5	461	180	100	1.2	6.9	2.6	6.3	DE-02 R1 - 14	233	60	23	0.3	1.1	0.5	0.4
DE-02 R2 - 5	89	159	187	0.2	2.5	1.1	1.6	DE-02 R2 - 14	39	69	202	0.3	0.8	0.4	0.3
%RSD	**95**	**8.6**	**43**	**107.0**	**66.2**	**55.7**	**84.9**	**%RSD**	**101**	**10**	**112**	**1.9**	**26**	**13.9**	**10.3**
DE-02 R1 - 6	600	210	36	0.9	3.3	0.7	0.8	DE-02 R1 - 15	28	47	28	0.2	1.0	0.4	0.4
DE-02 R2 - 6	2.1	48	54	0.1	1.2	0.3	0.3	DE-02 R2 - 15	-2.2	66	47	0.2	0.7	0.3	0.3
%RSD	**140**	**89**	**29**	**102.5**	**68.0**	**42.9**	**55.5**	**%RSD**	**166**	**23**	**37**	**2.6**	**27**	**20.6**	**12.3**
DE-02 R1 - 7	2.2	36	26	0.1	1.2	0.2	0.5	DE-02 R1 - 16	60	53	29	0.5	1.0	0.6	0.4
DE-02 R2 - 7	54	58	116	0.2	1.3	0.3	0.4	DE-02 R2 - 16	-2.0	67	61	0.3	0.7	0.4	0.3
%RSD	**130**	**32**	**89**	**20.1**	**2.6**	**23.0**	**15.3**	**%RSD**	**151**	**17**	**49**	**32.1**	**25**	**27.4**	**17.3**
DE-02 R1 - 8	53	33	33	0.1	1.2	0.2	0.4								
DE-02 R2 - 8	16	58	38	0.2	1.0	0.3	0.4								
								Median							
%RSD	**76**	**39**	**10**	**57.9**	**10.4**	**21.1**	**9.5**	%RSD	95.4	33.4	45.8	34.4	26.7	42.9	39.6

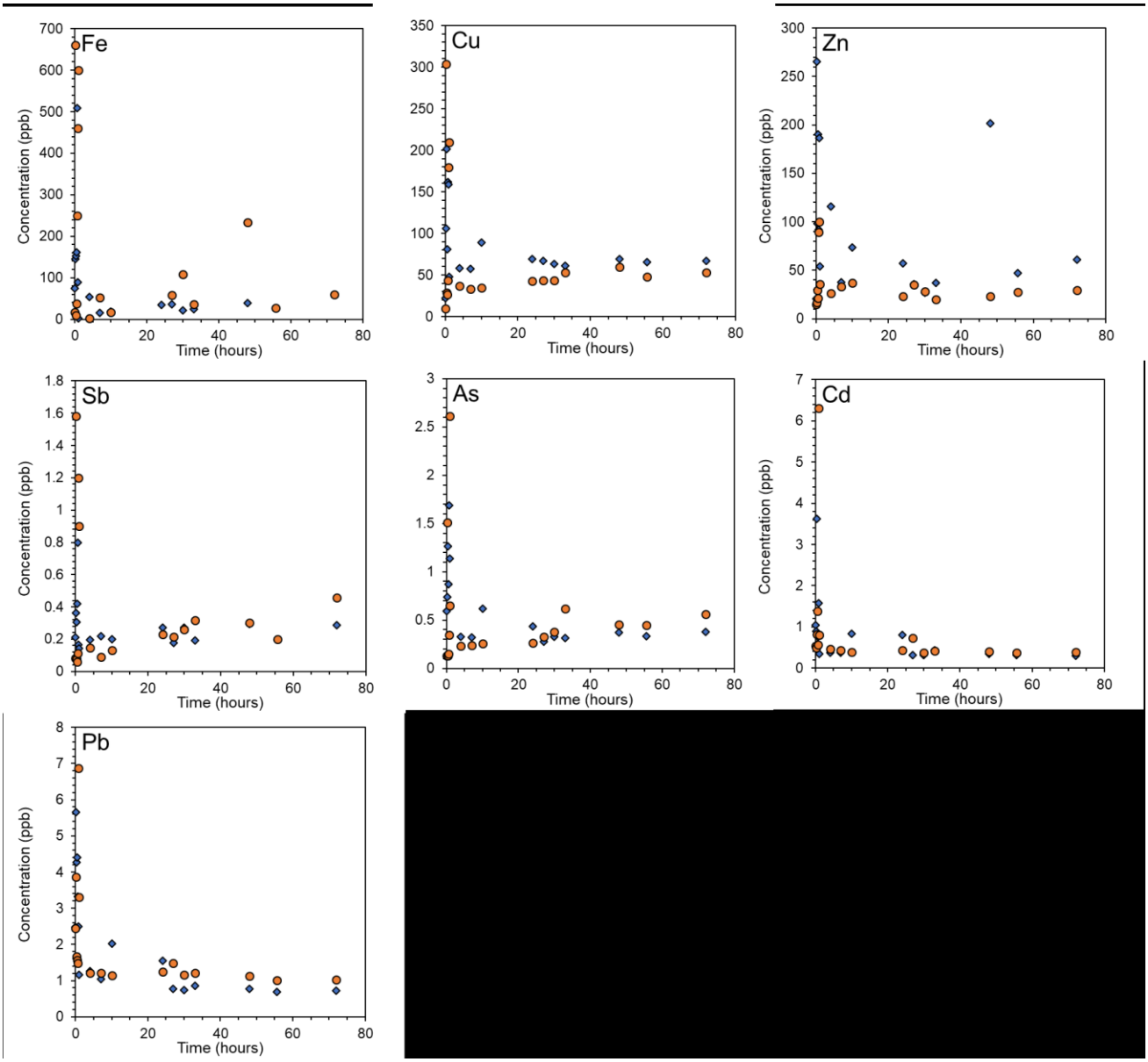

Figure A.4. Duplicate measurements of DE-02 over four days.

A.9 ICP-MS and ICP-OES quality control for sequential leaching in Chapter 5

Table A.13. Average element concentrations of rock standards GSPN-2, JMn-1, RTS-1, CH-4, NOD-P-1 and GSPN-3 compared with published values for accuracy checking. Triplicates were measured for GSPN-2, JMn-1 and RTS-1 for accuracy and reproducibility. %RE – percentage relative error with respect to recommended published values. ± indicates one standard deviation.

wt.%	Average (n = 3)	GSPN-2	%RE	Average (n = 3)	JMn-1	%RE
Al	2.52 ± 0.11	2.75 ± 0.11	9.4	2.22 ± 0.05	2.27 ± 0.08	3.2
Ca	1.68 ± 0.06	1.91 ± 0.13	11.9	2.50 ± 0.17	2.08 ± 0.13	-20.1
Cu	0.69 ± 0.02	0.69 ± 0.04	0.7	1.06 ± 0.02	1.11 ± 0.10	5.1
Fe	10.13 ± 0.10	10.87 ± 0.16	7.3	9.98 ± 0.15	10.07 ± 0.29	0.9
Mn	20.10 ± 0.10	24.70 ± 0.40	22.9	21.44 ± 0.20	25.63 ± 0.43	19.5
ppm	Average (n = 3)	GSPN-2	%RE	Average (n = 3)	JMn-1	%RE
Zn	570 ± 10	918 ± 66	61.0	715 ± 42	1068 ± 109	49.3
Sr	769 ± 5	869 ± 74	13.0	729 ± 10	792 ± 57	8.6

wt.%	Average (n = 3)	RTS-1	%RE	Measured	CH-4	%RE
Al	4.30 ± 0.23	4.26 ± 0.15	1.1	7.67 ± 0.05	7.73 ± 0.45	0.7
Ca	2.97 ± 0.29	2.67 ± 0.09	10.0	2.04 ± 0.01	1.96 ± 0.13	-4.0
Fe	20.79 ± 0.47	19.64 ± 0.71	5.5	5.84 ± 0.02	5.42 ± 0.18	7.2
Cu				0.231 ± 0.002	0.20 ± 0.01	13.3
ppm	Average (n = 3)	RTS-1	%RE	Measured	CH-4	%RE
Cu	674 ± 59	595 ± 18	11.7			
Mn	1780 ± 30	1900	6.8	434 ± 3	430 ± 50	-1.0
Zn	385 ± 22	553 ± 31	43.4	149 ± 0.8	200 ± 20	34.5
Sr	59 ± 1	60	1.7	206 ± 1	209 ± 20	1.5

wt.%	Measured	Nod P-1	%RE	Measured	GSPN-3	%RE
Al	2.31 ± 0.02	2.46 ± 0.10	6.5	2.26 ± 0.02	2.49 ± 0.16	10.2
Ca	2.09 ± 0.04	2.24 ± 0.01	7.1	1.467 ± 0.013	1.608 ± 0.122	9.6
Cu	1.235 ± 0.002	1.150 ± 0.005	6.9	1.418 ± 0.003	1.360 ± 0.050	4.0
Fe	5.97 ± 0.03	5.89 ± 0.04	1.5	4.46 ± 0.02	4.70 ± 0.19	3.0
Mn	26.3 ± 0.2	29.60 ± 0.13	12.5	27.5 ± 0.4	32.2 ± 0.5	17.3
ppm	Measured	Nod P-1	%RE	Measured	GSPN-3	%RE
Zn	1050 ± 2	1600 ± 6	52.4	1045 ± 2	1600 ± 200	53.2
Sr	613 ± 8	680 ± 3	10.9	518 ± 5	561 ± 62	8.3

A.10 Sequential leaching duplicate analysis for Chapter 5

Table A.14. Duplicate testing of 82_HY_06 and 86_HY_04 to determine reproducibility of the experiment. The majority of elements and leach steps 2, 3 and 4 exhibit good precision. Leach step 1 typically is poor due to these elements lying close or below the limit of detection. Ca exhibits poor reproducibility. *86_HY_04 (2) tube cracked during experiment, resulting in a loss of fluid that has led to the poor results.

ppm	Al (ppm)	Cu (ppm)	Fe (ppm)	Mn (ppm)	Ca (ppm)	Sr (ppm)	Zn (ppm)
82_HY_06$_a$ (1) - Leach 1	200	<100	300	40	117800	213	<LOD
82_HY_06$_a$ (2) - Leach 1	50	100	100	20	50100	102	<LOD
Average	125	100	200	30	83950	158	N/A
Standard deviation	106	N/A	141	14	47871	78	N/A
% standard deviation	84.85	N/A	70.71	47.14	57.02	49.83	N/A
82_HY_06$_a$ (1) - Leach 2	30	125700	2100	50	670	27	307
82_HY_06$_a$ (2) - Leach 2	<LOD	128500	2200	60	650	26	314
Average	30	127100	2150	55	660	27	311
Standard deviation	N/A	1980	71	7	14	1	5
% standard deviation	N/A	1.56	3.29	12.86	2.14	2.67	1.59
82_HY_06$_a$ (1) - Leach 3	350	30200	294100	120	9500	39	1010
82_HY_06$_a$ (2) - Leach 3	300	29800	286600	120	700	19	990
Average	325	30000	290350	120	5100	29	1000
Standard deviation	35	283	5303	0	6223	14	14
% standard deviation	10.88	0.94	1.83	0.00	122.01	48.77	1.41
82_HY_06$_a$ (1) - Leach 4	80	3200	64500	<LOD	5000	25	360
82_HY_06$_a$ (2) - Leach 4	30	3000	60300	<LOD	400	9	340
Average	55	3100	62400	N/A	2700	17	350
Standard deviation	35	141	2970	N/A	3253	11	14
% standard deviation	64	5	5	N/A	120	67	4
86_HY_04 (1) - Leach 1	<LOD	<100	<LOD	<LOD	4600	76	<LOD
86_HY_04 (2) - Leach 1	19	100	<LOD	10	5500	76	<LOD
Average	19	100	N/A	10	5050	76	N/A
Standard deviation	N/A	N/A	N/A	N/A	636	0	N/A
% standard deviation	N/A	N/A	N/A	N/A	12.60	0.00	N/A
86_HY_04 (1) - Leach 2	150	12000	1200	50	2100	21	350
86_HY_04 (2) - Leach 2	170	11300	900	50	4600	21	351
Average	160	11650	1050	50	3350	21	351
Standard deviation	14	495	212	0	1768	0	1
% standard deviation	8.84	4.25	20.20	0.00	52.77	0.00	0.20
86_HY_04 (1) - Leach 3	1240	13800	327400	2170	1300	114	2360
86_HY_04 (2) - Leach 3	1300	13700	328400	2130	500	113	2390
Average	1270	13750	327900	2150	900	114	2375
Standard deviation	42	71	707	28	566	1	21
% standard deviation	3.34	0.51	0.22	1.32	62.85	0.62	0.89
86_HY_04 (1)- Leach 4	220	900	59800	10	3900	16	580
86_HY_04 (2)- Leach 4*	80	400	24000	10	600	11	220
Average	150	650	41900	10	2250	14	400
Standard deviation	99	354	25314	0	2333	4	255
% standard deviation	66.00	54.39	60.42	0.00	103.71	26.19	63.64

A.11 Sequential leaching control test and blank analysis for Chapter 5

Table A.15. Geochemical analysis of control sample (82_HY_06a) and analysis of leach solutions. Control test reveals that minerals bearing Cu, Fe, Mn, Zn or Al do not come out of solution through the action of shaking. Analysis of blanks indicate there is no chemical contamination, however leach 1 for Zn shows some contamination.

ppm	Ca (ppm)	Al (ppm)	Cu (ppm)	Fe (ppm)	Mn (ppm)	Sr (ppm)	Zn (ppm)
82_HY_06a (control) - 1 hour	70800	<LOD	<LOD	<LOD	<LOD	2168	1
82_HY_06a (control) - 24 hours	69600	<LOD	<LOD	<LOD	<LOD	2171	1
82_HY_06a (control) - 4 hours	70900	5	<LOD	<10	10	2235	<LOD
82_HY_06a (control) - 48 hours	67200	<LOD	5	<LOD	10	2099	<LOD
Blank - Leach 1 (1)	<1	<1	<LOD	<LOD	<1	<1	<LOD
Blank - Leach 1 (2)	<LOD	<LOD	<1	<LOD	<1	<LOD	8
Blank - Leach 1 (3)	3	<1	<1	<LOD	<1	<1	<LOD
Blank - Leach 1 average	<3	<1	<1	<1	<1	<1	8
Blank - Leach 2 (1)	<LOD	<1	<1	<1	<LOD	<1	<LOD
Blank - Leach 2 (2)	<LOD	<LOD	<LOD	<LOD	<LOD	<LOD	<1
Blank - Leach 2 (3)	2	<1	<LOD	<1	<LOD	<1	<LOD
Blank - Leach 2 average	<2	<1	<1	<1	<1	<1	<1
Blank - Leach 3 (1)	<LOD	<1	<LOD	<1	<1	<1	<1
Blank - Leach 3 (2)	2	<1	<LOD	<1	<LOD	<1	<LOD
Blank - Leach 3 (3)	2	<1	<1	<1	<LOD	<1	<LOD
Blank - Leach 3 average	2	<1	<1	<1	<1	<1	<1
Blank - Leach 4 (1)	35	<1	<1	<1	<LOD	<1	<LOD
Blank - Leach 4 (2)	77	<1	<1	<1	<1	<1	<LOD
Blank - Leach 4 (3)	3	<1	<LOD	<1	<LOD	<1	<LOD
Blank - Leach 4 average	38	<1	<1	<1	<1	<1	<1

Appendix B **Supplementary material to Chapter 4**

B.1 Bulk geochemical composition of FeOOH and massive sulphide samples

Table B.1. Contents of major and trace elements in FeOOH and massive sulphide samples from Semyenov hydrothermal field. Where Mn is >1000 ppm (0.1 wt.%), value was obtained by ICP-OES, below is measured by ICP-MS. Other data obtained by ICP-MS. b.d.l – below detection limit. Table 1 of 2.

	Na (wt.%)	Mg	Al	Ca	Mn	Fe	Cu	Li (ppm)	Sc	Ti	Co	Ni	Zn	As	Sr	Nb	Cd	Sb	Ba	W
28_DR_03	1.33	0.62	0.12	0.77	3.66	28.99	0.48	15.7	1.1	80	29	40	2500	260	370	0.6	1.1	9.3	980	2.3
28_DR_04	1.00	0.29	0.12	0.22	0.02	29.30	4.18	1.2	0.5	40	14	b.d.l	820	260	890	0.1	0.3	11.8	1030	1.35
28_DR_05	1.04	0.28	0.01	0.20	0.03	37.29	0.08	1.5	0.1	<10	5	b.d.l	2120	160	100	<0.1	0.3	37.8	40	0.67
28_DR_18	1.22	0.26	0.14	0.81	0.01	31.99	3.77	1.4	0.6	40	5	b.d.l	970	290	680	0.2	0.5	11.5	1004	1.60
39_HY_02	1.48	1.05	0.32	0.67	7.51	20.48	0.14	102	2.1	240	11	45	840	200	480	2.2	2.7	26.8	9580	3.5
66_HY_05	0.82	0.75	0.15	0.72	0.19	29.99	2.48	3.9	1.2	120	30	40	1060	240	270	1.0	0.6	8.2	880	1.85
71_DR_01	1.76	0.70	0.19	0.83	11.58	21.47	0.16	143	0.9	140	59	19	1370	100	400	0.9	0.8	5.8	2930	1.26
71_DR_02	1.83	0.72	0.12	0.70	7.23	20.53	0.06	128	0.3	60	9	50	630	57	230	0.3	0.6	3.8	290	0.82
71_DR_03	1.7	0.67	0.14	0.75	9.29	20.24	0.25	104	0.4	80	63	10	940	65	290	0.4	0.6	3.8	1150	0.92
71_DR_04	1.03	0.88	0.23	1.18	0.06	36.46	0.20	11.3	1.3	110	15	10	1150	300	530	1.2	0.9	13.1	6810	3.8
71_DR_07	1.62	0.78	0.12	0.61	4.74	22.29	0.06	72	0.4	60	9	40	600	59	190	0.3	0.4	2.7	590	0.61
71_DR_09	1.42	0.93	0.59	1.50	1.07	31.82	0.19	5.5	7.0	420	11	80	770	970	550	5.4	0.6	22.0	7530	8.4
71_DR_12	1.41	0.70	0.26	1.01	5.98	24.84	0.16	90	0.9	160	35	50	670	160	420	1.2	0.7	6.7	7720	1.92
77_HY_02	2.58	0.69	0.46	1.53	2.48	24.64	0.87	3.0	1.2	180	13	10	290	160	490	0.9	0.5	3.8	5370	4.1
77_HY_03	1.47	2.05	1.00	0.56	1.38	18.65	6.90	7.1	2.5	510	59	b.d.l	130	170	1180	2.0	0.2	3.5	9760	2.3
82_HY_01	0.61	0.63	0.24	1.00	0.62	34.68	1.84	3.6	1.4	330	38	12	310	330	210	1.7	0.6	23.7	390	2.2
82_HY_05	2.17	0.87	0.22	1.41	0.04	31.38	1.96	4.0	1.4	170	10	50	380	360	300	0.6	0.7	17.1	1630	2.6
82_HY_06a	0.55	0.18	0.04	0.22	<0.01	30.01	16.79	0.6	0.2	<10	4	b.d.l	910	160	80	<0.1	1.3	14.4	50	0.45
82_HY_06b	0.07	0.01	0.01	0.01	<0.01	34.65	0.37	0.1	0.1	10	29	b.d.l	4370	750	0	<0.1	11.9	9.9	10	1.21
82_HY_09	0.60	0.87	0.22	0.44	0.44	37.90	0.30	7.2	3.7	270	26	50	1100	810	120	4.3	1.0	30.7	100	5.0
82_HY_10	1.12	0.98	0.62	1.92	0.56	28.73	1.73	5.5	2.9	480	63	16	560	460	320	2.5	0.5	19.4	1180	4.5
82_HY_11	0.61	0.71	0.26	0.55	0.29	34.52	0.29	6.7	2.2	130	53	90	1610	460	240	1.3	1.0	17.4	1001	3.1
86_HY_02	0.05	0.01	0.09	0.01	<0.01	33.74	0.11	0.2	0.1	10	29	b.d.l	280	81	20	0.1	0.5	1.5	290	0.42
86_HY_04	1.24	0.57	0.17	0.80	0.30	29.32	2.42	0.9	1.8	50	25	b.d.l	3820	590	330	0.8	0.6	21.8	7540	4.9

86_HY_07	0.11	0.02	0.09	0.00	<0.01	33.87	2.01	0.5	0.1	20	49	b.d.l	610	80	10	0.1	0.8	6.6	200	0.44
	Na (wt.%)	**Mg**	**Al**	**Ca**	**Mn**	**Fe**	**Cu**	**Li (ppm)**	**Sc**	**Ti**	**Co**	**Ni**	**Zn**	**As**	**Sr**	**Nb**	**Cd**	**Sb**	**Ba**	**W**
86_HY_08	1.81	0.58	0.02	0.85	7.21	27.72	0.04	40	0.1	10	1	b.d.l	2400	130	330	<0.1	1.6	9.6	600	2.4
86_HY_09	1.2	0.66	0.08	0.55	0.01	33.15	0.93	1.1	0.1	10	7	<10	5520	470	840	0.1	1.0	16.2	1275	3.1
87_MC_01	1.24	0.62	0.23	1.04	1.58	31.07	0.26	9.8	1.0	130	85	250	2430	210	370	0.8	0.5	4.9	170	1.02
90_HY_04a	1.53	1.00	0.11	1.09	9.15	28.96	0.40	63	0.6	20	36	140	1880	460	560	0.2	2.5	27.1	3540	6.3
90_HY_04b	0.18	0.02	0.01	0.04	0.01	29.25	15.23	0.1	<0.1	<10	2	b.d.l	2400	30	510	<0.1	8.6	11.4	3250	0.61
90_HY_04c	0.20	0.09	0.01	0.34	0.01	31.69	6.03	0.1	<0.1	<10	3	b.d.l	1850	130	410	<0.1	3.2	10.4	170	0.39
90_HY_05	0.71	0.46	0.29	0.72	0.87	35.84	0.35	2.2	2.7	440	14	70	1110	200	180	3.2	0.4	16.1	2170	5.2
90_HY_06	1.03	0.35	0.48	3.08	1.36	36.51	0.36	3.1	3.0	230	14	40	800	180	380	5.0	0.4	16.0	4560	6.5
94_HY_01	2.11	1.11	1.75	0.38	1.31	20.71	1.04	10.2	4.2	1250	18	90	2640	220	250	8.0	0.9	9.1	7460	2.9
94_HY_04	1.03	0.58	0.72	0.61	1.38	26.26	4.44	2.2	3.0	790	15	70	690	320	510	1.3	0.3	12.0	7890	3.2
94_HY_05	1.07	0.30	0.17	0.29	0.40	33.2	8.87	1.0	0.7	110	10	b.d.l	460	130	80	0.5	0.8	17.1	370	0.97
94_HY_06	0.77	0.35	0.21	0.58	0.64	31.9	8.71	1.0	0.8	130	61	b.d.l	990	200	310	0.4	0.3	9.0	4150	1.79
102_HY_03	1.12	0.42	0.34	1.42	1.24	37.59	0.29	2.7	2.4	390	163	70	2260	190	240	2.9	0.4	41.8	2160	4.4
102_HY_04	0.94	0.41	0.16	1.11	0.74	31.99	2.01	1.1	0.9	150	74	40	1620	250	400	0.9	0.7	5.1	920	1.6
102_HY_05	0.69	0.30	0.24	0.43	0.07	35.84	0.09	1.1	1.8	50	56	<10	3530	220	200	0.4	0.5	19.4	1770	1.2
102_HY_06	1.76	0.87	0.97	5.48	3.67	26.14	1.71	5.7	8.8	1170	261	160	1650	470	1010	10.1	0.8	13.0	5900	10.9
102_HY_07	1.37	0.49	0.49	3.18	1.84	31.59	0.34	3.6	3.9	530	102	80	1160	250	570	4.2	0.4	10.5	10550	7.9

Table B.2. Contents of major and trace elements in FeOOH and massive sulphide samples from Semenov hydrothermal field. Where Mn is >1000 ppm (>1 wt.%), value was obtained by ICP-OES, below is measured by ICP-MS. Other data obtained by ICP-MS. <b.d.l – below detection limit. Table 2 of 2.

Sample	Pb (ppm)	Bi	Th	U	Sample	Pb (ppm)	Bi	Th	U
28_DR_03	32	0.11	0.30	6.6	86_HY_08	150	0.03	0.01	8.1
28_DR_04	486	1.2	0.14	15.8	86_HY_09	256	0.29	0.03	8.3
28_DR_05	606	0.05	0.01	15.2	87_MC_01	4	0.05	0.57	9.1
28_DR_18	511	1.0	0.09	16.4	90_HY_04a	14	0.05	0.08	6.9
39_HY_02	51	0.20	1.40	2.0	90_HY_04b	98	0.05	0.01	3.6
66_HY_05	17	0.21	0.67	5.3	90_HY_04c	195	0.05	<0.01	4.4
71_DR_01	39	0.09	0.85	1.9	90_HY_05	204	0.10	1.63	37.6
71_DR_02	16	0.05	0.26	1.1	90_HY_06	201	0.16	2.54	36.1
71_DR_03	9	0.05	0.33	1.3	94_HY_01	96	1.6	3.32	3.9
71_DR_04	28	1.9	0.48	12.3	94_HY_04	170	3.1	0.87	10.6
71_DR_07	12	0.03	0.27	0.9	94_HY_05	339	0.60	0.46	15.8
71_DR_09	68	0.49	3.16	7.5	94_HY_06	42	5.3	0.20	32.3
71_DR_12	19	0.52	0.78	4.9	102_HY_03	467	0.20	1.75	43.6
77_HY_02	57	1.0	0.78	7.7	102_HY_04	22	0.08	0.33	8.2
77_HY_03	284	2.2	1.51	7.5	102_HY_05	250	0.05	0.12	53.3
82_HY_01	190	15.1	2.06	16.7	102_HY_06	154	0.49	6.26	8.4
82_HY_05	258	6.9	0.74	8.4	102_HY_07	369	0.28	2.78	12.0
82_HY_06a	392	8.5	0.01	31.3					
82_HY_06b	300	1.7	0.04	2.3					
82_HY_09	108	0.93	2.25	9.6					
82_HY_10	142	7.7	2.10	8.9					
82_HY_11	373	1.1	0.73	22.5					
86_HY_02	58	1.0	0.12	3.0					
86_HY_04	423	0.07	0.19	10.0					
86_HY_07	131	5.1	0.17	7.1					

B.2 REE composition of FeOOH and massive sulphide samples

Table B.3. Contents of REE in FeOOH and massive sulphide samples collected at Semyenov hydrothermal field. $Ce/Ce^* = (Ce_n)/((La_n \times Nd_n) \times 0.5)$. $Eu/Eu^* = (Eu_n)/((Sm_n \times Gd_n) \times 0.5)$. X_n indicates that the element is normalised by carbonaceous chondrite after Barrat et al. (2012). LREE = La-Sm and HREE = Eu-Lu.

Sample ID	La	Ce	Pr	Nd	Sm	Eu	Gd	Tb	Dy	Ho	Er	Tm	Yb	Lu	ΣLREE	ΣHREE	ΣREE	LREE/ HREE	Ce/Ce*	Eu/Eu*	La_n/Yb_n
28_DR_03	7.9	7.1	1.82	7.7	1.61	0.51	1.90	0.26	1.76	0.36	1.04	0.15	0.98	0.150	26.1	7.10	33.2	3.67	0.45	0.88	5.79
28_DR_04	2.8	2.0	0.54	2.4	0.71	1.27	0.70	0.10	0.63	0.13	0.41	0.06	0.43	0.066	8.41	3.78	12.2	2.22	0.40	5.45	4.71
28_DR_05	1.2	0.6	0.15	0.6	0.12	0.08	0.16	0.02	0.13	0.03	0.09	0.01	0.07	0.013	2.78	0.60	3.38	4.68	0.36	1.80	12.95
28_DR_18	2.8	2.6	0.63	2.8	0.86	1.29	0.88	0.13	0.80	0.17	0.51	0.07	0.53	0.080	9.67	4.46	14.1	2.17	0.48	4.46	3.73
39_HY_02	15.3	26.6	3.82	15.8	3.30	1.39	3.45	0.49	3.10	0.60	1.71	0.24	1.61	0.239	64.8	12.8	77.6	5.05	0.85	1.25	6.78
66_HY_05	7.7	11.3	1.75	7.2	1.53	0.53	1.76	0.25	1.70	0.35	1.03	0.15	0.99	0.154	29.4	6.93	36.4	4.25	0.75	0.98	5.54
71_DR_01	7.9	12.7	1.88	7.7	1.62	0.77	1.72	0.24	1.54	0.30	0.82	0.11	0.74	0.106	31.8	6.34	38.1	5.01	0.80	1.39	7.58
71_DR_02	2.0	2.8	0.51	2.2	0.45	0.34	0.48	0.07	0.43	0.09	0.24	0.03	0.23	0.033	7.98	1.94	9.92	4.11	0.67	2.21	6.24
71_DR_03	3.8	4.5	0.81	3.3	0.69	0.38	0.77	0.11	0.70	0.14	0.41	0.05	0.37	0.053	13.1	2.99	16.1	4.38	0.62	1.60	7.34
71_DR_04	3.8	6.4	0.86	3.5	0.79	0.51	0.97	0.15	1.04	0.22	0.66	0.09	0.64	0.107	15.4	4.38	19.7	3.51	0.86	1.75	4.21
71_DR_07	2.9	3.2	0.64	2.7	0.54	0.31	0.63	0.09	0.57	0.12	0.34	0.05	0.31	0.048	9.94	2.47	12.4	4.03	0.58	1.60	6.53
71_DR_09	29.7	48.1	7.23	29.6	6.44	1.93	7.39	1.11	7.54	1.56	4.72	0.69	4.94	0.783	121.1	30.7	151.7	3.95	0.80	0.85	4.30
71_DR_12	6.9	10.2	1.48	6.0	1.22	0.70	1.36	0.20	1.28	0.26	0.74	0.10	0.70	0.105	25.8	5.45	31.3	4.74	0.78	1.64	7.02
77_HY_02	5.9	17.3	1.81	7.5	1.71	1.05	1.72	0.25	1.62	0.30	0.86	0.12	0.80	0.126	34.2	6.86	41.1	4.98	1.29	1.86	5.23
77_HY_03	8.6	21.1	2.92	12.1	2.63	1.64	2.63	0.39	2.47	0.47	1.31	0.19	1.22	0.180	47.4	10.5	57.9	4.51	1.02	1.89	5.05
82_HY_01	16.6	28.8	3.99	16.6	3.58	0.92	4.10	0.60	3.97	0.80	2.34	0.34	2.25	0.347	69.5	15.7	85.1	4.44	0.86	0.72	5.27
82_HY_05	13.6	11.1	3.18	13.6	2.92	0.95	3.59	0.54	3.89	0.85	2.65	0.39	2.65	0.438	44.4	15.9	60.3	2.78	0.41	0.88	3.66
82_HY_06a	0.8	0.7	0.14	0.6	0.11	0.04	0.17	0.03	0.18	0.04	0.12	0.02	0.10	0.017	2.34	0.70	3.04	3.32	0.55	0.82	5.39
82_HY_06b	0.1	0.2	0.02	0.1	0.01	0.00	0.01	0.00	0.01	0.00	0.01	0.00	0.00	0.001	0.35	0.04	0.39	10.05	0.97	0.78	18.59
82_HY_09	11.9	30.2	2.99	12.3	2.82	0.69	3.43	0.54	3.72	0.76	2.30	0.34	2.30	0.384	60.3	14.5	74.7	4.17	1.24	0.67	3.70
82_HY_10	19.3	25.3	4.48	18.9	3.99	1.05	4.75	0.70	4.93	1.06	3.24	0.47	3.05	0.522	72.0	19.8	91.7	3.64	0.66	0.73	4.53

Appendix B

Sample ID	La	Ce	Pr	Nd	Sm	Eu	Gd	Tb	Dy	Ho	Er	Tm	Yb	Lu	ΣLREE	ΣHREE	ΣREE	LREE/ HREE	Ce/Ce*	Eu/Eu*	La_n/Yb_n
82_HY_11	6.5	10.3	1.44	6.0	1.41	0.80	1.84	0.29	2.14	0.49	1.57	0.25	1.74	0.298	25.6	9.4	35.1	2.72	0.82	1.51	2.66
86_HY_02	0.2	0.5	0.05	0.2	0.03	0.02	0.02	0.00	0.02	0.00	0.01	0.00	0.01	0.001	0.94	0.08	1.02	11.60	1.08	1.79	21.88
86_HY_04	9.3	4.5	1.87	8.0	1.66	0.82	2.17	0.32	2.33	0.53	1.65	0.24	1.58	0.275	25.4	9.92	35.3	2.56	0.26	1.30	4.22
86_HY_07	0.9	1.4	0.14	0.5	0.07	0.03	0.05	0.01	0.05	0.01	0.03	0.00	0.02	0.004	2.89	0.19	3.08	14.93	0.96	1.67	34.01
86_HY_08	2.5	4.9	0.73	3.7	0.99	0.60	1.18	0.13	0.68	0.11	0.25	0.03	0.13	0.017	12.8	3.13	15.9	4.09	0.89	1.69	13.16
86_HY_09	1.2	0.9	0.14	0.5	0.10	0.55	0.13	0.02	0.14	0.04	0.11	0.02	0.12	0.020	2.84	1.16	3.99	2.46	0.52	14.79	6.96
87_MC_01	7.1	7.2	1.55	6.5	1.34	0.31	1.54	0.22	1.48	0.31	0.92	0.13	0.77	0.134	23.7	5.82	29.5	4.07	0.53	0.66	6.57
90_HY_04a	3.6	1.8	0.66	2.8	0.60	0.44	0.79	0.12	0.85	0.20	0.66	0.10	0.67	0.112	9.49	3.93	13.4	2.42	0.28	1.93	3.88
90_HY_04b	0.5	0.6	0.03	0.1	0.01	0.15	0.01	<0.01	0.01	<0.01	0.01	<0.01	<0.01	0.001	1.25	0.20	1.45	6.28	1.14	34.53	85.94
90_HY_04c	0.2	0.2	0.01	0.0	0.01	0.02	0.01	<0.01	0.01	<0.01	0.01	<0.01	<0.01	0.002	0.46	0.06	0.52	7.85	1.00	5.55	29.09
90_HY_05	17.4	31.2	4.44	18.2	4.08	1.63	4.45	0.67	4.35	0.84	2.36	0.34	2.22	0.350	75.3	17.2	92.5	8.73	0.87	1.16	5.58
90_HY_06	26.5	45.8	6.53	26.7	5.78	2.15	6.35	0.93	5.99	1.15	3.20	0.45	2.77	0.448	111.2	23.4	134.7	7.53	0.85	1.08	6.83
94_HY_01	15.7	26.7	4.12	16.4	3.56	1.16	3.71	0.56	3.76	0.75	2.21	0.33	2.18	0.355	66.5	15.0	81.6	6.85	0.81	0.96	5.15
94_HY_04	14.6	16.2	3.21	13.5	2.97	1.54	3.45	0.49	3.33	0.72	2.18	0.31	2.02	0.342	50.5	14.4	64.9	3.51	0.58	1.46	5.17
94_HY_05	5.7	15.3	2.19	10.0	2.70	1.51	2.79	0.41	2.49	0.46	1.36	0.21	1.40	0.219	35.9	10.9	46.7	3.31	1.06	1.67	2.90
94_HY_06	4.7	6.1	1.06	4.6	0.96	0.46	1.30	0.19	1.31	0.29	0.87	0.12	0.75	0.124	17.4	5.41	22.8	3.22	0.67	1.24	4.49
102_HY_03	24.3	37.3	6.15	24.9	5.56	1.75	5.95	0.88	5.62	1.08	3.01	0.42	2.65	0.404	98.2	21.8	120.0	5.25	0.74	0.92	6.55
102_HY_04	8.9	5.7	1.58	6.4	1.33	0.36	1.63	0.23	1.64	0.35	1.06	0.15	0.96	0.151	24.0	6.53	30.5	3.67	0.37	0.75	6.64
102_HY_05	3.1	2.9	0.78	3.4	0.77	0.48	0.94	0.14	0.92	0.20	0.58	0.08	0.57	0.092	10.9	4.00	14.9	2.74	0.45	1.70	3.88
102_HY_06	90.8	114.1	22.29	91.0	19.01	4.69	20.33	2.92	18.47	3.48	9.57	1.32	8.56	1.276	337.2	70.6	407.9	4.78	0.62	0.72	7.59
102_HY_07	38.4	49.6	9.20	37.2	7.85	2.88	8.37	1.19	7.41	1.38	3.70	0.51	3.14	0.476	142.3	29.1	171.3	8.62	0.64	1.08	8.73

B.3 Sr-Nd-Pb isotope systematics

Table B.4. Sr-Nd-Pb isotopic composition of the Fe-oxyhydroxide and sulphide (82_HY_06$_b$ & 90_HY_04$_b$) samples at Semenov hydrothermal field.

2SE – two-standard error.

Sample ID	$^{206}Pb/^{204}Pb$	2SE	$^{207}Pb/^{204}Pb$	2SE	$^{208}Pb/^{204}Pb$	2SE	$^{87}Sr/^{86}Sr$	2SE	$^{143}Nd/^{144}Nd$	2SE	εNd
28_DR_03	18.8546	0.0002	15.5490	0.0010	38.3690	0.0032	0.709036	0.000005	0.512156	0.000006	-9.40
39_HY_02							0.707028	0.000007	0.512106	0.000007	-10.39
66_HY_05	18.8858	0.0002	15.5775	0.0008	38.5510	0.0020	0.708939	0.000006	0.512067	0.000007	-11.13
71_DR_01	19.0127	0.0002	15.5708	0.0008	38.6250	0.0022	0.708498	0.000007	0.512074	0.000006	-11.00
82_HY_01	18.9306	0.0002	15.5639	0.0009	38.4990	0.0025	0.709185	0.000006	0.512022	0.000005	-12.02
82_HY_05	18.9278	0.0002	15.5565	0.0008	38.4620	0.0023	0.708463	0.000006	0.512066	0.000006	-11.16
82_HY_06$_a$	18.9345	0.0002	15.5570	0.0009	38.4680	0.0022					
82_HY_06$_b$	18.9324	0.0002	15.5541	0.0008	38.4600	0.0023					
82_HY_09	18.9431	0.0002	15.5791	0.0008	38.5620	0.0023	0.709220	0.000008	0.512003	0.000007	-12.39
82_HY_10	18.9306	0.0002	15.5637	0.0009	38.4980	0.0021	0.709222	0.000006	0.512038	0.000008	-11.70
86_HY_04	18.8471	0.0002	15.5440	0.0009	38.3440	0.0022	0.707575	0.000005	0.512097	0.000006	-10.56
86_HY_09	18.8627	0.0002	15.5456	0.0009	38.3660	0.0020					
90_HY_04$_b$	18.8661	0.0003	15.545	0.0011	38.3720	0.0023					
94_HY_01	18.8661	0.0002	15.5562	0.0009	38.4310	0.0056	0.707953	0.000006	0.512082	0.000006	-10.84
94_HY_04	18.8610	0.0002	15.5487	0.0008	38.3690	0.0020	0.707482	0.000006	0.512222	0.000007	-8.11
94_HY_05	18.8580	0.0002	15.5464	0.0008	38.3600	0.0025			0.512381	0.000007	-5.02
94_HY_06	18.8470	0.0001	15.5501	0.0008	38.3660	0.0020	0.708237	0.000005	0.512234	0.000007	-7.87
102_HY_03	18.8938	0.0002	15.5534	0.0007	38.4000	0.0021	0.708715	0.000006	0.512148	0.000006	-9.56
102_HY_04	18.8548	0.0002	15.5647	0.0007	38.4400	0.0019	0.709061	0.000006	0.512043	0.000008	-11.60
102_HY_05	18.8618	0.0002	15.5462	0.0008	38.3610	0.0019	0.708593	0.000006	0.512213	0.000008	-8.29
102_HY_06	18.8771	0.0002	15.5676	0.0008	38.4710	0.0019	0.708481	0.000006	0.512087	0.000009	-10.75

B.4 Eh and pH diagram of Fe- and Mn-species and mineral stabilities for seawater at 2°C

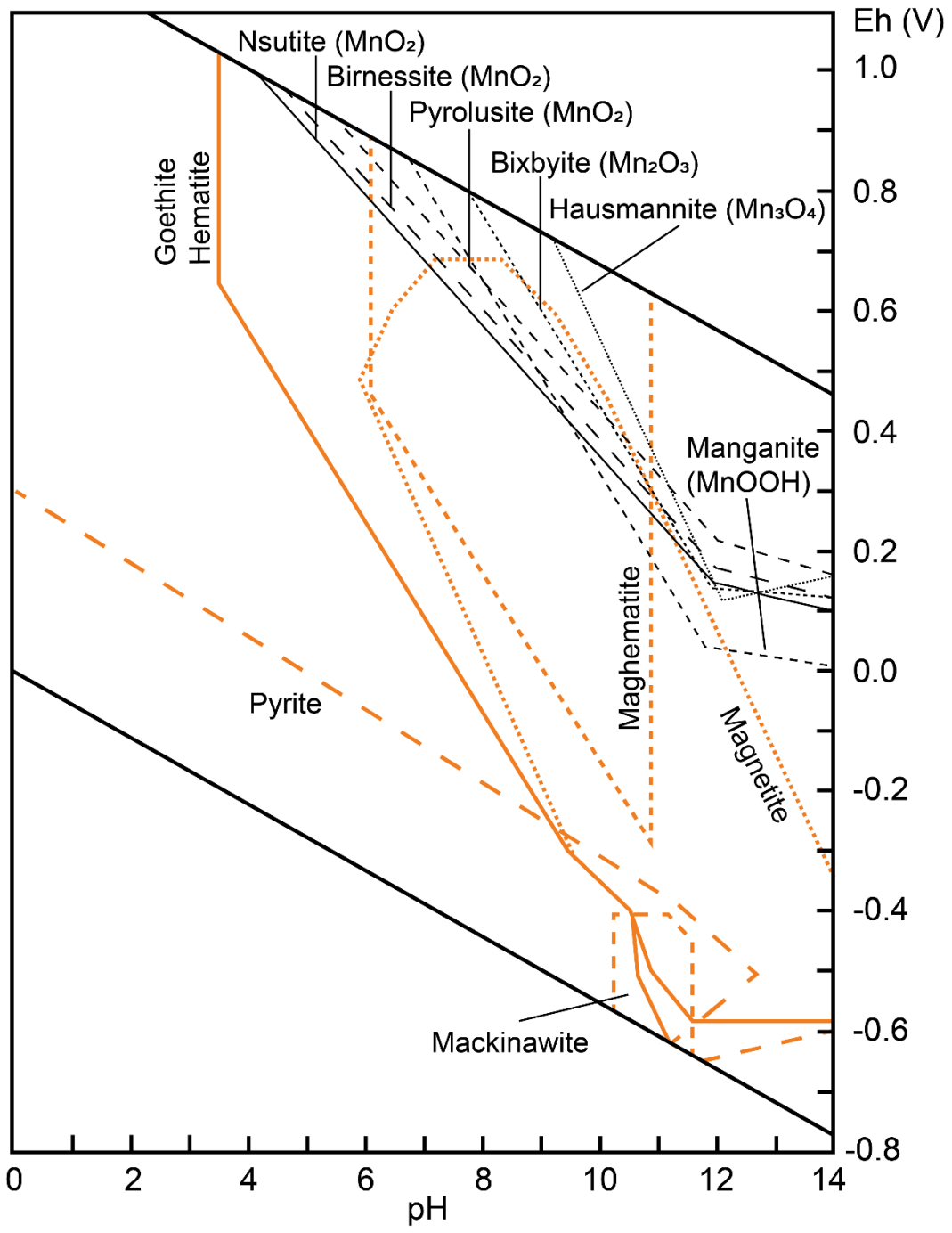

Figure B.1. Eh, pH diagrams for the solid phases of Mn and Fe calculated for deep-seawater conditions at 2°C. Figure modified after Glasby and Schulz (1999).

B.5 Estimated sediment component of bulk FeOOH samples

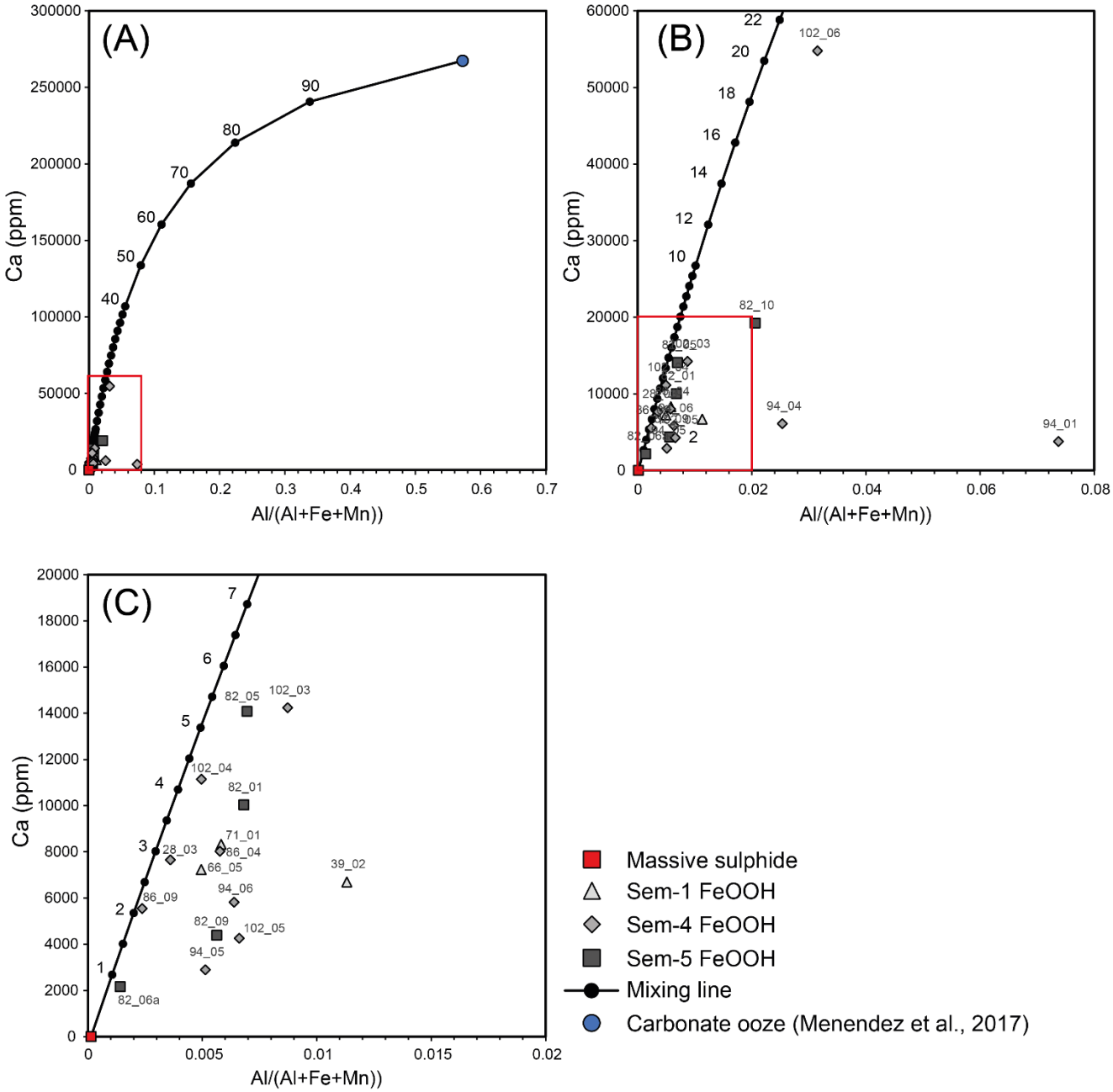

Figure B.2. Sulphide-sediment theoretical mixing lines produced from Eq. 1 and Eq. 2. Values of % sediment acquired from Al/(Al+Fe+Mn) vs Ca (ppm) mixing lines N/A values are either where no isotopic analysis was measured or FeOOH Pb isotopic ratio lies below that of the massive sulphide or sulphide-sediment mix and therefore, unable to obtain a W/R value. Note values are approximate.

B.6 Calculated F/R ratio

Table B.5. Derived F/R ratio of FeOOH samples at Semenov with estimated sediment content derived from Figure S2.1. N/A values where FeOOH Pb isotopic ratio lies below that of the massive sulphide or sulphide-sediment mix or deviate considerably from the mixing line and therefore, unable to obtain a F/R value. Note values are approximate.

Sample	$^{206}Pb/^{204}Pb$	$^{207}Pb/^{204}Pb$	$^{208}Pb/^{204}Pb$	Estimated sediment content (%)	Calculated F/R ratio
28_03	18.855	15.549	38.368	3.0	$8.5x10^5$
66_05	18.886	15.577	38.551	2.5	$1.0x10^7$
82_01	18.931	15.564	38.498	4.0	$1.0x10^6$
82_05	18.928	15.557	38.462	5.5	$1.0x10^5$
82_06a	18.935	15.557	38.468	0.8	$3.0x10^5$
82_09	18.943	15.579	38.562	1.5	$3.0x10^6$
82_10	18.931	15.564	38.498	7.5	$8.5x10^5$
86_04	18.847	15.544	38.344	3.0	N/A
86_09	18.863	15.546	38.367	2.0	$1.5x10^4$
94_01	18.866	15.556	38.431	1.5	$3.0x10^6$
94_04	18.861	15.549	38.369	2.5	$8.0x10^5$
94_05	18.858	15.546	38.360	1.0	$2.0x10^5$
94_06	18.847	15.550	38.366	2.0	N/A
102_03	18.894	15.553	38.400	5.5	$2.0x10^6$
102_04	18.855	15.565	38.440	4.0	N/A
102_05	18.862	15.546	38.361	1.5	$1.5x10^5$
102_06	18.877	15.568	38.471	21.0	$6.0x10^6$

Appendix C **Supplementary materials to Chapter 5**

C.1 Quantitative XRD data

Table C.1. Quantitative XRD data of samples used in the study. Typically, ferrihydrite cannot be measured as it is an amorphous mineral, as a result, the amorphous content is assumed to be ferrihydrite. Measurable ferrihydrite is possible in some cases such as a small amount in 94_HY_06. A Chi^2 of less than 5 is considered a good fit for quantitative XRD analysis.

	66_HY_05	82_HY_01	82_HY_05	82_HY_06$_a$	86_HY_04	94_HY_04	94_HY_06	102_HY_04	102_HY_05
Akaganeite (% volume)		2.9							2.6
Error		1.2							0.5
Atacamite (% volume)	1.4			9.6				1.7	
Error	2.2			0.5				0.4	
Barytes (% volume)					1.85	3.2		3.7	
Error					0.1			0.3	
Calcite (% volume)		0.9	2.5		0.8			2.3	
Error		1.65	0.2					0.5	
Ferrihydrite (% volume)							1.5		
Error							0.9		
Goethite (% volume)	14.5	22	17.3	17.2	20.2	13.5	8.2	13.3	18.4
Error	5	2.2	0.4	0.8	0.65	0.3	0.5	0.6	1.7
Quartz (% volume)		1.4	1.3			2.1		2	2.3
Error		0.3	0.2			0.2		0.4	1
Haydeeite (% volume)							1.2		
Error							0.2		
Paratacamite (% volume)				3.9			2.6		
Error				0.3			0.2		
Chlorite (% volume)				2.5					
Error				1.5					
Smectite (% volume)	32.8								
Error	4.55								
Amorphous content (% volume)	51.4	73	78.9	66.8	76.2	81.2	86.4	77	76.7
Error	12.9	4.3	0.6	2.1	1	0.5	1.1	1.3	2.9
Chi^2	4.74	3.78	2.35	3.93	2.59	2.41	2.82	3.1	3.38

C.2 Morphologies of FeOOH

FeOOH occurs across all samples in the study and displays ten distinct morphologies. The most common forms include FeOOH I and II, which exhibit subhedral to anhedral, porous textures and are massive (FeOOH I) or granular (FeOOH II), which can contain relict pyrite, suggesting a pyrite protolith. FeOOH III forms vein-like structures, with one instance of chalcopyrite observed, while FeOOH IV exhibits non-porous colloform textures. Other forms include the highly porous dendritic grains of FeOOH V, relatively large, dark grey to light grey, rounded grains of FeOOH VI, and tabular grains of FeOOH VII, all present in specific samples. FeOOH VIII and IX are characterized by greenish-grey (FeOOH VIII) or bluish-grey (FeOOH IX) porous grains, with FeOOH IX likely originating from chalcopyrite weathering (Figure 5.2D). Lastly, FeOOH X appears as framboidal grains, replacing framboidal pyrite (Figure 5.2F). FeOOH morphologies associated with sulphide protoliths are classified as pyrite-derived (py-FeOOH; e.g., Figure 5.1H) or chalcopyrite-derived (ccp-FeOOH; e.g., Figure 5.2D).

C.3 Summary data - Median

Table C.2. Median values of trace elemental data of sulphide minerals, FeOOH and atacamite. a Elements obtained by quantitative SEM-EDS. Note, values obtained for modified FeOOH exclude py-FeOOH and ccp-FeOOH. B.d.l – below detection limit. N.A – not analysed.

	Primary sulphides		Weathering products			
	Pyrite (n=43)	Chalcopyrite (n=18)	Py FeOOH (n=6)	Ccp FeOOH (n=9)	Modified FeOOH (n=215)	Atacamite (n=30)
Na[a] (wt.%)	<LOD	<LOD	0.16	0.26	0.43	<LOD
Mg[a] (wt.%)	<LOD	<LOD	0.3	0.34	0.32	<LOD
Si (wt.%)	<0.1	<0.1	1.9	1.5	3.1	<LOD
S[a] (wt.%)	53.15	34.45	0.15	0.47	0.15	<LOD
Cl[a] (wt.%)	<LOD	<LOD	0.26	0.19	0.35	15.64
Ca (wt.%)	0.17	0.30	0.14	0.31	0.40	0.01
Fe (wt.%)	46.55	30.78	49.63	45.52	47.55	0.72
Cu (wt.%)	0.36	31.20	3.10	4.36	2.84	57.36
Zn (wt.%)	0.12	0.02	0.20	0.18	0.12	0.02
Al (ppm)	900	1550	1000	3100	400	50
Mn (ppm)	5	2	6	3	20	<1
Co (ppm)	41	9	7	35	2	3
Ni (ppm)	1	<1	9	2	5	<1
As (ppm)	404	8	976	28	174	11
Mo (ppm)	60	43	346	495	173	40
Ag (ppm)	4.9	18.5	0.2	25.6	<0.1	<0.1
In (ppm)	1.6	6.7	11.4	9.7	0.1	<0.1
Sb (ppm)	9	2	36	23	8	<1
Au (ppm)	0.5	<0.1	1.3	0.3	<0.1	<0.1
Pb (ppm)	81	26	85	144	26	<1
Bi (ppm)	4.8	0.8	1.0	7.8	<0.1	5
ΣREE (ppm)	0.1	0.2	1.7	0.7	5.8	0.1

C.4 Correlation matrix of pyrite analyses by LA-ICP-MS

Table C.3. Spearman correlation illustrating the relationship of various elements obtained by LA-ICP-MS of pyrite (n=43).

	Al	Si	Ca	Mn	Fe	Co	Ni	Cu	Zn	As	Se	Mo	Ag	In	Sb	Te	Ce	Au	Pb	Bi	REE
Al		0.32	0.80	-0.23	0.03	0.69	0.03	0.38	-0.14	0.04	0.10	0.38	-0.26	0.20	0.34	-0.01	0.58	-0.39	-0.07	0.47	0.51
Si	0.32		0.45	0.23	0.06	0.28	0.54	0.79	0.08	-0.10	0.37	0.63	0.19	0.51	0.52	0.30	0.77	-0.02	0.17	0.27	0.85
Ca	0.80	0.45		-0.26	-0.24	0.74	0.14	0.45	-0.14	-0.17	0.30	0.33	-0.33	0.10	0.31	0.18	0.60	-0.49	-0.13	0.27	0.62
Mn	-0.23	0.23	-0.26		0.13	-0.23	0.46	0.13	0.35	-0.19	0.08	0.22	0.25	0.14	0.30	-0.39	0.07	0.44	0.31	-0.13	0.06
Fe	0.03	0.06	-0.24	0.13		-0.26	-0.01	0.10	0.12	0.14	-0.30	0.04	0.27	0.12	0.12	-0.19	0.02	0.06	0.16	-0.04	-0.01
Co	0.69	0.28	0.74	-0.23	-0.26		0.14	0.38	-0.17	-0.08	0.25	0.44	-0.22	0.15	0.36	0.26	0.54	-0.36	-0.02	0.50	0.48
Ni	0.03	0.54	0.14	0.46	-0.01	0.14		0.37	-0.06	-0.46	0.17	0.66	0.26	-0.05	0.32	0.06	0.36	0.23	0.12	0.24	0.40
Cu	0.38	0.79	0.45	0.13	0.10	0.38	0.37		-0.05	-0.27	0.18	0.71	0.39	0.60	0.50	0.23	0.77	-0.23	0.14	0.14	0.82
Zn	-0.14	0.08	-0.14	0.35	0.12	-0.17	-0.06	-0.05		0.23	0.15	0.00	0.09	0.42	0.44	-0.11	-0.02	0.32	0.64	-0.01	0.00
As	0.04	-0.10	-0.17	-0.19	0.14	-0.08	-0.46	-0.27	0.23		0.25	-0.42	-0.41	0.38	-0.03	0.31	-0.14	0.00	0.04	0.37	-0.15
Se	0.10	0.37	0.30	0.08	-0.30	0.25	0.17	0.18	0.15	0.25		0.11	-0.29	0.28	0.20	0.41	0.18	-0.08	0.12	0.39	0.28
Mo	0.38	0.63	0.33	0.22	0.04	0.44	0.66	0.71	0.00	-0.42	0.11		0.40	0.34	0.52	0.07	0.62	-0.07	0.28	0.35	0.60
Ag	-0.26	0.19	-0.33	0.25	0.27	-0.22	0.26	0.39	0.09	-0.41	-0.29	0.40		0.20	0.32	-0.13	0.02	0.44	0.41	-0.19	0.08
In	0.20	0.51	0.10	0.14	0.12	0.15	-0.05	0.60	0.42	0.38	0.28	0.34	0.20		0.52	0.26	0.47	-0.03	0.41	0.28	0.51
Sb	0.34	0.52	0.31	0.30	0.12	0.36	0.32	0.50	0.44	-0.03	0.20	0.52	0.32	0.52		-0.07	0.45	0.26	0.66	0.29	0.50
Te	-0.01	0.30	0.18	-0.39	-0.19	0.26	0.06	0.23	-0.11	0.31	0.41	0.07	-0.13	0.26	-0.07		0.16	-0.27	-0.14	0.35	0.22
Ce	0.58	0.77	0.60	0.07	0.02	0.54	0.36	0.77	-0.02	-0.14	0.18	0.62	0.02	0.47	0.45	0.16		-0.23	0.03	0.23	0.95
Au	-0.39	-0.02	-0.49	0.44	0.06	-0.36	0.23	-0.23	0.32	0.00	-0.08	-0.07	0.44	-0.03	0.26	-0.27	-0.23		0.37	-0.14	-0.18
Pb	-0.07	0.17	-0.13	0.31	0.16	-0.02	0.12	0.14	0.64	0.04	0.12	0.28	0.41	0.41	0.66	-0.14	0.03	0.37		0.09	0.10
Bi	0.47	0.27	0.27	-0.13	-0.04	0.50	0.24	0.14	-0.01	0.37	0.39	0.35	-0.19	0.28	0.29	0.35	0.23	-0.14	0.09		0.19
REE	0.51	0.85	0.62	0.06	-0.01	0.48	0.40	0.82	0.00	-0.15	0.28	0.60	0.08	0.51	0.50	0.22	0.95	-0.18	0.10	0.19	

C.5 Mann Whitney U-test

Table C.4. Mann-Whitney U-test comparing the geochemical composition between various mineral populations. With data obtained by LA-ICP-MS and SEM-EDS. The P-value indicates the probability that the difference in these minerals accept the null hypothesis (i.e., there is no significant difference between these two minerals) or reject the null hypothesis (i.e., the difference between these minerals is significant). The significant p-value is 0.05, thus values below this value are considered significant differences. *Measurements are solely obtained by SEM-EDS. Modified FeOOH is obtained from 82_HY_06$_a$ with unmodified to minimally modified FeOOH acquired from 82_HY_06$_b$

	Chalcopyrite vs pyrite		Py-FeOOH vs ccp-FeOOH		Py/ccp-FeOOH vs modified FeOOH		Modified vs unmodified FeOOH in 82_HY_06*	
	P-value	Decision	P-value	Decision	P-value	Decision	P-value	Decision
Na*			0.25	Accept	0.01	Reject	0.071	Accept
Mg*			0.8	Accept	0.995	Accept	0.085	Accept
Al	0.003	Reject	0.529	Accept	0.002	Reject		
Si	0.308	Accept	0.008	Reject	<.001	Reject	<0.001	Reject
S*			0.149	Accept	0.004	Reject	<0.001	Reject
Cl*			1	Accept	0.047	Reject	<0.001	Reject
Ca	<.001	Reject	0.328	Accept	0.006	Reject	<0.001	Reject
Mn	<.001	Reject	0.113	Reject	<.001	Reject		
Fe	<.001	Reject	<.001	Reject	0.765	Accept	<0.001	Reject
Co	0.121	Accept	0.012	Reject	<.001	Reject		
Ni	<.001	Reject	<.001	Reject	0.019	Reject		
Cu	<.001	Reject	0.272	Accept	0.041	Reject	<0.001	Reject
Zn	<.001	Reject	0.776	Accept	0.005	Reject	<0.001	Reject
As	<.001	Reject	0.036	Reject	0.716	Reject		
Se	<.001	Reject	0.388	Accept	0.003	Reject		
Mo	0.038	Reject	0.689	Accept	0.002	Reject		
Ag	0.021	Reject	0.002	Reject	<.001	Reject		
Cd	0.005	Reject	0.864	Accept	0.002	Reject		
In	<.001	Reject	0.529	Accept	0.042	Reject		
Sb	<.001	Reject	0.607	Accept	0.005	Reject		
Te	0.069	Accept	0.181	Accept	0.057	Accept		
La	0.454	Accept	0.113	Accept	<.001	Reject		
Ce	0.308	Accept	0.005	Reject	0.058	Accept		
Pr	0.329	Accept	0.018	Reject	<.001	Reject		
Nd	0.664	Accept	0.026	Reject	<.001	Reject		
Sm	0.465	Accept	0.026	Reject	<.001	Reject		
Eu	0.062	Accept	0.272	Accept	0.004	Reject		
Gd	0.656	Accept	0.018	Reject	<.001	Reject		
Tb	0.143	Accept	0.012	Reject	0.003	Reject		
Dy	0.342	Accept	0.145	Accept	0.001	Reject		
Er	0.847	Accept	0.088	Accept	<.001	Reject		
Yb	0.065	Accept	0.145	Accept	<.001	Reject		
Au	<.001	Reject	0.181	Accept	<.001	Reject		
Pb	<.001	Reject	0.529	Accept	<.001	Reject		
Bi	0.015	Reject	0.328	Accept	0.037	Reject		

C.6 Correlation matric of chalcopyrite analyses by LA-ICP-MS

Table C.5. Spearman correlation illustrating the relationship of various elements obtained by LA-ICP-MS of chalcopyrite (n=18).

	Al	Si	Ca	Mn	Fe	Co	Ni	Cu	Zn	As	Se	Mo	Ag	Cd	In	Sb	Te	Ce	Au	Pb	Bi	REE
Al		-0.14	0.96	0.06	-0.32	0.39	-0.06	-0.36	-0.08	-0.23	-0.35	0.15	-0.40	-0.54	-0.34	-0.06	-0.51	-0.37	-0.30	0.14	0.25	-0.46
Si	-0.14		-0.07	0.49	0.07	0.00	0.42	-0.27	0.80	0.10	0.73	0.57	0.58	0.34	0.55	0.68	0.19	0.82	0.33	0.69	0.18	0.81
Ca	0.96	-0.07		0.13	-0.31	0.39	-0.06	-0.43	-0.04	-0.16	-0.30	0.17	-0.39	-0.54	-0.29	-0.05	-0.46	-0.32	-0.23	0.13	0.24	-0.40
Mn	0.06	0.49	0.13		0.01	-0.04	0.57	-0.47	0.64	0.27	0.57	0.35	0.47	0.65	0.57	0.23	0.49	0.42	0.01	0.45	0.53	0.42
Fe	-0.32	0.07	-0.31	0.01		-0.27	0.16	0.60	0.11	0.06	0.03	-0.07	0.16	0.25	0.25	0.05	0.04	0.14	0.00	-0.01	-0.28	0.11
Co	0.39	0.00	0.39	-0.04	-0.27		-0.11	-0.68	0.02	0.62	-0.18	0.33	0.04	-0.34	-0.25	0.26	-0.09	-0.05	0.04	0.33	0.68	-0.01
Ni	-0.06	0.42	-0.06	0.57	0.16	-0.11		-0.15	0.44	0.09	0.75	0.33	0.35	0.50	0.35	0.29	0.29	0.48	-0.11	0.36	0.15	0.41
Cu	-0.36	-0.27	-0.43	-0.47	0.60	-0.68	-0.15		-0.21	-0.49	-0.25	-0.30	-0.08	0.01	0.05	-0.19	-0.14	-0.09	0.02	-0.32	-0.76	-0.15
Zn	-0.08	0.80	-0.04	0.64	0.11	0.02	0.44	-0.21		0.18	0.55	0.78	0.82	0.41	0.72	0.80	0.35	0.80	0.47	0.86	0.26	0.78
As	-0.23	0.10	-0.16	0.27	0.06	0.62	0.09	-0.49	0.18		0.15	0.27	0.46	0.34	0.04	0.28	0.58	0.24	0.33	0.31	0.61	0.35
Se	-0.35	0.73	-0.30	0.57	0.03	-0.18	0.75	-0.25	0.55	0.15		0.27	0.47	0.61	0.57	0.41	0.32	0.73	0.15	0.41	0.19	0.71
Mo	0.15	0.57	0.17	0.35	-0.07	0.33	0.33	-0.30	0.78	0.27	0.27		0.75	0.01	0.25	0.92	0.23	0.71	0.61	0.92	0.23	0.68
Ag	-0.40	0.58	-0.39	0.47	0.16	0.04	0.35	-0.08	0.82	0.46	0.47	0.75		0.54	0.56	0.80	0.62	0.84	0.72	0.80	0.21	0.87
Cd	-0.54	0.34	-0.54	0.65	0.25	-0.34	0.50	0.01	0.41	0.34	0.61	0.01	0.54		0.55	0.07	0.69	0.41	0.07	0.20	0.27	0.44
In	-0.34	0.55	-0.29	0.57	0.25	-0.25	0.35	0.05	0.72	0.04	0.57	0.25	0.56	0.55		0.32	0.20	0.64	0.11	0.37	0.21	0.59
Sb	-0.06	0.68	-0.05	0.23	0.05	0.26	0.29	-0.19	0.80	0.28	0.41	0.92	0.80	0.07	0.32		0.25	0.80	0.73	0.92	0.12	0.81
Te	-0.51	0.19	-0.46	0.49	0.04	-0.09	0.29	-0.14	0.35	0.58	0.32	0.23	0.62	0.69	0.20	0.25		0.35	0.43	0.25	0.19	0.48
Ce	-0.37	0.82	-0.32	0.42	0.14	-0.05	0.48	-0.09	0.80	0.24	0.73	0.71	0.84	0.41	0.64	0.80	0.35		0.58	0.74	0.08	0.97
Au	-0.30	0.33	-0.23	0.01	0.00	0.04	-0.11	0.02	0.47	0.33	0.15	0.61	0.72	0.07	0.11	0.73	0.43	0.58		0.58	-0.17	0.64
Pb	0.14	0.69	0.13	0.45	-0.01	0.33	0.36	-0.32	0.86	0.31	0.41	0.92	0.80	0.20	0.37	0.92	0.25	0.74	0.58		0.36	0.71
Bi	0.25	0.18	0.24	0.53	-0.28	0.68	0.15	-0.76	0.26	0.61	0.19	0.23	0.21	0.27	0.21	0.12	0.19	0.08	-0.17	0.36		0.11
REE	-0.46	0.81	-0.40	0.42	0.11	-0.01	0.41	-0.15	0.78	0.35	0.71	0.68	0.87	0.44	0.59	0.81	0.48	0.97	0.64	0.71	0.11	

C.7 Correlation matrix of all FeOOH analyses by LA-ICP-MS

Table C.6. Spearman correlation illustrating the relationship of various elements obtained by LA-ICP-MS of FeOOH (n=230).

	Na	Mg	Al	Si	P	S	Cl	Ca	Fe	Co	Ni	Cu	Zn	As	Mo	Ag	In	Sb	Ce	Au	Pb	Bi	REE
Na		0.43	-0.31	0.60	0.41	-0.38	0.19	0.68	-0.22	-0.25	0.27	-0.56	-0.09	-0.30	-0.68	-0.28	-0.54	-0.55	0.30	-0.32	-0.49	-0.50	0.32
Mg	0.43		0.01	-0.03	0.60	-0.23	-0.08	0.26	-0.03	0.03	0.62	-0.40	-0.17	0.15	-0.24	-0.20	-0.18	-0.02	0.23	-0.25	-0.28	0.13	0.36
Al	-0.31	0.01		-0.18	-0.01	-0.14	-0.33	-0.26	0.06	0.58	0.22	0.12	0.16	0.22	0.38	0.14	0.26	0.35	0.31	0.23	0.22	0.46	0.32
Si	0.60	-0.03	-0.18		-0.05	-0.51	0.02	0.80	-0.24	-0.21	-0.15	-0.31	0.14	-0.65	-0.70	-0.34	-0.75	-0.84	0.52	-0.24	-0.66	-0.72	0.41
P	0.41	0.60	-0.01	-0.05		-0.25	0.00	0.16	-0.03	0.00	0.63	-0.34	-0.34	0.40	-0.14	-0.24	-0.04	0.12	0.28	-0.17	-0.17	0.23	0.41
S	-0.38	-0.23	-0.14	-0.51	-0.25		0.37	-0.39	-0.07	-0.09	-0.28	0.45	-0.08	0.42	0.26	0.39	0.50	0.49	-0.51	0.26	0.59	0.19	-0.52
Cl	0.19	-0.08	-0.33	0.02	0.00	0.37		0.01	-0.13	-0.18	-0.05	0.07	-0.08	0.20	-0.15	0.20	0.22	0.05	-0.33	-0.03	0.25	-0.15	-0.36
Ca	0.68	0.26	-0.26	0.80	0.16	-0.39	0.01		-0.24	-0.25	-0.05	-0.32	-0.02	-0.59	-0.71	-0.36	-0.76	-0.76	0.55	-0.44	-0.65	-0.63	0.50
Fe	-0.22	-0.03	0.06	-0.24	-0.03	-0.07	-0.13	-0.24		0.06	0.28	-0.27	0.31	0.13	0.37	-0.04	0.09	0.15	0.06	-0.01	0.05	0.06	0.04
Co	-0.25	0.03	0.58	-0.21	0.00	-0.09	-0.18	-0.25	0.06		0.29	0.15	0.32	0.08	0.27	0.27	0.17	0.20	0.24	0.30	0.17	0.31	0.17
Ni	0.27	0.62	0.22	-0.15	0.63	-0.28	-0.05	-0.05	0.28	0.29		-0.37	0.03	0.37	0.09	-0.21	0.12	0.24	0.30	-0.08	-0.01	0.25	0.43
Cu	-0.56	-0.40	0.12	-0.31	-0.34	0.45	0.07	-0.32	-0.27	0.15	-0.37		-0.08	0.15	0.30	0.33	0.42	0.34	-0.28	0.23	0.53	0.21	-0.29
Zn	-0.09	-0.17	0.16	0.14	-0.34	-0.08	-0.08	-0.02	0.31	0.32	0.03	-0.08		-0.17	0.10	0.24	-0.04	-0.13	0.13	0.23	0.09	-0.20	-0.04
As	-0.30	0.15	0.22	-0.65	0.40	0.42	0.20	-0.59	0.13	0.08	0.37	0.15	-0.17		0.38	0.23	0.68	0.78	-0.34	0.29	0.59	0.64	-0.18
Mo	-0.68	-0.24	0.38	-0.70	-0.14	0.26	-0.15	-0.71	0.37	0.27	0.09	0.30	0.10	0.38		0.20	0.70	0.73	-0.36	0.26	0.56	0.58	-0.34
Ag	-0.28	-0.20	0.14	-0.34	-0.24	0.39	0.20	-0.36	-0.04	0.27	-0.21	0.33	0.24	0.23	0.20		0.33	0.31	-0.27	0.59	0.49	0.18	-0.39
In	-0.54	-0.18	0.26	-0.75	-0.04	0.50	0.22	-0.76	0.09	0.17	0.12	0.42	-0.04	0.68	0.70	0.33		0.85	-0.58	0.29	0.85	0.62	-0.49
Sb	-0.55	-0.02	0.35	-0.84	0.12	0.49	0.05	-0.76	0.15	0.20	0.24	0.34	-0.13	0.78	0.73	0.31	0.85		-0.48	0.32	0.71	0.78	-0.36
Ce	0.30	0.23	0.31	0.52	0.28	-0.51	-0.33	0.55	0.06	0.24	0.30	-0.28	0.13	-0.34	-0.36	-0.27	-0.58	-0.48		-0.23	-0.46	-0.32	0.92
Au	-0.32	-0.25	0.23	-0.24	-0.17	0.26	-0.03	-0.44	-0.01	0.30	-0.08	0.23	0.23	0.29	0.26	0.59	0.29	0.32	-0.23		0.33	0.22	-0.35
Pb	-0.49	-0.28	0.22	-0.66	-0.17	0.59	0.25	-0.65	0.05	0.17	-0.01	0.53	0.09	0.59	0.56	0.49	0.85	0.71	-0.46	0.33		0.44	-0.42
Bi	-0.50	0.13	0.46	-0.72	0.23	0.19	-0.15	-0.63	0.06	0.31	0.25	0.21	-0.20	0.64	0.58	0.18	0.62	0.78	-0.32	0.22	0.44		-0.18
REE	0.32	0.36	0.32	0.41	0.41	-0.52	-0.36	0.50	0.04	0.17	0.43	-0.29	-0.04	-0.18	-0.34	-0.39	-0.49	-0.36	0.92	-0.35	-0.42	-0.18	

C.8 Correlation matrix of py-FeOOH and ccp-FeOOH analyses by LA-ICP-MS

Table C.7. Spearman correlation illustrating the relationship of various elements obtained by LA-ICP-MS of py FeOOH and ccp FeOOH (n=16). Due to low sample size, only moderate or strong correlations are considered (i.e., >0.50 or <-0.50).

	Na	Al	Mg	Si	Cl	S	Ca	Mn	Fe	Co	Ni	Cu	Zn	As	Mo	Ag	In	Sb	Ce	Au	Pb	Bi
Na		-0.48	0.10	0.07	-0.43	0.48	0.12	0.60	-0.45	-0.21	-0.05	0.21	-0.55	-0.43	-0.10		-0.88	-0.55	0.10	0.26	-0.17	-0.32
Al	-0.48		-0.47	0.21	0.38	-0.13	0.62	-0.52	0.03	0.58	-0.07	0.01	0.32	-0.45	0.58	-0.23	0.38	0.40	-0.39	-0.52	0.28	0.28
Mg	0.10	-0.47		-0.25	-0.54	0.16	-0.02	0.23	-0.49	0.02	-0.77	-0.05	-0.09	0.00	-0.63	0.10	-0.36	0.13	-0.05	-0.03	-0.41	-0.29
Si	0.07	0.21	-0.25		0.02	-0.38	0.35	0.13	0.61	-0.53	0.71	-0.34	0.16	-0.03	0.55	-0.68	-0.01	0.08	0.88	-0.09	-0.11	-0.72
Cl	-0.43	0.38	-0.54	0.02		0.06	0.11	-0.43	0.04	0.27	-0.14	-0.18	0.48	-0.06	0.27	0.17	0.45	-0.15	-0.38	-0.57	0.48	0.37
S	0.48	-0.13	0.16	-0.38	0.06		-0.23	0.13	-0.31	0.04	-0.19	0.39	-0.37	-0.23	-0.23	0.26	-0.32	0.02	-0.69	0.42	0.26	0.24
Ca	0.12	0.62	-0.02	0.35	0.11	-0.23		-0.13	0.02	0.34	-0.17	-0.03	0.09	-0.46	0.41	-0.16	-0.05	-0.06	-0.20	-0.48	0.08	-0.15
Mn	0.60	-0.52	0.23	0.13	-0.43	0.13	-0.13		-0.06	-0.65	0.03	0.22	-0.62	0.34	-0.43	0.07	-0.58	-0.02	0.48	0.83	-0.52	-0.36
Fe	-0.45	0.03	-0.49	0.61	0.04	-0.31	0.02	-0.06		-0.44	0.76	-0.58	0.43	0.49	0.19	-0.87	0.35	0.16	0.52	-0.25	-0.06	-0.38
Co	-0.21	0.58	0.02	-0.53	0.27	0.04	0.34	-0.65	-0.44		-0.54	0.35	0.16	-0.34	0.11	0.39	0.37	0.06	-0.63	-0.39	0.42	0.70
Ni	-0.05	-0.07	-0.77	0.71	-0.14	-0.19	-0.17	0.03	0.76	-0.54		-0.23	0.17	0.29	0.32	-0.55	0.20	0.20	0.64	0.23	0.01	-0.42
Cu	0.21	0.01	-0.05	-0.34	-0.18	0.39	-0.03	0.22	-0.58	0.35	-0.23		-0.69	-0.27	-0.04	0.54	-0.34	-0.02	-0.46	0.36	0.09	-0.12
Zn	-0.55	0.32	-0.09	0.16	0.48	-0.37	0.09	-0.62	0.43	0.16	0.17	-0.69		-0.03	0.31	-0.46	0.85	0.33	0.01	-0.45	0.46	0.57
As	-0.43	-0.45	0.00	-0.03	-0.06	-0.23	-0.46	0.34	0.49	-0.34	0.29	-0.27	-0.03		-0.61	-0.29	0.07	0.04	0.39	-0.09	-0.56	0.00
Mo	-0.10	0.58	-0.63	0.55	0.27	-0.23	0.41	-0.43	0.19	0.11	0.32	-0.04	0.31	-0.61		-0.15	0.29	0.13	0.03	-0.14	0.52	-0.26
Ag		-0.23	0.10	-0.68	0.17	0.26	-0.16	0.07	-0.87	0.39	-0.55	0.54	-0.46	-0.29	-0.15		-0.49	-0.80	-0.27	0.23	0.15	0.56
In	-0.88	0.38	-0.36	-0.01	0.45	-0.32	-0.05	-0.58	0.35	0.37	0.20	-0.34	0.85	0.07	0.29	-0.49		0.45	-0.17	-0.44	0.47	0.54
Sb	-0.55	0.40	0.13	0.08	-0.15	0.02	-0.06	-0.02	0.16	0.06	0.20	-0.02	0.33	0.04	0.13	-0.80	0.45		-0.22	0.37	0.08	0.06
Ce	0.10	-0.39	-0.05	0.88	-0.38	-0.69	-0.20	0.48	0.52	-0.63	0.64	-0.46	0.01	0.39	0.03	-0.27	-0.17	-0.22		0.11	-0.36	-0.44
Au	0.26	-0.52	-0.03	-0.09	-0.57	0.42	-0.48	0.83	-0.25	-0.39	0.23	0.36	-0.45	-0.09	-0.14	0.23	-0.44	0.37	0.11		0.13	-0.28
Pb	-0.17	0.28	-0.41	-0.11	0.48	0.26	0.08	-0.52	-0.06	0.42	0.01	0.09	0.46	-0.56	0.52	0.15	0.47	0.08	-0.36	0.13		0.39
Bi	-0.32	0.28	-0.29	-0.72	0.37	0.24	-0.15	-0.36	-0.38	0.70	-0.42	-0.12	0.57	0.00	-0.26	0.56	0.54	0.06	-0.44	-0.28	0.39	

C.9 Additional LA-ICP-MS profiles

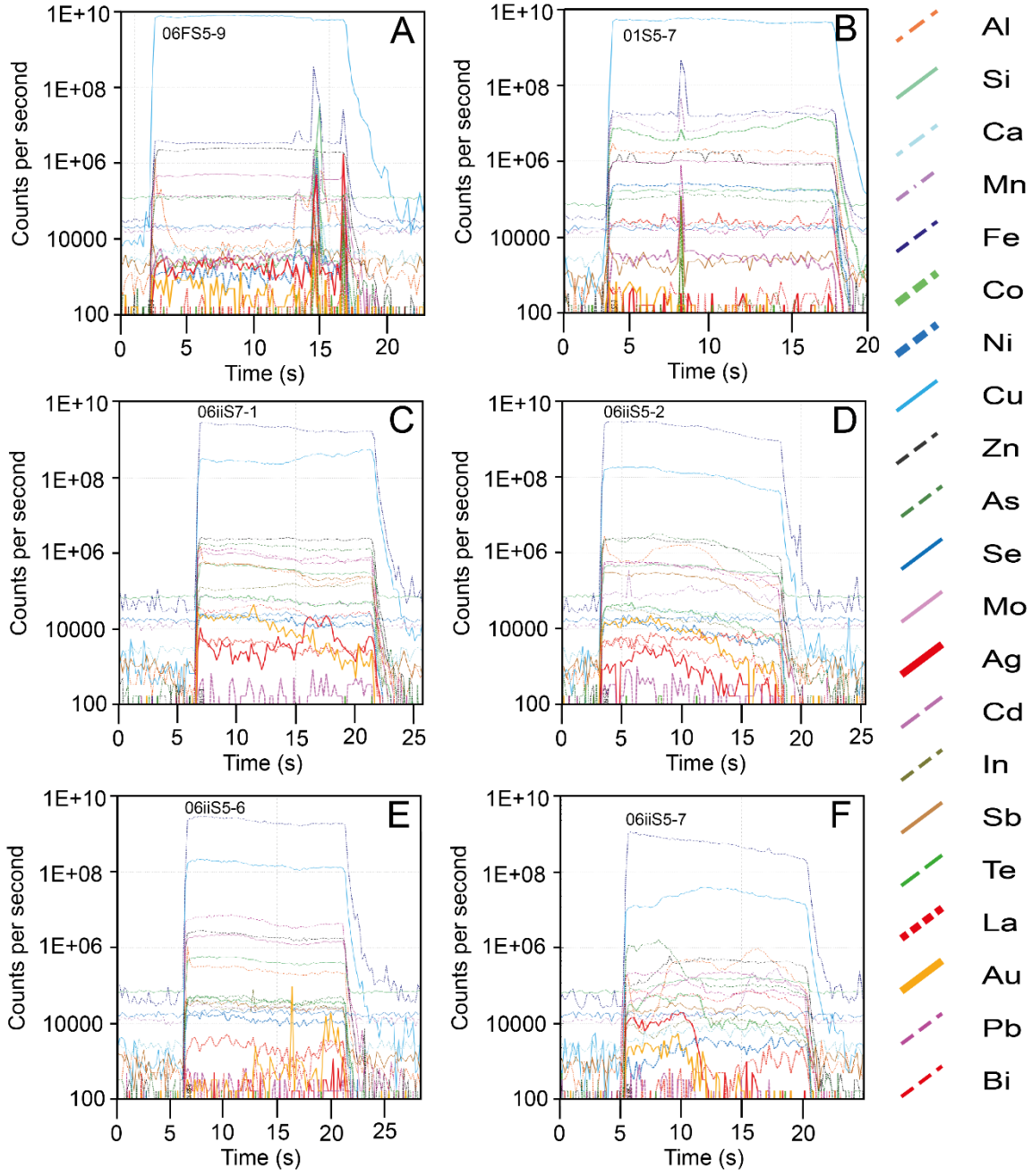

Figure C.1. Additional LA-ICP-MS depth profiles for of FeOOH and atacamite. **(A)** and **(B)** Atacamite with spikes of elements including Fe, As, Au, Ag, La, Sb, Mo suggesting inclusions of FeOOH or Fe-sulphide (06FS5-9 and 01S5-7). **(C)** Py-FeOOH phase with contradicting Au and Ag trends suggesting these metals are not retained together (06iiS7-1). **(D)** Co-enrichment of Au and Ag in py-FeOOH (06iiS5-2). **(E)** Individual spike of Au in py-FeOOH (06iiS5-6). **(F)** Pyrite grain with Au and Ag broad peak within sample 94_HY_06 (06iiS5-7).

C.10 Correlation matrix of all FeOOH analyses in sample 82_HY_06$_a$ and 82_HY_06$_b$ by SEM-EDS

Table C.8. Spearman correlation illustrating the relationship of various elements obtained by SEM-EDS for recently formed FeOOH in 82_HY_06$_b$ and modified FeOOH in 82_HY_06$_a$ (n=87-248).

	O	S	Si	Cu	Fe	Zn	Cl	P	Na	Mg	Ca
O		0.53	-0.08	-0.48	0.74	0.07	-0.47	0.20	0.20	0.20	-0.24
S	0.53		-0.45	-0.43	0.50	-0.11	-0.38	0.06	-0.01	0.19	-0.49
Si	-0.08	-0.45		0.40	-0.54	0.02	0.20	0.44	0.29	-0.06	0.22
Cu	-0.48	-0.43	0.40		-0.71	0.48	0.46	0.02	0.01	-0.12	0.50
Fe	0.74	0.50	-0.54	-0.71		0.30	-0.50	-0.16	-0.04	0.15	-0.44
Zn	0.07	-0.11	0.02	0.48	0.30		-0.04	-0.26	-0.20	0.08	-0.49
Cl	-0.47	-0.38	0.20	0.46	-0.50	-0.04		-0.22	0.17	-0.12	0.53
P	0.20	0.06	0.44	0.02	-0.16	-0.26	-0.22		-0.06	0.08	-0.27
Na	0.20	-0.01	0.29	0.01	-0.04	-0.20	0.17	-0.06		-0.07	0.52
Mg	0.20	0.19	-0.06	-0.12	0.15	0.08	-0.12	0.08	-0.07		0.06
Ca	-0.24	-0.49	0.22	0.50	-0.44	-0.49	0.53	-0.27	0.52	0.06	

C.11 Sequential leaching dataset

Table C.9. Elemental results in the leaching of nine samples of secondary FeOOH from Semenov. Bulk data obtained from Bishop et al. (2025b). Where total of leach solution is above bulk data, the total of leach solutions are used instead. Leach 1 (magnesium chloride) extracts sorbed metals, leach 2 (Na-acetate) extracts atacamite mineral phases, leach 3 (hydroxylamine-HCl in acetic acid) extracts easily reducible Fe-oxides and ferrihydrite and leach 4 (Na-dithionite) targets crystalline Fe-oxides and FeOOH such as goethite.

		Fe (wt.%)	Cu	Ca	Al (ppm)	Mn	Zn (ppm)	Sr (ppm)
	Leach 1	<LOD	0.01	0.35	<LOD	10	<LOD	88
	Leach 2	0.28	1.41	0.25	60	60	100	101
66_HY_05	Leach 3	27.22	0.92	0.08	520	1280	490	47
	Leach 4	4.82	0.06	0.08	120	10	150	12
	Bulk	32.32	2.48	0.72	1500	1900	1060	274
	Leach 1	<LOD	0.00	0.46	30	0	<LOD	77
	Leach 2	0.13	0.32	0.97	220	100	30	112
82_HY_01	Leach 3	21.14	0.67	0.11	2000	5010	130	29
	Leach 4	9.95	0.35	0.31	480	20	560	18
	Bulk	34.68	1.84	1.00	2400	6200	720	210
	Leach 1	0.00	0.00	0.70	40	<LOD	<LOD	114
	Leach 2	0.08	0.10	0.52	190	90	40	85
82_HY_05	Leach 3	26.62	1.08	0.12	2370	2820	290	34
	Leach 4	4.73	0.10	0.09	270	10	80	13
	Bulk	31.43	1.96	1.41	2200	2920	410	300
	Leach 1	0.02	0.00	8.39	130	30	<LOD	158
	Leach 2	0.22	12.71	0.07	<LOD	60	310	26
82_HY_06a	Leach 3	29.04	3.00	0.51	330	120	1000	29
	Leach 4	6.24	0.31	0.33	60	<LOD	350	17
	Bulk	35.51	16.79	0.22	520	210	1660	230
	Leach 1	0.00	0.00	0.50	20	0	10	76
	Leach 2	0.11	1.16	0.33	160	50	440	21
86_HY_04	Leach 3	36.46	1.38	0.09	1270	2150	2375	114
	Leach 4	4.19	0.07	0.22	150	10	490	13
	Bulk	40.76	2.61	1.15	1700	3000	3990	330
	Leach 1	<LOD	0.01	0.40	70	<LOD	10	118
	Leach 2	0.25	2.11	0.18	120	90	150	90
94_HY_04	Leach 3	32.34	2.29	0.12	1380	7570	540	35
	Leach 4	1.61	0.04	1.26	220	20	60	45
	Bulk	34.20	4.44	1.97	7200	13800	760	510
	Leach 1	<LOD	<LOD	0.25	80	10	20	69
	Leach 2	0.28	6.70	0.23	330	110	190	97
94_HY_06	Leach 3	32.31	2.10	0.12	830	4250	740	13
	Leach 4	2.84	0.08	0.01	130	<LOD	70	60
	Bulk	35.43	8.88	0.61	2100	6400	1020	310
	Leach 1	0.00	<LOD	0.43	20	10	20	99
	Leach 2	0.50	1.30	0.41	170	180	240	152
102_HY_04	Leach 3	38.90	0.93	0.09	650	6170	1070	73
	Leach 4	3.19	0.02	0.80	102	10	140	31
	Bulk	42.59	2.26	1.73	1600	7400	1620	400
	Leach 1	0.00	0.00	1.08	40	10	50	83
	Leach 2	0.15	0.00	0.19	90	50	300	58
102_HY_05	Leach 3	23.00	0.02	0.05	980	780	960	30
	Leach 4	14.84	0.02	0.06	600	<LOD	1050	15
	Bulk	38.00	0.09	1.37	2400	840	3530	200

C.12 Pourbaix diagram of thiosulphate-goethite stabilisation field

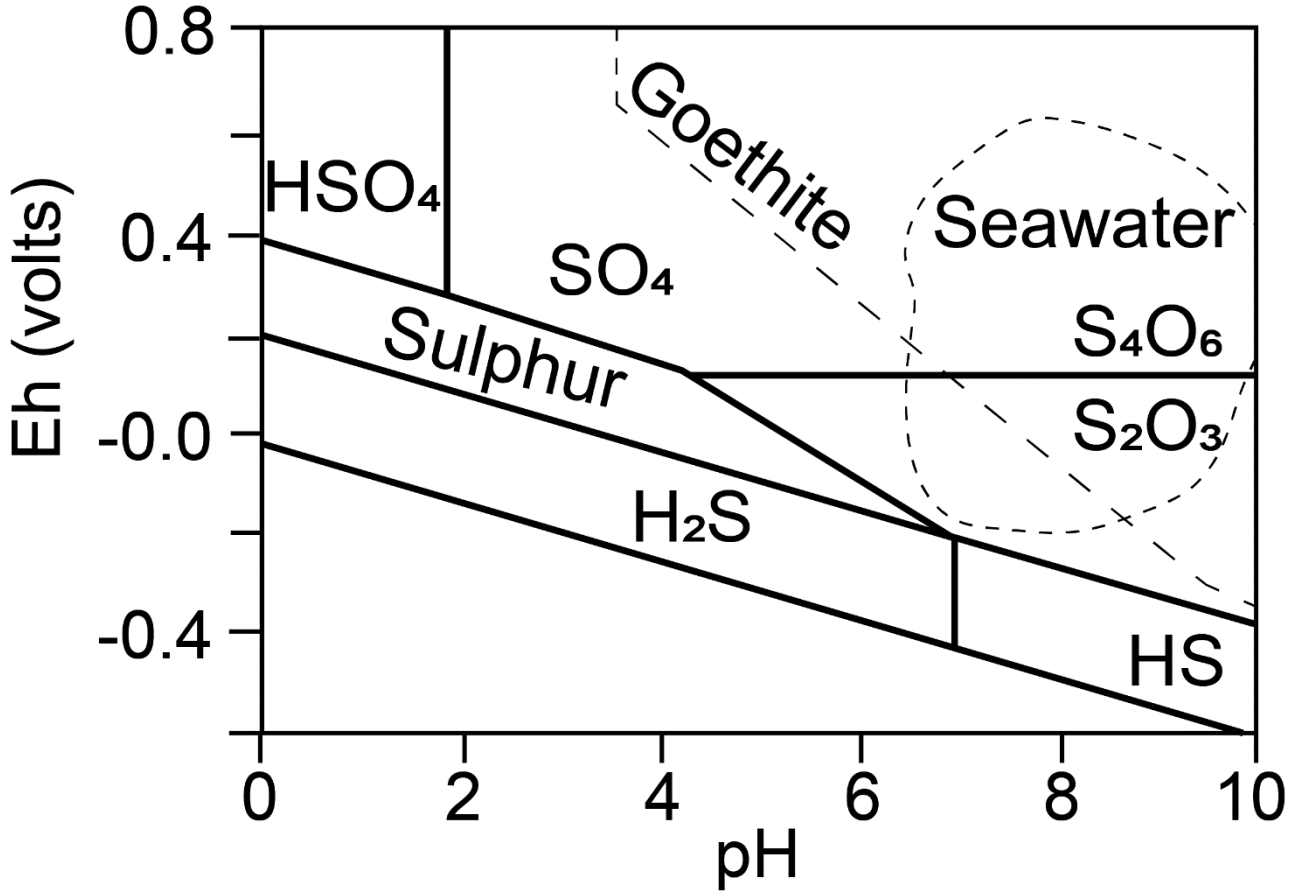

Figure C.2. Stability relations in the system S-O2-H2O in the absence of sulphate after Webster (1986) with stability field of goethite in seawater at 2°C after Glasby and Schulz (1999) and typical pH-Eh of seawater after Becking et al. (1960).

Appendix D **Supplementary materials to Chapter 6**

D.1 Effects of DO (%) on the concentration of metals in seawater

Table D.1. Correlation coefficient (R^2) of the concentration of metals presented within the study and dissolved oxygen (DO; %) and time

DE-02	DO	Time	Cu	Zn	As	Sb	Cd	Pb
DO	1.00							
Time	0.06	1.00						
Cu	0.26	0.01	1.00					
Zn	0.14	0.05	0.12	1.00				
As	0.16	0.04	0.74	0.09	1.00			
Sb	0.00	0.43	0.10	0.00	0.46	1.00		
Cd	0.27	0.09	0.70	0.08	0.27	0.01	1.00	
Pb	0.85	0.92	0.00	0.42	0.00	0.06	0.02	1.00

DE-03	DO	Time	Cu	Zn	As	Sb	Cd	Pb
DO	1.00							
Time	0.89	1.00						
Cu	0.86	0.74	1.00					
Zn	0.12	0.08	0.07	1.00				
As	0.09	0.14	0.03	0.00	1.00			
Sb	0.05	0.05	0.10	0.00	0.01	1.00		
Cd	0.10	0.06	0.20	0.03	0.14	0.02	1.00	
Pb	0.36	0.27	0.33	0.00	0.11	0.13	0.00	1.00

DE-05	DO	Time	Cu	Zn	As	Sb	Cd	Pb
DO	1.00							
Time	0.26	1.00						
Cu	0.01	0.47	1.00					
Zn	0.21	0.97	0.51	1.00				
As	0.03	0.18	0.28	0.22	1.00			
Sb	0.02	0.14	0.21	0.13	0.04	1.00		
Cd	0.16	0.96	0.59	0.95	0.18	0.21	1.00	
Pb	0.13	0.95	0.61	0.95	0.19	0.19	0.98	1.00

DE-06	DO	Time	Cu	Zn	As	Sb	Cd	Pb
DO	1.00							
Time	0.07	1.00						
Cu	0.06	0.05	1.00					
Zn	0.00	0.01	0.01	1.00				
As	0.56	0.29	0.00	0.02	1.00			
Sb	0.07	0.22	0.05	0.03	0.21	1.00		
Cd	0.02	0.00	0.00	0.05	0.06	0.06	1.00	
Pb	0.41	0.32	0.15	0.00	0.01	0.13	0.00	1.00

DE-07	DO	Time	Cu	Zn	As	Sb	Cd	Pb
DO	1.00							
Time	0.95	1.00						
Cu	0.08	0.12	1.00					
Zn	0.08	0.05	0.55	1.00				
As	0.01	0.01	0.62	0.57	1.00			
Sb	N/A	N/A	N/A	N/A	N/A	1.00		
Cd	0.84	0.94	0.24	0.00	0.08	N/A	1.00	
Pb	N/A	N/A	N/A	N/A	N/A	N/A	N/A	1.00

DE-10	DO	Time	Cu	Zn	As	Sb	Cd	Pb
DO	1.00							
Time	0.29	1.00						
Cu	0.01	0.01	1.00					
Zn	N/A	N/A	N/A	N/A				
As	N/A	N/A	N/A	N/A	N/A			
Sb	N/A	N/A	N/A	N/A	N/A	N/A		
Cd	N/A	N/A	N/A	N/A	N/A	N/A	N/A	
Pb	N/A	N/A	N/A	N/A	N/A	N/A	N/A	N/A

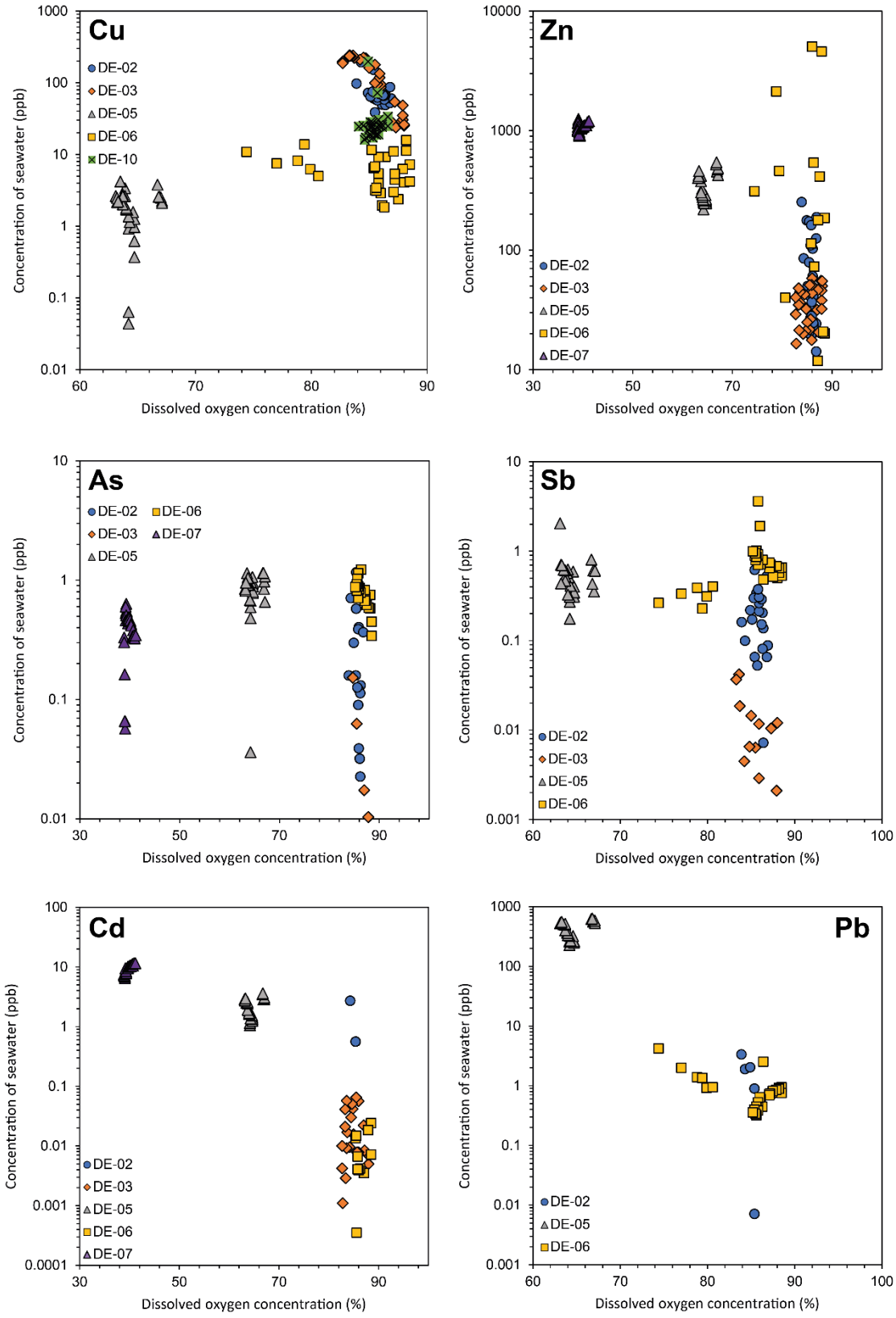

Figure D.1. Bivariate plots comparing DO against the concentration of Cu, Zn, As, Sb, Cd and Pb in seawater.

D.2 Concentration of Fe in seawater

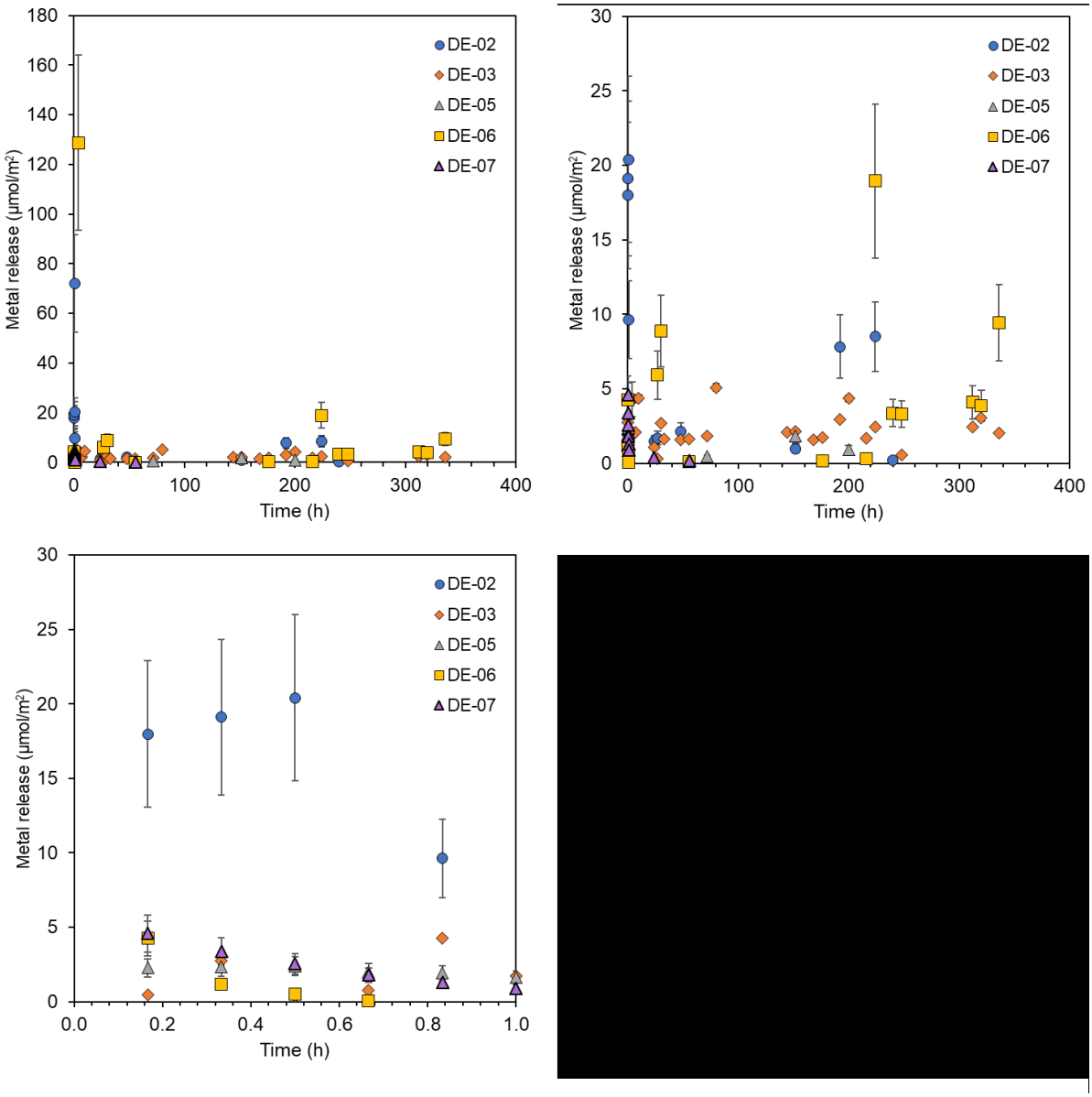

Figure D.2. Metal release of Fe leached over time with all samples showing the full experiment duration at the top, with the first hour shown at the bottom.

D.3 Concentration of metals in seawater over time

Table D.2. Concentration of metals (ppb) in seawater over time. Full dataset can be found after Bishop et al. (2025c). <LOD – below limit of detection.

ppb					Fe						Zn		
Time (h)	DE-02	DE-03	DE-05	DE-06	DE-07	DE-10	Time (h)	DE-02	DE-03	DE-05	DE-06	DE-07	DE-10
0	**25**	**90**	**14**	**47**	**15**	<LOD	**0**	**13**	**7**	**33**	**82**	**28**	<LOD
0.2	145	86	38	115	542	<LOD	0.2	266	30	237	439	1238	<LOD
0.3	153	58	39	66	404	<LOD	0.3	98	20	311	82	1249	<LOD
0.5	162	114	39	55	308	<LOD	0.5	190	49	270	2254	1232	<LOD
0.7	508	86	35	49	222	<LOD	0.7	92	34	266	588	1203	<LOD
0.8	89	33	34	30	164	<LOD	0.8	187	43	270	112	1168	<LOD
1.0	<LOD	67	31	37	118	<LOD	1.0	54	47	263	167	1154	<LOD
4.0	54	28	9	2082	<LOD	<LOD	4.0	116	40	277	200	1079	<LOD
7.0	<LOD	38	8	35	<LOD	<LOD	7.0	38	28	284	45	1022	<LOD
10.0	<LOD	49	9	30	<LOD	<LOD	10.0	73	40	264	147	998	<LOD
24.0	35	75	6	35	60	<LOD	24.0	57	50	306	313	972	<LOD
27.0	36	47	7	141	<LOD	<LOD	27.0	36	40	278	37	972	<LOD
30.0	22	336	6	187	<LOD	<LOD	30.0	27	24	283	148	943	<LOD
33.0	24	16	6	37	<LOD	<LOD	33.0	37	20	295	4719	917	<LOD
48.0	39	40	8	17	<LOD	<LOD	48.0	202	16	311	540	904	<LOD
55.7	<LOD	92	6	49	35	<LOD	55.7	47	41	307	30	909	<LOD
72.0	<LOD	770	18	22	<LOD	<LOD	72.0	61	41	342	306	940	<LOD
80.0	23	26	7	25	<LOD	<LOD	80.0	123	21	322	139	924	<LOD
144.0	<LOD	34	13	45	<LOD	<LOD	144.0	63	27	395	47	1042	<LOD
152.0	31	258	33	17	<LOD	<LOD	152.0	33	19	432	71	1042	<LOD
168.0	2	429	12	10	<LOD	<LOD	168.0	36	35	436	667	1040	<LOD
176.0	11	21	9	49	<LOD	<LOD	176.0	54	20	419	5175	1065	<LOD
192.1	77	54	10	26	<LOD	<LOD	192.1	58	32	442	19	1095	<LOD
200.0	16	56	24	39	<LOD	<LOD	200.0	49	32	433	241	1079	<LOD
216.2	<LOD	69	10	52	<LOD	<LOD	216.2	37	37	476	48	1109	<LOD
224.0	82	37	10	347	<LOD	<LOD	224.0	40	39	474	35	1102	<LOD
240.0	26	29	10	101	<LOD	<LOD	240.0	32	18	441	32	1102	<LOD
248.0	<LOD	67	10	99	<LOD	<LOD	248.0	33	28	491	71	1108	<LOD
312.1	<LOD	18	12	112	<LOD	<LOD	312.1	41	15	501	29	1183	<LOD
320.0	21	15	12	108	<LOD	<LOD	320.0	175	24	540	48	1173	<LOD
336.0	18	37	11	196	<LOD	<LOD	336.0	138	32	561	42	1202	<LOD

Table D.2. Continued

Cu							As						
Time (h)	DE-02	DE-03	DE-05	DE-06	DE-07	DE-10	Time (h)	DE-02	DE-03	DE-05	DE-06	DE-07	DE-10
0.0	**8.9**	**4.3**	**1.2**	**5.9**	<LOD	**3.3**	**0.0**	**0.59**	**0.34**	**0.58**	**0.29**	**0.39**	<LOD
0.2	106	41	1.2	21	<LOD	28	0.2	0.74	0.35	0.91	0.53	0.45	<LOD
0.3	202	36	1.2	16	<LOD	37	0.3	1.26	0.31	0.99	0.38	<LOD	<LOD
0.5	81	43	2.1	17	<LOD	28	0.5	0.87	0.35	1.05	0.41	<LOD	<LOD
0.7	162	45	1.6	25	<LOD	28	0.7	1.69	0.31	1.12	0.43	0.44	<LOD
0.8	159	38	1.8	14	<LOD	29	0.8	1.14	0.28	1.23	0.40	<LOD	<LOD
1.0	48	39	2.1	13	<LOD	34	1.0	0.35	0.27	1.19	0.45	0.45	<LOD
4.0	58	50	2.1	19	<LOD	29	4.0	0.33	0.25	1.13	1.43	0.55	<LOD
7.0	58	67	2.4	11	<LOD	27	7.0	0.32	0.29	1.24	0.50	0.71	<LOD
10.0	89	74	2.3	12	<LOD	29	10.0	0.62	0.30	1.25	0.61	0.68	<LOD
24.0	69	116	2.7	16	<LOD	28	24.0	0.44	0.31	1.31	0.71	0.99	<LOD
27.0	67	131	2.5	21	<LOD	31	27.0	0.28	0.33	0.61	0.83	0.90	<LOD
30.0	63	130	2.9	28	<LOD	28	30.0	0.33	0.27	1.05	0.99	0.92	<LOD
33.0	61	133	2.9	14	<LOD	28	33.0	0.31	0.31	1.21	0.84	0.92	<LOD
48.0	69	159	4.6	9.1	<LOD	31	48.0	0.37	0.29	1.23	0.87	0.91	<LOD
55.7	66	177	3.0	12	<LOD	76	55.7	0.33	0.28	1.21	0.92	0.96	<LOD
72.0	67	235	3.8	13	<LOD	27	72.0	0.38	0.40	1.21	0.96	0.87	<LOD
80.0	71	217	3.2	10	<LOD	25	80.0	0.42	0.26	1.21	0.91	0.83	<LOD
144.0	73	273	3.9	21	<LOD	22	144.0	0.52	0.27	1.32	1.06	0.83	<LOD
152.0	76	297	5.4	8.5	<LOD	22	152.0	0.56	0.48	1.37	1.09	0.80	<LOD
168.0	75	297	3.8	8.4	<LOD	23	168.0	0.71	0.30	1.30	1.02	0.85	<LOD
176.0	75	291	3.8	10	<LOD	24	176.0	0.61	0.32	1.16	1.07	0.85	<LOD
192.1	78	297	3.3	18	<LOD	22	192.1	0.63	0.28	1.14	0.95	0.82	<LOD
200.0	83	309	3.6	13	<LOD	22	200.0	0.70	0.26	1.16	1.35	0.83	<LOD
216.2	75	320	3.4	10	<LOD	20	216.2	0.70	0.24	1.24	1.05	0.80	<LOD
224.0	84	327	3.8	10	<LOD	21	224.0	0.71	0.24	1.16	1.14	0.79	<LOD
240.0	85	318	3.4	11	<LOD	201	240.0	0.68	0.24	1.04	1.11	0.75	<LOD
248.0	84	315	3.7	15	<LOD	31	248.0	0.74	0.29	1.25	1.12	0.71	<LOD
312.1	88	271	3.3	11	<LOD	19	312.1	0.97	0.21	1.32	1.24	0.70	<LOD
320.0	96	264	5.0	15	<LOD	20	320.0	0.96	0.27	1.37	1.15	0.72	<LOD
336.0	96	248	3.7	22	<LOD	28	336.0	0.94	0.24	1.37	1.10	0.72	<LOD

Table D.2. Continued

Sb							Cd						
Time (h)	DE-02	DE-03	DE-05	DE-06	DE-07	DE-10	Time (h)	DE-02	DE-03	DE-05	DE-06	DE-07	DE-10
0.0	**0.21**	**0.09**	**0.04**	**0.07**	<LOD	<LOD	**0.0**	**1.04**	**0.34**	**0.33**	**0.33**	**0.32**	<LOD
0.2	0.36	<LOD	0.28	0.31	<LOD	<LOD	0.2	0.89	0.36	1.06	0.33	6.5	<LOD
0.3	0.31	0.10	0.16	0.38	<LOD	<LOD	0.3	3.62	0.33	1.11	0.31	6.8	<LOD
0.5	0.42	<LOD	0.23	0.43	<LOD	<LOD	0.5	0.58	0.36	1.14	0.29	6.8	<LOD
0.7	0.80	<LOD	0.28	0.28	<LOD	<LOD	0.7	0.76	0.33	1.20	0.33	7.0	<LOD
0.8	0.17	0.09	0.25	0.36	<LOD	<LOD	0.8	1.57	0.30	1.19	0.30	7.0	<LOD
1.0	0.14	0.10	0.28	0.44	<LOD	<LOD	1.0	0.35	0.34	1.25	0.32	7.0	<LOD
4.0	0.19	0.09	0.32	0.52	<LOD	<LOD	4.0	0.37	0.33	1.31	0.31	7.2	<LOD
7.0	0.22	0.06	0.28	0.53	<LOD	<LOD	7.0	0.38	0.34	1.26	0.31	7.2	<LOD
10.0	0.20	0.04	0.32	0.56	<LOD	<LOD	10.0	0.84	0.35	1.27	0.33	7.5	<LOD
24.0	0.27	0.08	0.45	0.68	<LOD	<LOD	24.0	0.80	0.39	1.40	0.35	8.0	<LOD
27.0	0.18	<LOD	0.25	0.60	<LOD	<LOD	27.0	0.32	0.34	1.51	0.31	7.8	<LOD
30.0	0.27	<LOD	0.39	0.67	<LOD	<LOD	30.0	0.31	0.34	1.45	0.31	7.7	<LOD
33.0	0.19	<LOD	0.27	0.70	<LOD	<LOD	33.0	0.43	0.32	1.45	0.34	8.0	<LOD
48.0	0.29	0.10	0.44	0.55	<LOD	<LOD	48.0	0.35	0.31	1.62	0.29	7.9	<LOD
55.7	0.19	0.09	0.47	0.71	<LOD	<LOD	55.7	0.32	0.32	1.50	0.32	8.6	<LOD
72.0	0.29	0.09	0.43	0.72	<LOD	<LOD	72.0	0.31	0.40	1.66	0.32	8.5	<LOD
80.0	0.26	0.10	0.40	0.67	<LOD	<LOD	80.0	0.33	0.35	1.64	0.33	9.4	<LOD
144.0	0.37	0.09	0.46	0.76	<LOD	<LOD	144.0	0.35	0.38	2.01	0.31	9.6	<LOD
152.0	0.34	<LOD	0.47	0.73	<LOD	<LOD	152.0	0.31	0.39	2.07	0.31	9.4	<LOD
168.0	0.41	<LOD	0.36	0.81	<LOD	<LOD	168.0	0.33	0.37	2.11	0.33	10.0	<LOD
176.0	0.36	0.09	1.45	1.85	<LOD	<LOD	176.0	0.32	0.35	2.31	0.33	10.1	<LOD
192.1	0.41	0.11	0.52	0.72	<LOD	<LOD	192.1	0.33	0.35	2.22	0.32	10.1	<LOD
200.0	0.46	0.06	0.34	3.44	<LOD	<LOD	200.0	0.37	0.39	2.23	0.33	10.3	<LOD
216.2	0.49	0.13	0.52	0.81	<LOD	<LOD	216.2	0.34	0.35	2.37	0.29	10.2	<LOD
224.0	0.53	0.08	0.46	1.01	<LOD	<LOD	224.0	0.34	0.36	2.30	0.33	10.5	<LOD
240.0	0.51	<LOD	0.46	0.93	<LOD	<LOD	240.0	0.32	0.34	2.29	0.33	10.3	<LOD
248.0	0.50	0.12	0.29	0.90	<LOD	<LOD	248.0	0.33	0.38	2.36	0.34	11.0	<LOD
312.1	0.50	<LOD	0.46	0.87	<LOD	<LOD	312.1	0.33	0.34	2.44	0.28	11.1	<LOD
320.0	0.57	<LOD	0.59	0.95	<LOD	<LOD	320.0	0.67	0.35	2.72	0.34	11.4	<LOD
336.0	0.71	<LOD	0.34	1.00	<LOD	<LOD	336.0	0.58	0.34	2.81	0.31	11.4	<LOD

Table D.2. Continued

	Pb					
Time (h)	DE-02	DE-03	DE-05	DE-06	DE-07	DE-10
0.0	**2.5**	**0.78**	**1.7**	**0.65**	<LOD	<LOD
0.2	5.7	0.50	156	4.54	<LOD	<LOD
0.3	4.3	0.46	177	2.49	<LOD	<LOD
0.5	4.4	0.48	183	1.94	<LOD	<LOD
0.7	3.3	0.47	182	1.90	<LOD	<LOD
0.8	2.5	0.32	184	1.51	<LOD	<LOD
1.0	<LOD	0.39	179	1.52	<LOD	<LOD
4.0	<LOD	0.28	171	2.99	<LOD	<LOD
7.0	<LOD	0.59	180	1.36	<LOD	<LOD
10.0	<LOD	0.29	185	1.52	<LOD	<LOD
24.0	<LOD	0.31	220	1.35	<LOD	<LOD
27.0	<LOD	0.33	223	1.50	<LOD	<LOD
30.0	<LOD	0.26	228	1.47	<LOD	<LOD
33.0	<LOD	<LOD	229	1.44	<LOD	<LOD
48.0	<LOD	0.25	251	1.41	<LOD	<LOD
55.7	<LOD	<LOD	249	1.32	<LOD	<LOD
72.0	<LOD	0.30	278	1.33	<LOD	<LOD
80.0	<LOD	<LOD	276	1.32	<LOD	<LOD
144.0	<LOD	0.29	339	1.29	<LOD	<LOD
152.0	<LOD	0.37	346	1.20	<LOD	<LOD
168.0	<LOD	0.29	355	1.06	<LOD	<LOD
176.0	<LOD	<LOD	360	1.24	<LOD	<LOD
192.1	<LOD	0.23	368	1.13	<LOD	<LOD
200.0	<LOD	0.38	373	1.06	<LOD	<LOD
216.2	<LOD	0.24	381	1.01	<LOD	<LOD
224.0	<LOD	0.31	387	1.06	<LOD	<LOD
240.0	<LOD	0.25	365	1.00	<LOD	<LOD
248.0	<LOD	0.26	397	1.02	<LOD	<LOD
312.1	<LOD	<LOD	399	0.95	<LOD	<LOD
320.0	<LOD	<LOD	428	0.96	<LOD	<LOD
336.0	<LOD	0.26	434	0.98	<LOD	<LOD

D.4 Correlations of seawater concentration against bulk concentration of the sample (Cu)

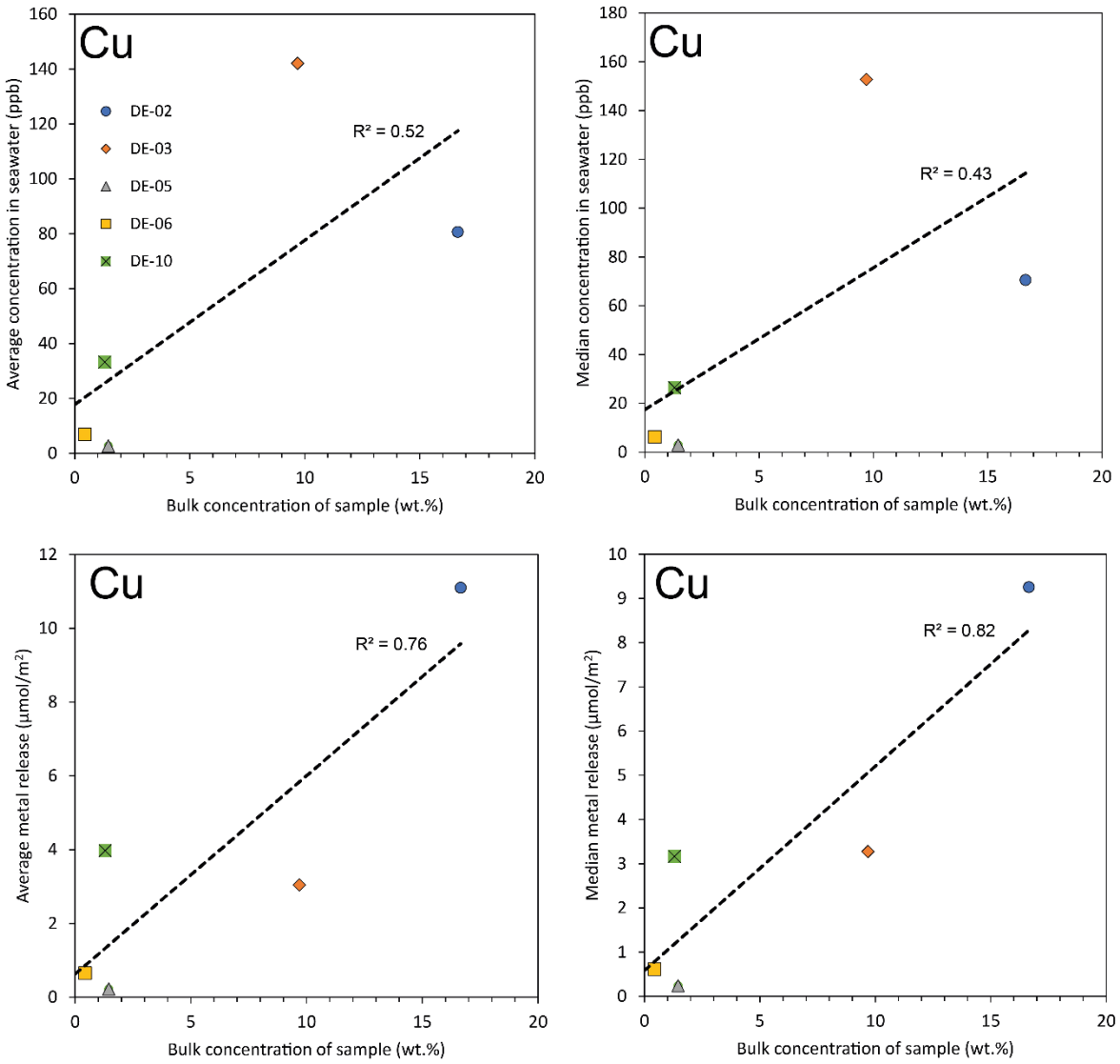

Figure D.3. Bivariate plots illustrating the relationship between both bulk concentration of Cu in seawater and metal release into seawater against the bulk concentration of Cu in the sulphide samples.

D.5 Correlations of seawater concentration against bulk concentration of the sample (Zn)

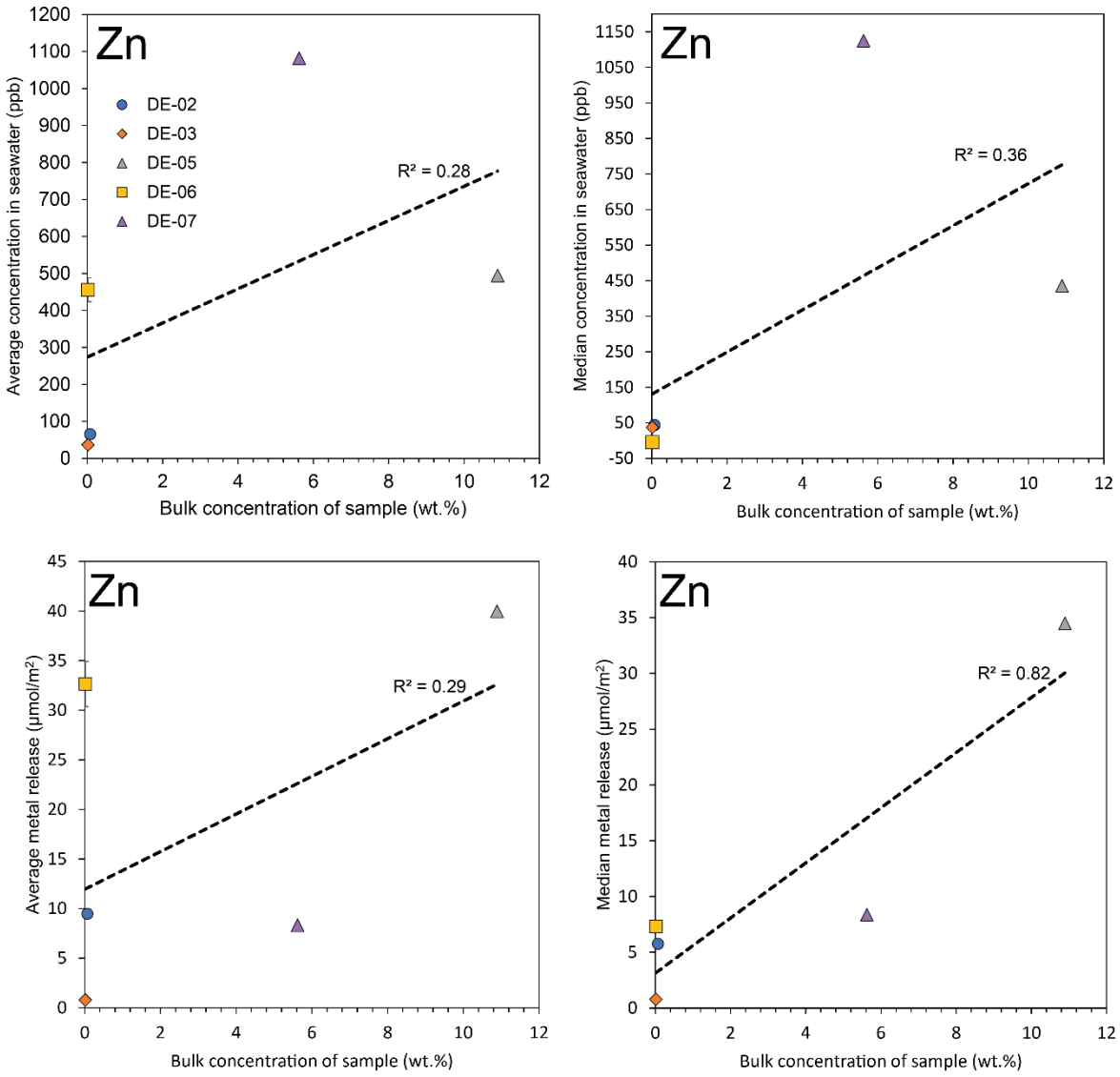

Figure D.3. Bivariate plots illustrating the relationship between both bulk concentration of Zn in seawater and metal release into seawater against the bulk concentration of Zn in the sulphide samples.

D.6 Calculations – Metal loss in slurry riser

The following parameters are based after the successful pilot ore extraction study after Ishiguro et al., (2018).

- 16 tonnes of sulphide ore was collected after the 23 minutes pilot study
- It takes seven minutes for the ore to go from the seafloor to onboard, considering the length of the riser at approximately 1,600 metres.

The following assumptions are made

- Surface area of the ore is constant
- Cu content is constant.
- Oxidation rate is constant
- Mineralogy is constant

Following calculation steps are for Cu based on sample DE-02.

Step 1. Calculate how much ore is transported every seven-minute cycle.

The sulphide ore is only subject the oxidation within the riser, while it is likely it will also be oxidised onboard, that is out of the scope of this study.

Initially, we need to calculate how much sulphide ore is transported every seven-minute cycle

(7/23) x 16 tonnes = 4.86957 tonnes of ore transported every cycle.

Step 2. Scaling the oxidation rate to the ore load

Here, we use the mass loss rate (see supplementary A.11) of this study and extrapolate it to the amount of ore transported every cycle.

We need to account for the volume of seawater in the study (which is 0.7 litres) and the oxidation rate of 0.0922 ppb/hour/0.7 litre

0.0922 * 0.7 = 0.06454 ppb/hour. Which is equivalent to 0.06454 µg lost per hour

Now, this can be scale from the sample used in this study (2.0368 g) to the amount of sulphide ore transported per cycle

((4.86957 tonnes x 1000) / (2.0368 g / 1000)) x 0.06454 µg = 154302 µg of Cu lost per hour

= 0.1543 g of Cu lost per hour

Now to determine how much Cu is lost per seven-minute cycle

=0.1543 x (7/60) = 0.018 g of Cu lost per cycle

Step 3. Calculate annual Cu loss

So, per hour there are 8.57 cycles

We can scale that up to cycles per day = 205.714

And again, up to a year = 75085.7

If there is a loss of 0.018 g of Cu per cycle, we can calculate the amount of Cu loss over a year

=0.0185 x 75085.7 = 1351.68 g

= 1.35 kg of Cu loss annually.

To account for natural variability in sulphide powder samples, oxidation rate calculations incorporate the %RSD values shown in Supplementary A.6. This approach provides upper and lower bounds for each measurement based on sample heterogeneity. For Cu, sample DE-02 shows a baseline oxidation rate of 0.0922 ppb/hour with a %RSD of 33.4%. Using this variability, the calculated range extends from 0.0614 ppb/hour (lower bound) to 0.123 ppb/hour (upper bound). Similarly, Zn measurements exhibit a %RSD of 45.8%. Applying this variability to samples DE-05 (baseline: 0.8509 ppb/hour) and DE-07 (baseline: 0.8888 ppb/hour) yields oxidation rate ranges of 0.461–1.241 ppb/hour and 0.482–1.296 ppb/hour, respectively.

D.7 Calculations – Metal loss in stockpiles

Step 1: Calculate total Cu/Zn in the sample

Total Cu/Zn in sample (g) = (Cu/Zn concentration (wt.%) / 100) x mass of sample (g)

Step 2: Convert dissolution rate to mass loss rate

Mass Loss Rate (μg/hour)=Cu/Zn Dissolution Rate* (μg/L/hour)×Volume of Seawater (L)

*Cu/Zn dissolution rate is obtained by plotting dissolved Cu/Zn concentration (ppb) against time and adding a linear trendline, which provides an equation in the form of y=mx+b. The slope m (in units of μg/L/hour) represents the Cu dissolution rate, or the increase in concentration over time. This rate reflects the average Cu/Zn released per hour in the experiment and was used for subsequent calculations.

Step 3: Length of time until full oxidation

For this step, we need to convert the mass loss rate from μg/hour to g/hour by simply dividing by $1x10^6$

Time until full oxidation (years) = (Mass loss rate (g/hour) / Total Cu/Zn in sample (g)) / 8760 (hours)

Step 4: Annual release of Cu/Zn

Annual release of Cu/Zn (g) = Mass loss rate (g/hour) x 8760 (hours)

Step 5: Scaling up to 1,000 tonnes

Annual release of 1,000 tonnes of sulphide ore (g) = Annual release of Cu/Zn x ($1x10^9$ / sample mass (g))

Step 6: Annual economic expenditure of stockpiling 1,000 tonnes of sulphide ore

Quantity of Cu/Zn lost in one year for 1,000 tonnes (g) x price of Cu/Zn (USD/g)

To account for natural variability in sulphide powder samples, oxidation rate calculations incorporate the %RSD values shown in Supplementary A.6. This approach provides upper and lower bounds for each measurement based on sample heterogeneity. For Cu, sample DE-02 shows a baseline oxidation rate of 0.0922 ppb/hour with a %RSD of 33.4%. Using this variability, the calculated range extends from 0.0614 ppb/hour (lower bound) to 0.123 ppb/hour (upper bound). Similarly, Zn measurements exhibit a %RSD of 45.8%. Applying this variability to samples DE-05 (baseline: 0.8509 ppb/hour) and DE-07 (baseline: 0.8888

ppb/hour) yields oxidation rate ranges of 0.461–1.241 ppb/hour and 0.482–1.296 ppb/hour, respectively.

Bibliography

Abkhoshk, E., Jorjani, E., Al-Harahsheh, M. S., Rashchi, F., & Naazeri, M. (2014). Review of the hydrometallurgical processing of non-sulfide zinc ores. *Hydrometallurgy*, *149*, 153-167. https://doi.org/10.1016/j.hydromet.2014.08.001

Abouchami, W., Galer, S. J. G., & Koschinsky, A. (1999). Pb and nd isotopes in NE atlantic Fe-Mn crusts: Proxies for trace metal paleosources and paleocean circulation. *Geochimica Et Cosmochimica Acta*, *63*(10), 1489-1505. https://doi.org/10.1016/S0016-7037(99)00068-X

Abraitis, P. K., Pattrick, R. A. D., Kelsall, G. H., & Vaughan, D. J. (2004). Acid leaching and dissolution of major sulphide ore minerals: Processes and galvanic effects in complex systems. *Mineralogical Magazine*, *68*(2), 343-351. https://doi.org/10.1180/0026461046820191

Agranier, A., Blichert-Toft, J., Graham, D., Debaille, V., Schiano, P., & Albarede, F. (2005). The spectra of isotopic heterogeneities along the Mid-Atlantic Ridge. *Earth and Planetary Science Letters*, *238*(1-2), 96-109. https://doi.org/10.1016/j.epsl.2005.07.011

Ali, S. H., Giurco, D., Arndt, N., Nickless, E., Brown, G., Demetriades, A., Durrheim, R., Enriquez, M. A., Kinnaird, J., Littleboy, A., Meinert, L. D., Oberhänsli, R., Salem, J., Schodde, R., Schneider, G., Vidal, O., & Yakovleva, N. (2017). Mineral supply for sustainable development requires resource governance. *Nature*, *543*(7645), 367-372. https://doi.org/10.1038/nature21359

Alt, J. C. (1995). Subseafloor processes in mid-ocean ridge hydrothermal systems. In S. E. Humphris, R. A. Zierenberg, L. S. Mullineaux, & R. E. Thomson (Eds.), *Seafloor hydrothermal systems: Physical, chemical, biological, and geological interactions* (pp. 85–114). American Geophysical Union. https://doi.org/10.1029/GM091p0085

Alt, J. C. (1988). Hydrothermal oxide and nontronite deposits on seamounts in the eastern pacific. *Marine Geology*, *81*(1), 227-239. https://doi.org/10.1016/0025-3227(88)90029-1

Anthony, J. W., Bideaux, R. A., Bladh, K. W., & Nichols, M. C. (2025). *Handbook of mineralogy*. Retrieved 03-05-2025 from http://www.handbookofmineralogy.org/

ANZG. (2018). Australian and New Zealand guidelines for fresh and marine water quality. https://www.waterquality.gov.au/anz-guidelines

ANZG. (2023). Toxicant default guideline values for aquatic ecosystem protection: Dissolved copper in marine water. https://www.waterquality.gov.au/anz-guidelines/guideline-values/default/water-quality-toxicants

Australian Government. (2024). Australia's critical minerals list and strategic materials list. 20 June 2023; updated 20 February 2024. Retrieved 3 February 2025 from https://www.industry.gov.au/publications/australias-critical-minerals-list-and-strategic-materials-list

Baker, E., & Beaudoin, Y. (2013). Deep sea minerals: Sea-floor massive sulphides, a physical, biological, environmental and technical review (Vol. 1A). Secretariat of the Pacific Community.

Balistrieri, L. S., & Murray, J. W. (1982). The adsorption of Cu, Pb, Zn, and Cd on goethite from major ion seawater. *Geochimica Et Cosmochimica Acta*, *46*(7), 1253-1265. https://doi.org/10.1016/0016-7037(82)90010-2

Barrat, J. A., Zanda, B., Moynier, F., Bollinger, C., Liorzou, C., & Bayon, G. (2012). Geochemistry of CI chondrites: Major and trace elements, and Cu and Zn isotopes. *Geochimica Et Cosmochimica Acta*, *83*, 79-92. https://doi.org/10.1016/j.gca.2011.12.011

Barrie, C. T., & Hannington, M. D. (1999). Volcanic-associated massive sulfide deposits: Processes and examples in modern and ancient settings. *Reviews in Economic Geology*, *8*, 1-11.

Beaulieu, S. E., & Szafrański, K. M. (2020). Interridge global database of active submarine hydrothermal vent fields version 3.4 PANGAEA. https://doi.org/10.1594/PANGAEA.917894

Becking, L. G. M. B., Kaplan, I. R., & Moore, D. (1960). Limits of the natural environment in terms of pH and oxidation-reduction potentials. *The Journal of Geology*, *68*(3), 243-284. https://doi.org/10.1086/626659

Beltenev, V., Ivanov, A., Rozhdestvenskaya, I., Cherkashov, G., Stepanova, T., Shilov, V., Pertsev, A., Davydov, M., Egorov, I., Melekestseva, I., Narkevsky, E., & Ignatov, V. (2007). A new hydrothermal field at 13°30′N on the Mid-Atlantic Ridge. *InterRidge News*, *16*, 9-10.

Beltenev, V., Ivanov, A., Rozhdestvenskaya, I., Cherkashov, G., Stepanova, T., Shilov, V., Davydov, M., Laiba, A., Kaylio, V., Narkevsky, E., Pertsev, A., Dobretzova, I., Gustaytis, A., Popova, Y., Amplieva, E., & Evrard, C. (2009). New data about hydrothermal fields on the Mid-Atlantic Ridge between 11° - 14° N: 32nd cruise of R/V Professor Logatchev. In (Vol. 18, pp. 13-17). InterRidge News.

Ben Othman, D., White, W. M., & Patchett, J. (1989). The geochemistry of marine sediments, island arc magma genesis, and crust-mantle recycling. *Earth and Planetary Science Letters*, *94*(1), 1-21. https://doi.org/10.1016/0012-821X(89)90079-4

Benedetti, M., & Boulëgue, J. (1991). Mechanism of gold transfer and deposition in a supergene environment. *Geochimica Et Cosmochimica Acta*, *55*(6), 1539-1547. https://doi.org/10.1016/0016-7037(91)90126-P

Benjamin, M. M. (1983). Adsorption and surface precipitation of metals on amorphous iron oxyhydroxide. *Environmental Science & Technology*, *17*(11), 686-692. https://doi.org/10.1021/es00117a012

Benjamin, M. M., & Leckie, J. O. (1981). Multiple-site adsorption of Cd, Cu, Zn, and Pb on amorphous iron oxyhydroxide. *Journal of Colloid and Interface Science*, *79*(1), 209-221. https://doi.org/10.1016/0021-9797(81)90063-1

Berquó, T. S., Banerjee, S. K., Ford, R. G., Penn, R. L., & Pichler, T. (2007). High crystallinity Si-ferrihydrite: An insight into its Néel temperature and size dependence of magnetic properties. *Journal of Geophysical Research: Solid Earth*, *112*(B2). https://doi.org/10.1029/2006JB004583

Bilenker, L. D., Romano, G. Y., & McKibben, M. A. (2016). Kinetics of sulfide mineral oxidation in seawater: Implications for acid generation during in situ mining of seafloor hydrothermal vent deposits. *Applied Geochemistry*, *75*, 20-31. https://doi.org/10.1016/j.apgeochem.2016.10.010

Binns, R., Scott, S., Bogdanov, Y., Lisitzin, A., Gordeev, V., Gurvich, E., Finlayson, E., Boyd, T., Dotter, L., Wheller, G., & Muravyev, K. (1993). Hydrothermal oxide and gold-rich sulfate

deposits of Franklin Seamount, western Woodlark Basin, Papua New Guinea. *Economic Geology*, *88*, 2122-2153. https://doi.org/10.2113/gsecongeo.88.8.2122

Bird, P. (2003). An updated digital model of plate boundaries. *Geochemistry, Geophysics, Geosystems*, *4*(3). https://doi.org/10.1029/2001GC000252

Bishop, C., Murton, B., Lichtschlag, A., & Roberts, S. (2025a). Geochemical composition, isotopic measurements and X-ray diffraction (XRD) results of Fe-oxyhydroxide and massive sulphide samples from Semenov Hydrothermal Field of the Mid-Atlantic Ridge during the RRS James Cook cruise JC224 (March-April 2022). NERC EDS British Oceanographic Data Centre NOC. https://doi.org/doi:10.5285/2e0aa2c7-6331-62b9-e063-7086abc06891

Bishop, C., Murton, B., Lichtschlag, A., & Roberts, S. (2025b). Images and descriptions of Fe-oxyhydroxide and massive sulphide samples from Semenov Hydrothermal Field of the Mid-Atlantic Ridge during the RRS James Cook cruise JC224 (March-April 2022). NERC EDS British Oceanographic Data Centre NOC. https://doi.org/10.5285/2e0a9d33-56f6-622d-e063-7086abc06e59

Bishop, C., Murton, B., Lichtschlag, A., & Roberts, S. (2025c). Geochemical and mineralogical analysis of sulphide materials and seawater from oxidative dissolution experiments, from samples obtained from Wetar Island, Indonesia (~2002), from RV Celtic Explorer cruise CE11009 (2011) and from RRS James Cook cruises JC082 (2013) and JC138 (2016). NERC EDS British Oceanographic Data Centre NOC. https://doi.org/doi:10.5285/2ea9a7f7-c47f-2bff-e063-7086abc06652

Bishop, C., Josso, P., Lichtschlag, A., Roberts, S., Belgrano, T., Milton, J., Lesage, M., & Murton, B. (2025d). Geochemical analyses, sequential leaching and X-ray diffraction (XRD) results of Fe-oxyhydroxide and massive sulphide samples from the Semenov Hydrothermal Field, Mid-Atlantic Ridge, during RRS James Cook cruise JC224 (March-April 2022). NERC EDS British Oceanographic Data Centre NOC. https://doi.org/doi:10.5285/3724bb78-2139-edbe-e063-7086abc0903f

Bishop, C., Josso, P., Lichtschlag, A., Roberts, S., Belgrano, T., Lesage, M., & Murton, B. (2025e). Raw laser-ablation inductively couple plasma mass spectrometer (LA-ICP-MS) data and images of laser-ablation (LA) targets of Fe-oxyhydroxide and massive sulphide samples from the Semenov Hydrothermal Field of the Mid-Atlantic Ridge during the RRS James Cook cruise JC224 (March-April 2022). NERC EDS British Oceanographic Data Centre NOC. https://doi.org/doi:10.5285/373699c7-6323-d4fa-e063-7086abc08606

Bishop, C., Josso, P., Lichtschlag, A., Roberts, S., Belgrano, T., Milton, J., Lesage, M., & Murton, B. (2025f). Raw laser-ablation time-of-flight inductively couple plasma mass spectrometer (LA-TOF-ICP-MS) data from sample 82_HY_06 from the Semenov Hydrothermal Field of the Mid-Atlantic Ridge during the RRS James Cook cruise JC224 (March-April 2022). NERC EDS British Oceanographic Data Centre NOC. https://doi.org/doi:10.5285/37352554-2193-8984-e063-7086abc047f5

Blowes, D. W., Ptacek, C. J., Jambor, J. L., & Weisener, C. G. (2003). 9.05 - The geochemistry of acid mine drainage. In H. D. Holland & K. K. Turekian (Eds.), *Treatise on geochemistry* (pp. 149-204). Pergamon. https://doi.org/10.1016/B0-08-043751-6/09137-4

Boschen, R. E., Rowden, A. A., Clark, M. R., & Gardner, J. P. A. (2013). Mining of deep-sea seafloor massive sulfides: A review of the deposits, their benthic communities, impacts from mining, regulatory frameworks and management strategies. *Ocean & Coastal Management*, *84*, 54-67. https://doi.org/10.1016/j.ocecoaman.2013.07.005

Boström, K. (1973). The origin and fate of ferromanganoan active ridge sediments. *Stockholm Contributions in Geology*, *27*, 149-243.

Bowers, T. S., Vondamm, K. L., & Edmond, J. M. (1985). Chemical evolution of mid-ocean ridge hot springs. *Geochimica Et Cosmochimica Acta*, *49*(11), 2239-2252. https://doi.org/10.1016/0016-7037(85)90224-8

Bridgestock, L., Rehkämper, M., van de Flierdt, T., Paul, M., Milne, A., Lohan, M. C., & Achterberg, E. P. (2018). The distribution of lead concentrations and isotope compositions in the eastern tropical atlantic ocean. *Geochimica Et Cosmochimica Acta*, *225*, 36-51. https://doi.org/10.1016/j.gca.2018.01.018

Brunauer, S., Emmett, P. H., & Teller, E. (1938). Adsorption of gases in multimolecular layers. *Journal of the American Chemical Society*, *60*(2), 309-319. https://doi.org/10.1021/ja01269a023

Burton, K. W., Cenki-Tok, B., Mokadem, F., Harvey, J., Gannoun, A., Alard, O., & Parkinson, I. J. (2012). Unradiogenic lead in earth's upper mantle. *Nature Geoscience*, *5*(8), 570-573. https://doi.org/10.1038/ngeo1531

Cai, W.J., & Sayles, F. L. (1996). Oxygen penetration depths and fluxes in marine sediments. *Marine Chemistry*, *52*(2), 123-131. https://doi.org/10.1016/0304-4203(95)00081-X

Calmano, W., Ahlf, W., & Förstner, U. (1988). Study of metal sorption/desorption processes on competing sediment components with a multichamber device. *Environmental Geology and Water Sciences*, *11*(1), 77-84. https://doi.org/10.1007/BF02587766

Cann, J. R., Blackman, D. K., Smith, D. K., McAllister, E., Janssen, B., Mello, S., Avgerinos, E., Pascoe, A. R., & Escartin, J. (1997). Corrugated slip surfaces formed at ridge-transform intersections on the Mid-Atlantic Ridge. *Nature*, *385*, 329-332. https://doi.org/10.1038/385329a0

Carreiro-Silva, M., Martins, I., Riou, V., Raimundo, J., Caetano, M., Bettencourt, R., Rakka, M., Cerqueira, T., Godinho, A., Morato, T., & Colaço, A. (2022). Mechanical and toxicological effects of deep-sea mining sediment plumes on a habitat-forming cold-water octocoral. *Frontiers in Marine Science*, 9, Article 915650. https://doi.org/10.3389/fmars.2022.915650

Cherkashov, G., Ivanov, V., Bel'tenev, V., Lazareva, L., Rozhdestvenskaya, I., Samovarov, M., Poroshina, I., Sergeev, M., Stepanova, T., Dobretsova, I., & Kuznetsov, V. (2013). Massive sulfide ores of the northern equatorial Mid-Atlantic Ridge. *Oceanology*, *53*. https://doi.org/10.1134/S0001437013050032

Cherkashov, G., Kuzntetsov, V., Kuksa, K., Tabuns, E., Maksimov, F., & Beltenev, V. (2017). Sulfide geochronology along the northern equatorial Mid-Atlantic Ridge. *Ore Geology Reviews*, *87*. https://doi.org/10.1016/j.oregeorev.2016.10.015

Claff, S., Sullivan, L., Burton, E., & Bush, R. (2010). A sequential extraction procedure for acid sulfate soils: Partitioning of iron. *Geoderma*, *155*, 224-230. https://doi.org/10.1016/j.geoderma.2009.12.002

Clout, J. M. F., & Manuel, J. R. (2015). 2 - mineralogical, chemical, and physical characteristics of iron ore. In L. Lu (Ed.), *Iron ore* (pp. 45-84). Woodhead Publishing. https://doi.org/10.1016/B978-1-78242-156-6.00002-2

Constantinou, G. (1972). *The geology and genesis of the sulphide ores of Cyprus* (Unpublished doctoral dissertation). Imperial College London (University of London).

Constantinou, G., & Govett, G. J. S. (1972). Genesis of sulphide deposits, ochre and umber of Cyprus. *Institution of Mining and Metallurgy, Transactions, Section B Applied Earth Science*, *81*(783), B34-B46.

Constantinou, G., & Govett, G. J. S. (1973). Geology, geochemistry, and genesis of cyprus sulfide deposits. *Economic Geology*, *68*(6), 843-858. https://doi.org/10.2113/gsecongeo.68.6.843

Cornell, R. M., & Schwertmann, U. (2003). *The iron oxides: Structure, properties, reactions, occurrences and uses* (2nd Edition ed.). Wiley-VCH, Weinheim. https://doi.org/10.1002/3527602097

Corvellec, H., Stowell, A. F., & Johansson, N. (2022). Critiques of the circular economy. *Journal of Industrial Ecology*, *26*(2), 421-432. https://doi.org/10.1111/jiec.13187

Deady, E., Moon, C., Moore, K., Goodenough, K. M., & Shail, R. K. (2022). Bismuth: Economic geology and value chains. *Ore Geology Reviews*, *143*, 104722. https://doi.org/10.1016/j.oregeorev.2022.104722

Debaar, H. J. W., Bacon, M. P., Brewer, P. G., & Bruland, K. W. (1985). Rare-earth elements in the Pacific and Atlantic oceans. *Geochimica Et Cosmochimica Acta*, *49*(9), 1943-1959. https://doi.org/10.1016/0016-7037(85)90089-4

Debret, B., Andreani, M., & Godard, M. (2024). A review of abyssal serpentinite geochemistry and geodynamics. *Earth-Science Reviews*, *258*, 104910. https://doi.org/10.1016/j.earscirev.2024.104910

Dekov, V. M., Kamenov, G. D., Stummeyer, J., Thiry, M., Savelli, C., Shanks, W. C., Fortin, D., Kuzmann, E., & Vertes, A. (2007). Hydrothermal nontronite formation at Eolo Seamount (Aeolian volcanic arc, Tyrrhenian Sea). *Chemical Geology*, *245*(1-2), 103-119. https://doi.org/10.1016/j.chemgeo.2007.08.006

Dekov, V. M., Petersen, S., Garbe-Schonberg, C. D., Kamenov, G. D., Perner, M., Kuzmann, E., & Schmidt, M. (2010). Fe-Si-oxyhydroxide deposits at a slow-spreading centre with thickened oceanic crust: The Lilliput hydrothermal field (9° 33' S, Mid-Atlantic Ridge). *Chemical Geology*, *278*(3-4), 186-200. https://doi.org/10.1016/j.chemgeo.2010.09.012

Dekov, V., Boycheva, T., Halenius, U., Petersen, S., Billström, K., Stummeyer, J., Kamenov, G., & Shanks, W. (2011). Atacamite and paratacamite from the ultramafic-hosted Logatchev seafloor vent field (14 degrees 45 ' N, Mid-Atlantic Ridge). *Chemical Geology*, *286*(3-4), 169-184. https://doi.org/10.1016/j.chemgeo.2011.05.002

Dickson, A. G. (1984). pH scales and proton-transfer reactions in saline media such as sea water. *Geochimica Et Cosmochimica Acta*, *48*(11), 2299-2308. https://doi.org/10.1016/0016-7037(84)90225-4

Ding, Y., Long, Y., Wang, W., Wei, Z., & Cai, S. (2023). Iron (oxyhydr)oxides are responsible for the stabilization of Cu and Zn in amd after treatment with limestone. *PeerJ*(11:e14663). https://doi.org/10.7717/peerj.14663

Douville, E., Bienvenu, P., Charlou, J. L., Donval, J. P., Fouquet, Y., Appriou, P., & Gamo, T. (1999). Yttrium and rare earth elements in fluids from various deep-sea hydrothermal systems. *Geochimica Et Cosmochimica Acta*, *63*(5), 627-643. https://doi.org/10.1016/S0016-7037(99)00024-1

Dunk, R. M., & Mills, R. A. (2006). The impact of oxic alteration on plume-derived transition metals in ridge flank sediments from the East Pacific Rise. *Marine Geology*, *229*(3), 133-157. https://doi.org/10.1016/j.margeo.2006.03.007

Dutrieux, A. M. (2020). *Rise and fall of a hydrothermal system: A tale of metalliferous sediments (TAG hydrothermal field, MAR, 26° N).* (Doctoral dissertation, University of Southampton, UK). University of Southampton ePrints. https://eprints.soton.ac.uk/445271/

Dutrieux, A. M., Lichtschlag, A., Barriga, F. J. A. S., Martins, S., Milinovic, J., & Murton, B. J. (2023). Metal preservation and mobilization in sediments at the TAG Hydrothermal Field, Mid-Atlantic Ridge. *Geochemistry, Geophysics, Geosystems*, *24*(6), e2023GC010879. https://doi.org/10.1029/2023GC010879

Eggins, S. M., & Shelley, J. M. G. (2002). Compositional heterogeneity in NIST SRM 610-617 glasses. *Geostandards Newsletter*, *26*(3), 269-286. https://doi.org/10.1111/j.1751-908X.2002.tb00634.x

Elderfield, H., Hawkesworth, C. J., Greaves, M. J., & Calvert, S. E. (1981). Rare earth element geochemistry of oceanic ferromanganese nodules and associated sediments. *Geochimica Et Cosmochimica Acta*, *45*(4), 513-528. https://doi.org/10.1016/0016-7037(81)90184-8

Emmons, W. H. (1917). The enrichment of ore deposits (U.S. Geological Survey Bulletin No. 625). U.S. Government Printing Office. https://pubs.usgs.gov/publication/b625

Escartin, J. (2014). ODEMAR oceanic detachment faults at the Mid-Atlantic Ridge. Cruise report. N/O Pourquoi Pas? – ROV Victor 6000 – AUV Abyss 6000. 16 Nov - 19 Dec 2013, Mindelo (Cape Verde) - Point a Pitre (Guadeloupe). https://doi.org/10.13155/47149

Escartin, J., Mevel, C., Petersen, S., Bonnemains, D., Cannat, M., Andreani, M., Augustin, N., Bézos, A., Chavagnac, V., Choi, Y., GODARD, M., Haaga, K., Hamelin, C., ILDEFONSE, B., Jamieson, J., John, B., Leleu, T., Macleod, C. j., Massot-campos, M., . . . Garcia, R. (2017). Tectonic structure, evolution, and the nature of oceanic core complexes and their detachment fault zones (13°20′N and 13°30′N, Mid Atlantic Ridge). *Geochemistry, Geophysics, Geosystems*, *18*(4), 1451-1482. https://doi.org/10.1002/2016gc006775

European Commission. (2023). *Study on the critical raw materials for the eu 2023 – final report*. Publications Office of the European Union. https://data.europa.eu/doi/10.2873/725585

Fallon, E. K., Petersen, S., Brooker, R. A., & Scott, T. B. (2017). Oxidative dissolution of hydrothermal mixed-sulphide ore: An assessment of current knowledge in relation to seafloor massive sulphide mining. *Ore Geology Reviews*, *86*, 309-337. https://doi.org/10.1016/j.oregeorev.2017.02.028

Fallon, E. K., Niehorster, E., Brooker, R. A., & Scott, T. B. (2018). Experimental leaching of massive sulphide from tag active hydrothermal mound and implications for seafloor mining. *Marine Pollution Bulletin*, *126*, 501-515. https://doi.org/10.1016/j.marpolbul.2017.10.079

Fallon, E. K., Frische, M., Petersen, S., Brooker, R. A., & Scott, T. B. (2019). Geological, mineralogical and textural impacts on the distribution of environmentally toxic trace elements in seafloor massive sulfide occurrences. *Minerals*, *9*(3). https://doi.org/10.3390/min9030162

Fanka, A., & Tadthai, J. (2023). Petrology and geochemistry of li-bearing pegmatites and related granitic rocks in southern thailand: Implications for petrogenesis and lithium potential in thailand [Original Research]. *Frontiers in Earth Science*, *Volume 11 - 2023*. https://doi.org/10.3389/feart.2023.1221485

Faure, A. (1998). *Principles and applications of geochemistry*. Prentice Hall.

Firstova, A., Stepanova, T., Cherkashov, G., Goncharov, A., & Babaeva, S. (2016). Composition and formation of gabbro-peridotite hosted seafloor massive sulfide deposits from the

Ashadze-1 Hydrothermal Field, Mid-Atlantic Ridge. *Minerals*, *6*(1). https://doi.org/10.3390/min6010019

Firstova, A., Stepanova, T., Sukhanova, A., Cherkashov, G., & Poroshina, I. (2019). Au and Te minerals in seafloor massive sulphides from Semyenov-2 Hydrothermal Field, Mid-Atlantic Ridge. *Minerals*, *9*(5). https://doi.org/10.3390/min9050294

Firstova, A., Cherkashov, G., Stepanova, T., Sukhanova, A., Poroshina, I., & Bel'tenev, V. (2022). New data for the internal structure of ultramafic hosted seafloor massive sulfides (SMS) deposits: Case study of the Semenov-5 Hydrothermal Field (13°31′ N, MAR). *Minerals*, *12*(12). https://doi.org/10.3390/min12121593

Fouquet, Y., Wafik, A., Cambon, P., Mevel, C., Meyer, G., & Gente, P. (1993). Tectonic setting and mineralogical and geochemical zonation in the Snake Pit sulfide deposit (Mid-Atlantic Ridge at 23 degrees N). *Economic Geology*, *88*(8), 2018-2036. https://doi.org/10.2113/gsecongeo.88.8.2018

Fouquet, Y., Knott, R., Cambon, P., Fallick, A., Rickard, D., & Desbruyeres, D. (1996). Formation of large sulfide mineral deposits along fast spreading ridges. Example from off-axial deposits at 12°43′N on the East Pacific Rise. *Earth and Planetary Science Letters*, *144*(1), 147-162. https://doi.org/10.1016/0012-821X(96)00142-2

Fouquet, Y., Henry, K., Knott, R., & Cambon, P. (1998). Geochemical section of the TAG hydrothermal mound. *Proceedings of the Ocean Drilling Program: Scientific Results*, *158*, 363-387. https://doi.org/10.2973/odp.proc.sr.158.216.1998

Fouquet, Y., Cambon, P., Etoubleau, J., Charlou, J. L., Ondreas, H., Barriga, F. J. A. S., Cherkashov, G., Semkova, T., Poroshina, I., Bohn, M., Donval, J. P., Henry, K., Murphy, P., & Rouxel, O. (2010). Geodiversity of hydrothermal processes along the Mid-Atlantic Ridge and ultramafic-hosted mineralization: A new type of oceanic Cu-Zn-Co-Au volcanogenic massive sulfide deposit. *Diversity of Hydrothermal Systems on Slow Spreading Ocean Ridges*, *188*, 321-367. https://doi.org/10.1029/2008gm000746

Francheteau, J., Needham, H. D., Choukroune, P., Juteau, T., Seguret, M., Ballard, R. D., Fox, P. J., Normark, W., Carranza, A., Cordoba, D., Guerrero, J., Rangin, C., Bougault, H., Cambon, P., & Hekinian, R. (1979). Massive deep-sea sulfide ore-deposits discovered on the east pacific rise. *Nature*, *277*(5697), 523-528. https://doi.org/10.1038/277523a0

Franklin, J. M., Lydon, J. W., & Sangster, D. F. (1981). Volcanic-associated massive sulfide deposits. In B. J. Skinner (Ed.), Economic Geology Seventy-Fifth Anniversary Volume (pp. 485–627). Society of Economic Geologists. https://doi.org/10.5382/av75.15

Franklin, J. M., Gibson, H. L., Jonasson, I. R., & Galley, A. G. (2005). Volcanogenic massive sulfide deposits. In J. W. Hedenquist, J. F. H. Thompson, R. J. Goldfarb, & J. P. Richards (Eds.), *Economic Geology 100th Anniversary Volume* (pp. 525–560). Society of Economic Geologists. https://doi.org/10.5382/AV100.17

Froelich, P. N., Klinkhammer, G. P., Bender, M. L., Luedtke, N. A., Heath, G. R., Cullen, D., Dauphin, P., Hammond, D., Hartman, B., & Maynard, V. (1979). Early oxidation of organic matter in pelagic sediments of the eastern equatorial atlantic: Suboxic diagenesis. *Geochimica Et Cosmochimica Acta*, *43*(7), 1075-1090. https://doi.org/10.1016/0016-7037(79)90095-4

Fuchida, S., Ishibashi, J., Shimada, K., Nozaki, T., Kumagai, H., Kawachi, M., Matsushita, Y., & Koshikawa, H. (2018). Onboard experiment investigating metal leaching of fresh hydrothermal sulfide cores into seawater. *Geochemical Transactions*, *19*. https://doi.org/10.1186/s12932-018-0060-9

Gale, A., Dalton, C. A., Langmuir, C. H., Su, Y. J., & Schilling, J. G. (2013). The mean composition of ocean ridge basalts. *Geochemistry Geophysics Geosystems*, *14*(3), 489-518. https://doi.org/10.1029/2012gc004334

Garbe-Schönberg, D., & Müller, S. (2014). Nano-particulate pressed powder tablets for LA-ICP-MS. *Journal of Analytical Atomic Spectrometry*, 29(6), 990–1000. https://doi.org/10.1039/C4JA00007B

Gartman, A., Payan, D., Au, M., Reeves, E., Jamieson, J., Gini, C., & Roerdink, D. (2024). Hydrothermal plume fallout, mass wasting, and volcanic eruptions contribute to sediments at Loki's Castle Vent Field, Mohns Ridge. *Geochemistry, Geophysics, Geosystems*, *25*. https://doi.org/10.1029/2023GC011094

Gebco Bathymetric Compilation Group. (2024). The GEBCO_2024 Grid - a continuous terrain model of the global oceans and land. NERC EDS British Oceanographic Data Centre NOC. https://doi.org/doi:10.5285/1c44ce99-0a0d-5f4f-e063-7086abc0ea0f

Gini, C., Jamieson, J. W., Reeves, E. P., Gartman, A., Barreyre, T., Babechuk, M. G., Jørgensen, S. L., & Robert, K. (2024). Iron oxyhydroxide-rich hydrothermal deposits at the high-temperature Fåvne Vent Field, Mohns Ridge. *Geochemistry, Geophysics, Geosystems*, *25*(6), e2024GC011481. https://doi.org/10.1029/2024GC011481

Glasby, G. P., & Schulz, H. D. (1999). Eh pH diagrams for Mn, Fe, Co, Ni, Cu and As under seawater conditions: Application of two new types of Eh pH diagrams to the study of specific problems in marine geochemistry. *Aquatic Geochemistry*, *5*(3), 227-248. https://doi.org/10.1023/A:1009663322718

Goldhaber, M. B. (1983). Experimental study of metastable sulfur oxyanion formation during pyrite oxidation at pH 6-9 and 30 degrees C. *American Journal of Science*, 283(3), 193–217. https://doi.org/10.2475/ajs.283.3.193

Görn, M. G., Bolanz, R. M., Parry, S., Göttlicher, J., Steininger, R., & Majzlan, J. (2021). Incorporation of Mo^{6+} in ferrihydrite, goethite, and hematite. *Clays and Clay Minerals*, *69*(2), 188-204. https://doi.org/10.1007/s42860-021-00116-x

Goss, C. J. (1987). The kinetics and reaction mechanism of the goethite to hematite transformation. *Mineralogical Magazine*, *51*(361), 437-451. https://doi.org/10.1180/minmag.1987.051.361.11

Grant, J. A. (1986). The isocon diagram; a simple solution to Gresens' equation for metasomatic alteration. *Economic Geology*, *81*(8), 1976-1982. https://doi.org/10.2113/gsecongeo.81.8.1976

Green, C. J., Lederer, G. W., Parks, H. L., & Zientek, M. L. (2020). Grade and tonnage model for tungsten skarn deposits—2020 update (U.S. Geological Survey Scientific Investigations Report 2020–5085, 23 pp.). U.S. Geological Survey. https://doi.org/10.3133/sir20205085

Gresens, R. L. (1967). Composition-volume relationships of metasomatism. *Chemical Geology*, *2*, 47-65. https://doi.org/10.1016/0009-2541(67)90004-6

Grundl, T., & Delwiche, J. (1993). Kinetics of ferric oxyhydroxide precipitation. *Journal of Contaminant Hydrology*, *14*(1), 71-87. https://doi.org/10.1016/0169-7722(93)90042-Q

Gwyther, D. (2008). Environmental impact statement, solwara 1 project. *Nautilus Minerals Niugini Limited, Main Report Coffey Natural Systems, Brisbane*.

Hannington, M., Herzig, P., Scott, S., Thompson, G., & Rona, P. (1991). Comparative mineralogy and geochemistry of gold-bearing sulfide deposits on the mid-ocean ridges. *Marine Geology*, *101*(1), 217-248. https://doi.org/10.1016/0025-3227(91)90073-D

Hannington, M. D., & Jonasson, I. R. (1992). Fe and Mn oxides at seafloor hydrothermal vents. In H. C. W. Skinner & R. W. Fitzpatrick (Eds.), *Biomineralization: Processes of iron and manganese: Modern and ancient environments* (Catena Supplement 21, pp. 351–370). Schweizerbart Science Publishers.

Hannington, M. D. (1993). The formation of atacamite during weathering of sulfides on the modern sea-floor. *Canadian Mineralogist*, *31*, 945-956.

Hannington, M. D., Petersen, S., Jonasson, I. R., & Franklin, J. M. (1994). Hydrothermal activity and associated mineral deposits of the seafloor. *Geological Survey of Canada, Open File, 2915c, Natural Resources Canada*. https://doi.org/10.4095/82631

Hannington, M. D., Jonasson, I. R., Herzig, P. M., & Petersen, S. (1995). Physical and chemical processes of seafloor mineralization at mid-ocean ridges. In *Seafloor hydrothermal systems: Physical, chemical, biological, and geological interactions* (pp. 115-157). https://doi.org/10.1029/GM091p0115

Hannington, M. D., Herzig, P., Petersen, S., Gregoire, D. C., & Belanger, P. (1998a). Data report: Major and trace element geochemistry of shipboard samples from site 957, TAG Hydrothermal Field, Mid-Atlantic Ridge. *Proceedings of the Ocean Drilling Program: Scientific Results*, *158*, 27-40. https://doi.org/doi:10.2973/odp.proc.sr.158.203.1998

Hannington, M. D., Galley, A. G., Herzig, P. M., & Petersen, S. (1998b). Comparison of the TAG mound and stockwork complex with Cyprus-type massive sulfide deposits. *Proceedings of the Ocean Drilling Program: Scientific Results*(158), 389-415. https://doi.org/10.2973/odp.proc.sr.158.217.1998

Hannington, M. D., de Ronde, C. E. J., & Petersen, S. (2005). Sea-floor tectonics and submarine hydrothermal systems. In J. W. Hedenquist, J. F. H. Thompson, R. J. Goldfarb, & J. P. Richards (Eds.), *Economic Geology 100th Anniversary Volume* (pp. 111–141). Society of Economic Geologists. https://doi.org/10.5382/AV100.06

Hannington, M., Jamieson, J., Monecke, T., Petersen, S., Goldfarb, R. J., Marsh, E. E., & Monecke, T. (2010). Modern sea-floor massive sulfides and base metal resources: Toward an estimate of global sea-floor massive sulfide potential. In R. J. Goldfarb, E. E. Marsh, & T. Monecke (Eds.), *The challenge of finding new mineral resources: Global metallogeny, innovative exploration, and new discoveries* (Vol. 15, pp. 317-338). Society of Economic Geologists. https://doi.org/10.5382/SP.15.2.001

Hannington, M., Jamieson, J., Monecke, T., Petersen, S., & Beaulieu, S. (2011). The abundance of seafloor massive sulfide deposits. *Geology*, *39*, 1155-1158. https://doi.org/10.1130/G32468.1

Hart, S. R. (1984). A large-scale isotope anomaly in the southern hemisphere mantle. *Nature*, *309*(5971), 753-757. https://doi.org/10.1038/309753a0

Haymon, R. M. (1983). Growth history of hydrothermal black smoker chimneys. *Nature*, *301*(5902), 695-698. https://doi.org/10.1038/301695a0

Haymon, R. M., & Kastner, M. (1981). Hot spring deposits on the East Pacific Rise at 21°N: Preliminary description of mineralogy and genesis. *Earth and Planetary Science Letters*, *53*(3), 363-381. https://doi.org/10.1016/0012-821X(81)90041-8

Haynes, W. M. (Ed.). (2016). *CRC handbook of chemistry and physics (97th ed.). CRC Press.* https://doi.org/10.1201/9781315380476

Hein, J.R. (2004). Cobalt-rich ferromanganese crusts: Global distribution, composition, origin and research activities. In: Minerals other than polymetallic nodules of the International Seabed Area; Proceedings of a workshop held on 26-30 June 2000, International Seabed Authority, Kingston, Jamaica, volume 1, 188-256.

Hein, J. R., & Koschinsky, A. (2014). 13.11 Deep-ocean ferromanganese crusts and nodules. In H. D. Holland & K. K. Turekian (Eds.), Treatise on geochemistry (2nd ed., Vol. 13, pp. 273–291). Elsevier. https://doi.org/10.1016/B978-0-08-095975-7.01111-6

Hein, J. R., Konstantinova, N., Mikesell, M., Mizell, K., Fitzsimmons, J. N., Lam, P. J., Jensen, L. T., Xiang, Y., Gartman, A., Cherkashov, G., Hutchinson, D. R., & Till, C. P. (2017). Arctic deep water ferromanganese-oxide deposits reflect the unique characteristics of the arctic ocean. *Geochemistry, Geophysics, Geosystems*, *18*(11), 3771-3800. https://doi.org/10.1002/2017GC007186

Hein, J. R., Mizell, K., Koschinsky, A., & Conrad, T. A. (2013). Deep-ocean mineral deposits as a source of critical metals for high- and green-technology applications: Comparison with land-based resources. *Ore Geology Reviews*, *51*, 1-14. https://doi.org/10.1016/j.oregeorev.2012.12.001

Hein, J. R., Schulz, M. S., Dunham, R. E., Stern, R. J., & Bloomer, S. H. (2008). Diffuse flow hydrothermal manganese mineralization along the active Mariana and southern Izu-Bonin arc system, western Pacific. *Journal of Geophysical Research-Solid Earth*, 113(B8). https://doi.org/10.1029/2007JB005432

Hein, K. A. A., & Tshibubudze, A. (2016). Manganese deposits of the Oudalan province in the northeast of Burkina Faso, and Ansongo Inlier in eastern Mali. *Ore Geology Reviews*, *78*, 645-651. https://doi.org/10.1016/j.oregeorev.2015.11.008

Hekinian, R., & Fouquet, Y. (1985). Volcanism and metallogenesis of axial and off-axial structures on the East Pacific Rise near 13 degrees N. *Economic Geology*, *80*(2), 221-249. https://doi.org/10.2113/gsecongeo.80.2.221

Hekinian, R., Hoffert, M., Larque, P., Cheminee, J. L., Stoffers, P., & Bideau, D. (1993). Hydrothermal Fe and Si oxyhydroxide deposits from south-Pacific intraplate volcanos and East Pacific Rise axial and off-axial regions. *Economic Geology and the Bulletin of the Society of Economic Geologists*, *88*(8), 2099-2121. https://doi.org/10.2113/gsecongeo.88.8.2099

Hem, J. D. (1985). Study and interpretation of the chemical characteristics of natural water (Water-Supply Paper 2254). U.S. Geological Survey. https://pubs.usgs.gov/publication/wsp2254

Hepburn, L. E., Butler, I. B., Boyce, A., & Schröder, C. (2020). The use of operationally-defined sequential Fe extraction methods for mineralogical applications: A cautionary tale from Mössbauer spectroscopy. *Chemical Geology*, *543*, 119584. https://doi.org/10.1016/j.chemgeo.2020.119584

Herzig, P. M., & Hannington, M. D. (1995). Polymetallic massive sulfides at the modern seafloor a review. *Ore Geology Reviews*, *10*(2), 95-115. https://doi.org/10.1016/0169-1368(95)00009-7

Herzig, P. M., Hannington, M. D., Scott, S. D., Maliotis, G., Rona, P. A., & Thompson, G. (1991). Gold-rich sea-floor gossans in the Troodos Ophiolite and on the Mid-Atlantic Ridge. *Economic*

Geology and the Bulletin of the Society of Economic Geologists, *86*(8), 1747-1755. https://doi.org/10.2113/gsecongeo.86.8.1747

Hiemstra, T. (2018). Surface structure controlling nanoparticle behavior: Magnetism of ferrihydrite, magnetite, and maghemite. *Environmental Science: Nano*, *5*(3), 752-764. https://doi.org/10.1039/C7EN01060E

Hiemstra, T., & Van Riemsdijk, W. H. (2009). A surface structural model for ferrihydrite i: Sites related to primary charge, molar mass, and mass density. *Geochimica Et Cosmochimica Acta*, *73*(15), 4423-4436. https://doi.org/10.1016/j.gca.2009.04.032

Holmes, P. R., & Crundwell, F. K. (2000). The kinetics of the oxidation of pyrite by ferric ions and dissolved oxygen: An electrochemical study. *Geochimica Et Cosmochimica Acta*, *64*(2), 263-274. https://doi.org/10.1016/S0016-7037(99)00296-3

Hou, X., Han, X., Hu, X., & Liu, J. (2024). Formation mechanism of Fe oxyhydroxides and behavior of metals during the oxidation of submarine sulfides at the Wocan-1 hydrothermal field, Carlsberg Ridge. *Ore Geology Reviews*, *174*, 106307. https://doi.org/10.1016/j.oregeorev.2024.106307

Hrischeva, E., & Scott, S. D. (2007). Geochemistry and morphology of metalliferous sediments and oxyhydroxides from the endeavour segment, Juan de Fuca Ridge. *Geochimica Et Cosmochimica Acta*, *71*(14), 3476-3497. https://doi.org/10.1016/j.gca.2007.03.024

Hu, S., Tao, C., Liao, S., Guan, Y., Yin, X., Zhu, C., Liang, J., & Guo, Z. (2023). Oxidative dissolution of sulfide minerals tends to accumulate more dissolved heavy metals in deep seawater environments than in shallow seawater environments. *Environmental Science & Technology*, *57*, 21438-21447. https://doi.org/10.1021/acs.est.3c07507

Hu, S., Tao, C., Liao, S., Zhu, C., & Qiu, Z. (2022). Transformation of minerals and mobility of heavy metals during oxidative weathering of seafloor massive sulfide and their environmental significance. *Science of the Total Environment*, *819*, 153091. https://doi.org/10.1016/j.scitotenv.2022.153091

Huminicki, D. M. C., & Rimstidt, J. D. (2009). Iron oxyhydroxide coating of pyrite for acid mine drainage control. *Applied Geochemistry*, *24*(9), 1626-1634. https://doi.org/10.1016/j.apgeochem.2009.04.032

Humphris, S. E., Herzig, P. M., Miller, D. J., & Shipboard Scientific Party. (1996). *Proceedings of the Ocean Drilling Program, Initial Reports, Volume 158*. Ocean Drilling Program, Texas A&M University. https://doi.org/10.2973/odp.proc.ir.158.1996

Humphris, S. E., Herzig, P. M., Miller, D. J., Alt, J. C., Becker, K., Brown, D., Brügmann, G., Chiba, H., Fouquet, Y., Gemmell, J. B., Guerin, G., Hannington, M. D., Holm, N. G., Honnorez, J. J., Iturrino, G. J., Knott, R., Ludwig, R., Nakamura, K., Petersen, S., . . . Zhao, X. (1995). The internal structure of an active sea-floor massive sulphide deposit. *Nature*, *377*(6551), 713-716. https://doi.org/10.1038/377713a0

Hunter, K. A. (1998). The temperature dependence of pH in surface seawater. *Deep Sea Research Part I: Oceanographic Research Papers*, *45*(11), 1919-1930. https://doi.org/10.1016/S0967-0637(98)00047-8

Idoine, M. E., Raycraft, E. R., Hobbs, S. F., Everett, P., Evans, E. J., Mills, A. J., Currie, D., Horn, S., & Shaw, R. A. (2024). *World mineral production 2018-22*. British Geological Survey, Keyworth, Nottingham. https://nora.nerc.ac.uk/id/eprint/537241

Ishiguro, S., Masuda, M., Komatsu, M., Norihiro, Y., & Seiya, K. (2018). Development of the pilot system for test of excavating and ore lifting of seafloor polymetallic sulfides. *Mitsubishi heavy industries technical review*, *55*(3), 1-7.

Jambor, J. L., & Dutrizac, J. E. (1998). Occurrence and constitution of natural and synthetic ferrihydrite, a widespread iron oxyhydroxide. *Chemical Reviews*, *98*(7), 2549-2586. https://doi.org/10.1021/cr970105t

Jamieson, J. W., & Gartman, A. (2020). Defining active, inactive, and extinct seafloor massive sulfide deposits. *Marine Policy*, *117*. https://doi.org/10.1016/j.marpol.2020.103926

Janecky, D. R., & Seyfried, W. E. (1984). Formation of massive sulfide deposits on oceanic ridge crests - incremental reaction models for mixing between hydrothermal solutions and seawater. *Geochimica Et Cosmochimica Acta*, *48*(12), 2723-2738. https://doi.org/10.1016/0016-7037(84)90319-3

Jochum, K. P., Nohl, U., Herwig, K., Lammel, E., Stoll, B., & Hofmann, A. W. (2005). Georem: A new geochemical database for reference materials and isotopic standards. *Geostandards and Geoanalytical Research*, *29*(3), 333-338. https://doi.org/10.1111/j.1751-908X.2005.tb00904.x

Jochum, K. P., Wilson, S. A., Becker, H., Garbe-Schönberg, D., Groschopf, N., Kadlag, Y., Macholdt, D. S., Mertz-Kraus, R., Otter, L. M., Stoll, B., Stracke, A., Weis, U., Haug, G. H., & Andreae, M. O. (2016). FeMnOx-1: A new microanalytical reference material for the investigation of Mn–Fe rich geological samples. *Chemical Geology*, *432*, 34-40. https://doi.org/10.1016/j.chemgeo.2016.03.026

Johnson, N. E., Craig, J. R., & Rimstidt, J. D. (1986). Compositional trends in tetrahedrite. *The Canadian Mineralogist*, *24*(2), 385-397.

Jolly, W. T. (1974). Behavior of Cu, Zn, and Ni during prehnite-pumpellyite rank metamorphism of the Keweenawan basalts, northern Michigan. *Economic Geology*, *69*(7), 1118-1125. https://doi.org/10.2113/gsecongeo.69.7.1118

Jørgensen, B. B., Wenzhöfer, F., Egger, M., & Glud, R. N. (2022). Sediment oxygen consumption: Role in the global marine carbon cycle. *Earth-Science Reviews*, *228*, 103987. https://doi.org/10.1016/j.earscirev.2022.103987

Juliani, C., & Ellefmo, S. L. (2018). Resource assessment of undiscovered seafloor massive sulfide deposits on an Arctic mid-ocean ridge: Application of grade and tonnage models. *Ore Geology Reviews*, *102*, 818-828. https://doi.org/10.1016/j.oregeorev.2018.10.002

Kaiser, H. F. (1974). An index of factorial simplicity. *Psychometrika*, *39*(1), 31-36. https://doi.org/10.1007/BF02291575

Kalinin, Y. A., Palyanova, G. A., Naumov, E. A., Kovalev, K. R., & Pirajno, F. (2019). Supergene remobilization of Au in Au-bearing regolith related to orogenic deposits: A case study from Kazakhstan. *Ore Geology Reviews*, *109*, 358-369. https://doi.org/10.1016/j.oregeorev.2019.04.019

Kennedy, C. B., Scott, S. D., & Ferris, F. G. (2004). Hydrothermal phase stabilization of 2-line ferrihydrite by bacteria. *Chemical Geology*, *212*(3), 269-277. https://doi.org/10.1016/j.chemgeo.2004.08.017

Knight, R. D., Roberts, S., & Cooper, M. J. (2018). Investigating monomineralic and polymineralic reactions during the oxidation of sulphide minerals in seawater: Implications for mining seafloor massive sulphide deposits. *Applied Geochemistry*, *90*, 63-74. https://doi.org/10.1016/j.apgeochem.2017.12.027

Knott, R., Fouquet, Y., Honnorez, J., & Bohn, M. (1998). Petrology of hydrothermal mineralization: A vertical section through the TAG mound. *Proceedings of the Ocean Drilling Program: Scientific Results*, *158*, 5-26. https://doi.org/10.2973/odp.proc.sr.158.201.1998

Kooner, Z. S. (1993). Comparative study of adsorption behavior of copper, lead, and zinc onto goethite in aqueous systems. *Environmental Geology*, *21*(4), 242-250. https://doi.org/10.1007/BF00775914

Koschinsky, A., & Hein, J. R. (2003). Uptake of elements from seawater by ferromanganese crusts: Solid-phase associations and seawater speciation. *Marine Geology*, *198*(3), 331-351. https://doi.org/10.1016/S0025-3227(03)00122-1

Koski, R. A., Jonasson, I. R., Kadko, D. C., Smith, V. K., & Wong, F. L. (1994). Compositions, growth mechanisms, and temporal relations of hydrothermal sulfide-sulfate-silica chimneys at the northern cleft segment, juan de fuca ridge. *Journal of Geophysical Research: Solid Earth*, *99*(B3), 4813-4832. https://doi.org/10.1029/93JB02871

Krasnov, S. G., Cherkashev, G. A., Stepanova, T. V., Batuyev, B. N., Krotov, A. G., Malin, B. V., Maslov, M. N., Markov, V. F., Poroshina, I. M., Samovarov, M. S., Ashadze, A. M., Lazareva, L. I., & Ermolayev, I. K. (1995). Detailed geological studies of hydrothermal fields in the north Atlantic. *Geological Society, London, Special Publications*, *87*(1), 43-64. https://doi.org/10.1144/GSL.SP.1995.087.01.05

Krijthe, J. H. (2015). *Rtsne: T-distributed stochastic neighbor embedding using barnes-hut implementation. R package version 0.17*. https://github.com/jkrijthe/Rtsne

Kuznetsov, V., Maksimov, F., Zheleznov, A., Cherkashov, G., BeL'Tenev, V., & Lazareva, L. (2011). Th-230/U chronology of ore formation within the Semyenov hydrothermal district (13°31′ N) at the Mid-Atlantic Ridge. *Geochronometria*, *38*(1), 72-76. https://doi.org/10.2478/s13386-011-0001-1

Lang, D. C., Bailey, I., Wilson, P. A., Beer, C. J., Bolton, C. T., Friedrich, O., Newsam, C., Spencer, M. R., Gutjahr, M., Foster, G. L., Cooper, M. J., & Milton, J. A. (2014). The transition on North America from the warm humid Pliocene to the glaciated Quaternary traced by eolian dust deposition at a benchmark North Atlantic Ocean drill site. *Quaternary Science Reviews*, *93*, 125-141. https://doi.org/10.1016/j.quascirev.2014.04.005

Leckie, J. O., Benjamin, M. M., Hayes, K., Kaufman, G., & Altmann, S. (1980). Adsorption/coprecipitation of trace elements from water with iron oxyhydroxide (Technical Report). Stanford University, Department of Civil Engineering. https://doi.org/10.2172/5101674

Lehrmann, B., Cooper, M. J., Milton, J. A., & Murton, B. J. (2022). Formation, remobilisation and alteration processes at inactive hydrothermal vents: Insights from elemental analysis of Cu-(Fe-)S sulfides from TAG, Mid-Atlantic Ridge. *Mineralium Deposita*, *57*(8), 1431-1448. https://doi.org/10.1007/s00126-022-01106-2

Lesage, M., Juliani, C., & Ellefmo, S. L. (2018). Economic block model development for mining seafloor massive sulfides. *Minerals*, *8*(10). https://doi.org/10.3390/min8100468

Li, J., Sun, M., Qi, W., Zhou, Z., Hohl, S. V., & He, Z. (2024). Geochemical and Sr-Nd-Pb-Fe isotopic constraints on the formation of Fe-Si oxyhydroxide deposits at the ultraslow-spreading southwest Indian Ridge. *Geochemistry, Geophysics, Geosystems*, *25*(2), e2023GC011185. https://doi.org/10.1029/2023GC011185

Liao, S., Tao, C., Li, H., Barriga, F. J. A. S., Liang, J., Yang, W., Yu, J., & Zhu, C. (2018). Bulk geochemistry, sulfur isotope characteristics of the Yuhuang-1 hydrothermal field on the

ultraslow-spreading southwest Indian Ridge. *Ore Geology Reviews*, *96*, 13-27. https://doi.org/10.1016/j.oregeorev.2018.04.007

Lilley, M. D., Feely, R. A., & Trefry, J. H. (1995). Chemical and biochemical transformations in hydrothermal plumes. In *Seafloor hydrothermal systems: Physical, chemical, biological, and geological interactions* (pp. 369-391). https://doi.org/10.1029/GM091p0369

Lipton, I., Gleeson, E., & Munro, P. (2018). *Preliminary economic assessment of the solwara 1 project, bismarck sea, papua new guinea.* Report prepared by AMC Consultants Pty Ltd for Nautilus Minerals Inc., Issue. https://www.nautilusminerals.com

Long, E. R., Macdonald, D. D., Smith, S. L., & Calder, F. D. (1995). Incidence of adverse biological effects within ranges of chemical concentrations in marine and estuarine sediments. *Environmental Management*, *19*(1), 81-97. https://doi.org/10.1007/BF02472006

Lonsdale, P. (1977). Clustering of suspension-feeding macrobenthos near abyssal hydrothermal vents at oceanic spreading centers. *Deep Sea Research*, *24*(9), 857-863. https://doi.org/10.1016/0146-6291(77)90478-7

Lowell, S., Shields., J. E., Thomas, M. A., & Thommes, M. (2004). *Characterization of porous solids and powders: Surface area, pore size and density* (Vol. 1). Springer Dordrecht. https://doi.org/10.1007/978-1-4020-2303-3

Lundgren, D. G., & Silver, M. (1980). Ore leaching by bacteria. *Annual Review of Microbiology*, *34*, 263-283. https://doi.org/10.1146/annurev.mi.34.100180.001403

Lydon, J. W. (1984). Some observations on the mineralogical and chemical zonation patterns of volcanogenic sulphide deposits of Cyprus. *In Current research: part A, Geological Survey of Canada, Paper, 84-1A, 611-616.* https://doi.org/10.4095/119718

Lyle, M., Wilson, P. A., Janecek, T. R., et al. (2002). Leg 199 preliminary report. Proceedings of the Ocean Drilling Program, 199. https://doi.org/10.2973/odp.proc.ir.199.2002

MacQueen, J. B. (1967). Some methods for classification and analysis of multivariate observations. In L. M. Le Cam & J. Neyman (Eds.), *Proceedings of the 5th berkeley symposium on mathematical statistics and probability* (Vol. 5.1, pp. 281-297). University of California Press. http://projecteuclid.org/euclid.bsmsp/1200512992

Maechler, M., Rousseeuw, P., Struyf, A., Hubert, M., & Hornik, K. (2023). *Cluster: Cluster analysis basics and extensions. R package version 2.1.6* https://CRAN.R-project.org/package=cluster

Majima, H. (1969). How oxidation affects selective flotation of complex sulphide ores. *Canadian Metallurgical Quarterly*, *8*(3), 269-273. https://doi.org/10.1179/cmq.1969.8.3.269

Mann, A. W. (1984). Mobility of gold and silver in lateritic weathering profiles; some observations from western Australia. *Economic Geology*, *79*(1), 38-49. https://doi.org/10.2113/gsecongeo.79.1.38

Mann, H. B., & Whitney, D. R. (1947). On a test of whether one of two random variables is stochastically larger than the other. *The Annals of Mathematical Statistics*, *18*(1), 50-60. http://www.jstor.org/stable/2236101

Martin, A. J., McDonald, I., Jenkin, G. R. T., McFall, K. A., Boyce, A. J., Jamieson, J. W., & MacLeod, C. J. (2021). A missing link between ancient and active mafic-hosted seafloor hydrothermal systems – magmatic volatile influx in the exceptionally preserved Mala VMS deposit, Troodos, Cyprus. *Chemical Geology*, *567*, 120127. https://doi.org/10.1016/j.chemgeo.2021.120127

Martin, A. J., McDonald, I., Jamieson, J. W., Jenkin, G. R. T., McFall, K. A., Piercey, G., MacLeod, C. J., & Layne, G. D. (2022). Mineral-scale variation in the trace metal and sulfur isotope composition of pyrite: Implications for metal and sulfur sources in mafic VMS deposits. *Mineralium Deposita*, *57*(6), 911-933. https://doi.org/10.1007/s00126-021-01080-1

Martin, A. J., MacLeod, C. J., McFall, K. A., McDonald, I., Jamieson, J. W., & Cox, S. (2023). Ultramafic-hosted Ni-Cu-Co-(As) mineralization from an ancient oceanic transform fault zone in the Troodos Ophiolite, Cyprus: An analogue for ultramafic sea-floor massive sulfide mineralization? *Economic Geology*, *118*(5), 1125-1147. https://doi.org/10.5382/econgeo.4996

Maslennikov, V. V., Ayupova, N. R., Herrington, R. J., Danyushevskiy, L. V., & Large, R. R. (2012). Ferruginous and manganiferous haloes around massive sulphide deposits of the Urals. *Ore Geology Reviews*, *47*, 5-41. https://doi.org/10.1016/j.oregeorev.2012.03.008

Maslennikov, V. V., Cherkashov, G. A., Firstova, A. V., Ayupova, N. R., Beltenev, V. E., Melekestseva, I. Y., Artemyev, D. A., Tseluyko, A. S., & Blinov, I. A. (2023). Trace element assemblages of pseudomorphic iron oxyhydroxides of the Pobeda-1 Hydrothermal Field, 17°08.7′ N, Mid-Atlantic Ridge: The development of a halmyrolysis model from LA-ICP-MS data. *Minerals*, *13*(1). https://doi.org/10.3390/min13010004

McKnight, P. E., & Najab, J. (2010). Mann-whitney u test. In I. B. Weiner & W. E. Craighead (Eds.), *The corsini encyclopedia of psychology* (pp. 1-1). https://doi.org/10.1002/9780470479216.corpsy0524

McLennan, S. M. (1989). Rare earth elements in sedimentary rocks: Influence of provenance and sedimentary processes. In B. R. Lipin & G. A. McKay (Eds.), Geochemistry and mineralogy of rare earth elements (pp. 169-200). De Gruyter. https://doi.org/10.1515/9781501509032-010

Mehta, A. P., & Murr, L. E. (1983). Fundamental-studies of the contribution of galvanic interaction to acid-bacterial leaching of mixed metal sulfides. *Hydrometallurgy*, *9*(3), 235-256. https://doi.org/10.1016/0304-386x(83)90025-7

Meier, D. V., Pjevac, P., Bach, W., Markert, S., Schweder, T., Jamieson, J., Petersen, S., Amann, R., & Meyerdierks, A. (2019). Microbial metal-sulfide oxidation in inactive hydrothermal vent chimneys suggested by metagenomic and metaproteomic analyses. *Environmental Microbiology*, *21*(2), 682-701. https://doi.org/10.1111/1462-2920.14514

Melekestseva, I. Y., Tret'yakov, G. A., Nimis, P., Yuminov, A. M., Maslennikov, V. V., Maslennikova, S. P., Kotlyarov, V. A., Beltenev, V. E., Danyushevsky, L. V., & Large, R. (2014). Barite-rich massive sulfides from the Semenov-1 hydrothermal field (Mid-Atlantic Ridge, 13°30.87 ' N): Evidence for phase separation and magmatic input. *Marine Geology*, *349*, 37-54. https://doi.org/10.1016/j.margeo.2013.12.013

Melekestseva, I. Y., Maslennikov, V. V., Maslennikova, S. P., Danyushevsky, L. V., & Large, R. (2017a). Covellite of the Semenov-2 hydrothermal field (13°31.13′N, Mid-Atlantic Ridge): Enrichment in trace elements according to LA ICP MS analysis. *Doklady Earth Sciences*, *473*(1), 291-295. https://doi.org/10.1134/S1028334x17030060

Melekestseva, I. Y., Maslennikov, V. V., Tret'yakov, G. A., Nimis, P., Beltenev, V. E., Rozhdestvenskaya, I. I., Maslennikova, S. P., Belogub, E. V., Danyushevsky, L., Large, R., Yuminov, A. M., & Sadykov, S. A. (2017b). Gold- and silver-rich massive sulfides from the Semenov-2 hydrothermal field, 13°31.13′N, Mid-Atlantic Ridge: A case of magmatic contribution? *Economic Geology*, *112*(4), 741-773. https://doi.org/10.2113/econgeo.112.4.741

Melekestseva, I., Maslennikov, V. V., Safina, N. P., Nimis, P., Maslennikova, S., Beltenev, V., Rozhdestvenskaya, I., Danyushevsky, L., Large, R., Artemyev, D., Kotlyarov, V., & Toffolo, L. (2018). Sulfide breccias from the Semenov-3 hydrothermal field, Mid-Atlantic Ridge: Authigenic mineral formation and trace element pattern. *Minerals*, *8*(8). https://doi.org/10.3390/min8080321

Melekestseva, I. Y., Maslennikov, V. V., Ayupova, N. R., Belogub, E. V., Maslennikova, S. P., Bel'tenev, V. E., Danyushevsky, L., & Large, R. (2020a). Behavior of trace elements during oxidation of sphalerite of the Irinovskoe hydrothermal sulfide field (13° 20 ' N, Mid-Atlantic Ridge). *Geology of Ore Deposits*, *62*(3), 254-259. https://doi.org/10.1134/S1075701520030058

Melekestseva, I., Maslennikov, V., Tret'yakov, G., Maslennikova, S., Danyushevsky, L., Kotlyarov, V., Large, R., Beltenev, V., & Khvorov, P. (2020b). Trace element geochemistry of sulfides from the Ashadze-2 hydrothermal field (12°58 ' N, Mid-Atlantic Ridge): Influence of host rocks, formation conditions or seawater? *Minerals*, *10*(9). https://doi.org/10.3390/min10090743

Melekestseva, I., Kotlyarov, V., Tret'yakov, G., Shilovskikh, V., Khvorov, P., Belogub, E., Beltenev, V., Filippova, K., & Sadykov, S. (2022). The heavy-metal fingerprint of the Irinovskoe hydrothermal sulfide field, 13°20′ N, Mid-Atlantic Ridge. *Minerals*, *12*(12). https://doi.org/10.3390/min12121626

Menendez, A., James, R. H., Roberts, S., Peel, K., & Connelly, D. (2017). Controls on the distribution of rare earth elements in deep-sea sediments in the North Atlantic ocean. *Ore Geology Reviews*, *87*, 100-113. https://doi.org/10.1016/j.oregeorev.2016.09.036

Meysman, F. J. R. (2018). Cable bacteria take a new breath using long-distance electricity. *Trends in Microbiology*, *26*(5), 411-422. https://doi.org/10.1016/j.tim.2017.10.011

Michel, F. M., Ehm, L., Liu, G., Han, W. Q., Antao, S. M., Chupas, P. J., Lee, P. L., Knorr, K., Eulert, H., Kim, J., Grey, C. P., Celestian, A. J., Gillow, J., Schoonen, M. A. A., Strongin, D. R., & Parise, J. B. (2007). Similarities in 2- and 6-line ferrihydrite based on pair distribution function analysis of X-ray total scattering. *Chemistry of Materials*, *19*(6), 1489-1496. https://doi.org/10.1021/cm062585n

Middelburg, J. J. (2019). Carbon processing at the seafloor. In J. J. Middelburg (Ed.), *Marine carbon biogeochemistry : A primer for earth system scientists* (pp. 57-75). Springer International Publishing. https://doi.org/10.1007/978-3-030-10822-9_4

Miller, D. J. (1998). Data report: Geochemical analyses of massive sulfides and sediment samples from the TAG hydrothermal mound. In P. M. Herzig, S. E. Humphris, J. Miller, & R. A. Zierenberg (Eds.), *Proceedings of ocean drilling programme* (Vol. 158, pp. 41-46).

Mills, R., Elderfield, H., & Thomson, J. (1993). A dual origin for the hydrothermal component in a metalliferous sediment core from the Mid-Atlantic Ridge. *Journal of Geophysical Research: Solid Earth*, *98*(B6), 9671-9681. https://doi.org/10.1029/92JB01414

Mills, R. A., & Elderfield, H. (1995). Rare-earth element geochemistry of hydrothermal deposits from the active TAG Mound, 26°N Mid-Atlantic Ridge. *Geochimica Et Cosmochimica Acta*, *59*(17), 3511-3524. https://doi.org/10.1016/0016-7037(95)00224-N

Mitchell, R. (2015). Primary and secondary niobium mineral deposits associated with carbonatites. *Ore Geology Reviews*, *64*, 626-641. https://doi.org/10.1016/j.oregeorev.2014.03.010

Mondillo, N., Herrington, R., & Boni, M. (2021). Bauxites. In D. Alderton & S. A. Elias (Eds.), *Encyclopedia of geology (second edition)* (pp. 694-707). Academic Press. https://doi.org/10.1016/B978-0-08-102908-4.00046-1

Monecke, T., Petersen, S., Hannington, M. D., Grant, H., Samson, I. M., Verplanck, P. L., & Hitzman, M. W. (2016). The minor element endowment of modern sea-floor massive sulfides and comparison with deposits hosted in ancient volcanic successions. In P. L. Verplanck & M. W. Hitzman (Eds.), Rare earth and critical elements in ore deposits (Vol. 18, pp. 245-306). Society of Economic Geologists. https://doi.org/10.5382/Rev.18.11

Moon, E. M., & Peacock, C. L. (2012). Adsorption of Cu(ii) to ferrihydrite and ferrihydrite–bacteria composites: Importance of the carboxyl group for Cu mobility in natural environments. *Geochimica Et Cosmochimica Acta*, *92*, 203-219. https://doi.org/10.1016/j.gca.2012.06.012

Morato, T., Juliano, M., Pham, C. K., Carreiro-Silva, M., Martins, I., & Colaco, A. (2022). Modelling the dispersion of seafloor massive sulphide mining plumes in the Mid Atlantic Ridge around the Azores. *Frontiers in Marine Science*, *9*. https://doi.org/10.3389/fmars.2022.910940

Moses, C. O., Kirk Nordstrom, D., Herman, J. S., & Mills, A. L. (1987). Aqueous pyrite oxidation by dissolved oxygen and by ferric iron. *Geochimica Et Cosmochimica Acta*, *51*(6), 1561-1571. https://doi.org/10.1016/0016-7037(87)90337-1

Mottl, M. J. (1983). Metabasalts, axial hot springs, and the structure of hydrothermal systems at mid-ocean ridges. *Geological Society of America Bulletin*, *94*(2), 161-180. https://doi.org/10.1130/0016-7606(1983)94<161:MAHSAT>2.0.CO;2

Mudd, G. M., Weng, Z., Jowitt, S. M., Turnbull, I. D., & Graedel, T. E. (2013). Quantifying the recoverable resources of by-product metals: The case of cobalt. *Ore Geology Reviews*, *55*, 87-98. https://doi.org/10.1016/j.oregeorev.2013.04.010

Mudd, G. M., & Jowitt, S. M. (2014). A detailed assessment of global nickel resource trends and endowments. *Economic Geology*, *109*(7), 1813-1841. https://doi.org/10.2113/econgeo.109.7.1813

Mudd, G., Josso, P., Shaw, R., Luce, A., Singh, S., Horn, S., Bide, T., Currie, D., Elliott, H., Grant, H. L. J., Halkes, R., Idoine, N., Mitchell, C., Watkins, I., Price, F., & Petavratzi, E. (2024). UK 2024 criticality assessment. *British Geological Survey Open Report*, *OR/24/047*, 235pp.

Murnane, R., & Clague, D. A. (1983). Nontronite from a low-temperature hydrothermal system on the Juan de Fuca Ridge. *Earth and Planetary Science Letters*, *65*(2), 343-352. https://doi.org/10.1016/0012-821X(83)90172-3

Murton, B. J., Huhnerbach Veit, J., & Garrard Jo, J. (2012). Hybis: A new concept in versatile, 6000-m rated robotic underwater vehicles. *Further Advances in Unmanned Marine Vehicles*, 45-67. https://doi.org/10.1049/PBCE077E_ch3

Murton, B. J., Lehrmann, B., Dutrieux, A. M., Martins, S., de la Iglesia, A. G., Stobbs, I. J., Barriga, F. J. A. S., Bialas, J., Dannowski, A., Vardy, M. E., North, L. J., Yeo, I. A. L. M., Lusty, P. A. J., & Petersen, S. (2019). Geological fate of seafloor massive sulphides at the TAG hydrothermal field (Mid-Atlantic Ridge). *Ore Geology Reviews*, *107*, 903-925. https://doi.org/10.1016/j.oregeorev.2019.03.005

Murton, B. J., & Rona, P. A. (2015). Carlsberg ridge and Mid-Atlantic Ridge: Comparison of slow spreading centre analogues. *Deep-Sea Research Part II-Topical Studies in Oceanography*, *121*, 71-84. https://doi.org/10.1016/j.dsr2.2015.04.021

Murton, B. J., & Shipboard Scientific Party. (2018). *Cruise report: Expedition JC138: 29th June-8th August 2016, Mid Atlantic Ridge, 26°8.38'N; 44°49.92'W, National Oceanography Centre Southampton*. https://www.bodc.ac.uk/resources/inventories/cruise_inventory/reports/jc138.pdf

Murton, B. J., & Shipboard Scientific Party. (2022). *Cruise report: Expedition JC224: Project ULTRA Cruise #1, 3rd March - 20th May 2022, 13°30'N Mid Atlantic ridge, National Oceanography Centre, Southampton*. https://www.bodc.ac.uk/resources/inventories/cruise_inventory/reports/jc224.pdf

Nambu, M. (1968). New mineral akaganeite, β-FeOOH, from Akagane mine, Iwate Prefecture, Japan. *The Journal of the Japanese Association of Mineralogists, Petrologists and Economic Geologists*, *59*(4), 143-151. https://doi.org/10.2465/ganko1941.59.143

Nicholson, R. V., Gillham, R. W., & Reardon, E. J. (1988). Pyrite oxidation in carbonate-buffered solution: 1. Experimental kinetics. *Geochimica Et Cosmochimica Acta*, *52*(5), 1077-1085. https://doi.org/10.1016/0016-7037(88)90262-1

OECD. (2019). *Global material resources outlook to 2060: Economic drivers and environmental consequences*. OECD Publishing, Paris. https://doi.org/10.1787/9789264307452-en

Olivares, J. A., & Houk, R. S. (1986). Suppression of analyte signal by various concomitant salts in inductively coupled plasma mass spectrometry. *Analytical Chemistry*, *58*(1), 20-25. https://doi.org/10.1021/ac00292a008

Parameswaran, N., González, E., Burwicz-Galerne, E., Braack, M., & Wallmann, K. (2025). NN-TOC v1: Global prediction of total organic carbon in marine sediments using deep neural networks. *Geoscientific Model Development*, *18*(9), 2521-2544. https://doi.org/10.5194/gmd-18-2521-2025

Paton, C., Hellstrom, J., Paul, B., Woodhead, J., & Hergt, J. (2011). Iolite: Freeware for the visualisation and processing of mass spectrometric data. *Journal of Analytical Atomic Spectrometry. 26, 2508-2518*. https://doi.org/10.1039/C1JA10172B

Patten, C. G. C., Coltat, R., Junge, M., Peillod, A., Ulrich, M., Manatschal, G., & Kolb, J. (2022). Ultramafic-hosted volcanogenic massive sulfide deposits: An overlooked sub-class of VMS deposit forming in complex tectonic environments. *Earth-Science Reviews*, *224*, 103891. https://doi.org/10.1016/j.earscirev.2021.103891

Paul, B., Petrus, J., Savard, D., Woodhead, J., Hergt, J., Greig, A., Paton, C., & Rayner, P. (2023). Time resolved trace element calibration strategies for LA-ICP-MS. *Journal of Analytical Atomic Spectrometry*, *38*(10), 1995-2006. https://doi.org/10.1039/D3JA00037K

Pelleter, E.-L., Principaud, M., Alix, A.-S., Boissier, A., Cheron, S., Besson, F., Altorffer, V., Guérin, C., Gaillot, A., Pierre, D., Rospabé, M., Giunta, T., Grenet, L., Cathalot, C., Cambon, M.-A., & Fouquet, Y. (2024). Diversity, spatial distribution and evolution of inactive and weakly active hydrothermal deposits in the TAG hydrothermal field. *Frontiers in Earth Science*, *12*. https://www.frontiersin.org/articles/10.3389/feart.2024.1304993

Peltonen, P., Kontinen, A., Huhma, H., & Kuronen, U. (2008). Outokumpu revisited: New mineral deposit model for the mantle peridotite-associated Cu-Co-Zn-Ni-Ag-Au sulphide deposits. *Ore Geology Reviews*, *33*(3-4), 559-617. https://doi.org/10.1016/j.oregeorev.2007.07.002

Pertsev, A. N., Bortnikov, N. S., Vlasov, E. A., Beltenev, V. E., Dobretsov, I. G., & Ageeva, O. A. (2012). Recent massive sulfide deposits of the Semenov ore district, Mid-Atlantic Ridge, 13°31′ N: Associated rocks of the oceanic core complex and their hydrothermal

alteration. *Geology of Ore Deposits*, *54*(5), 334-346. https://doi.org/10.1134/S1075701512050030

Petersen, S. (2000). *The geochemical and mineralogical evolution of the TAG hydrothermal field, Mid-Atlantic Ridge, 26° N*. (Unpublished doctoral dissertation, Technical University Bergakademie Freiberg, Germany).

Petersen, S., Herzig, P. M., & Hannington, M. D. (2000). Third dimension of a presently forming VMS deposit: TAG hydrothermal mound, Mid-Atlantic Ridge, 26°N. *Mineralium Deposita*, *35*(2-3), 233-259. https://doi.org/10.1007/s001260050018

Petersen, S., Kraschell, A., Augustin, N., Jamieson, J., Hein, J. R., & Hannington, M. D. (2016). News from the seabed - geological characteristics and resource potential of deep-sea mineral resources. *Marine Policy*, *70*, 175-187. https://doi.org/10.1016/j.marpol.2016.03.012

Petersen, S., Lehrmann, B., & Murton, B. J. (2018). Modern seafloor hydrothermal systems: New perspectives on ancient ore-forming processes. *Elements*, *14*(5), 307-312. https://doi.org/10.2138/gselements.14.5.307

Pollard, A. M., Thomas, R. G., & Williams, P. A. (1989). Synthesis and stabilities of the basic copper(ii) chlorides atacamite, paratacamite and botallackite. *Mineralogical Magazine*, *53(373)*, 557-563. https://doi.org/10.1180/minmag.1989.053.373.06

Poulton, S. W., & Canfield, D. E. (2005). Development of a sequential extraction procedure for iron: Implications for iron partitioning in continentally derived particulates. *Chemical Geology*, *214*(3-4), 209-221. https://doi.org/10.1016/j.chemgeo.2004.09.003

Ran, Y., Fu, J., Rate, A. W., & Gilkes, R. J. (2002). Adsorption of Au(i, iii) complexes on Fe, Mn oxides and humic acid. *Chemical Geology*, *185*(1), 33-49. https://doi.org/10.1016/S0009-2541(01)00393-X

Ravizza, G., Blusztajn, J., & Prichard, H. M. (2001). Re–Os systematics and platinum-group element distribution in metalliferous sediments from the Troodos Ophiolite. *Earth and Planetary Science Letters*, *188*(3), 369-381. https://doi.org/10.1016/S0012-821X(01)00337-5

Reimers, C. E., Kalhorn, S., Emerson, S. R., & Nealson, K. H. (1984). Oxygen consumption rates in pelagic sediments from the central Pacific: First estimates from microelectrode profiles. *Geochimica Et Cosmochimica Acta*, *48*(5), 903-910. https://doi.org/10.1016/0016-7037(84)90183-2

Reith, F., Lengke, M. F., Falconer, D., Craw, D., & Southam, G. (2007). The geomicrobiology of gold. *The ISME Journal*, *1*(7), 567-584. https://doi.org/10.1038/ismej.2007.75

Restreppo, G. A., Wood, W. T., & Phrampus, B. J. (2020). Oceanic sediment accumulation rates predicted via machine learning algorithm: Towards sediment characterization on a global scale. *Geo-Marine Letters*, *40*(5), 755-763. https://doi.org/10.1007/s00367-020-00669-1

Robertson, A. H. F., & Fleet, A. J. (1976). The origins of rare earths in metalliferous sediments of the Troodos Massif. Cyprus. *Earth and Planetary Science Letters*, *28*(3), 385-394. https://doi.org/10.1016/0012-821X(76)90200-4

Rona, P. A. (1984). Hydrothermal mineralization at seafloor spreading centers. *Earth-Science Reviews*, *20*(1), 1-104. https://doi.org/10.1016/0012-8252(84)90080-1

Rona, P. A. (1988). Hydrothermal mineralization at oceanic ridges. *Canadian Mineralogist*, *26*, 431-465.

Rose, A. W. (1976). The effect of cuprous chloride complexes in the origin of red-bed copper and related deposits. *Economic Geology*, *71*(6), 1036-1048. https://doi.org/10.2113/gsecongeo.71.6.1036

Roy, S. (1992). Environments and processes of manganese deposition. *Economic Geology*, *87*(5), 1218-1236. https://doi.org/10.2113/gsecongeo.87.5.1218

Rusakov, V., Shilov, V., Ryzhenko, B., Gablina, I., Roshchina, I., Kuz'mina, T., Kononkova, N., & Dobretsova, I. (2013). Mineralogical and geochemical zoning of sediments at the Semenov cluster of hydrothermal fields, 13°31′-13°30′ N, Mid-Atlantic Ridge. *Geochemistry International*, *51*, 646-669. https://doi.org/10.1134/S0016702913050066

Sahlström, F., Strmić Palinkaš, S., Hjorth Dundas, S., Sendula, E., Cheng, Y., Wold, M., & Pedersen, R. B. (2023). Mineralogical distribution and genetic aspects of cobalt at the active Fåvne and Loki's castle seafloor massive sulfide deposits, Arctic mid-ocean ridges. *Ore Geology Reviews*, *153*, 105261. https://doi.org/10.1016/j.oregeorev.2022.105261

Sajih, M., Bryan, N. D., Livens, F. R., Vaughan, D. J., Descostes, M., Phrommavanh, V., Nos, J., & Morris, K. (2014). Adsorption of radium and barium on goethite and ferrihydrite: A kinetic and surface complexation modelling study. *Geochimica Et Cosmochimica Acta*, *146*, 150-163. https://doi.org/10.1016/j.gca.2014.10.008

Schippers, A., Jozsa, P., & Sand, W. (1996). Sulfur chemistry in bacterial leaching of pyrite. *Applied and environmental microbiology*, *62*(9), 3424-3431. https://doi.org/10.1128/aem.62.9.3424-3431.1996

Schmidt, K., Koschinsky, A., Garbe-Schönberg, D., Carvalho, L., & Seifert, R. (2007). Geochemistry of hydrothermal fluids from the ultramafic-hosted Logatchev field, 15°N MAR. *Chemical Geology*, *242*, 1-21. https://doi.org/10.1016/j.chemgeo.2007.01.023

Schwertmann, U., & Murad, E. (1983). Effect of pH on the formation of goethite and hematite from ferrihydrite. *Clays and Clay Minerals*, *31*(4), 277-284. https://doi.org/10.1346/CCMN.1983.0310405

Schwertmann, U. (1991). Solubility and dissolution of iron oxides. In Y. Chen & Y. Hadar (Eds.), *Iron nutrition and interactions in plants* (Developments in Plant and Soil Sciences, Vol. 43, pp. 3–27). Springer. https://doi.org/10.1007/978-94-011-3294-7_1

Schwertmann, U., Stanjek, H., & Becher, H. H. (2004). Long-term in vitro transformation of 2-line ferrihydrite to goethite/hematite at 4, 10, 15 and 25°C. *Clay Minerals*, *39*(4), 433-438. https://doi.org/10.1180/0009855043940145

Scotney, P. M. (2002). The geology and genesis of massive sulphide, barite-gold deposits on Wetar Island, Indonesia (Unpublished doctoral dissertation, University of Southampton). University of Southampton ePrints. http://eprints.soton.ac.uk/464943/

Seal, R. R., II, Schulz, K. J., & DeYoung, J. H., Jr. (2017). Antimony. In K. J. Schulz, J. H. DeYoung Jr., R. R. Seal II, & D. C. Bradley (Eds.), Critical mineral resources of the United States—Economic and environmental geology and prospects for future supply (pp. C1–C17). U.S. Geological Survey Professional Paper 1802. https://doi.org/10.3133/pp1802C

Seewald, J. S., & Seyfried, W. E. (1990). The effect of temperature on metal mobility in subseafloor hydrothermal systems - constraints from basalt alteration experiments. *Earth and Planetary Science Letters*, *101*(2-4), 388-403. https://doi.org/10.1016/0012-821X(90)90168-W

Seyfried, W. E., & Mottl, M. J. (1982). Hydrothermal alteration of basalt by sea-water under seawater-dominated conditions. *Geochimica Et Cosmochimica Acta*, *46*(6), 985-1002. https://doi.org/10.1016/0016-7037(82)90054-0

Sharkey, J. B., & Lewin, S. Z. (1971). Conditions governing the formation of atacamite and paratacamite. *The American Mineralogist, 56*, 179-192.

Sillitoe, R. H., & McKee, E. H. (1996). Age of supergene oxidation and enrichment in the Chilean porphyry copper province. *Economic Geology*, *91*(1), 164-179. https://doi.org/10.2113/gsecongeo.91.1.164

Simpson, S., Angel, B., Hamilton, I., Spadaro, D., & Binet, M. (2007). Water and sediment characterization and toxicity assessment for the Solwara 1 project. *Environmental Impact Statement; Natural Minerals Inc.: Australia; Appendices*, 4-7.

Simpson, S. L., & Spadaro, D. A. (2016). Bioavailability and chronic toxicity of metal sulfide minerals to benthic marine invertebrates: Implications for deep sea exploration, mining and tailings disposal. *Environmental Science & Technology*, *50*(7), 4061-4070. https://doi.org/10.1021/acs.est.6b00203

Singer, P. C., & Stumm, W. (1970). Acidic mine drainage. Rate-determining step. *Science*, *167*(3921), 1121-1123. https://doi.org/10.1126/science.167.3921.1121

SPC. (2013). *Deep sea minerals: Sea-floor massive sulphides, a physical, biological, environmental, and technical review* (E. Baker & Y. Beaudoin, Eds.; Vol. 1A). Secretariat of the Pacific Community.

Spinelli, G. A., Giambalvo, E. G., & Fisher, A. T. (2004). Hydrologic properties and distribution of sediments. In E. E. Davis & H. Elderfield (Eds.), *Hydrogeology of the oceanic lithosphere* (pp. 151-188). Cambridge University Press.

Standish, C. D., Milton, J. A., Page, T. M., Brown, R. M., Douglas, D., Paul, B., Schlatt, L., & Foster, G. L. (2024). 2d geochemical imaging of biogenic marine carbonates using la-tof-icp-ms at 1 and 2 μm pixel resolution. *Chemical Geology*, *670*, 122438. https://doi.org/10.1016/j.chemgeo.2024.122438

Stauber, J. L., Adams, M. S., Batley, G. E., Golding, L. A., Hargreaves, I., Peeters, L., Reichelt-Brushett, A. J., & Simpson, S. L. (2022). A generic environmental risk assessment framework for deep-sea tailings placement. *Science of the Total Environment*, *845*. https://doi.org/10.1016/j.scitotenv.2022.157311

Sulzberger, B., Suter, D., Siffert, C., Banwart, S., & Stumm, W. (1989). Dissolution of fe(iii)(hydr)oxides in natural waters; laboratory assessment on the kinetics controlled by surface coordination. *Marine Chemistry*, *28*(1), 127-144. https://doi.org/10.1016/0304-4203(89)90191-6

Sun, S. s., & McDonough, W. F. (1989). Chemical and isotopic systematics of oceanic basalts: Implications for mantle composition and processes. *Geological Society, London, Special Publications*, *42*(1), 313-345. https://doi.org/10.1144/GSL.SP.1989.042.01.19

Sylvan, J. B., Toner, B. M., & Edwards, K. J. (2012). Life and death of deep-sea vents: Bacterial diversity and ecosystem succession on inactive hydrothermal sulfides. *mBio*, *3*(1). https://doi.org/10.1128/mBio.00279-11

Ta, K., Wu, Z., Peng, X., Luan, Z., & Chen, S. (2021). Formation and origin of Fe-Si oxyhydroxide deposits at the ultra-slow spreading Southwest Indian Ridge. *Deep Sea Research Part I: Oceanographic Research*, *170*, 103491. https://doi.org/10.1016/j.dsr.2021.103491

Tabelin, C. B., Corpuz, R. D., Igarashi, T., Villacorte-Tabelin, M., Alorro, R. D., Yoo, K., Raval, S., Ito, M., & Hiroyoshi, N. (2020). Acid mine drainage formation and arsenic mobility under strongly acidic conditions: Importance of soluble phases, iron oxyhydroxides/oxides and nature of oxidation layer on pyrite. *Journal of Hazardous Materials*, *399*, 122844. https://doi.org/10.1016/j.jhazmat.2020.122844

Tanaka, T., Togashi, S., Kamioka, H., Amakawa, H., Kagami, H., Hamamoto, T., Yuhara, M., Orihashi, Y., Yoneda, S., Shimizu, H., Kunimaru, T., Takahashi, K., Yanagi, T., Nakano, T., Fujimaki, H., Shinjo, R., Asahara, Y., Tanimizu, M., & Dragusanu, C. (2000). JNdi-1: A neodymium isotopic reference in consistency with LaJolla neodymium. *Chemical Geology*, *168*(3), 279-281. https://doi.org/10.1016/S0009-2541(00)00198-4

Taylor, R. N., Ishizuka, O., Michalik, A., Milton, J. A., & Croudace, I. W. (2015). Evaluating the precision of Pb isotope measurement by mass spectrometry. *Journal of Analytical Atomic Spectrometry*, *30*(1), 198-213. https://doi.org/10.1039/c4ja00279b

Tivey, M. K. (2007). Generation of seafloor hydrothermal vent fluids and associated mineral deposits. *Oceanography*, *20*(1), 50-65. https://doi.org/10.5670/oceanog.2007.80

Toffolo, L., Nimis, P., Tret'yakov, G. A., Melekestseva, I. Y., & Beltenev, V. E. (2020). Seafloor massive sulfides from mid-ocean ridges: Exploring the causes of their geochemical variability with multivariate analysis. *Earth-Science Reviews*, *201*, 102958. https://doi.org/10.1016/j.earscirev.2019.102958

Toner, B., Santelli, C., Marcus, M., Wirth, R., Chan, C., McCollom, T., Bach, W., & Edwards, K. (2009). Biogenic iron oxyhydroxide formation at mid-ocean ridge hydrothermal vents: Juan de Fuca Ridge. *Geochimica Et Cosmochimica Acta*, *73*, 388-403. https://doi.org/10.1016/j.gca.2008.09.035

Trading Economics. (2024). *Commodity prices*. Retrieved October 2024 from https://tradingeconomics.com/

Tronc, E., Belleville, P., Jolivet, J. P., & Livage, J. (1992). Transformation of ferric hydroxide into spinel by iron(ii) adsorption. *Langmuir*, *8*(1), 313-319. https://doi.org/10.1021/la00037a057

Tucholke, B. E., Behn, M. D., Buck, W. R., & Lin, J. (2008). Role of melt supply in oceanic detachment faulting and formation of megamullions. *Geology*, *36*(6), 455-458. https://doi.org/10.1130/g24639a.1

U.S. Geological Survey. (2024). *Mineral Commodity Summaries 2024* (Mineral Commodity Summaries 2024, 212 pp.). U.S. Geological Survey. https://doi.org/10.3133/mcs2024

van der Maaten, L. J. P., & Hinton, G. E. (2008). Visualizing high-dimensional data using t-SNE. *Journal of Machine Learning Research*, *9*, 2579-2605.

Van Dover, C. L. (2011). Mining seafloor massive sulphides and biodiversity: What is at risk? *ICES Journal of Marine Science*, *68*(2), 341-348. https://doi.org/10.1093/icesjms/fsq086

Vikentyev, I. V., Belogub, E. V., Novoselov, K. A., & Moloshag, V. P. (2017). Metamorphism of volcanogenic massive sulphide deposits in the Urals. Ore geology. *Ore Geology Reviews*, *85*, 30-63. https://doi.org/10.1016/j.oregeorev.2016.10.032

Von Damm, K. L., Edmond, J. M., Grant, B., Measures, C. I., Walden, B., & Weiss, R. F. (1985). Chemistry of submarine hydrothermal solutions at 21 °N, East Pacific Rise. *Geochimica Et Cosmochimica Acta*, *49*(11), 2197-2220. https://doi.org/10.1016/0016-7037(85)90222-4

Vu, H. P., Shaw, S., Brinza, L., & Benning, L. G. (2013). Partitioning of Pb(ii) during goethite and hematite crystallization: Implications for Pb transport in natural systems. *Applied Geochemistry*, *39*, 119-128. https://doi.org/10.1016/j.apgeochem.2013.10.001

Wang, S., Li, C., Li, B., Dang, Y., Ye, J., Zhu, Z., Zhang, L., & Shi, X. (2022). Constraints on fluid evolution and growth processes of black smoker chimneys by pyrite geochemistry: A case study of the Tongguan hydrothermal field, South Mid-Atlantic Ridge. *Ore Geology Reviews*, *140*, 104410. https://doi.org/10.1016/j.oregeorev.2021.104410

Watari, T., Nansai, K., & Nakajima, K. (2021). Major metals demand, supply, and environmental impacts to 2100: A critical review. *Resources, Conservation and Recycling*, *164*, 105107. https://doi.org/10.1016/j.resconrec.2020.105107

Weaver, P. P. E., Billett, D. S. M., & Van Dover, C. L. (2018). Environmental risks of deep-sea mining. In M. Salomon & T. Markus (Eds.), *Handbook on marine environment protection : Science, impacts and sustainable management* (pp. 215-245). Springer International Publishing. https://doi.org/10.1007/978-3-319-60156-4_11

Webber, A. P., Roberts, S., Murton, B. J., & Hodgkinson, M. R. S. (2015). Geology, sulfide geochemistry and supercritical venting at the Beebe Hydrothermal Vent Field, Cayman Trough. *Geochemistry, Geophysics, Geosystems*, *16*(8), 2661-2678. https://doi.org/10.1002/2015GC005879

Webster, J. G. (1986). The solubility of gold and silver in the system Au-Ag-S-O2-H2O at 25°C and 1 atm. *Geochimica Et Cosmochimica Acta*, *50*(9), 1837-1845. https://doi.org/10.1016/0016-7037(86)90242-5

Webster, J. G., & Mann, A. W. (1984). The influence of climate, geomorphology and primary geology on the supergene migration of gold and silver. *Journal of Geochemical Exploration*, *22*(1-3), 21-42. https://doi.org/10.1016/0375-6742(84)90004-9

Wells, D. M. (1998). Rare earth element systematics in ancient and modern hydrothermal systems (Doctoral dissertation, University of Southampton, UK). University of Southampton ePrints. https://eprints.soton.ac.uk/42176/

Weng, Z., Jowitt, S. M., Mudd, G. M., & Haque, N. (2015). A detailed assessment of global rare earth element resources: Opportunities and challenges. *Economic Geology*, *110*(8), 1925-1952. https://doi.org/10.2113/econgeo.110.8.1925

Wheeler, A. J., Murton, B., Copley, J., Lim, A., Carlsson, J., Collins, P., Dorschel, B., Green, D., Judge, M., Nye, V., Benzie, J., Antoniacomi, A., Coughlan, M., & Morris, K. (2013). Moytirra: Discovery of the first known deep-sea hydrothermal vent field on the slow-spreading Mid-Atlantic Ridge north of the Azores. *Geochemistry, Geophysics, Geosystems*, *14*(10), 4170-4184. https://doi.org/10.1002/ggge.20243

Wickham, H. (2016). *ggplot2: Elegant graphics for data analysis*. Springer-Verlag New York. https://doi.org/10.1007/978-3-319-24277-4

Wickham, H., & Bryan, J. (2023). *Readxl: Read excel files.*, https://github.com/tidyverse/readxl

Wickham, H., François, R., Henry, L., Müller, K., & Vaughan, D. (2023). *Dplyr: A grammar of data manipulation. R package version 1.1.4*. https://github.com/tidyverse/dplyr

Wilson, S. C., Murton, B. J., & Taylor, R. N. (2013). Mantle composition controls the development of an oceanic core complex. *Geochemistry Geophysics Geosystems*, *14*(4), 979-995. https://doi.org/10.1002/ggge.20046

Woods, T. L., & Garrels, R. M. (1986). Phase relations of some cupric hydroxy minerals. *Economic Geology*, *81*(8), 1989-2007. https://doi.org/10.2113/gsecongeo.81.8.1989

Yang, B., Zeng, Z., & Wang, X. (2015). Characteristics of Sr, Nd and Pb isotopic compositions of hydrothermal Si-Fe-Mn-oxyhydroxides at the PACMANUS hydrothermal field, Eastern Manus Basin. *Acta Oceanologica Sinica*, *34*(8), 27-34. https://doi.org/10.1007/s13131-015-0706-8

Yesares, L., Saez, R., Nieto, J. M., de Almodovar, G. R., & Cooper, S. (2014). Supergene enrichment of precious metals by natural amalgamation in the Las Cruces weathering profile (Iberian Pyrite Belt, SW Spain). *Ore Geology Reviews*, *58*, 14-26. https://doi.org/10.1016/j.oregeorev.2013.10.004

Yin, Y., Wang, T., & Zhang, C. (2025). Numerical study of the land-sourced iron precipitation and its effects on porewater flow at subterranean estuaries. *Chemical Geology*, *682*, 122744. https://doi.org/10.1016/j.chemgeo.2025.122744

Yu, J., Tao, C., Liao, S., Alveirinho Dias, Á., Liang, J., Yang, W., & Zhu, C. (2021). Resource estimation of the sulfide-rich deposits of the Yuhuang-1 hydrothermal field on the ultraslow-spreading Southwest Indian Ridge. *Ore Geology Reviews*, *134*, 104169. https://doi.org/10.1016/j.oregeorev.2021.104169

Zeng, Z., Wang, X., Zhang, G., Yin, X., Chen, D., & Wang, X. (2008). Formation of Fe-oxyhydroxides from the East Pacific Rise near latitude 13°N: Evidence from mineralogical and geochemical data. *Science in China Series D: Earth Sciences*, *51*(2), 206-215. https://doi.org/10.1007/s11430-007-0131-8

Zeng, Z., Chen, D., Yin, X., Wang, X., Zhang, G., & Wang, X. (2010). Elemental and isotopic compositions of the hydrothermal sulfide on the East Pacific Rise near 13°N. *Science China Earth Sciences*, *53*(2), 253-266. https://doi.org/10.1007/s11430-010-0013-3